Earthquake ground motion in Belgium: Contribution to a high quality database, Analysis of anelastic attenuation, and Evaluation of ground motion models

Mahsa Onvani

Royal Observatory of Belgium
Université catholique de Louvain

Thesis submitted in Fulfilment of the Requirements of
Degree of Doctor in Engineering Sciences and Technology

Supervisors

Dr. Kris **Vanneste**	*Royal Observatory of Belgium*
Prof. Dr. João Saraiva Esteves Pacheco de **Almeida**	*Université catholique de Louvain*

Thesis committe

Prof. Dr. Paul **Fisette** [jury president]	*Université catholique de Louvain*
Prof. Dr. Hadrien **Rattez** [secretary]	*Université catholique de Louvain*
Dr. Thierry **Camelbeeck**	*Royal Observatory of Belgium*
Dr. Paola **Traversa**	*Électricité de France (EDF)*
Dr. Helen **Crowley**	*Global Earthquake Model (GEM)*
Prof. Dr. Hervé **Degée**	*Hasselt University*

Summary

This PhD research was carried out within the framework of the BELSHAKE project, a BELSPO-funded project in the Seismology & Gravimetry department of the Royal Observatory of Belgium that aims to improve the understanding of earthquake ground motions in Belgium and adjacent regions. Belgium is characterized by a low to moderate level of seismicity, yet seismic hazard assessment remains essential for infrastructure design, risk mitigation, and nuclear safety. Reliable hazard assessment requires both high quality observational data and robust ground motion models adapted to regional conditions.

The BELSHAKE project was structured around two main objectives. The first was to compile a comprehensive database of earthquake ground motions for Belgium, including systematic collection and uniform processing. The second objective was to develop the capacity to model earthquake ground motions in Belgium, through the analysis of seismic attenuation, the evaluation of existing ground-motion models (GMMs), and the development or calibration of regionally appropriate models.

This thesis contributes to both objectives by:

- Contribution to the compilation of a high-quality ground-motion dataset, including importing all waveforms and recording stations, and applying waveforms quality check,
- implementing a windowing workflow,
- applying different approaches to check data consistency,
- analysis of attenuation in Belgium through the high-frequency anelastic attenuation parameter kappa,
- evaluation of the goodness of fit of published ground motion prediction models with respect to the BELSHAKE database.

The compilation of the database required a systematic inventory of all available digital waveform data in the archive of the Royal Observatory of Belgium (ROB), supplemented by international data repositories. Approximately 344 earthquakes events with local magnitudes (M_L) ranging from 2.0 to 5.8, focal depths shallower than 30 km, and hypocentral distances (R_{hypo}) up to 500 km, were imported, and relevant source

parameters and station metadata were extracted for each. Raw waveform data were downloaded into a dedicated archive, and an automated time-windowing was developed to capture noise, P, S, and coda windows. Two windowing algorithms from the literature (Goulet et al., 2014; Perron et al., 2018) were implemented and tested on the BELSHAKE data. The comparison revealed that the Goulet method provides robust definitions of signal windows (P, S and coda), while the Perron method offers more sophisticated treatment of noise windows. This thesis therefore proposes and validated a hybrid approach, combining the strengths of both methods. This innovation increased the reliability of the windowing step and decreased the number of waveforms without a noise window.

A visual inspection of each record, each component, and each window ensured the removal, correction, or flagging of problems such as timing errors, low signal-to-noise ratios, clipping, or other anomalies. This information was added to the metadata and used to categorize the waveforms into good, intermediate, and bad quality. The P- and S-wave arrivals were also checked and adjusted when necessary. This was a very important step to ensure high-quality data, and only the good and intermediate quality records identified during the visual check were considered in the next processing steps. The processing was also performed on an event-by-event basis using established tools, the reliable frequency range was evaluated for each record and the intensity measures were computed from these high-quality processed records.

To evaluate data quality, a series of consistency checks were applied to the intensity measures. Instrument response problems were identified and corrected where possible, and problematic records were flagged. Residual analyses were then performed against a generic GMM. These steps allowed the detection and correction of component swaps, anomalous amplitudes, and resonance issues, while also confirming the overall compatibility of BELSHAKE with external datasets such as the French RESIF database (Traversa et al., 2020). Although some minor issues remain under investigation, the resulting dataset is of high quality and suitable for robust scientific analysis.

Understanding seismic attenuation in Belgium is important for adapting ground-motion models to local conditions. The high-frequency anelastic attenuation parameter κ was computed using the classic method of Anderson and Hough (1984) for about 7,800 event–station pairs using acceleration Fourier amplitude spectra of S-waves. The resulting κ values were then analyzed as a function of distance to separate site-specific (κ_0) and path-dependent (κ_r) components. Three estimation methods were compared: the Free kappa gradient, the Joint kappa gradient, and Mixed effects regression methods. Station-specific κ_0 values range from ~14 to 59 ms for the H component and from ~12 to 53 ms for the Z component for all stations in Belgium. The regional κ_r ranges from 0.13 to 0.17 ms/km for the H component, and from 0.05 to 0.1 ms/km for the Z component. Considering an average S-wave velocity of 3.6 km/s, the frequency-independent quality factors (Q) range from ~1600 to 2100 for the H component, and from 2700 to 3900 for the Z component. These results advance our understanding of anelastic attenuation in Belgium and will support the development of improved GMMs and seismic hazard models for stable continental regions.

The BELSHAKE dataset was used to test the compatibility of the 20 published GMMs with the geological context of Belgium. These GMMs were developed based on European, NGA-West (Next Generation of Ground-Motion Attenuation Models for the western United States), NGA-East (Next Generation of Ground-Motion Attenuation Models for the Central and Eastern US), Japanese, global, and regional datasets. Multiple statistical measures were employed to evaluate the goodness of fit of these GMMs. The comparison revealed that some European (Akkar et al., 2014; Bindi et al., 2014), NGA-West (Abrahamson et al., 2014; Campbell and Bozorgnia, 2014), and regional models (Edwards and Douglas, 2013) performed consistently well, while others showed systematic biases or poor fit. The final ranking highlights a subset of GMMs that are best suited for seismic hazard studies in Belgium, providing guidance for future national and regional assessments.

The outcomes of this thesis support improved seismic hazard assessment in Belgium by providing a quality-checked ground-motion dataset, regional and site-specific attenuation (κ) estimates, and a systematic comparison of published GMMs to this dataset. Together, these contributions form a coherent and transparent foundation for hazard studies in low-to-moderate seismicity regions, strengthening the scientific basis for earthquake-resistant design and risk mitigation in Belgium and beyond.

Acknowledgements

The journey of this PhD has been long and demanding, shaped not only by academic work but also by significant personal challenges and responsibilities along the way. It has been a period of both professional growth and profound life changes, requiring resilience, patience, and perseverance. I would like to take this opportunity to express my sincere gratitude to those who have guided, supported, and stood by me throughout these years, making it possible to reach this point.

First and foremost, I would like to express my deepest gratitude to my supervisor, Dr. Kris Vanneste. Without his vision, insight, structured guidance, and continuous support, this thesis would not have been possible. I am especially thankful for his ability to guide me through both the technical and conceptual aspects of this research. He was always available when I needed advice, and his involvement and trust played a crucial role in shaping this work.

I would also like to sincerely thank Prof. João Almeida for accepting to supervise this thesis that was not directly within his main field of expertise. I am deeply grateful for his constant support. He was always willing to listen and help, not only in academic matters but also during difficult moments.

I am especially grateful for the time both of my supervisors took to support me during periods of high stress, particularly when I was affected by the situation in my home country.

I would like to thank the members of my supervisory panel for their valuable input and guidance: Dr. Paola Traversa and Dr. Helen Crowley. My thanks go to Dr. Paola Traversa, for her insightful suggestions, encouragement, and for generously sharing her experience and ideas throughout this project. I would like to extend my gratitude to Dr. Crowley, whom I sincerely thank for accepting to be part of this journey and for bringing an important engineering perspective to this work.

My sincere thanks also go to Dr. Koen Van Noten, whose work formed an important basis for this research. I am thankful for his guidance, his readiness to help, and the many fruitful discussions that enriched this thesis.

I would like to sincerely thank Dr. Thomas Lecocq for his valuable remarks at every stage of this work, for his help in structuring and finalizing the thesis, and for his continuous support. I am particularly grateful for his kindness, his

willingness to listen, and the time he took to support me during the most challenging moments of this journey.

My sincere thanks also go to Dr. Michel Van Camp, our former manager, for his kindness, early guidance, and thoughtful support. I particularly appreciated his understanding and encouragement during difficult times, especially when I was affected by news from my home country.

I would like to extend my gratitude to all the members of my jury. I sincerely thank them for dedicating their time to reading, evaluating, and validating my work. I would like to extend my gratitude to Dr. Thierry Camelbeeck, whose extensive experience and deep knowledge I greatly benefited from over the years; Prof. Hervé Degée, for his valuable engineering insights; Prof. Paul Fisette and Prof. Hadrien Ratez, for kindly accepting the roles of president and secretary of my PhD defense.

I would like to express my sincere appreciation to the Royal Observatory of Belgium, to our director, Dr. Ronald van der Linden, and to the kind colleagues in the HR and accounting departments, for providing a supportive and well-organized environment that made it possible for me to carry out this research.

I am also very thankful to my colleagues. Special thanks to Giovanni for his help throughout the project; to Bert and Stefaan for all I learned during fieldwork; and to Fabienne and Marc for their kindness over the years. I also warmly thank all my colleagues Ben, Raphaël, Martin, Anita, Marthe, Sylvain, Jasper and Niel for creating such a positive and supportive working atmosphere.

On a personal level, I would like to express my deepest gratitude to my husband, Ghassem. His constant support, patience, and understanding have been essential throughout this journey. He took on far more than his share of responsibilities at home, especially in caring for our children, giving me the time and space to focus on this work. Without his dedication and generosity, this thesis would not have been possible.

I am deeply grateful to my family. My mother has always been my strongest supporter; she encouraged me to apply for this PhD position in the first place, and in every difficult moment, she reassured me that I can do it and that everything will be alright. My father has always been supportive and proud of me, which has given me great strength throughout this journey. My brothers have always believed in me even more than I believed in myself,

encouraging me to give my very best. My kind sister, who came to support me and take care of the children during an important stage of this thesis, has my heartfelt thanks.

Finally, my deepest and most heartfelt gratitude goes to my children, Diyar and Della. They are my greatest source of hope, motivation, and happiness. From them, I learn every day to try, and try again, even after failure. They remind me of what truly matters, beyond every challenge and achievement.

Table of Contents

Table of Figures

List of Tables

List of Abbreviation and Symbols

ABM — Anglo-Brabant Massif (crustal domain)
ACC — Accelerometer
AI — Arias Intensity
ARD — Ardennes (crustal domain)
ASDF — Adaptable Seismic Data Format
ASI — Acceleration Spectrum Intensity
BB — Broadband Seismometer
CAV — Cumulative Absolute Velocity
CMS — Conditional Mean Spectrum
DB — Database
EC8 — Eurocode 8
EDR — Euclidean Distance-Based Ranking
EIDA — European Integrated Data Archive
EPA — Effective Peak Acceleration
EPD — Effective Peak Displacement
EPV — Effective Peak Velocity
ESM — Engineering Strong Motion Database
FAS — Fourier Amplitude Spectrum
FFT — Fast Fourier Transform
FKG — Free Kappa Gradient (method)
GMM — Ground-Motion Model
GMPE — Ground-Motion Prediction Equation
GM — Geometric Mean of horizontal components
HAIN — Hainaut (crustal domain)
HI — Housner Intensity
IM — Intensity Measure
ITACA — Italian Accelerometric Archive
JKG — Joint Kappa Gradient (method)
LLH — Log-Likelihood
LH — Likelihood
LP — Long-Period Seismometer
MBE — Mean Bias Error
MER — Mixed-Effects Regression (method)
M_L — Local Magnitude
M_w — Moment Magnitude
NGA-East — Next Generation Attenuation (Central & Eastern North America)

NGA-West — Next Generation Attenuation (Western United States)
PGA — Peak Ground Acceleration
PGD — Peak Ground Displacement
PGV — Peak Ground Velocity
PSHA — Probabilistic Seismic Hazard Analysis
Q — Quality Factor (attenuation)
R^2 — Coefficient of determination (measure of goodness of fit in regression analysis)
RESIF — French Seismological Network Database
RMS — Root Mean Square
ROB — Royal Observatory of Belgium
RotD50 — Median horizontal component over all orientations
RotD100 — Maximum horizontal component over all orientations
RVG — Roer Valley Graben (crustal domain)
SA — Spectral Acceleration
SNR — Signal-to-Noise Ratio
SP — Short-Period Seismometer
UHS — Uniform Hazard Spectrum
V_{S30} — Time-averaged shear-wave velocity in the upper 30 m
κ — High-frequency attenuation parameter (kappa)
κ_0 — Site kappa (zero-distance intercept)
κ_{r_s} — Kappa distance gradient of a station
κ_r — Kappa distance gradient of a crustal domain
t^* — Attenuation parameter related to path effects
Δσ — Stress drop
f — Frequency
f_{min} — Minimum usable frequency
f_{max} — Maximum usable frequency
H — Horizontal component
Z — Vertical component
M — Earthquake magnitude
R — Source-to-site distance
R_{epi} — Epicentral distance
R_{hypo}— Hypocentral distance
S — Site conditions
T — Structural period

1 Introduction

1.1 State of the art and objectives

Probabilistic seismic hazard analysis (PSHA) provides a quantitative framework for estimating the likelihood of exceeding different levels of ground shaking at a given site, by integrating information on earthquake occurrence, source characteristics, wave propagation, and site effects. Within this framework, ground-motion models (GMMs) play a central role, as they quantify how earthquake shaking depends on earthquake magnitude (M), source-to-site distance (R), site conditions (S), and other source and path parameters. The choice and parametrization of GMMs therefore represent one of the dominant sources of epistemic uncertainty in PSHA. Several studies have emphasized that constraining and testing GMMs requires high-quality ground-motion databases with well-documented metadata, careful data selection, and consistent processing. As a consequence, the reliability of hazard estimates, structural response predictions, and engineering decisions strongly depends on the quality and representativeness of the underlying ground-motion data.

This dependence on observational data has motivated the development of large, high-quality ground-motion databases. Over the last decades, numerous national and international initiatives have focused on compiling uniformly processed and well-documented strong-motion datasets to support the development and validation of ground-motion models. Notable examples include the NGA-West (Western United States; Ancheta et al., 2014)and NGA-East (Central & Eastern North America; Goulet et al., 2014) projects, the KiK-net database (Japan; Dawood et al., 2016), the ITACA database (Italy; Pacor et al., 2011), the RESORCE database (Europe and Middle East; Akkar et al., 2014), the Engineering Strong Motion (ESM) database (pan-European; Luzi et al., 2016), and the the RESIF/EPOS-France dataset (France; Buscetti et al., 2025). These databases provide uniformly processed recordings accompanied by detailed event, station, and site metadata, and have substantially improved the understanding of ground-motion variability and the characterization of source, path, and site effects across a wide range of tectonic environments.

However, these datasets are predominantly based on moderate-to-large earthquakes recorded in tectonically active regions, and their applicability to stable, low-to-moderate seismicity environments remains uncertain. This limitation is particularly evident in intraplate regions such as Belgium, where seismicity is characterized by low occurrence rates, a dominance of small-magnitude earthquakes, and a relative scarcity of strong-motion recordings. As a result, seismic hazard assessments in Belgium have historically relied on GMMs developed for other regions, without direct validation against local data. Existing logic-tree approaches incorporate multiple models from different tectonic environments, often with subjective weighting based on assumed applicability. Sensitivity analyses indicate that the ground-motion component is one of the dominant contributors to epistemic uncertainty in Belgian PSHA, highlighting the need for region-specific data and analysis.

Despite the continuous recording of seismic data by the Belgian seismic network over several decades, these data have not been systematically compiled and exploited for ground-motion modelling purposes. This represents a significant gap with respect to the international state of the art. Recent studies in other low-seismicity regions, such as Switzerland, the United Kingdom, and France, have demonstrated that the development of dedicated ground-motion databases based on weak-motion recordings is both feasible and valuable for improving regional hazard assessments.

In this context, the BELSHAKE project was initiated to bridge this gap by building a comprehensive ground-motion database for Belgium and by developing the capacity to model ground motion in a regionally consistent framework. The project is structured around two main objectives: (1) the systematic compilation and processing of ground-motion recordings, and (2) the characterization and modelling of ground-motion properties, including attenuation and model validation.

Building on this framework, the present thesis contributes to the BELSHAKE project by implementing and validating a complete workflow from raw waveform data to engineering-relevant ground-motion parameters. The objectives of the thesis, which are addressed through the main contributions of this work and correspond to the main chapters of the thesis, are as follows:

- the contribution to the compilation of a high-quality ground-motion dataset, including the systematic collection of waveform data, station metadata, and the application of waveform quality control procedures;
- the implementation and validation of a hybrid waveform windowing workflow adapted to the characteristics of the Belgian dataset;
- the application of multiple approaches for internal consistency checking and validation of derived intensity measures;

- the characterization of seismic attenuation in Belgium through the analysis of the high-frequency anelastic attenuation parameter κ;
- the evaluation of published ground-motion models with respect to the BELSHAKE dataset using a multi-metric statistical framework.

By addressing these objectives, this work aims to reduce epistemic uncertainty in ground-motion modelling for Belgium and to provide a robust, data-driven basis for seismic hazard assessment and engineering applications in low-to-moderate seismicity regions. The BELSHAKE database, to which this thesis contributed, is described in detail in the paper *The BELSHAKE Database of Earthquake Ground Motion in Belgium*.

1.2 The BELSHAKE database

Belgium and adjacent parts of north-western Europe are characterized by low to moderate seismicity and therefore by a relative scarcity of strong-motion recordings. Although seismic activity is generally low, several moderate earthquakes have demonstrated the potential for significant ground shaking in the region. Notable examples include the 1992 Roermond earthquake (M_w = 5.3), located in the Roer Valley Graben, and the 1983 Liège earthquake, which highlighted the need for improved seismic monitoring in Belgium.

In probabilistic seismic hazard analyses, the ground-motion component often contributes to a large portion of the total epistemic uncertainty, and the absence of local data for testing or adjusting imported models tends to preserve that uncertainty. Reliable seismic hazard assessment requires both high-quality observational data and robust ground-motion models that are adapted to regional conditions. However, in Belgium, the limited availability of strong-motion data and the predominance of small-magnitude events restrict the direct applicability of models developed for other tectonic environments. As a consequence, national seismic hazard assessments for Belgium have historically relied on GMMs and datasets from other regions, for example southern Europe or California (Vanneste et al., 2014), which may not fully represent the attenuation characteristics and site conditions of intraplate environments. In addition to tectonic earthquakes, induced seismicity associated with historical mining activity is observed in parts of Belgium, particularly in the Hainaut region. These events are typically shallow and may exhibit different ground-motion characteristics, further complicating the regional seismic hazard characterization.

1.2.1 Data availability and network evolution

In chapter 2, the present thesis contributes to the compilation of a dedicated ground-motion database for Belgium and its surrounding regions, referred to as the BELSHAKE database. The database is primarily based on the digital waveform archive of the Royal Observatory of Belgium (ROB), which has been built up since 1985, following the 1983 Liège earthquake, in parallel with the progressive densification and modernization of the Belgian seismic network. The flatfile of the *Belgian ground-motion database (BELSHAKE)* is publicly available on Zenodo.

Initially, the network consisted of a limited number of digital short-period sensors with event-based recording. From the late 1990s onward, accelerometers were progressively introduced in seismically active areas, followed by the installation of broadband sensors in the early 2000s. Over the past four decades, this evolution has led to a mixed network of short-period and broadband seismometers and accelerometers, with continuous data streams and integration into the European Integrated Data Archive (EIDA), while continuous recording became standard from around 2005 onwards.

As a result, the archive is heterogeneous, with varying sampling rates, dynamic ranges, and recording modes. In particular, earlier records often lack pre-event noise windows due to triggered acquisition systems or, more commonly, due to data trimming practices implemented to reduce storage requirements. These characteristics must be carefully accounted for when designing a consistent ground-motion database.

1.2.2 Data selection and limitations

Explicit criteria for selecting events were defined in the project proposal, based on the start of digital recording in Belgium (1985), minimum magnitude thresholds, event type, and spatial windows around the country, as detailed in chapter 2. Using these criteria, around ∼6400 digital seismograms, ∼5840 from 327 tectonic earthquakes and ∼580 from 17 induced earthquakes with M_L ≥ 2 were selected in and around Belgium. Additional waveform data from neighboring countries were incorporated for key regional earthquakes, most notably the 1992 Roermond event and its aftershocks. The dataset includes both tectonic and induced events. The spatial distribution of the selected events is shown in Figure 1. Events with M_L < 2.5 are restricted to a smaller region around Belgium, indicated by the dashed boundary, while larger-magnitude events are included from a broader area.

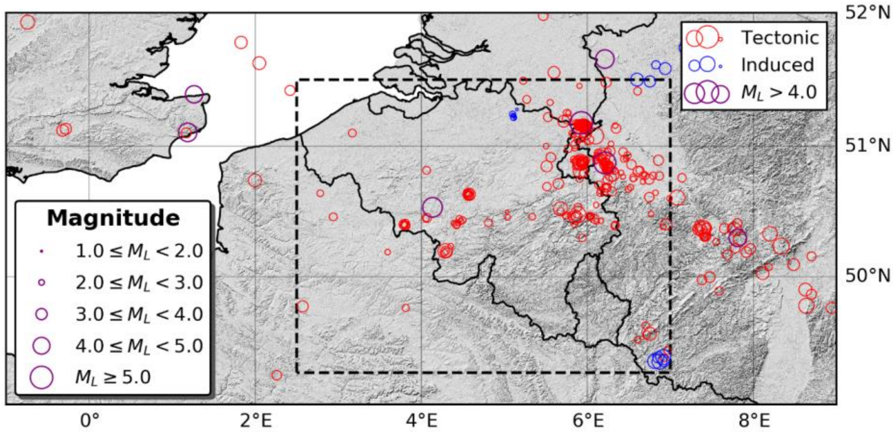

Figure 1. Distribution of the selected events used in this study. Symbol size scales with magnitude, and colors distinguish tectonic (red) and induced (blue) events. Events with M_L < 2.5 are restricted to a smaller region around Belgium, indicated by the dashed boundary, whereas larger-magnitude events are included from the entire area shown in the map. Purple circles highlight events with M_L > 4.0

The magnitude distribution of the dataset is strongly skewed toward small events, with the majority of recordings corresponding to earthquakes in the range M_L 2–4, and only a limited number of events exceeding M_L 4. This reflects the natural seismicity of the region but also implies that the dataset provides limited direct constraints on strong ground motions relevant for engineering design.

Moreover, a large proportion of the recordings correspond to moderate-to-large epicentral distances, which further limits the availability of near-source observations that are particularly important for constraining attenuation and source characteristics. In addition, many recordings are obtained at relatively large epicentral distances, and early records may be affected by limited dynamic range or clipping, particularly for larger events. To compensate for these limitations, waveform data from neighbouring countries were incorporated for key earthquakes, ensuring better representation of moderate-magnitude events such as the Roermond earthquake. All waveform data are stored in a dedicated ASDF-based library, a hierarchical data format designed for managing large seismological waveform datasets together with their metadata (Krischer et al., 2016), preserving both raw and processed waveforms, ensuring full traceability of the processing workflow.

1.3 Waveform quality control

A fundamental requirement for the development of reliable ground-motion datasets is the careful verification of waveform quality before any processing or parameter extraction is carried out. Raw recordings often contain issues which can significantly bias intensity measures if left untreated. Published descriptions of large ground-motion databases repeatedly highlight the importance of waveform-level quality control as a prerequisite for producing consistent datasets.

In particular, the reliability of derived ground-motion parameters such as peak values, response spectra, and Fourier amplitude spectra depends critically on the integrity of the original waveform data. Even small imperfections in the raw waveform, if not properly identified and corrected, may propagate through the processing chain and lead to systematic biases in engineering-relevant intensity measures.

Waveform quality affects not only the accuracy of ground-motion parameters, but also the reliability of phase-onset information such as P- and S-wave arrival times. These phase picks are fundamental inputs for determining source-to-site distances, for defining time windows, and for computing several intensity measures. Published processing guidelines consistently recommend manual verification or correction of P- and S-wave picks when automatic procedures fail, especially in low-signal or noisy conditions. Studies focused on preprocessing for strong-motion engineering analyses also underscore the need to detect and remove spikes, repair isolated disturbances, and correct baseline shifts to prevent drifts in velocity or displacement (Boore and Bommer, 2005). As shown in previous database projects, correcting such problems can substantially improve the stability of response spectra and Fourier amplitude spectra, thereby improving the consistency of the processed dataset.

1.3.1 Quality control procedure in BELSHAKE

In the context of BELSHAKE, before processing, all components of each record were visually inspected, and the noise, P-wave, S-wave and coda windows were evaluated independently. Problems such as timing errors, spikes, disturbances, data gaps, clipping, baseline shifts, incomplete windows, or the presence of fore- or aftershocks were systematically identified, with representative examples shown in chapter 2.

This systematic visual inspection was applied to the entire dataset, comprising approximately around 6400 records, and constituted one of the most time-consuming stages of the database construction. The inspection was performed component by component, and window by window ensuring that issues were correctly identified and treated without affecting the remaining components and windows. When possible, issues were corrected, for example by applying timing shifts, removing spikes through interpolation, trimming disturbances, or correcting baseline offsets. Problems that could not be fixed were flagged explicitly in the database.

In addition, the identification and correction of timing inconsistencies were supported by comparing observed and expected P-wave arrival times, allowing the detection of systematic timing shifts in certain records. Baseline corrections were applied interactively where necessary to remove long-period drifts that could otherwise affect velocity and displacement estimates.

1.3.2 Quality classification and dataset reliability

Based on these checks, all records were assigned to three quality categories: good, intermediate, and poor. Good and intermediate records were considered reliable and retained for processing, while poor quality records were excluded from further steps. This classification provides a necessary transition from data selection to waveform processing and ground-motion analysis, ensuring that the dataset used in later stages is of sufficient quality.

Overall, this procedure resulted in the classification of approximately 94% of the records as reliable (good or intermediate quality), while a smaller fraction of records was excluded due to severe quality issues such as high noise level, clipping, missing data, or irreparable disturbances. Although this filtering slightly reduced data coverage, particularly for larger-magnitude events, it ensured that subsequent analyses are based on robust and physically meaningful signals. The explicit storage of identified problems, applied corrections, and quality flags within the database also provides full traceability and allows users to apply additional filtering criteria depending on the requirements of specific applications, such as ground-motion modelling or structural response analysis.

1.4 Signal windowing and waveform processing

Accurate waveform windowing is a critical prerequisite for reliable ground-motion processing, as it defines the noise, P-, S-, and coda-wave windows required for signal-to-noise ratio estimation. It also allows the computation of intensity measures over different signal windows. Two established windowing procedures Goulet et al., (2014), used in NGA-East, and Perron et al., (2018), developed for the KiK-net dataset, were examined and applied to the BELSHAKE waveforms in chapter 3.

1.4.1 Windowing methods and comparison

The Goulet method (*Figure 2*) defines six windows (noise, P, S+Lg, coda, combined P+S, and full record) based on arrival times and distance-dependent duration models, while the Perron method (*Figure 3*) defines four windows (noise, P-wave, S-wave, and signal window), and includes an algorithm for selecting pre- or post-event noise windows using duration and energy criteria.

The Goulet approach relies on physically based duration models and ensures continuous signal windows, which is advantageous for capturing the full energy content of seismic phases. In contrast, the Perron method introduces a more flexible and data-driven strategy for noise-window selection, accounting for both window duration and spectral energy levels, which is particularly beneficial for datasets with incomplete or disturbed pre-event noise.

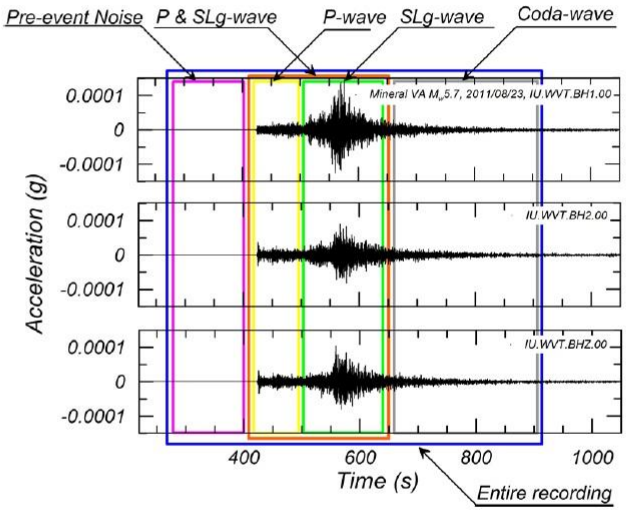

Figure 2. Schematic drawing of the six time windows used in Goulet method (Goulet et al., 2014)

Comparison of the two methods shows that Goulet provides longer S-wave windows and contiguous S and coda windows, whereas Perron offers a more robust noise-window selection, especially for records with incomplete or disturbed pre-event noise.

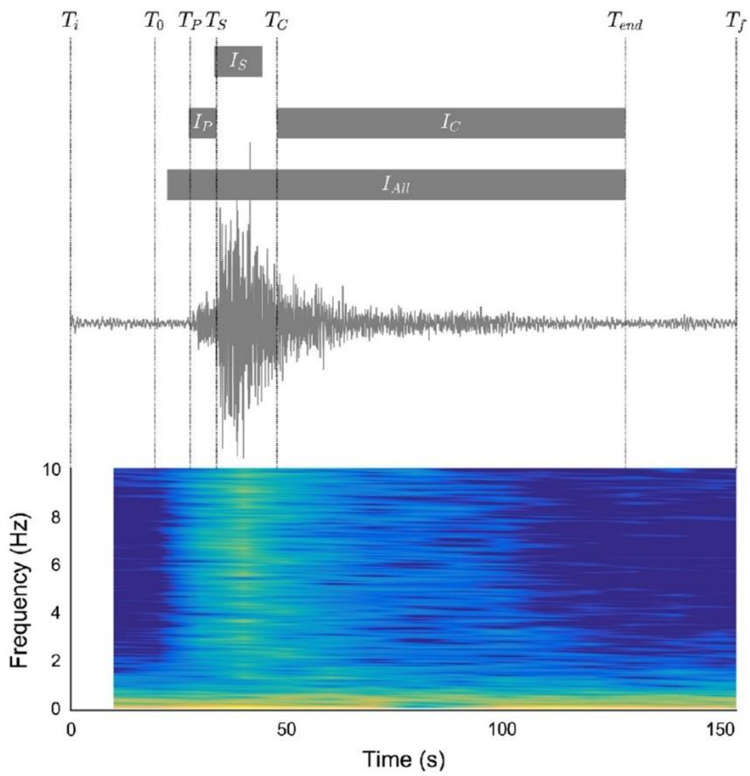

Figure 3. Schematic drawing of the P, S, coda and full record time windows used in Perron method (Perron et al., 2018)

1.4.2 Hybrid windowing strategy for BELSHAKE

Because many BELSHAKE records have limited or disturbed pre-event noise, a hybrid procedure was adopted: Goulet was used for the P-, S-, and coda windows, and Perron, with modifications to reduce rejection of usable data, was used for the noise window.

The modifications applied to the Perron method were specifically designed to minimize the number of rejected records in the BELSHAKE dataset, by allowing shorter or partially disturbed noise windows to be retained when they still provide usable information for SNR estimation. Additional noise-window flags were introduced to handle cases with short or disturbed noise windows. This hybrid procedure ensures coherent window definitions and, by reducing the number of records without a noise window, provides the necessary input for signal-to-noise ratio (SNR) estimation, determination of the usable frequency range, and the subsequent ground-motion processing steps.

1.4.3 Signal to noise ratio and usable frequency range

The SNR is computed as the ratio between the Fourier amplitude spectra (FAS) of the signal and the noise window. In the BELSHAKE dataset, the signal window is defined as the combination of the P-wave and S-wave windows.

A threshold value of SNR ≥ 3 is adopted to define the frequency range over which the signal is considered reliable. Frequencies for which the SNR falls below this threshold are excluded from further analysis, as they are dominated by noise and may lead to biased estimates of spectral amplitudes and derived intensity measures. An example is shown in Figure 4 for station BE.DOU.

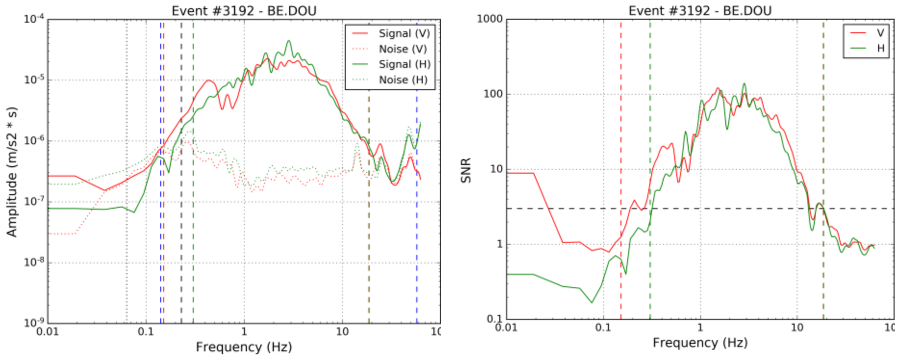

Figure 4. Example of signal-to-noise ratio (SNR) analysis for station BE.DOU during the earthquake in LEBACH (DE) with M_L = 3.4. Left: Fourier amplitude spectra (FAS) of signal and noise windows for horizontal and vertical components. Right: corresponding SNR curves, with the selected usable frequency range defined by the SNR ≥ 3 threshold. Vertical dashed lines indicate the lower and upper frequency limits.

The left panel presents the Fourier amplitude spectra of the signal and noise windows for both horizontal and vertical components. The right panel shows the corresponding SNR curves, together with the selected frequency band defined by the SNR ≥ 3 criterion. The lower and upper frequency limits are indicated by vertical dashed lines, in between which the SNR exceeds the threshold, defining the usable frequency range for further analysis.

1.4.4 Waveform processing

Following windowing, in the framework of the project a semi-automated workflow was developed to process all waveform data in the BELSHAKE archive in a uniform way, based on the review of processing schemes applied in existing ground-motion databases. Starting from the raw data, which have optionally been manually pre-treated without actual modification (e.g., trimming, time shift) or more invasively (spike removal, baseline correction of distorted waveforms), the processing flow consists of the following steps:

a. Mean removal and linear detrending of the entire record.
b. Two-sided tapering of the entire record using fixed taper lengths instead of taper rates. The lengths of the left and right tapers are evaluated separately, depending on the length of the available pre-event noise and post-signal (P or S) window, with a maximum of 1 second and a minimum corresponding to 5 samples.
c. Restitution of the entire record to the native ground-motion type (velocity or acceleration) of the instrument. This is a critical step, in which the instrument response is removed and amplitudes are converted to physical ground-motion units. In this step, a waterlevel of 40 dB is applied, which means that frequencies where the instrument response is below 1/100 of the maximum response are not amplified by more than a factor of 100. We do not apply pre-filtering here, because this actually corresponds to zero-phase filtering, which requires specific measures to avoid artefacts. Although it is possible to restitute velocity records directly to acceleration as well, we prefer not to do this to avoid a problem in the python package we use (ObsPy) identified by Perron et al., (2022), who found that this operation results in suppression of high frequencies when a waterlevel is applied.
d. Differentiation of velocity records to acceleration. This is done in the frequency domain, because we found that simple time-domain differentiation may cause distortions for data with very-high frequency content (close to Nyquist frequency).
e. Computation of Fourier amplitude spectra (FAS) for signal (P + S) and noise windows. These are used to estimate the signal-to-noise ratio (SNR) and determine the usable frequency range, as described in Section 1.4.3. The latter is done separately for the vertical and for the horizontal

(SH) components. Both the FAS and SNR are plotted at this stage (Figure 4), along with the minimum and maximum frequencies to allow visual inspection of the results. If the automatically determined frequency bounds are not satisfying, it is possible to manually override them. If the frequency range with good SNR is too narrow (< 0.7 in log space), processing of the record is halted. For records where the noise window is too short, the operator must set the frequency bounds manually, otherwise the record is skipped.

f. The entire record is again tapered with the same taper lengths as in the second step. This is to make sure zero-padding in the next step does not cause abrupt jumps.
g. Zero-phase bandpass filtering with prior zero-padding of the entire record. The lower corner frequency corresponds to the maximum of the minimum reliable frequency of the instrument (taken as frequency where response is 6 dB above the waterlevel of step c), the minimum frequency where SNR ≥ 3 (or imposed minimum frequency), the minimum frequency required to have a good spectral resolution (taken as 3 wavelengths) for the signal (P+S) window, and the minimum frequency that is assumed not to be affected by microseismic noise (0.23 Hz). The upper corner frequency corresponds to the minimum of the maximum reliable frequency of the instrument and the maximum frequency where SNR ≥ 3 (or the imposed maximum frequency). Note that the corner frequencies may be different for vertical and horizontal components (see step e). We apply a Butterworth filter with an order of 2 on both sides, where it should be noted that for a zero-phase filter this actually corresponds to an order of 4 due to the way it is implemented in ObsPy. Prior to filtering, the records are zero-padded on both sides with a pad length depending on the filter order and the lower corner frequency.
h. After filtering, the initial time scale is re-established by trimming the record to its original start and end times, and the record is tapered once more, but only on the left side (to have zero initial conditions), using the same taper length as before.
i. Next, the entire record is integrated twice in the time domain to obtain displacement, to which we fit a 6th order polynomial with the 0th and 1st coefficients constrained to 0.
j. The second derivative of the polynomial fit obtained in the previous step is subtracted from the acceleration time series of step h. This represents the final processed acceleration record.

k. The acceleration record is integrated in the time domain to obtain velocity, and once more to obtain displacement.
l. In the final step, the acceleration record is split into noise, P, S, signal (P+S) and full (P+S+coda) windows, which are tapered and zero-padded to the length of the P- or S-window, whichever is the longest, extended to the next power of 2.

This processing workflow was applied as part of the thesis to all reliable records in the BELSHAKE dataset on an event-by-event basis, ensuring that the automatically determined frequency limits and processing parameters are appropriate for each individual waveform. In particular, the automatically determined reliable frequency range is verified through inspection of the Fourier amplitude spectra (FAS) and corresponding signal-to-noise ratio (SNR) plots. This combination of hybrid windowing, SNR-based frequency selection, and consistent processing provides a robust foundation for the computation of intensity measures and subsequent ground-motion analysis. The processing and windowing procedures applied to the BELSHAKE dataset have also been described in the paper *Waveform Processing in BELSHAKE, the Belgian Ground-Motion Database*.

1.5 Intensity measures and dataset validation

1.5.1 Computation of intensity measures

After waveform selection, quality check, correction, windowing and processing applied consistently on a record-by-record basis, the next step is the computation and verification of intensity measures (IMs). Structural damage and seismic demand depend not only on magnitude and distance, but also on source, path and site parameters, frequency content, and structural period. For this reason, earthquake shaking strength is commonly described in terms of various IMs, which are used both to characterize the seismic hazard and the structural demand.

In the BELSHAKE project, a broad set of IMs is therefore computed from the processed reliable waveforms. These include peak ground acceleration (PGA), peak ground velocity (PGV), and peak ground displacement (PGD), response spectra, time-integral measures such as arias intensity (AI) and cumulative absolute velocity (CAV), and RMSa (root mean square acceleration), spectrum-integral and spectrum-average measures and duration metrics.

These intensity measures are computed following standardized procedures consistent with those used in major international databases (e.g., RESIF, ESM, NGA-East), ensuring comparability of the BELSHAKE dataset with existing ground-motion resources. Furthermore, IMs are only computed for records classified as reliable (good and intermediate quality), ensuring that the derived parameters are not biased by poor-quality waveforms.

1.5.2 Consistency checks and dataset validation

Using these IMs, a series of consistency checks were applied during this thesis to detect remaining problems that had not been identified in earlier stages, as described in chapter 4. These checks are essential because some inconsistencies are not visible at the waveform level but become apparent only when derived parameters are analysed systematically.

First, ratios of PGV computed from different horizontal components were analysed for the P, S, signal and full windows, and outliers were inspected. This revealed cases where one horizontal component had anomalously low amplitude and a set of records where vertical and horizontal components had been swapped. The affected components were flagged, their IMs removed, and the swapped records were corrected and reprocessed. This analysis demonstrates the importance of cross-validating different component definitions, as inconsistencies in sensor orientation or recording can directly affect engineering-relevant intensity measures.

Second, ratios between horizontal and vertical PGV were examined across all windows to identify anomalously high or low H/V values. Most high H/V ratios were associated with short-distance records and were retained as exceptional but not problematic; a smaller number of cases with suspicious H/V behavior, were flagged for further investigation, with resonance effects suspected in at least one station. These results highlight that not all outliers correspond to errors: some reflect genuine physical phenomena such as near-source effects or site amplification, which must be preserved in the dataset.

A third set of checks compared observed PGA and PGV values with predictions from a simple ground motion model (GMM) fitted to the BELSHAKE data, based on the functional form of Traversa et al., (2020). Total residuals were analysed for different components and windows. Inspection of the temporal evolution of station-specific residuals highlighted anomalous periods for four stations, which were traced to instrument-response issues during a specific deployment; an adjusted response, was inferred and used to recompute IMs. For some of these stations the anomalies are likely related to particular seismic sequences and have been documented but not modified. This residual-based analysis provides an additional level of validation by comparing observations with physically expected trends, allowing identification of both station-related issues and event-specific anomalies.

Overall, the consistency checks allowed the identification and correction or flagging of a limited number of problematic records (e.g. anomalous component amplitudes, swapped components, instrument-response issues, possible resonance effects), while confirming that the vast majority of IMs are coherent. These systematically flagged anomalies and updated IMs provide a transparent and well-documented basis for the subsequent attenuation analysis and GMM evaluation. This validation step therefore constitutes a critical bridge between data compilation and quantitative ground-motion modelling, ensuring that the dataset is both physically consistent and suitable for seismic hazard and engineering applications.

1.6 High-frequency anelastic attenuation kappa (κ)

1.6.1 Physical basis of high-frequency attenuation

In the next step the high-frequency anelastic attenuation is computed in terms of the kappa parameter (κ), as presented in chapter 5. This part constitutes a major component of the thesis, providing a systematic and data-driven characterization of attenuation across Belgium. κ values are computed for all reliable S-wave windows on horizontal and vertical components, using the classical Anderson and Hough (1984) definition and the previously defined processing, windowing and frequency-range constraints. The κ parameter represents the exponential decay of the high-frequency part of the acceleration Fourier spectrum and provides a practical proxy for near-surface and path attenuation effects. It is conceptually linked to the attenuation of seismic wave energy through the Earth, where energy loss arises from intrinsic anelastic mechanisms such as grain-boundary friction and fluid-related processes, as well as scattering caused by crustal heterogeneities.

The resulting κ values are first validated against independently estimated t^* values derived from displacement spectra. The parameter t^* represents the cumulative effect of anelastic attenuation along the propagation path. Under the assumption of frequency-independent attenuation, t^* becomes physically equivalent to κ, allowing a direct comparison between the two quantities. The observed strong linear relationship between κ and

t^{*} confirms the internal consistency and robustness of the κ estimates in our study.

1.6.2 Regional attenuation structure

To obtain meaningful κ–distance trends, records from induced and very shallow events had to be filtered out, and the remaining data are analysed within four crustal domains; Anglo-Brabant Massif (ABM), Ardennes (ARD), Roer Valley Graben (RVG), and Hainaut (HAIN), reflecting the main tectonic and crustal structures in Belgium. This regional subdivision allows attenuation to be interpreted in a geologically consistent framework and highlights spatial variability linked to crustal structure. Stations in transition zones between domains (ABM/RVG and ARD/RVG) were included in both relevant regions.

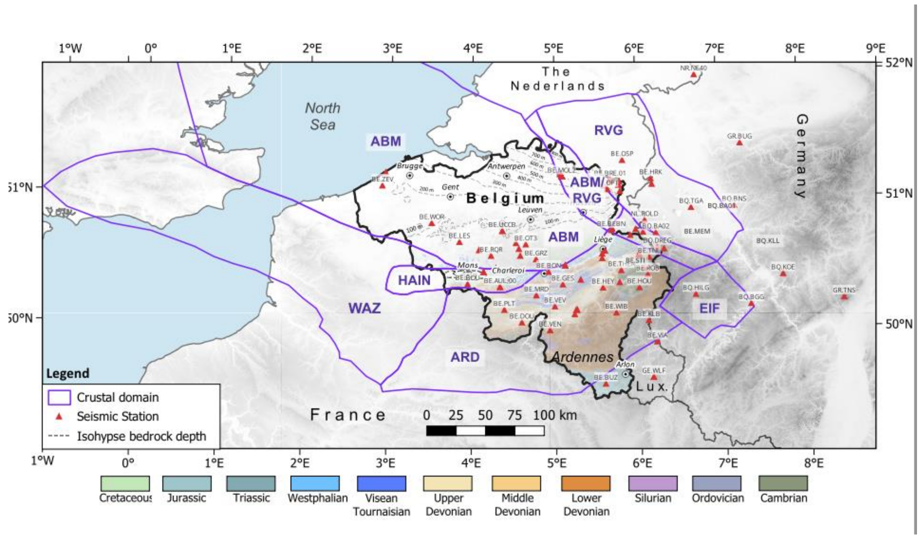

Figure 5. Crustal domains and stations where kappa was determined in Belgium. Background image depicts surface geology, with bedrock in the south and NNE-ward thickening sediment layers (100 m contour interval) in the north

1.6.3 Methodological framework for κ decomposition

On this basis, site-specific kappa value (κ_0) and regional kappa gradients (κ_r) are estimated using three approaches: a free kappa gradient method (FKG) applied station by station, a joint kappa gradient method (JKG) that enforces a common κ_r per crustal domain while allowing station-specific κ_0, and a mixed effects regression (MER) that combines domain-level fixed effects with station-level random effects. These three approaches reflect increasing levels of statistical integration: from purely local estimation of FKG, through partially constrained regional modelling of JKG, to a hierarchical framework of MER that simultaneously captures regional trends and station-specific variability. This progression allows a systematic evaluation of how data availability and spatial variability influence attenuation estimates.

The comparison shows that the MER model provides the most stable and internally consistent κ_0 and κ_r estimates, with JKG offering a simpler but compatible alternative, while the FKG is more sensitive to sparse or uneven data. Importantly, this comparative analysis highlights that attenuation parameters cannot be reliably estimated using purely station-based approaches when data coverage is heterogeneous, and that statistical models accounting for hierarchical structure significantly improve robustness.

1.6.4 Attenuation characteristics of the Belgian crust

Final station κ_0 values in Belgium range from about 14 to 59 ms on horizontal components and from about 12 to 53 ms on vertical components, and kappa gradient of crustal domains, κ_r values lie between 0.13–0.17 ms/km (horizontal) and 0.05–0.10 ms/km (vertical), corresponding to frequency-independent Q factors of roughly 1600–2100 and 2700–3900, respectively, for an average crustal S-wave velocity of 3.6 km/s. These values indicate moderate attenuation and relatively high Q factors, consistent with a tectonically stable intraplate crust while still reflecting significant regional variability.

Comparison with earlier Belgian studies revealed consistency in regional trends and station anomalies, while also demonstrating the advantages of modern statistical approaches in reducing outliers and stabilizing estimates.

κ_0 - V_{S30} comparisons with global trends indicated that κ_0 values are quite similar for all bedrock sites, both with low (800-1200 m/s), intermediate (1200-1800 m/s) and high (> 1800 m/s) V_{S30} values. This would imply that bedrock with high V_{S30} in Belgium does not show the low κ_0 values typical of hard rock in other regions of the world, Instead, the observed κ_0 values reflect the heterogeneity of the Belgian crust, supporting the asymptotic κ_0 conceptual model proposed by Ktenidou et al., (2015). In addition, comparison with neighbouring regions shows that Belgian attenuation properties occupy an intermediate position between low-attenuation stable regions and more attenuating tectonically active areas. In particular, Q values reported for mainland France are generally lower, typically on the order of

600–1200 depending on region and frequency range, indicating stronger attenuation compared to Belgium.

This contrast highlights the importance of regional calibration when transferring ground-motion models across neighbouring regions.

1.6.5 Relevance for ground-motion modelling and hazard assessment

These κ_0 and κ_r and Q estimates are stored in the BELSHAKE database, where they provide a consistent and application-ready description of attenuation across Belgian crustal domains. The site terms κ_0 and V_{S30} are key inputs for host-to-target ground-motion adjustments, which adapt GMMs developed for a reference (host) region to Belgian site (target) conditions by accounting for differences in near-surface attenuation. This makes the derived κ parameters directly relevant for ground-motion modelling and probabilistic seismic hazard assessment in Belgium.

The analysis of κ presented in this thesis is further developed in the paper *Analysis of the Site-Specific and Regional Components of Kappa across Crustal Domains in Belgium*, currently under review, with a preprint available on Research Square. The corresponding *BELSHAKE kappa dataset* is publicly available on Zenodo.

1.7 Evaluation of ground-motion prediction equations

A final contribution of this work, as described in chapter 6 is the systematic evaluation of published ground-motion models (GMMs) against the BELSHAKE dataset, covering a wide spectrum of GMM families (European, NGA-West, NGA-East, global, local/regional and induced seismicity models).

GMMs form the backbone of probabilistic seismic hazard analysis (PSHA), as they translate earthquake source characteristics and source-to-site distances into expected shaking intensities. However, their applicability is strongly dependent on the tectonic environment, magnitude range, and data used for their calibration. This makes their direct application in low-to-moderate seismicity regions, such as Belgium, inherently uncertain.

Using a suite of complementary statistical measures, capturing median bias, variance, likelihood, and distance-attenuation trends, the analysis quantifies how well each GMM reproduces characteristics observed in Belgium across PGA, PGV and spectral acceleration (SA). This multi-metric evaluation framework is essential because no single metric can fully capture model performance. While some models may reproduce median trends well, they may misrepresent variability or attenuation behaviour, leading to biased hazard estimates**.** This approach follows recommendations from recent comparative studies (e.g. Scherbaum et al., 2004; Scherbaum et al., 2009; Kale and Akkar, 2013), which emphasize the need for multi-metric testing to avoid over-favouring models with large sigmas or those that misrepresent attenuation while still fitting central trends.

1.7.1 Challenges of small-magnitude ground motions in low-seismicity regions

Small-magnitude ground motions are highly sensitive to regional seismological properties, particularly stress drop, crustal attenuation (Q), and the way amplitudes scale with magnitude (Atkinson & Morrison, 2009). These parameters vary significantly between tectonic environments, meaning that ground motions from small earthquakes in low-to-moderate seismicity regions often differ systematically from those observed in high-seismicity areas for which most GMMs are developed. As a consequence, many published GMMs tend to overpredict shaking for small events, because their magnitude-scaling terms and attenuation functions are not constrained by local weak-motion data. Because most BELSHAKE recordings correspond to small earthquakes (M_L 2–4), the evaluation focuses on assessing how candidate GMMs behave within this limited magnitude range.

1.7.2 Evaluation strategy

To address these challenges, this study adopts a structured evaluation strategy that combines careful GMM selection with a comprehensive statistical testing framework. Nearly 20 GMMs are selected from different model families, reflecting a wide range of tectonic environments, datasets, and modelling philosophies. This includes models developed for active crustal regions (NGA-West), stable continental regions (NGA-East), pan-European datasets, and induced seismicity contexts.

The evaluation explicitly considers different variants of each GMM (e.g. distance metrics, stress-drop assumptions, site conditions), ensuring that each model is tested under conditions that are as compatible as possible with the BELSHAKE dataset. This reduces biases associated with inconsistent model application and improves the robustness of the comparison.

Using multiple statistical measures including likelihood (LH), log-likelihood (LLH), Euclidean distance-based ranking (EDR), residual trends with distance, and mean bias error (MBE); the study evaluates both the central tendency and dispersion of model predictions. Particular emphasis is placed on the EDR metric, which balances bias and variability, and on residual trends with distance, which provide insight into whether GMMs correctly reproduce attenuation behaviour. This is critical because incorrect distance scaling can lead to systematic over- or underestimation of hazard at different distances.

1.7.3 Linking GMM performance to physical parameters

An important added value of this work is the explicit comparison between GMM parameter assumptions and independently derived seismological parameters from the BELSHAKE dataset, particularly attenuation (Q), kappa (κ), and stress drop. For example, the selected stochastic model of Douglas et al., (2013) uses attenuation and κ values that closely match those derived in this thesis (Q ≈ 1800, κ_0 ≈ 20–40 ms), providing a strong physical justification for its good performance. Similarly, the stress-drop ranges assumed in the model are consistent with those estimated from Belgian earthquakes. This consistency demonstrates that GMM performance is not only a statistical outcome but also reflects the physical realism of the underlying parameterization.

1.7.4 Implications for seismic hazard assessment in Belgium

Overall, the evaluation identifies a small subset of GMMs that best reproduce the ground-motion characteristics captured in BELSHAKE, providing a justified starting point for future seismic-hazard modelling in Belgium. The results show that models from the NGA-West2 family (e.g. Abrahamson et al., 2014; Campbell & Bozorgnia, 2014; Boore et al., 2014) generally provide stable and consistent performance, despite being developed for active tectonic regions. In addition, stochastic models tailored to small-magnitude events, such as Douglas et al., (2013), perform particularly well, highlighting the importance of appropriate magnitude scaling and attenuation parameterization.

A key outcome is that no single GMM dominates across all metrics; instead, a subset of models consistently performs well across multiple criteria. This supports the use of logic-tree approaches in PSHA, where multiple GMMs are combined to represent epistemic uncertainty. Furthermore, the evaluation demonstrates that some commonly used models systematically overpredict ground motions in Belgium, particularly at small magnitudes, confirming the need for region-specific validation before application.

1.8 Conclusions and perspectives

Taken together, these developments contributed to establishing the BELSHAKE database as the first systematically assembled and quality-controlled ground motion database for Belgium. The combination of waveform quality control, hybrid windowing, internal consistency checks, kappa characterization, and ground-motion model (GMM) performance evaluation provides a coherent methodological framework that supports seismic hazard modelling. By integrating these components, this thesis delivers a foundation to better understand ground-motion behaviour in a low-to-moderate seismicity environment, while directly enabling engineering applications. The database includes uniformly processed waveforms, a comprehensive set of intensity measures, detailed metadata, and site-specific attenuation parameters, allowing the selection of ground-motion records based on magnitude, distance, and site conditions, and their use in nonlinear dynamic analyses through compatibility with target response spectra.

In the context of probabilistic seismic hazard analysis (PSHA), the results of this work directly support the construction of logic-tree frameworks used to represent epistemic uncertainty. The evaluation of GMMs provides a basis for selecting appropriate models as logic-tree branches, while the use of multiple statistical performance metrics enables informed weighting of these branches. In addition, the κ_0, κ_r, and Q estimates derived in this thesis provide physically based constraints for host-to-target adjustments, allowing models developed in other regions to be adapted to Belgian conditions or incorporated as alternative branches reflecting regional attenuation properties. The characterization of data limitations and magnitude range further contributes to a more transparent and regionally consistent representation of uncertainty in seismic hazard assessments.

Overall, this work establishes a consistent workflow from raw seismic recordings to engineering-ready input for seismic hazard assessment, record selection, and structural design in Belgium.

2 The BELSHAKE database

Seismic hazard assessments depend strongly on ground-motion models (GMMs), which describe how earthquake shaking decreases with distance and varies with magnitude, site conditions, and other factors. However, the reliability of such analyses largely depends on the quality, completeness, and consistency of the ground-motion databases used. Over recent decades, several national and international initiatives have been developed to address this need by compiling well-documented and standardized datasets. Since the first recorded accelerogram from the 1940 El Centro earthquake, the systematic collection of strong-motion data has evolved into a cornerstone of modern seismology and earthquake engineering and in regions with frequent earthquakes, large strong-motion datasets have been collected, allowing well-calibrated regional models.

In contrast, Belgium and surrounding parts of northwestern Europe have low to moderate seismic activity, and therefore very few strong-motion recordings. Because of this data limitation, national hazard assessments for Belgium have had to rely on models developed in other regions, such as southern Europe or California, with regional adaptations such as host-to-target adjustments (Vanneste et al., 2014). In probabilistic seismic hazard analyses, the ground-motion model component usually contributes to a large share of the overall uncertainty. Without local data to test or adjust existing models, this uncertainty remains high.

Recent projects in other low-seismicity countries (for example, Switzerland, the United Kingdom, and France) have shown that even weak and moderate motion records, if properly processed and documented, can provide valuable information for testing and improving GMMs. Building on these advances and supported by progress in digital recording and international collaboration, ground-motion databases such as RESIF have been developed to support research in ground-motion prediction, site-response analysis, and structural performance assessment.

This chapter provides a review of different databases, focusing on data selection strategies, metadata requirements, and then shows how these insights informed the design and implementation of the BELSHAKE database. By compiling local earthquake recordings and documenting them in a transparent and standardized way, the BELSHAKE database will help reduce dependence on foreign datasets and improves the reliability of seismic hazard and risk assessments in Belgium.

2.1 Ground motion databases

Ground-motion databases form the empirical foundation of modern engineering seismology. They provide recorded earthquake waveforms together with associated event, station, and site metadata, which are essential for the development and testing of ground-motion prediction equations (GMMs), seismic hazard and risk assessment, and structural response analyses. The reliability of any ground-motion study strongly depends on the quality, consistency, and documentation of the underlying database, including waveform processing, selection criteria, and metadata completeness. Over the past decades, numerous national and international initiatives have been launched to compile, process, and disseminate strong-motion and weak-motion data. These databases differ in terms of geographical coverage, magnitude range, recording instrumentation, processing standards, and intended applications. Some focus primarily on regions with high seismicity and strong ground motions, while others target low-to-moderate seismicity regions or specific tectonic settings.

Table 1 provides a comprehensive overview of various seismic ground motion databases, listing their project details, database names, years of establishment, the number of records, and the magnitude range of earthquakes they cover. The databases span different time periods and geographical regions, reflecting a diverse range of seismic events and recording stations. Notable projects such as PEER, K-NET, TNSMN, COSMOS, and others are highlighted, each contributing significantly to the accumulation of strong motion data. Additionally, the inclusion of European projects like ESD, SHARE, SIGMA, RESORCE, NERA, ESM, and RRSM underscores the collaborative efforts to establish robust seismic databases for earthquake risk assessment and mitigation. In this study, special attention is given to ESM, RESIF, PEER NGA-East database, and ITACA. These databases were fully analyzed for various stages of the project, including data selection criteria, data processing steps, and data consistency checks. This focused examination ensures the relevance and applicability of our findings within the context of these key seismic databases.

Project	Name of database	Region of data	Time span of recording	Number of records	Magnitude range
	El centro accel-erogram	California, USA	1940		
PEER	PEER Strong Ground Motion Database https://peer.berkeley.edu/peer-strong-ground-motion-databases	Global (mainly California)	Since 1933	3000 records From 170 shallow crustal earthquakes 1400 recording stations	3–8
NIED	K-NET Kyoshin www.k-net.bosai.go.jp Kik-net kiban-Kyoshin www.kik.bosai.go.jp	Japan	Since 1996	1700 digital accelerometric stations in Japan K-NET: 1042 Kik-net: 691	2-9
TNSMN	Turkish National Strong Motion Network	Turkey	1976–2007	4500 timeseries 3000 events 240 stations	3–7.5
COSMOS	COSMOS Database Consortium of Organizations for strong-Motion observations system Different worldwide strong motion datasets www.cosmos-eq.org	World-wide	Since 1960s	9000 strong motion data 515 earthquakes 3000 stations	>5
National project for archiving Italian strong motion data	RAN Italian National Accelerometric Network	Italy	Since 1972	500 digital stations	3–7
S6 and S4 projects	ITACA Italian strong motion database http://itaca.mi.ingv.it	Italy	Alfa-version: 1972-2004 ITACA1-version: 1972-2009 Including strongest event 2008-2009	3955 three component waveforms 1802 earthquakes	≤6.9
FP5 5th framework	ESD European strong	Pan-	1973–2008	~2,000 records	3–7

programme of European commission Started on 1998	motion database First collection of pan-European strong motion data www.isesd.hi.is/ESD_Local/frameset.htm	European			
FP6 6th framework programme of European commission 2006-2010	NERIES / ESD ext. network of research infrastructures for european seismology project A new collection of accelerometric waveforms were added to ESD.	Pan-European	1995–2009	~8,000 waveforms	1–7.4
FP7 7th framework program of European commission Seismic harmonization in Europe project 2010-2014	SHARE	Pan European, Turkey, Italy, Japan, Central & Eastern North America	1972–2010	14,193 records Accelerograms from: • TR-NSMN • , ITACA, KiK-net , NGA	3–8
SIGMA Seismic ground motion assessment project	RESORCE Reference database for seismic ground-motion in Europe database	Pan-European	1973–2011	5882 multi components accelerograms 262 weak motion waveforms 1814 events Contains: pan-European strong motion data	2.8–7.8
7th framework program of the European commission 2010-2014	ESM Engineering strong motion database Linked to: EIDA European integrated data archive Complementary to:	Greece, Italy, Turkey, pan-European	1973-1999 1972-2015 1976-2007 1972 - 2008	2% from HEAD Greek dataforms and metadata 20% from ITACA 7% from TR-NSMN Turkish dataset 1% from ESD pan European data	4 - 7.5
NERA Network of European research infrastructures	RRSM Rapid response strong motion database Complementary to ESM Data are exclusively obtained from EIDA	Pan-European	Since 2010		≥ 3.5

	RESIF Dataset of Earthquake ground motion in mainland France	France	1996-2016	6500 quality checked records 468 earthquakes 379 stations	2.4 - 5.6 ≥ 3.5 Over whole French territory ≥ 2.5 in Eastern part
Next generation attenuation project	PEER NGA-East database	Central & Eastern North America	Since 1976	27000 time series 82 earthquakes 1271 recording stations	> 2.5

Table 1. Overview of major strong- and weak-motion ground-motion databases, including their geographical coverage, time span of recordings, approximate number of records, and magnitude ranges.

Taken together, the reviewed ground-motion databases illustrate that, despite differences in geographical scope, magnitude range, and intended application, similar principles are generally followed in the selection of earthquake records. In particular, most databases rely on a limited set of fundamental seismological and site-related parameters to define datasets that are suitable for engineering and hazard applications.

This synthesis provides the basis for identifying the data-selection criteria that are most relevant for the construction of the BELSHAKE database. These criteria, distilled from established practices in the literature and existing databases, are summarized and discussed in the following section.

2.2 Data selection practices in existing ground-motion databases

Building on the review of existing ground-motion databases presented in the previous section, this section focuses on the criteria used to select earthquake records for different purposes. The construction of a ground-motion database requires selection criteria that ensure consistency, data quality, and adequate coverage of relevant seismic parameters, while maintaining sufficient variability for ground-motion modelling and hazard analysis. In addition, engineering applications often impose further constraints to identify record sets that are representative of specific seismic scenarios and suitable for structural response analysis. Accordingly, data-selection criteria are discussed in two parts: first, the criteria commonly applied in the construction of ground-motion databases, with emphasis on those most relevant to this study; and second, the criteria used in engineering practice for record selection in structural response analyses.

2.2.1 Data selection criteria for ground motion databases

As the primary focus of this study, a more detailed examination was carried out of the RESIF, ITACA, ESM, and PEER NGA-East databases, scrutinizing them for more detailed insights into their selection criteria, metadata requirements, and other pertinent information. This examination allows us to better understand the nuances of these specific databases and their contributions to seismic research. The selection criteria are not always explicitly listed and may be quite different from one database to the other. The extracted selection criteria pertain to type of recording (analog or digital), type of instrument, (accelerometer, broadband or short-period seismometer), lower magnitude bound, distance range, number of records per event, available components, sampling frequency, usable frequency range, recording type (continuous or triggered). Below is a summary of selection criteria mentioned in the associated literature:

- Type of recording: some databases (e.g., ITACA and ESM) contain both analog and digital records, others only digital.
- Type of instrument: most databases contain only strong-motion data recorded with accelerometers, but the RESIF database for France also contains data from (broadband) seismic stations (recording ground velocity); in some stations, an accelerometric and a broadband sensor are co-located, allowing validation of broadband data.
- Data from both permanent and temporary stations are usually included (e.g., RESIF).
- Lower magnitude bound: this is variable from one database to the other. ITACA has a magnitude range of M_w = 2.5 up to 6.9. The RESIF database has a magnitude range of M_L 2.4 – 5.6 (M_w 2.0 – 5.2), complete down to M_L = 3.5 over the entire French territory, and down to M_L = 2.5 in the eastern part of France. The PEER NGA-East database contains all M_W > 4 and selected well-recorded $M_w \geq 2.5$

earthquakes. The ESM dataset is well sampled in the 4-6 magnitude range.

- Distance: In ITACA the distance ranges from 5 to 100 km. The ESM dataset is well sampled in epicentral distance range 10-200 km, with a significant number of waveforms related to strong events (6< M_w <7.5) recorded at epicentral distances larger than 10 km.
- Number of records per event: the PEER NGA-East database only includes earthquakes with 5 or more records within 100 km in order to avoid smaller earthquakes with too few records and to focus on distances < 100 km to characterize geometrical spreading and attenuation.
- Available components: ITACA only contains 3-component data. RESIF and PEER NGA-East only contain recordings with at least 2 good-quality horizontal components. Vertical components are also included if they comply with the quality standards, but single-vertical-component records are usually not retained. ESM database contains three component waveforms.
- Sampling frequency: the PEER NGA-East database contains records with sampling rates as low as 40 Hz, which after processing reduces the upper limit of the usable bandwidth to just above 15 Hz.
- Usable frequency range: in the RESIF database, waveforms for which the difference between the low-pass and high-pass filter corner frequencies is smaller than 0.7 in log units or includes less than 40% of the whole signal frequency range are rejected. This criterion is required for both horizontal components.
- Usable period range: In ESM the maximum usable period ranges from 2.5 to 10 s, and some waveforms have lower values (1-2.5 s) mainly because they are recorded by analog instruments, and limited number of records can be used up to 20s.
- Late-triggered records: in ITACA, an explicit identification and treatment is done of analog records triggered on the S-phase or later, and denoted as late-triggered. In PEER NGA-East, late-P-triggered records are flagged, but records that are triggered later are discarded;

- Problematic records (very short coda wave duration, clipping, large ringing, spikes) are usually discarded, but noise-dominated records not necessarily (PEER NGA-East).
- Records affected by microseisms: this issue seems to be only addressed in PEER NGA-East, but may be important for recordings from small magnitude events at large distances. The microseismic noise may overlap with the usable frequency range, but in order to keep earthquake signal at lower frequencies where data are sparse, the PEER NGA-East database does not exclude these records. Instead, the frequency ranges affected by microseisms are provided.

2.2.2 Data selection criteria for structural response analysis

The second outcome of the literature study is the most important data selection criteria for structural response analysis in seismic engineering. This is not the same as the data selection criteria for the ground-motion database, but is relevant because it gives an insight into the requirements for one of the most important end users of this database. Given the fact that recording time history signals for a given site is a random process which is practically impossible to reproduce, in recent years considerable effort has been expended on processing actual records to make them 'representative' of future input histories. Moreover, considerable effort in reducing dispersion in the analysis due to the usage of different earthquake records has also been made. Along these lines, the aim of this part of the thesis is to present the most recent methods developed for selecting an appropriate set of records. Real records have to fulfill anticipated earthquake scenarios (Katsanos, Sextos and Manolis, 210).

As mentioned in the Introduction, the selection of ground-motion records for structural response analyses is typically guided by a predefined target response spectrum representing the expected seismic demand at the site. This spectrum represents the seismic demand at a specific site, and can be defined in different ways depending on the application, including the uniform hazard spectrum (UHS), the conditional mean spectrum (CMS), code-based spectra (e.g., Eurocode 8 or ASCE 7), or scenario-based spectra derived from specific earthquake parameters. In practice, the target spectrum is further refined based on site conditions, structural period, and seismic scenario, and is then used as a reference for selecting and scaling records to ensure compatibility with the expected ground-motion characteristics and hazard level (Baker, 2011).

2.2.2.1 Record selection based on earthquake magnitude (M) and distance (R)

Earthquake magnitude (M) and distance (R) from the site of interest to the rupture zone are the most common parameters related to a seismic event. Therefore, identifying these characteristic (M, R) pairs is included in any selection procedure. Notably, depending on the risk metric targeted by the analysis, there exists a minimum magnitude (M_{min}) below which ground motions are of no practical engineering interest (Bommer and Crowley, 2017). In much research, magnitude has been considered an important earthquake record selection parameter, while the importance of the closest source-to-site distance has not been established (Bommer and Acevedo, 2004b; Stewart et al., 2002). It is confirmed that for the structural response, the closest source-to-site distance is statistically insignificant and an inadequate predictor of structural response and is therefore considered as a supplementary criterion in the selection procedure while the earthquake magnitude exerts an influence on various response quantities and is the most significant parameter in the selection process (Baker and Cornell, 2005).

2.2.2.2 Soil profile

The actual soil profile at the intended site is a selection criterion complementing both earthquake magnitude and distance, leading to (M, R, S) record sets (Youngs et al., 2006; Kurama and Farrow, 2003). The geotechnical profile influences seismic motions by modifying both their amplitude and the computed response spectra (Bommer and Acevedo, 2004b). Soil profile must be known with a high degree of confidence in order to be used in the selection process. Although deeper soil structure can also exert a strong influence in some cases, shear-wave velocity over the uppermost 30 m (V_{S30}) can be used as a suitable metric for site classification (Lee et al., 2000).

By applying (M, R, S) selection criteria, the number of records eligible for selection will drastically reduce when compared to the simpler (M, R) parameter pair. Therefore, in some cases it is advisable to relax the site classification matching criteria to ensure a reasonable number of records will be made available (Bommer and Acevedo, 2004b). However, it should be noted that consideration of local soil profile remains an important selection parameter.

2.2.2.3 Strong motion duration

Strong-motion duration is also a complementary criterion for the selection of real records. Duration of ground shaking is influenced by duration of the fault rupture, which is a function of magnitude that has already been discussed (Bommer and Scott, 2000).

It has been shown that duration is a secondary predictive parameter and to explore direct correlations between duration and damage would be futile (Hancock and Bommer, 2007). Duration influences energy-based models such as hysteretic ductility and equivalent number of cycles, while it is insignificant for displacement-based demand indices (Iervolino et al., 2006).

It is suggested by some seismic codes such as the ASCE Standards 4-98 that the duration of selected records shall be representative of the expected ground motion at the intended site for a given level of seismic hazard. Furthermore, the selection process should be based on both significant duration and spectral shape (Malhotra, 2003). In any case, the adoption of strong-motion duration in the record selection process must be carefully justified.

2.2.2.4 Seismotectonic environment and other geophysical/seismological parameters

Regional seismotectonic features and the degree to which these are reflected on the ground motions recorded during a seismic event are important issues in the data selection procedure. The influence of these effects comprising rupture mechanism, source environment, type of faulting, source path, and directivity of seismic waves on strong motions has been observed in many studies. Ground motions caused by buried rupture-type earthquakes in the period range around 1.0 s are significantly stronger than ground motions caused by surface rupture events (Kagawa et al., 2004). Some differences in the predicted response spectra derived from strong motions in shallow stable regions (Europe, Eastern USA) and in subduction zones (Japan, New Zealand, Taiwan) are shown by Campbell (Papageorgiou and Aki, 1983). In subduction zones peak ground motions attenuate more slowly than those from shallow crust earthquakes in tectonically active regions (Bolt et al., 2003; Lin and Lee, 2008).

However, in considering the 'overall' selection process, a balance needs to be reached because inclusion of criteria using seismotectonic environment features may significantly reduce the acceptable number of records required (Bommer and Acevedo, 2004b).

2.2.2.5 Acceleration to velocity ratio (a/v)

By considering characteristics of the recorded site and the seismotectonic features of the intended location, the acceleration to maximum velocity (a/v) ratio has been proposed as a complementary measure in the selection process (Katsanos et al., 2010b).

The (a/v) ratio for strong ground motions is related to earthquake magnitude, distance from source plus frequency content of accelerograms (Tso et al., 1992; Sawada et al., 1992). Consequently, accelerograms that cover the following ratios are believed to cover a wide range of earthquakes that are independent of the particular site, resulting in a conservative upper bound of expected ground motion. Aforementioned ratios can be grouped as 'low' (a/v < 0.80 $g/m/s$), 'intermediate' (0.80 < a/v < 1.20 $g/m/s$) and 'high' (a/v > 1.20 $g/m/s$). However, it is noted that this particular index shall be rather considered as a conservative upper bound of the expected ground motion, and not the sole criterion for a selection process (Kwon and Elnashai, 2006).

2.2.2.6 Record selection based on ground motion intensity measures

The computation of the mean probability of exceedance of a particular value for a specific demand is the core of recent developments in performance-based seismic design. The accuracy of the desired response variable is controlled by estimation of this probabilistic measure for a particular return period of a specific seismic event. Therefore, selection of recorded earthquake ground motions for dynamic excitation of a particular structure must be performed such that dispersion in the response quantities will remain relatively low (Katsanos et al., 2010b).

2.2.3 Required metadata

Alongside the ground motion records, comprehensive metadata needs to be provided. Metadata can be categorized in four main groups: event metadata, station metadata, event-station metadata and waveform metadata as described below:

2.2.3.1 Event metadata

These correspond to the main source parameters of the earthquakes that generated the recorded time series. These include:

- Event ID;
- Event name;
- Date and time;
- Location: latitude and longitude;
- Focal depth;
- Magnitude: M_L, M_S and/or M_w ;
- M_w determination: spectral computation / converted from M_L/ …;
- Event type: tectonic / induced.

Optional parameters that are more difficult to determine, but are useful to include if known:

- Focal mechanism;
- Stress drop;
- 3-D rupture plane (for M>~5.5 earthquakes).

2.2.3.2 Station metadata

Station metadata consist of at least:

- Station ID;
- Network code and station code;
- Country;
- Name of locality;
- Location: longitude, latitude, elevation, depth below surface;
- Emplacement: free surface, vault, posthole, borehole, underground tunnel, …;
- Housing structure: cabin, building (which floor / how many floors), …

In addition, it is very important to characterize the local site conditions:

- Soil classification (following Eurocode 8);
- V_{S30};
- V_{S30} determination: measured from full profile, inferred from a shallower (< 30 m) profile, inferred from geotechnical information

(N_{SPT}), inferred from H/V spectral ratio, inferred from similar site, inferred from geology; inferred from slope, not known…
- Surface geology: lithology, age, depth to bedrock;
- Site morphology.

It is also useful to collect supporting information, if available, but this does not necessarily have to be included in the database itself:

More detailed geotechnical information:

- SPT (Standard Penetration Test) logs;
- Fundamental frequencies of the soil;
- H/V spectral ratios;
- V_s/V_p profiles and dispersion curves;

In ITACA, the following maps are also provided:

- Location on a topographic map;
- Aerial view;
- Schematic geological map.

2.2.3.3 Event-Station metadata

These are metadata which are related to the combination of the station and the event, and include:

- Source-to-site distance: epicentral and hypocentral distance, and in the case of large ruptures/magnitudes (M > ~5.5) also Joyner-Boore distance and rupture distance;
- Azimuth (epicenter to station direction) and back-azimuth (station to epicenter);
- P- and S-wave arrival times.

This information is either available in the ROB database (arrival times) or can be computed from the event and station locations (distances and azimuths).

2.2.3.4 Waveform metadata

These metadata are specific for each waveform:

- Station ID;
- Event ID;
- Channel or component code and orientation;

- Time of first sample;
- Number of samples;
- Sampling rate;
- Duration (= number of samples / sampling rate);
- Data units;
- Valid frequency range (f_{min} / f_{max});
- Instrument type (accelerometer, broadband seismometer or short-period seismometer);
- Instrument model;
- Acquisition system (datalogger);
- Native ground-motion type (acceleration, velocity, or displacement);
- Type of recording: continuous or triggered, and in the latter case late or normal triggered;
- Instrument properties (natural frequency, damping, sensitivity, analog and digital gain, …) or full instrument response in StationXML format;
- Start time and end time of pre-event noise, P-wave, S-wave and coda-wave windows;
- Processing history;
- Data quality code;
- Data owner.

2.3 Evolution of the Belgian seismic network

Systematic recording of earthquake ground motion in Belgium is carried out by the Royal Observatory of Belgium (ROB), which operates the national seismic network. The network has evolved significantly over the past four decades, both in spatial coverage and in the quality of the instruments used. Digital seismic recording in Belgium began in 1985, following the damaging 1983 Liège earthquake (M_w = 4.7), which highlighted the need for improved monitoring capabilities. Initially, only a few stations were equipped with digital short-period sensors, and data were stored selectively for detected events. Over time, the number of stations and the diversity of instruments increased, leading to progressively better spatial coverage and data quality.

During the 1990s, the network was modernized with three-component short-period seismometers, replacing earlier single-component systems. From 1999 onward, the network was expanded with accelerometers in the most seismically active areas. These early accelerometers operated mainly in triggered mode, saving data only when an event was detected.

In the early 2000s, the ROB began installing broadband seismometers, providing a wider dynamic range and enabling recording of both local and regional earthquakes. From 2005, improvements in data storage and transmission allowed the first continuous recordings, initially for selected stations and later for the entire network. Continuous data streams became the standard recording mode by the mid-2010s. A major step forward occurred with the integration of Belgian stations into the European Integrated Data Archive (EIDA). Since 2024, most Belgian seismic and accelerometric stations stream their data in near real time to EIDA, ensuring standardized formats, permanent archiving, and open access for the scientific community.

Today, the Belgian seismic network consists of approximately 30 seismometers (short-period and broadband) and about 20 accelerometers, complemented by temporary installations deployed for aftershock sequences or local monitoring campaigns. Figure 6 shows a map of stations with at least 10 records in the BELSHAKE database. This gradual evolution has resulted in a heterogeneous archive, containing recordings with different sampling rates, dynamic ranges, and recording modes (continuous, triggered, and event-based). Thanks to the BELSHAKE database, all these hetereogeneous data are accessible in the same way.

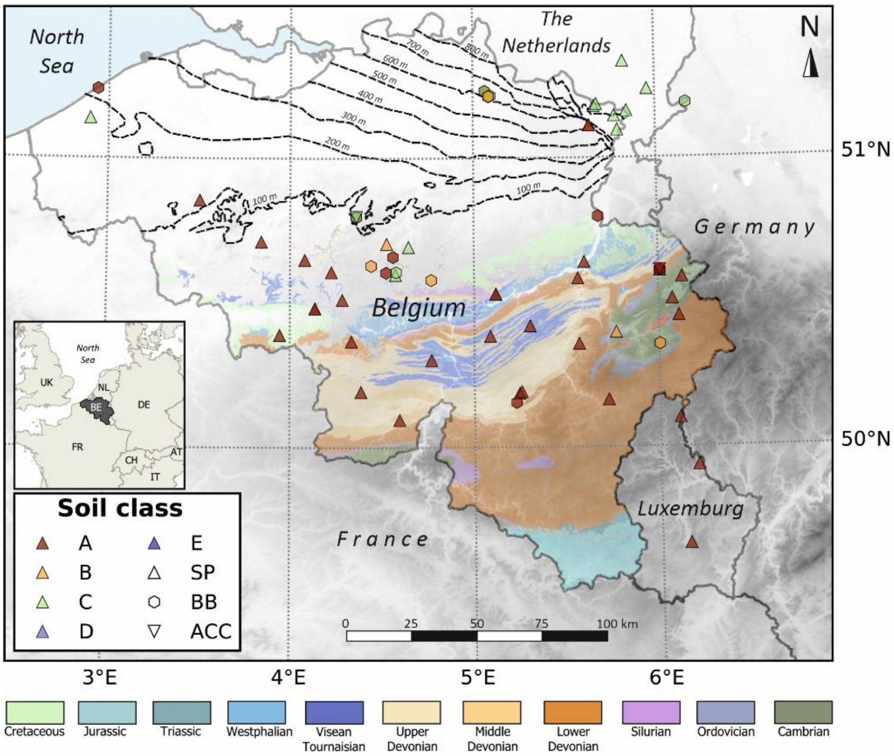

Figure 6. Location of seismic stations with ≥10 records in the BELSHAKE database. Symbol colors correspond to Eurocode 8 soil class (A-E) and symbol shapes to instrument type (SP=short-period; BB=broadband; ACC=accelerometer). Background image depicts simplified surface geology, with bedrock in the south and NNE-ward thickening sediment layers (100 m contour interval) in the north. Note that some of these stations were deployed in temporary networks, and some stations of the permanent network have been discontinued.

2.4 BELSHAKE data selection

The next task consisted of the systematic inventory of all available digital waveform data housed in the ROB archive. Data selection consists of three main steps:

2.4.1 Selection of events meeting the selection criteria.

This step involved two parts. In the first part the events were selected based on the following criteria:

- start date: 1985 (start of digital recording);

- magnitude: local magnitude M_L ≥ 2.5.
- event type: natural and induced earthquakes;
- location: epicenter in a rectangular area around Belgium between -1° and 9° E, and between 49° and 52° latitude;

These criteria led to the selection of 200 events from the ROB earthquake database.

In the second part we selected the events with 2 < M_L ≤ 2.5 in a smaller area around Belgium. The selection criteria for this part were defined as follows:

- start date: 1985;
- magnitude: local magnitude 2 ≤ M_L < 2.5;
- event type: natural and induced earthquakes;
- location: epicenter in a rectangular area around Belgium between 2.5° and -7° E, and between 49.25° and 51.5° latitude.

The second phase resulted in the selection of 182 events. In total, 382 events and 7,500 records were incorporated into the BELSHAKE database (Figure 1).

Additionally, twelve induced earthquakes with magnitudes between 1.0 and less than 2.0 were included due to their recordings at short epicentral distances. Alongside data from the permanent Belgian seismic network, waveform records from neighboring countries were included for certain key events to improve spatial coverage. In particular, the 1992 Roermond earthquake and its aftershocks were complemented with approximately 207 records imported from ten external networks in France, Germany, the Netherlands, the United Kingdom, and the Czech Republic. This integration compensates for limitations in early Belgian recordings, which were often clipped due to the small dynamic range of seismometers operating at that time. The inclusion of these external data ensures that the BELSHAKE database adequately represents significant regional events. The most significant earthquakes represented in BELSHAKE are those with local magnitudes (M_L) of 4.0 or higher, which provide the strongest ground-motion records in the region. These include the 1992 Roermond (M_w 5.3) earthquake in the Netherlands the largest and most important event in the dataset, as well as notable events such as Le Roeulx (1995, M_L 4.5), Alsdorf (2002, M_W 4.6), Folkestone (2007, M_L 4.3), Koblenz (2011, M_L 4.1), Goch (2011, M_L 4.3), and Ramsgate (2015, M_L 4.1). Together, these events provide a valuable set of moderate-magnitude records for developing regional ground-motion models.

For each event, we extracted the relevant source parameters from the ROB database.

2.4.2 The recording seismic stations for each event

Based on the information in the ROB station database, it can be determined which stations were operational at the time of each event. This information is then used to check if the ROB waveform archive contains data for the corresponding station and time. Station metadata is extracted from the ROB station database, and event-station metadata is subsequently computed. We also check if stations from neighboring networks are available from international data servers.

2.4.3 Waveform data

For each event and station, a suitable time window is calculated to capture the complete event, including pre-event noise and coda wave, and the corresponding raw waveform data are downloaded from the ROB waveform archive or international data servers into a dedicated BELSHAKE waveform archive. In each step, the associated metadata is extracted or computed and stored in the BELSHAKE database (see further).

2.5 Database structure

The BELSHAKE database consists of two main components: (1) a waveform archive containing raw and processed seismic data, and (2) a relational database storing event, station, processing, and derived-parameter metadata. The waveform archive forms the first main component of BELSHAKE.

For each event, a dedicated folder contains one file per station, stored in the Adaptable Seismic Data Format (ASDF; Krischer et al., 2016). This flexible format allows multiple waveforms, metadata, and auxiliary data to be kept in a single file. Each ASDF file includes the raw and processed waveform data, the corresponding instrument response information, relevant event and station metadata, and derived Fourier and response spectra. Intermediate processing steps are preserved through different “tags,” allowing full traceability of waveform processing.

The structure of the database was designed based on insights obtained from the literature study. Initially, it comprised five main tables representing the core components identified as essential for a comprehensive ground-motion dataset: events, stations, event–station relationships, waveforms, and waveform components. Each table corresponds to a distinct category of metadata necessary for accurate documentation, traceability, and data management. In particular, the initial BELSHAKE database includes the following tables and their corresponding columns:

Table “events”: contains event metadata

- ID: earthquake ID;
- name: name of locality closest to epicenter;
- datetime: origin time of earthquake;
- lon: longitude of epicenter (°);
- lat: latitude of epicenter (°);
- depth: focal depth (km);
- M_L: local magnitude;
- M_S: surface-wave magnitude;
- M_W: moment magnitude;
- M_W_method: method used to determine moment magnitude;
- errt: uncertainty on origin time (seconds);
- errh: uncertainty on epicentral location (km);
- errz: uncertainty on focal depth (km);
- type: event type (earthquake or induced earthquake);
- agency: agency providing earthquake source parameters;
- strike1/2: strike of first/second nodal plane of focal mechanism (°);
- dip1/2: dip of first/second nodal plane of focal mechanism (°);
- rake1/2: rake of first/second nodal plane of focal mechanism (°);
- operator: name of operator who last modified the database record;
- lastmod: date and time of last modification of database record.

Table “stations”: contains station metadata

- nw_stat_code: network and station code;
- place_name: name of locality where station is situated;
- country: country where station is located;
- lon: longitude of station (°);

- lat: latitude of station (°);
- altitude: absolute altitude of station (m);
- local_depth: depth relative to surface of station (m);
- emplacement: instrument emplacement (free surface, vault, posthole, borehole, underground tunnel);
- housing: housing structure in which the instrument is situated (cabin, building, …);
- soil_class: Eurocode 8 soil class;
- V_{S30} : shear-wave velocity in the upper 30 m at the site (m/s);
- V_{S30}_method: method with which V_{S30} was determined;
- lithology: lithology of geologic layer with which the instrument is in contact;
- geo_age: age of geologic layer in contact with the instrument;
- depth_to_bedrock: depth of bedrock below instrument (m);
- morphology_class: morphology of site where station is situated;
- operator: name of operator who last modified the database record;
- lastmod: date and time of last modification of database record.

Table “events_stations”: contains event-station metadata

- event_ID: earthquake ID;
- nw_stat_code: network + station code;
- instrument_type: type of instrument (accelerometer, broadband or short-period seismometer);
- R_{epi}: epicentral distance (km);
- R_{hypo}: hypocentral distance (km);
- R_{jb}: Joyner-Boore distance (km);
- R_{rup}: rupture distance (km);
- azimuth: azimuth from epicenter to station (°);
- back_azimuth: azimuth from station to epicenter (°);
- Ptime: time of P-wave arrival;
- Ptime_method: how Ptime was determined (database, theoretical or manual);
- P_takeoff_angle: takeoff angle of P wave at hypocenter (°);
- P_incidence_angle: incidence angle of P wave at station (°);

- P_comp_code: waveform component used to determine P-wave arrival;
- Stime: time of S-wave arrival;
- Stime_method: how Stime was determined;
- S_takeoff_angle: takeoff angle of S wave at hypocenter (°);
- S_incidence_angle: incidence angle of S wave at station (°);
- S_comp_code: waveform component used to determine S-wave arrival;
- operator: name of operator who last modified the database record;
- lastmod: date and time of last modification of database record.

Table "waveforms": contains waveform metadata that are common for all components

- event_ID: earthquake ID;
- nw_stat_code: network + station code;
- local_file_path: path to associated file in BELSHAKE waveform library;
- components: available components;
- native_gmt: native ground-motion type (acceleration, velocity or displacement);
- instrument_model: instrument model;
- instrument_type: type of instrument (accelerometer, broadband or short-period seismometer);
- datalogger: acquisition system model;
- recording_type: type of recording (continuous / discontinuous / triggered);
- original_format: format in which the waveform data were recorded;
- response_source: source of the instrument response information;
- noise_start/end: start time and end time of noise window;
- P_start/end: start and end time of P window;
- S_start/end: start and end time of S window;
- coda_start/end: start and end time of coda window;
- time_shift: time shift applied to waveform in case of timing problem;
- problems: list of problems (from predefined problem categories) found for this record;
- data_owner: institution owning the data;

- operator: name of operator who last modified the database record;
- lastmod: date and time of last modification of database record.

Table “wf_components”: waveform metadata that are possibly different for individual components

- event_ID: earthquake ID;
- nw_stat_code: network + station code;
- comp_code: component code;
- start_time: start time of component;
- end_time: end time of component;
- num_samples: number of data samples;
- sample_rate: sample rate at which the waveform data were recorded (Hz);
- sample_interval: time interval between data samples (= 1/sample_rate) (seconds);
- duration: total duration of component data (seconds);
- fmin: minimum reliable frequency (Hz);
- fmax: maximum reliable frequency (Hz);
- quality: data quality code;
- operator: name of operator who last modified the database record;
- lastmod: date and time of last modification of database record.

This database structure was then implemented in a relational database supporting the SQL (standard query language) standard.

During the course of this work, the database structure was expanded to include key tables such as intensity_measures, kappa, kappa_component, and crustal_domain+kappa.

Table “intensity_measures”: stores computed intensity parameters derived from processed waveforms.

- comp_code: component of motion (E, N, or Z);
- window: selected time window used for computation;
- PGA: peak ground acceleration (m/s^2);
- PGV: peak ground velocity (m/s);
- EPA: effective peak acceleration;
- EPV: effective peak velocity;

- EPD: effective peak displacement;
- AI: Arias intensity;
- HI: Housner intensity;
- ASI: acceleration spectrum intensity;
- D5–95: significant duration between 5% and 95% of cumulative energy;
- D5–75: duration between 5% and 75% of cumulative energy;
- D95_eff: effective duration up to 95% of total energy;
- Db5PcG: duration parameter based on 5% ground-motion energy;
- CAV: cumulative absolute velocity;
- sCAV: standardized cumulative absolute velocity;
- BCAV: bracketed cumulative absolute velocity;
- RMSa: root mean square acceleration;
- SA(0.01) – SA(4.00): spectral acceleration values computed at different periods (0.01–4.00s);
- operator: name of operator who last modified the database record;
- lastmod: date and time of last modification of database record.

Table "kappa": contains component-specific κ computation result for each record:

- event_ID: unique identifier of the earthquake;
- nw_stat_code: network + station code;
- comp_code: component code (E, N, or Z);
- f1: lower frequency limit of the fitting range (Hz);
- f2: upper frequency limit of the fitting range (Hz);
- kappa: computed kappa based on Anderson and Hough method;
- kappa_err: standard deviation of κ;
- log_y_intercept: intercept of the linear fit in logarithmic space;
- log_y_intercept_err: standard deviation of the intercept;
- operator: name of operator who last modified the database record;
- lastmod: date and time of last modification of database record.

Table "kappa_component": contains estimated site kappa (κ_0) kappa gradient (κ_{r_S}) for each station:

- nw_stat_code: station code;

- crustal_domain: the crustal domain to which the station belongs;
- comp_code: component code (H, Z);
- method: method used to estimate (FKG, JKG or MER);
- kappa0: estimated site kappa value of each station (κ_0);
- kappa0_sigma: standard deviation on κ_0 estimation;
- kappa_gradient:estimated kappa gradient of each station(κ_{r_S});
- kappa_gradient_sigma: standard deviation on κ_{r_S} estimation;
- n: number of records for each station after filetring;
- R_squared: coefficient of determination of fit for each station;
- preferred: flag indicating preferred κ_0 and κ_{r_S} estimation method;
- final κ_0: the final most reliable selected κ_0 for each station and component code;
- final κ_r: the final most reliable selected κ_{r_s} for each station and component code;
- operator: name of operator who last modified the database record;
- lastmod: date and time of last modification of database record.

Table "crustal_domains+kappa": contains the crustal domain data and estimated kappa values for each crustal domain:

- code; short name of the crustal domain;
- name: name of the crustal domain;
- wkt: : polygon geometry describing the polygon boundary;
- kappa_gradient: estimated κ_r of the crustal domain;
- kappa_gradient_sigma: standard deviation of the estimated κ_r of the crustal domain
- kappa_method: kappa estimation methos which was used for the final selected values.

Overall, the relational structure of the BELSHAKE database ensures logical consistency across all data entities, linking events, stations, and waveforms through unique identifiers such as event_ID and nw_stat_code. This design facilitates efficient data integration, traceability, and alignment with established international ground motion databases, supporting both current research objectives and potential future expansions.

2.6 Characteristics and composition of the BELSHAKE database

Figure 7 presents the magnitude–distance distributions of the BELSHAKE and RESIF datasets (Traversa et al., 2020), two key parameters for end users of ground-motion databases. For the BELSHAKE dataset (left panel), different colours indicate the type of recording instrument, including short-period (SP), long-period (LP), broadband (BB) seismometers, and accelerometers (ACC). The dataset is dominated by recordings from earthquakes in the magnitude range 2 < M_L < 4, with fewer events between 4 < M_L < 5, and only two larger earthquakes (M_L 5.0 Liège and M_L 5.8 Roermond). The magnitude coverage is therefore relatively good up to M_L ≈ 4 but decreases significantly for larger magnitudes. Hypocentral distances are mainly distributed between 20 and 300 km, although several short-distance recordings (<10 km) are available for smaller events (M_L < 3).

In comparison, the RESIF dataset (right panel) also contains a large number of events in the magnitude range 2–4.5, with additional coverage extending to magnitudes of about 5–5.5. While both datasets exhibit broadly similar magnitude–distance distributions, RESIF provides denser coverage in the M_L ≈ 4–5.5 range, whereas BELSHAKE offers relatively better sampling at short distances.

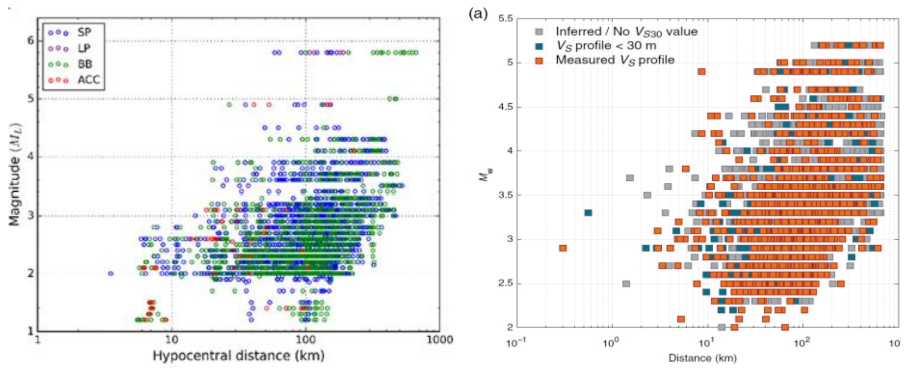

Figure 7. Right panel: Magnitude-distance plot of RESIF network. Left panel: Magnitude-distance plot of records with horizontal components and acceptable quality of the S window in the BELSHAKE database. Colors correspond to instrument types: Short-period seismometer (SP), long-period seismometer (LP), Broadband seismometer (BB), and Accelerometer (ACC)

Figure 8 provides visual representation through three histograms, offering insights into the coverage and characteristics of the BELSHAKE database. The first histogram indicates that the majority of events selected for the BELSHAKE database have magnitudes below 2.5, with the number of events decreasing sharply as magnitude increases. Only a small number of events have magnitudes greater than 4, showing that larger earthquakes are relatively rare in the region. The second histogram shows the distribution of records as a function of hypocentral distance. Very few records have a hypocentral distance of less than 10 km, while the majority were obtained at distances ranging from approximately 120 to 250 km. The third histogram illustrates the distribution of events with respect to the number of recording stations. Approximately 160 events were recorded by between 10 and 25 stations, while around 50 events were captured by 25 to 45 stations. Similarly, about 50 events were recorded by only 1 to 5 stations, suggesting that most events are moderately well recorded across the network.

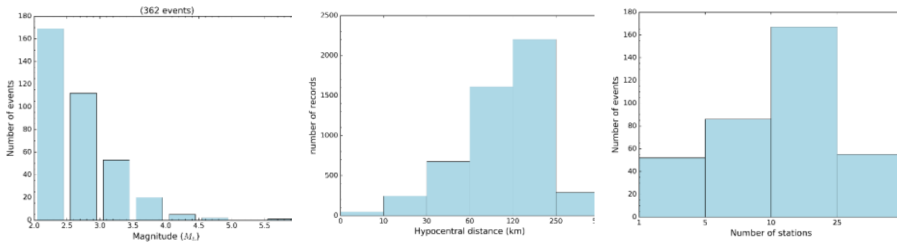

Figure 8. Histograms of magnitude (M_L), hypocentral distance and number of stations for the records in BELSHAKE

Figure 9 illustrates the distribution of tectonic (blue) versus induced (orange) earthquakes in the BELSHAKE database over the years. Approximately 95% of the recorded events in BELSHAKE are attributed to tectonic activity, while the remaining 5% are classified as induced earthquakes. Notably, induced earthquakes are observed to emerge from the year 2005 onwards, with all earthquakes before that period considered natural events.

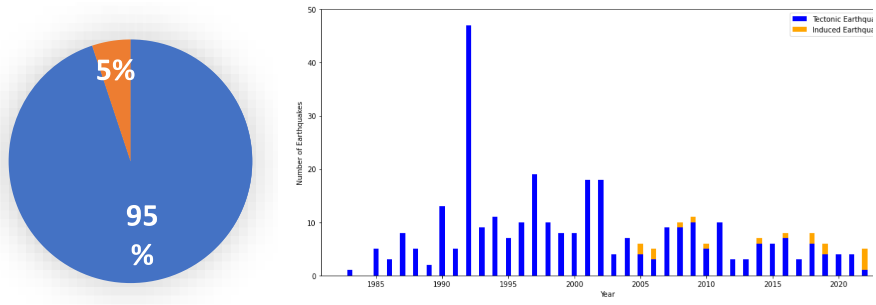

Figure 9. Tectonic vs. induced Earthquakes in BELSHAKE. Left: the percentage of tectonic (blue) vs induced (orange). Right: the number of tectonic vs induced events over the years

Figure 10 illustrates the seismic and accelerometric network of ROB. Since 1985, a total of 65 short-period stations, 49 broadband stations, and 17 accelerometers have been utilized to capture seismic events, contributing valuable data now incorporated into the BELSHAKE database. It is noteworthy to mention that some of these stations were temporary and are no longer operational. This underscores the evolving nature of the network and the need to consider the varying status of stations when analyzing seismic and accelerometric data.

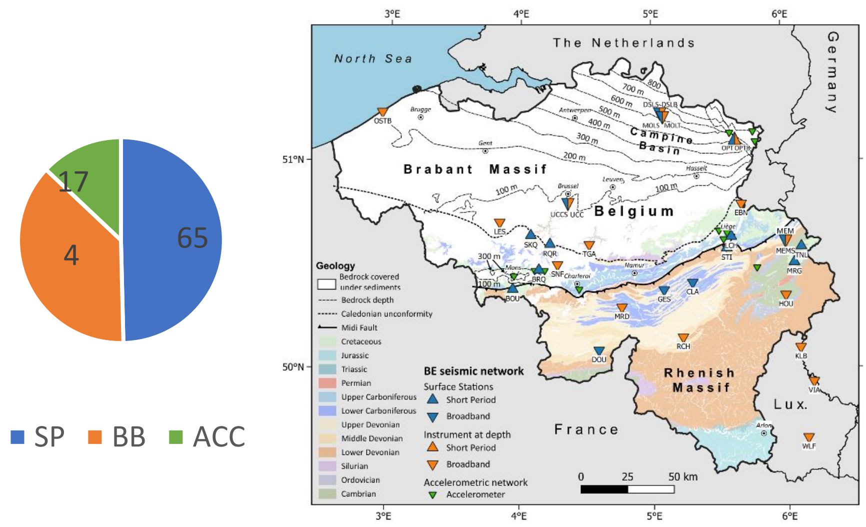

Figure 10. Left: the number of different instrument types employed for the records in the BELSHAKE database from 1985 (SP: Short-period, BB: Broadband and ACC: Accelerometer). Right: the current ROB seismic and accelerometric network

2.7 Waveform quality check

Prior to diving into the data processing stage, there's a crucial step in the BELSHAKE database workflow that requires a thorough visual examination of the imported waveforms. Positioned between the initial data selection and the actual processing, this phase demands careful attention, and it turned out to be one of the most time-consuming aspects of the entire process.

During this visual inspection, we conducted a comprehensive assessment of all components of each record, examining the noise, P-wave, S-wave, and coda windows separately to identify potential problems. This quality control procedure is essential for ensuring the reliability and integrity of the data. We specifically look out for potential problems in the waveforms, which may include, but are not limited to:

- Timing problems;
- Low signal-to-noise ratio;
- Presence of spikes;
- Presence of disturbances;
- Interruptions (data gaps);
- Clipping;
- Baseline distortion;
- Missing or incomplete phase windows;
- Presence of fore- or aftershocks in the noise and/or signal windows.

Examples of these problem categories are shown in Figure 11. Some problems that could be fixed were fixed:

- Most timing problems could be fixed by determining the time shift between the P-wave onset and the expected P-wave arrival, and reimporting the data with the time shift applied;
- Spikes could be removed by replacing them with interpolated values;

- Some distortions could be removed by interactive baseline removal;
- Disturbances that are not affecting the main signal phases (P and S) could be removed by trimming.

All remaining problems are not fixable and were left as such. The problems and, if applicable, fixes were imported in the database, in a way that they can be queried for any component and window. Based on these problem categories and fixes, we defined 3 different quality classes, and we developed a method to select only records having a specific quality, again at the level of component and window. These quality classes are:

- Good: no problems, only slightly trimmed ("curtailed"), with spikes that have been successfully removed or fore- or aftershocks that have been successfully trimmed;
- Intermediate: windows that are noisy or with corrected distortions;
- Poor: windows that are very noisy, clipped, missing, incomplete, disturbed, interrupted, have no waveform, or contain spikes, distortions, fore- or aftershocks that could not be removed.

We categorize records into two main groups: reliable records, which include both good and intermediate-quality records, and unreliable records, specifically referring to those of bad quality. Through this classification, we have determined that there are 7,093 records classified as reliable and 427 records categorized as unreliable. 94% of the records have thus been identified and selected as reliable. Consequently, in the subsequent steps of windowing and processing, only the records marked as reliable are utilized, ensuring that the data used for further analysis maintains a high level of quality and accuracy. Simultaneously with the visual quality control, we also corrected some P- and S-wave arrival times that were obviously wrong.

Timing problem

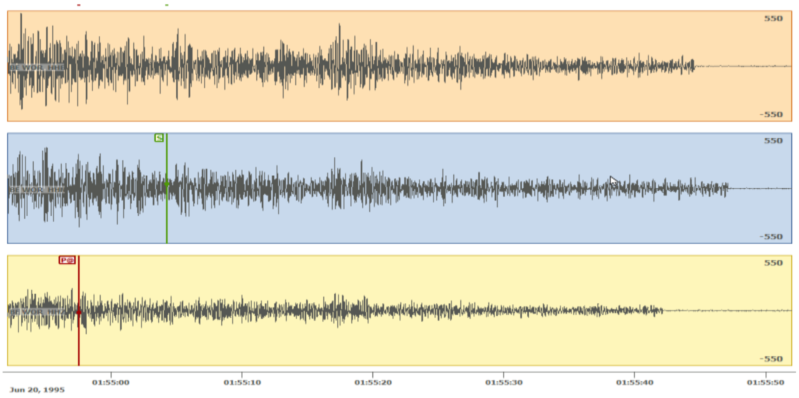

Low signal-to-noise ratio

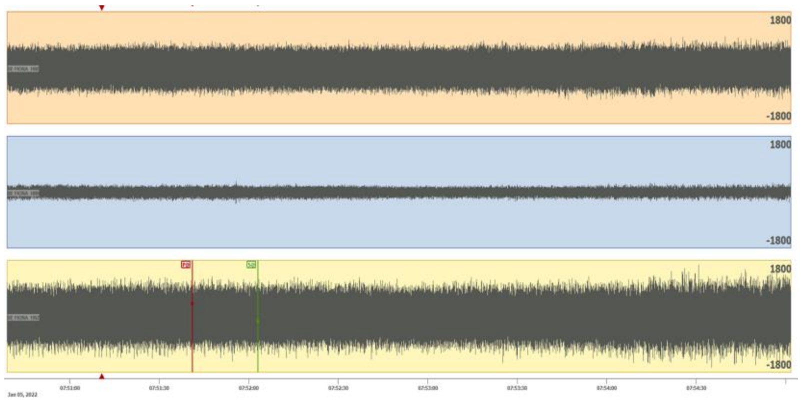

Presence of spikes

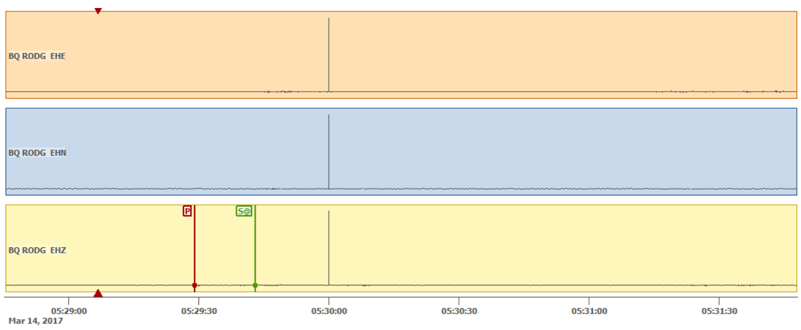

Disturbanc
e

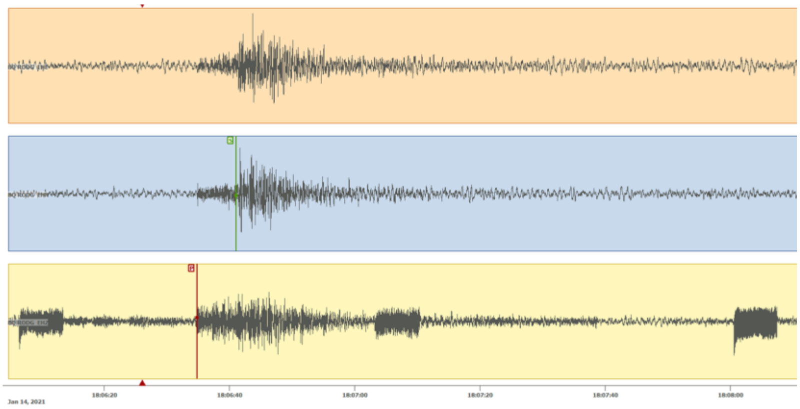

Data gaps

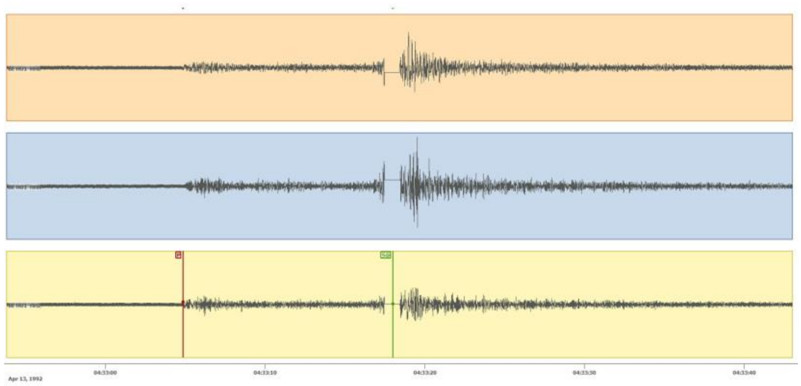

Clipping

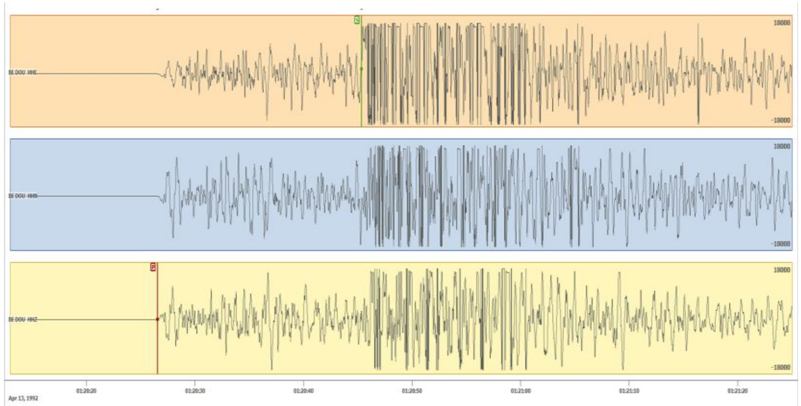

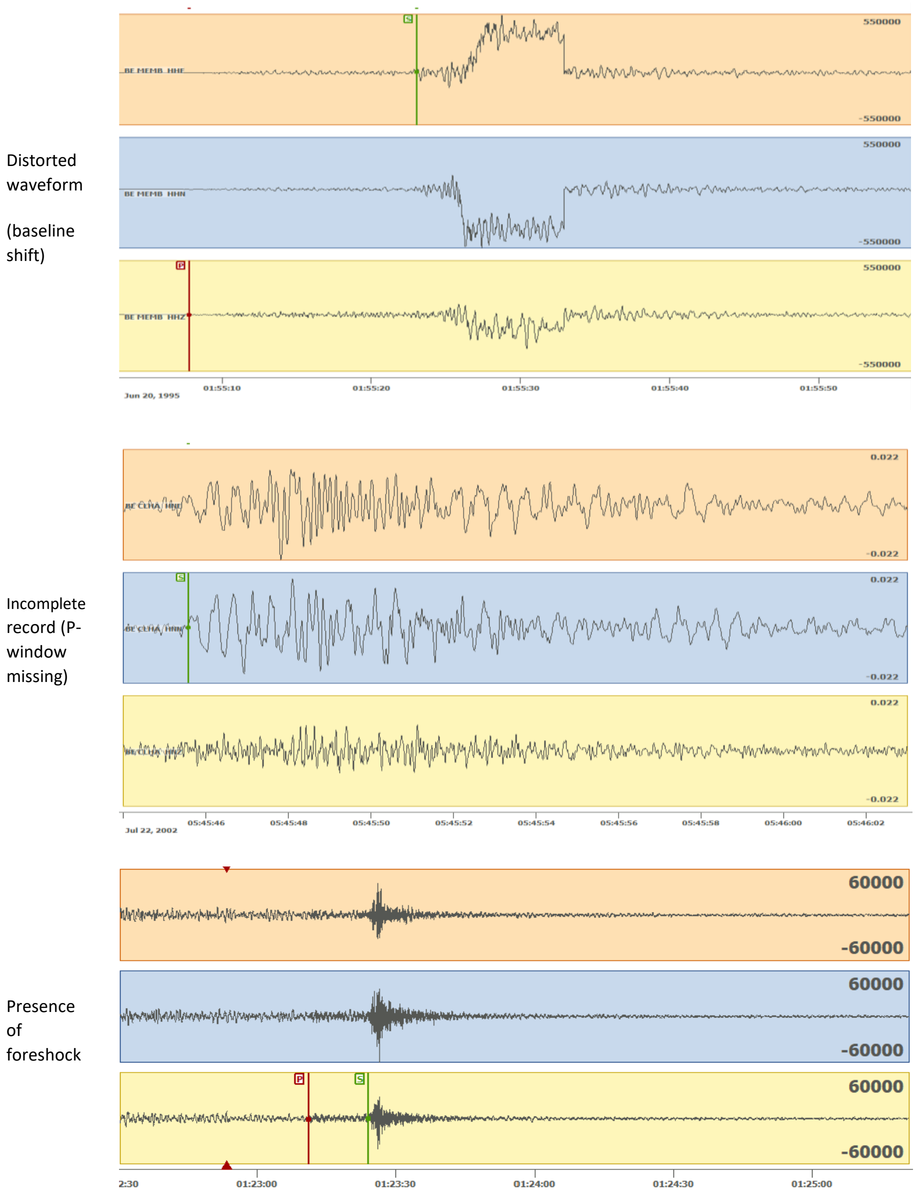

Figure 11. Illustration of waveform problem categories. For each category, a 3-component seismogram is shown. Red vertical lines correspond to P-wave arrival times, green lines to S-wave arrival times

2.8 Conclusion

The study of various international and European databases illustrates the diversity and collaborative efforts involved in establishing seismic databases for earthquake risk assessment and mitigation. In this study, we focused on key datasets such as RESIF, ITACA, ESM, and PEER NGA-East. The exploration highlighted important considerations and requirements for assembling a state-of-the-art ground-motion database, with particular attention to data selection criteria and metadata requirements and waveform processing steps. These insights guided the construction and implementation of the BELSHAKE database, which includes events with local magnitudes $ML \geq 2$ in Belgium and the surrounding area, totaling around ~6400 digital seismograms, ~5840 from 327 tectonic earthquakes and ~580 from 17 induced earthquakes. Raw waveform data, essential for seismic analysis, were downloaded and stored in the BELSHAKE waveform library along with all relevant metadata. This comprehensive dataset provides a solid foundation for future seismic hazard studies and earthquake engineering research in the region. Beyond its value as a structured data archive, BELSHAKE serves multiple scientific and engineering purposes. It provides a solid empirical basis for evaluating and developing regional ground-motion models (GMMs) through improved local constraints. It also contributes to the calibration of local magnitude scales and offers processed waveforms and derived parameters suitable for site-response studies and other seismological applications

A critical component of the database construction is the visual inspection and quality-control phase applied to all imported waveforms. Each record was examined in detail, allowing for the identification and correction of issues such as timing errors, spikes, clipping, waveform distortions, and low signal-to-noise ratios where possible. Based on this systematic inspection, all records were classified into three quality categories: good, intermediate, and bad. As a result, 94% of the total records were classified as reliable (good and intermediate) and retained for subsequent processing and analysis. Although the exclusion of bad-quality records slightly reduced data coverage at the highest magnitudes, this step was essential to ensure that only well-characterized and reliable waveforms were used in the subsequent stages. This limitation was partly counteracted by incorporating additional records for higher-magnitude events from stations in neighboring countries.

Together, the database design, waveform quality-control procedures, comprehensive documentation and integration of both local and neighboring network data, BELSHAKE complements existing European databases and strengthens the observational foundation for future seismic hazard and earthquake-engineering research in Belgium and north-western Europe.

3 Windowing

The preliminary step for many analysis procedures in engineering seismology is seismic signal windowing. The traces need to be windowed to isolate noise, P, S, and coda portions of the signal for diverse applications. Most importantly, for the data quality control and to determine the valid frequency range, signal to noise ratio (SNR) needs to be computed from the ratio between the Fourier amplitude spectrum (FAS) of the signal (P-window + S-window) and FAS of the noise window.

In this chapter, two main windowing algorithms have been investigated; Goulet et al., (2014) and Perron et al., (2018) which were applied in the NGA-East and KiK-net datasets respectively.

3.1 Goulet & Cramer method

Following the Goulet et al., (2014) procedure, six distinct time windows can be determined for each of the waveforms (Figure 2):

- pre-event noise (magenta box);
- P-wave window (yellow box);
- S+Lg-waves window (green box);
- coda wave window (gray box);
- combination of P- and S+SLg-waves window (orange box);
- the entire record (blue box).

The start and end times of the different windows are computed based on earthquake origin time, P-wave arrival time, S-wave arrival time, and hypocentral distance. The sub-sections below present the method for definition of the different windows.

3.1.1 Noise-wave time window

The noise window contains pre-event ground motion recorded before the P-wave arrival and is used to characterize background noise levels and assess signal-to-noise ratios. The start of the noise-window is selected based on the arrival of the P-wave and the duration of the SLg window. It is preferred to have pre-event noise window length equal to the duration of SLg-wave time window (T_{d-SLg}). If not enough pre-event noise window is recorded, then it can be shorter than SLg-wave time window.

$$t_{Noise-start} = t_{Noise-end} - T_{d-SLg}$$

In this formula and other formulas below, t denotes absolute times, and *T* denotes time-window durations. The end time of the pre-event noise window is selected based on arrival time of the P-wave. $t_{P-arrival}$ is the P-wave arrival time, and is usually determined on the Z component because the P-wave is more prominent in the vertical direction. To ensure that emergent P-wave arrivals, these are arrivals that are not sharp, but gradual, and hence more difficult to pick, are contained in the P-wave window; a buffer of 2.0 sec is considered.

$$t_{Noise-end} = t_{P-arrival} - 2.0$$

3.1.2 P-wave time window

The P-wave window captures the initial compressional wave arrival, typically characterized by relatively low amplitudes and higher frequencies. The P-wave window starts at the end of the pre-event noise window. Therefore, the $t_{P\text{-}start}$ is equal to $t_{noise\text{-}end}$.

$$t_{P-start} = t_{Noise-end}$$

The end of the P-wave time window corresponds to the S-wave arrival time ($t_{s-arrival}$) minus 0.5 seconds. This is necessary to accommodate a taper at the start of the *SLg*-wave time window. If $t_{s-arrival}$ is not in the database, it is calculated based on the Belgian velocity model and interactively adjusted if necessary.

$$t_{P-end} = t_{S-arrival} - 0.5$$

3.1.3 SLg-wave time window

The S-wave window includes the direct shear-wave arrival, which usually carries the largest amplitudes and contributes most strongly to engineering-relevant ground motion. The Lg-wave window contains crustally guided shear waves that propagate efficiently in continental regions and often dominate ground motion at regional distances. The SLg-wave time window starts at the end of the P-wave window. The end of it can be calculated based on the following equation:

$$t_{SLg-start} = t_{P-end}$$

$$t_{SLg-end} = t_{Lg-arrival} + t_{d-Lg} + T_{d-source}$$

$$T_{Lg-arrival} = t_0 + {}^{R_h}/_{3.6}$$

t_0 is the origin time, R_h is the hypocentral distance in km, and 3.6 is the assumed crustal shear wave velocity in km/sec (Camelbeeck, 1993).

T_{d-Lg} is the Lg-wave duration.

$$T_{d-Lg} = 8.71 + .026R_h$$

or more conservatively:

$$T_{d-Lg}\text{=}17.4 + .052R_h$$

This conservative approach (used in NGA-East project) provides a duration which is twice as long and may result in the capturing of a portion of the coda-waves in the SLg window. However, it ensures that the late arriving Lg waves are analyzed within the same time window.
$T_{d-source}$ is the source duration (in seconds) and is estimated as the inverse of the corner frequency of the event, which can be modeled (Brune, 1970) as:

$$T_{d-source} = {}^{1}/_{f_c}$$

$$f_c = 4.9.10^6 b \left(\frac{Ds}{M_0}\right)^{\frac{1}{3}}$$

$$M_0 = 10^{1.5M+16.05}$$

M is the earthquake magnitude and seismic moment (M_0) is a measure of the size of an earthquake. the Parameter b is the shear wave velocity at the source, and parameter Ds is the stress drop of the earthquake.

3.1.4 Coda-wave time window

The coda window captures the later, scattered wavefield following the direct phases, representing energy trapped. The coda time window starts at the end of the SLg-wave time window. Whenever possible, it is preferred to set coda-wave duration to twice the SLg-window duration.

$$t_{Coda-start} = t_{SLg-end}$$

$$t_{Coda-end} = t_{Slg-end} + 2.T_{d-SLg}$$

3.1.5 Entire recording time window

The time window for the entire recording includes the pre-event noise window, P-wave window, S+Lg wave window, coda window, and the remaining parts of the recorded waveform.
Figure 12 shows the application of the Goulet windowing method to a record in the BELSHAKE database. This waveform is recorded by the BE.MEMH station for the M_L = 3.7 earthquake near Ochtendung (DE) on 03/08/2007.

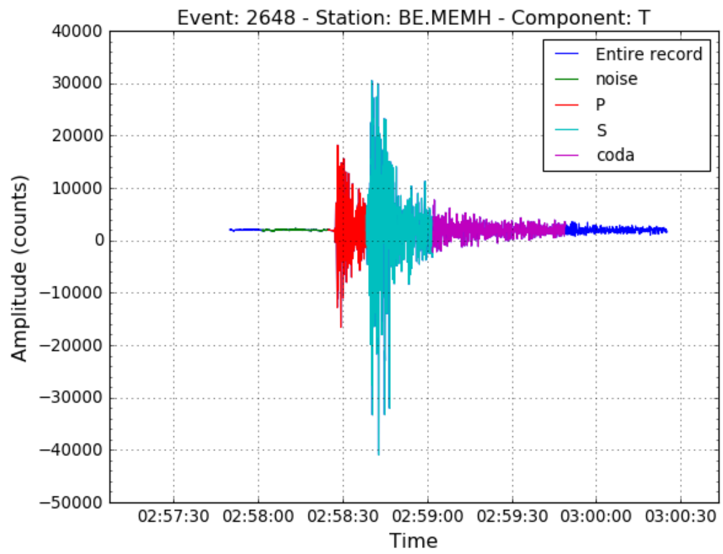

Figure 12. Application of Goulet method for a record in the BELSHAKE database

3.2 Perron method

The Perron et al., (2018) procedure defines four windows for each waveform (Figure 3) :

- pre-event or post-event noise window;
- P-wave window;
- S-wave window
- coda wave window.

The arrival times of P and S waves have also been used here to compute the start and end times of each window, except for the end time of the full signal (T_{end}), which is estimated from a spectrogram, and can thus not be calculated before actually reading the waveforms. Because of this, we used t_{coda_end} from Goulet method as T_{end}. Another parameter that is used to calculate the window lengths is the tapering rate (t_x); this ensures that the windows are long enough to taper the window edges, which is necessary to satisfy the infinite signal assumption for application of the Fourier transform later on in the processing flow. The following subsections describe the definitions for the different windows.

3.2.1 P-wave time window

The P-window starts slightly before $t_{P\_arrival}$ and ends at $t_{S-arrival}$. The duration of the P-window can be written as:

$$D_p = \frac{t_{S-arrival} - t_{P-arrival}}{1 - t_x}$$

The start and end of the P-wave window can be written as:

$$t_{P-start} = t_{P-arrival} - D_p{'}\, t_x$$

$$t_{P-end} = t_{S-arrival}$$

The P-wave window thus includes some noise before the P-wave onset to allow one-sided (left) tapering.

3.2.2 S-wave time window

The S-wave window duration (D_S) is calculated based on source duration and the difference between P-wave and S-wave arrival times, extended at both edges to allow tapering.

$$D_S = max\left\{ \begin{matrix} D_{Smin} \\ \frac{1}{f_c} + (t_{S-arrival} - t_{P-arrival}) \end{matrix} \right\} \Big/ (1 - 2t_x)$$

D_{Smin} is defined as a function of the spectral resolution at low frequency.

The start and end times of the S-wave can be written as:

$$t_{S-start} = t_{S-arrival} - D_S . t_x$$

$$t_{S-end} = \min\left\{ \begin{matrix} t_{S-arrival} + D_S(1 - t_x) \\ T_{end} \end{matrix} \right\}$$

3.2.3 Coda-wave time window

The formulation proposed here is similar to Aki (1969), but only based on T_P and T_S parameters:

$$t_{Coda-start} = 3.3t_{S-start} - 2.3t_{P-start}$$

$$t_{Coda-end} = T_{end}$$

3.2.4 Noise-wave time window

In most of the datasets, the pre-event noise window can be variable and short. A more complex algorithm for selection of the noise window has therefore been developed by Perron et al., (2018). The idea here is to select a noise window with sufficient duration, and also with a representative level of energy (without strong seismic signal included).

3.2.4.1 First parameter in noise window selection: duration

The Perron method considers two duration thresholds for the noise window selection: the target duration (D_t), which is the ideal length equal to the longest seismic signal requested (in general the S-window duration is considered), and the minimum duration to satisfy the f_{min} criterion (D_{min}).

To ensure a good spectral resolution of FAS, a certain window duration (D), and a certain number of wavelengths (N) are required. The longer the selected time window, the higher the number of wavelengths available for the FAS for each frequency. The minimal reliable frequency for the FAS is:

$$f_{min} = N/D_{min}$$

In practice, D_{min} is considered as 10 s, and N is considered as 3, which corresponds to f_{min}=0.3.

The pre-event noise window which can satisfy D_t is not always available. To have a window with sufficient duration, one pre-event noise window ($N1$) and two post-event noise windows, a short and a long one ($N2$ and $N3$), are evaluated. The duration of $N2$ is at least D_{min}; $N3$ is longer than $N2$ only when D_t is greater than D_{min} and the duration of $N1$. Their definitions are as follows:

$$N1 = \left[max\left\{\begin{matrix}(T_p - 0.1) - max\left\{\begin{matrix}D_{min}\\ D_t\end{matrix}\right\}\\ T_i\end{matrix}\right\};\ T_p - 0.1\right];$$

$$N2 = \left[max\left\{\begin{matrix}T_f - max\left\{\begin{matrix}D_{min}\\ D_{N1}\end{matrix}\right\}\\ T_s + D_s\end{matrix}\right\};\ T_f\right];$$

$$N3 = \left[max\left\{\begin{matrix}T_f - max\left\{\begin{matrix}D_{min}\\ D_{N1}\\ D_t\end{matrix}\right\}\\ T_s + D_s\end{matrix}\right\};T_f\right].$$

The preferred noise window is $N1$, but if $N1$ is too short or if there is a foreshock inside it then we have to choose one of the post-event noise windows. The post-event noise window can contain coda waves, but it cannot contain S-waves.

For the waveform in Figure 13, $N3$ is preferable to the two other noise windows because it is the only one that has the same duration as the targeted S-wave window.

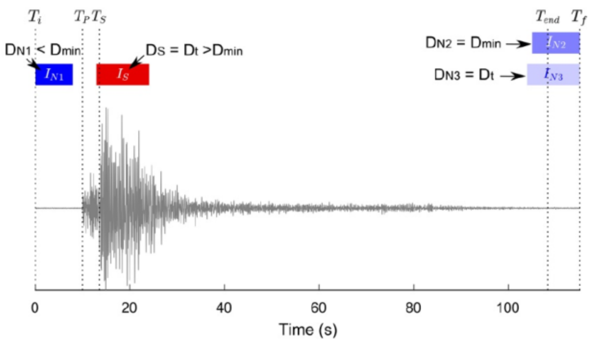

Figure 13. Example of noise window selection in perron method (Perron et al., 2018)

3.2.4.2 Second parameter in noise window selection: energy

The mean energy for the three noise windows is estimated based on the following equation:

$$E = \frac{\sum_{i=N_{min}}^{N_f} FAS_{EW}(f_i)^2 + FAS_{NS}(f_i)^2 + FAS_Z(f_i)^2}{3 \times (N_f - N_{min} + 1)}$$

FAS_X are the Fourier amplitude spectra computed for the three components (EW, NS and Z), N_{min} is the N corresponding to the minimum frequency ($f_{min} = N/D_{min}$) and N_f the number of frequency samples. A minimum pre-event noise duration of $1s$ is mandatory for these comparisons.

3.2.4.3 Noise window selection algorithm based on duration and energy

A scheme that takes into account the length of each window as well as their mean energy is shown below in Figure 14. The energy for the three noise window comparisons is weighed by some factors; $F1$, $F2$, $F3$ and $F4$ to allow $N1$, $N2$ or $N3$ to be favored and to minimize the number of rejected records due to lack of noise for SNR evaluation. The algorithm returns a flag that indicates which noise window has been selected and how. For the BELSHAKE database, we have selected the same values for these parameters as those applied by Perron et al., (2018) to the KiK-net dataset: D_{min}=10s, $F1$=5, $F2$=3, $F3$=2, $F4$=0.67.

However, for application in BELSHAKE, we modified the Perron procedure in order to minimize the number of rejected records and to favor $N1$. These modifications are indicated by the red boxes in Figure 14 and involved the addition of three additional flags:

- Noise flag 0b: pre-event noise window N1 is shorter than the minimum duration ($1s$) required to compute the FAS. As a result, it is not possible to compare its energy with the post-event noise windows $N2$ and $N3$, so that these cannot be selected either. However, because these may still be acceptable and could be selected based on visual inspection, we defined this separate category, keeping 0 only for those cases where the post-event noise windows are also too short (< D_{min});
- If $N1$ has the required target length (D_t) and its energy is lower than or comparable to that of N3 ($E_{N1} < F5.E_{N3}$, with $F5$=1.25), then always select it and in this case the noise flag is 1;

- Noise flag 1b: $N1$ is selected, even though it is shorter than D_t (but still longer than D_{min}); this occurs when $N2$ and/or $N3$ do not have the required duration, or if their energy is too high compared to $N1$;
- In order to further reduce the number of records with noise flag 0 or 0b, we defined an additional duration threshold (D_{noise_min}), which is the absolute minimum noise-window duration allowed ($2s$). This only applies to $N1$, when $N2$ and $N3$ cannot be selected, and the duration of $N1$ is shorter than D_{min}. These cases are indicated with noise flag -1b. For these records, it is not possible to compute the signal-to-noise ratio over the entire frequency range that is required, but they may still be useful for computing ground-motion values.

Table 2 lists the ten noise flags and their definitions.

Noise flag	Description
0	no noise window selected
0b	no noise window selected, but no possibility to judge post-event noise windows
1	pre-event noise window selected
1b	pre-event noise window selected, but shorter than D_t
-1	pre-event noise window selected without possibility to take post-event window
-1b	pre-event noise window selected, but shorter than D_{min}
2	short post-event noise window selected
-2	short post-event noise window selected without possibility to take pre-event window
3	long post-event-noise window selected
-3	long post-event noise window selected without possibility to take pre-event window

Table 2. Noise flags and their definitions. Red boxes correspond to additional flags defined for BELSHAKE

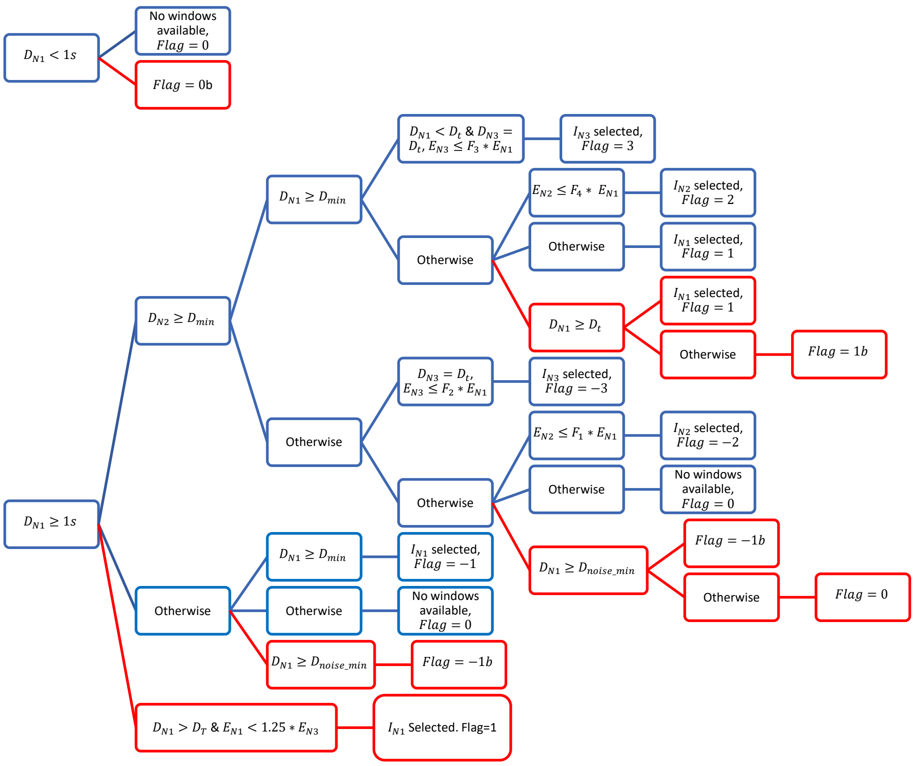

Figure 14. Scheme of the noise window selection algorithm, modified from Perron et al., (2018). Blue boxes correspond to original scheme; red boxes indicate modifications made in the frame of BELSHAKE

3.2.4.4 Implementation of the noise flag selection algorithm to the BELSHAKE database

In this section, we demonstrate an example for each of the ten noise flags in the BELSHAKE database and discuss the reasons for the selection of that particular noise flag by the noise flag selection algorithm. All the waveforms in the BELSHAKE database have been visually checked, and some of the problems have been solved. For instance, disturbed waveforms in noise window or coda window have been trimmed, spikes have been removed, baseline shifts, and time shifts have been adjusted. What is shown in the left figure is the corrected waveform windowed by the Goulet method. The right figure shows the corrected waveform windowed by the Perron method. In both figures, the dark blue color shows the entire window, the green shows the noise window (pre-event and post-event), the red corresponds to P-window, the light blue corresponds to S-window and the magenta shows the coda window.

The problems that the waveforms had before the correction, the status of the waveforms, and the new problems of the waveforms after the correction are written in the tables above them.

3.2.4.4.1 Noise flag = 0

The following figures show the waveforms windowed by Goulet and Perron for event ID = 5650, station code = BE.BLZ of the BELSHAKE database. The figure below shows the waveform problems before correction, the status, and the new problems.

waveform problems	status	new problems
noisy; noise window disturbed; P-window disturbed; S-window curtailed; coda window missing.	noise window disturbed fixed.	noise window missing.

Goulet-windowing

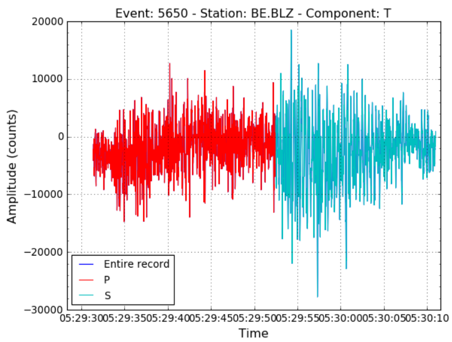

Perron-windowing

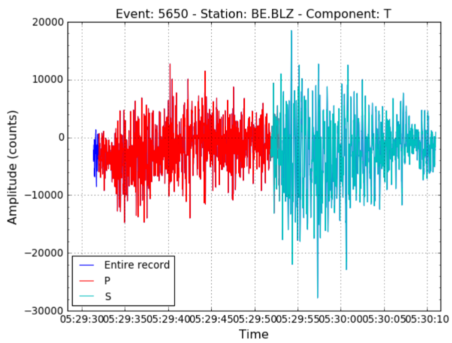

Figure 15. Application of two windowing methods on event ID = 5650, station code = BE.BLZ with noise flag = 0

The waveform was disturbed in the $N1$ noise window, therefore it was removed. With the Perron windowing the remaining $N1$ is very short but larger than 1s ($DN1 \geq 1s$), but it is smaller than the absolute minimum duration ($DN1 \leq D_{noise\_min}$). Therefore, the algorithm has selected noise flag = 0, which means that no noise window has been selected.

3.2.4.4.2 Noise flag = 0b

waveform problems	status	new problems
noisy; noise window disturbed; P-window disturbed; S-window disturbed; coda window disturbed.	noise window disturbed fixed; coda window disturbed fixed.	noise window missing; coda window missing.

Goulet-windowing Perron-windowing

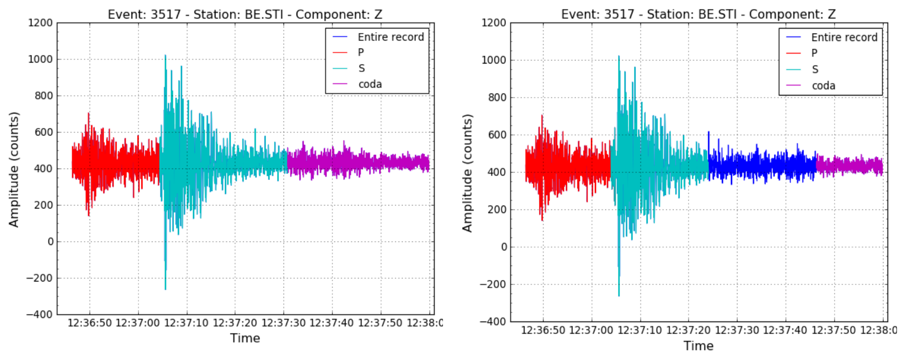

Figure 16. Application of two windowing methods on event ID = 3517, station code = BE.STI with noise flag = 0b

Based on the waveform problems, the $N1$ noise window was disturbed, and it was trimmed. As a result, $N1$ is too short ($DN1$<1s). So, it is not possible to compare its energy with $N2$ or $N3$. Therefore, the algorithm selects noise flag = 0b because it is still possible to perform a visual check to see if $N2$ or $N3$ are acceptable.

3.2.4.4.3 Noise flag = 1

waveform problems	**status**	**new problems**
noisy	-	-

Goulet-windowing | Perron-windowing

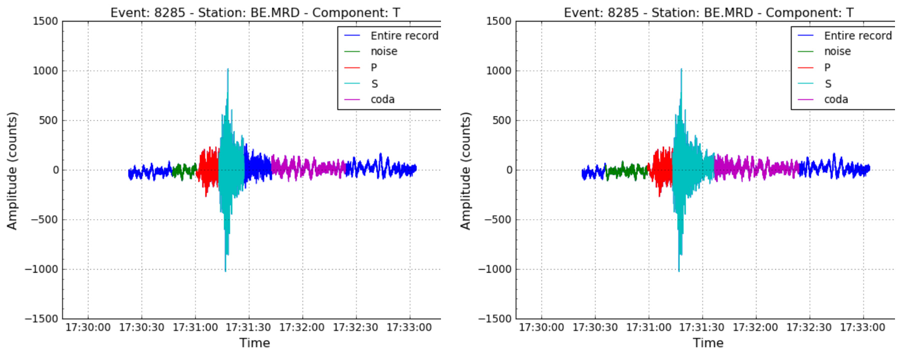

Figure 17. Application of two windowing methods on event ID = 8285, station code = BE.MRD with noise flag = 1

In this waveform the only problem is that the whole waveform is noisy. The pre-event noise window ($N1$) is present, it has the required length (D_t), and its energy is lower than or comparable to that of the post-event noise windows. Therefore, it is selected by the algorithm.

3.2.4.4.4 *Noise flag = 1b*

waveform problems	status	new problems
very noisy; noise window disturbed; coda window disturbed.	noise window disturbed fixed; coda window disturbed fixed.	noise window incomplete; coda window incomplete.

Goulet-windowing Perron-windowing

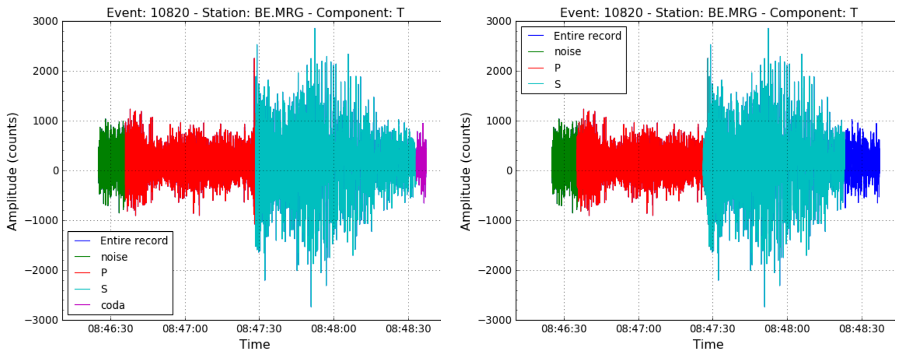

Figure 18. Application of two windowing methods on event ID = 10820, station code = BE.MRG with noise flag = 1b

In this example, $N1$ was partially disturbed and therefore it is partially trimmed. The remaining N1 window has a length bigger than D_{min} but shorter than target length (D_t). On the other hand, the coda window was disturbed, and it was almost completely trimmed. So, there is no chance to select $N2$ or $N3$. Therefore, the algorithm goes back to the pre-event noise window and selects 1b.

3.2.4.4.5 Noise flag = -1

waveform problems	status	new problems
noisy; Coda window disturbed.	coda window disturbed fixed	coda window missing

Goulet-windowing Perron-windowing

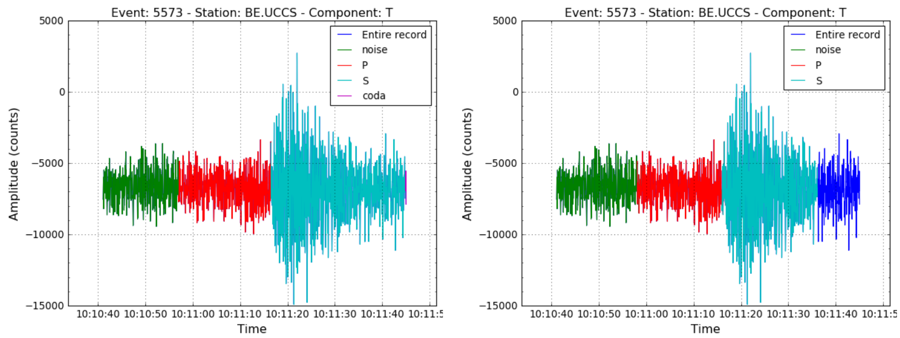

Figure 19. Application of two windowing methods on event ID = 5573, station code = BE.UCCS with noise flag = -1

In this example, the coda window was disturbed, and it was completely removed from the waveform. noise flag -1 is selected, meaning that the pre-event noise window $N1$ is selected, but it is not possible to take post-event noise windowselect $N2$ or $N3$ because they do not have the minimum required length ($DN2$ < Dmin).

3.2.4.4.6 *Noise flag = -1b*

waveform problems	status	new problems
noisy; noise window disturbed; coda window disturbed.	noise window disturbed fixed; coda window disturbed fixed.	noise window incomplete; coda window missing.

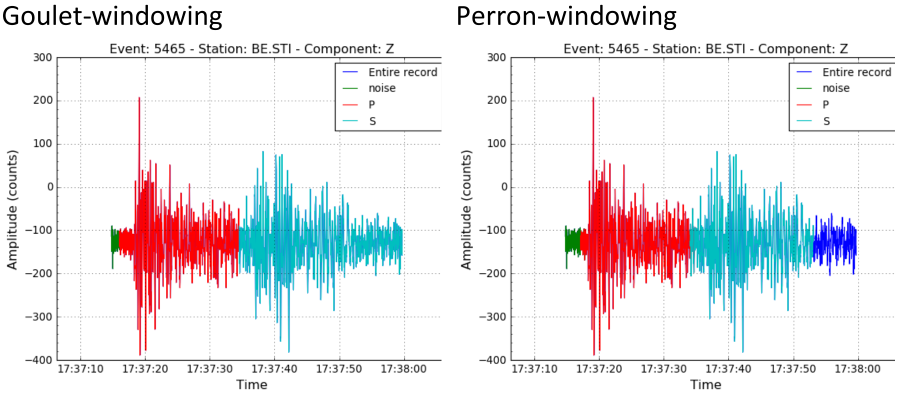

Figure 20. Application of two windowing methods on event ID = 5465, station code = BE.STI with noise flag = -1b

In this example, the coda window was removed again completely due to disturbance. Therefore, it is not possible to select $N2$ or $N3$. On the other hand, the pre-event noise window was partially trimmed due to disturbance, and it is incomplete ($DN1 < D_{min}$), but it is still longer than the absolute minimum duration ($DN1 \geq D_{noise\_min}$). Therefore, the algorithm selects the pre-event noise window although it is shorter than D_{min}.

3.2.4.4.7 Noise flag = 2

waveform problems	status	new problems
very noisy; coda window interrupted.	coda window interrupted fixed	coda window incomplete

Goulet-windowing Perron-windowing

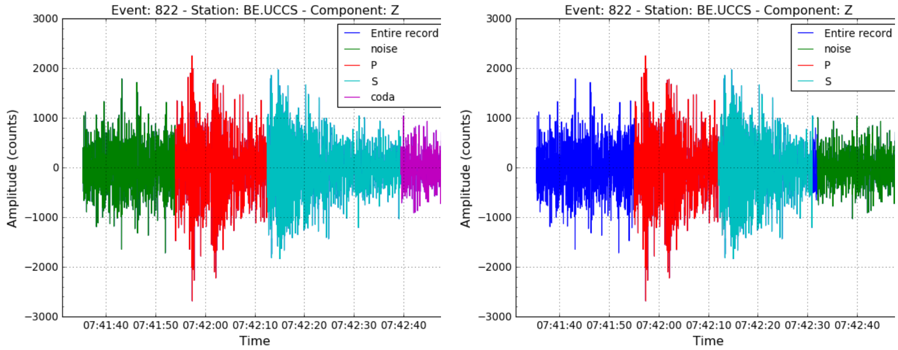

Figure 21. Application of two windowing methods on event ID = 822, station code = BE.UCCS with noise flag = 2

In this example, the waveform is very noisy, and the energy of $N1$ is too large compared to that of $N2$, and the post-event noise window has the minimum required length ($DN2 \geq D_{min}$) for $N2$, but is shorter than D_t, the length required for $N3$. Therefore, the algorithm selects $N2$.

3.2.4.4.8 Noise flag = -2

waveform problems	status	new problems
noisy; noise window disturbed; coda window disturbed.	noise window disturbed fixed; coda window disturbed fixed.	noise window incomplete

Goulet-windowing Perron-windowing

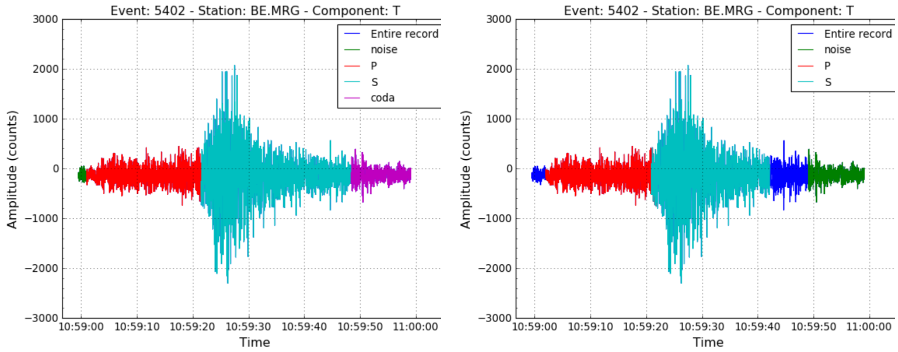

Figure 22. Application of two windowing methods on event ID = 5402, station code = BE.MRG with noise flag = -2

Here, $N1$ was disturbed and is almost removed. The remaining pre-event noise window is very short ($DN1 < D_{min}$), so it is not possible to select $N1$. On the other hand, the post-event noise window has the minimum required length ($DN2 \geq D_{min}$), but it is shorter than D_t, the length required for $N3$, and its energy does not exceed the relative energy level ($EN2 \leq F1 * EN1$). Therefore, the algorithm selects $N2$, without the possibility to select $N1$.

3.2.4.4.9 Noise flag = 3

waveform problems	status	new problems
Noisy	-	-

Goulet-windowing Perron-windowing

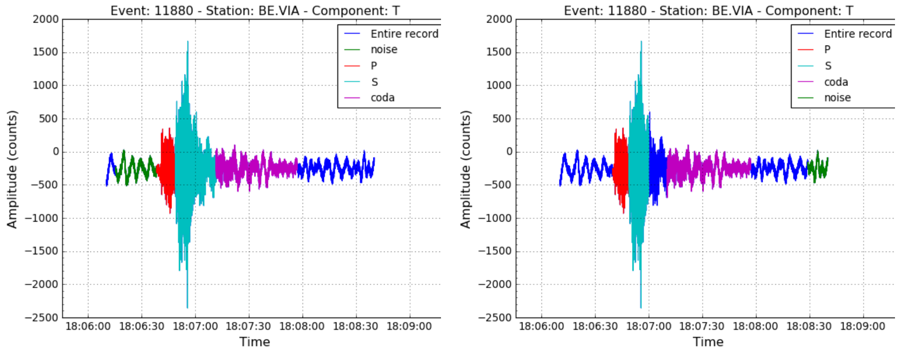

Figure 23. Application of two windowing methods on event ID = 11880, station code = BE.VIA with noise flag = 3

Here the waveform is noisy, $N1$ is not selected due to the relatively high energy. $N3$ is selected because its length satisfies the target length ($DN3 = D_t$) and its energy level is lower than that of $N1$.

3.2.4.4.10 Noise flag = -3

waveform problems	status	new problems
noise window disturbed; coda window disturbed.	noise window disturbed fixed; coda window disturbed fixed.	noise window missing

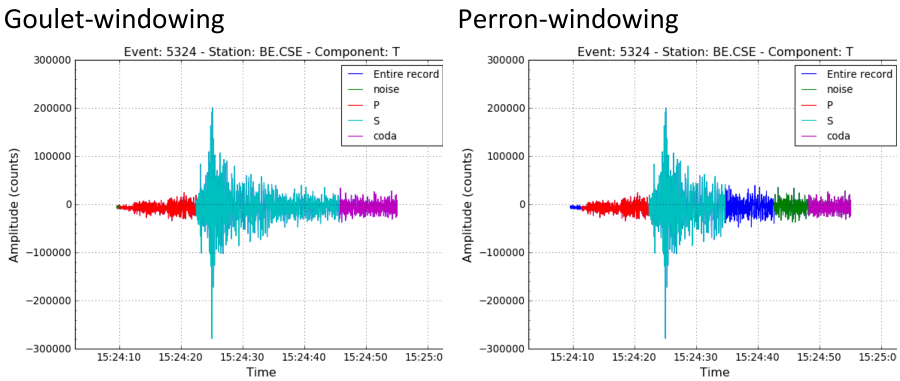

Figure 24. Application of two windowing methods on event ID = 5324, station code = BE.CSE with noise flag = -3

Here, the pre-event noise window was disturbed and is almost completely removed ($DN1<D_{min}$), so $N1$ is too short. $N3$ is selected because its length satisfies the target length ($DN3 = D_t$). Also, its energy does not exceed that of $N1$ ($EN3 \leq F2*EN1$).

3.2.4.5 Noise flag distribution in the BELSHAKE database

Table 3 shows the number of waveforms in the BELSHAKE database corresponding to each of the noise flags. The largest category belongs to the noise flag 3, the long post-event noise-window. Noise flag 1, corresponding to the pre-event noise window, is the second group. There are only few records with noise flag 0, and very few ones with noise flag 2, which is the short post-event noise window.

Noise flag	Number of records
0	42
0b	227
1	1761
1b	1101
-1	493
-1b	436
2	9
-2	106
3	2014
-3	210

Table 3. Distribution of 10 noise flags in the BELSHAKE

3.3 Comparison of Goulet and Perron methods

Figure 25 shows the two windowing methods applied to 4 different records, representing small and large magnitudes, and short and large epicentral distances.

Comparison of the two methods shows that:

- The Goulet method uses fixed tapering margins, whereas in the Perron method the tapering margins are variable because they are defined as a percentage of the window length.
- The P-window is very similar in the two windowing methods.
- The Goulet method provides longer S-windows than the Perron method.
- The Perron method sometimes results in separation between S-window and coda window, while in the Goulet method these windows are always contiguous.

Based on these observations, we prefer the Goulet method for the signal windows. However, the noise-window selection is more sophisticated in the Perron method, and more adapted to records with only short pre-event windows, as is the case in the KiK-net dataset used by Perron et al., (2018). Examination of our records shows that also in the BELSHAKE database many records have incomplete or missing pre-event noise windows, because:

- The noise windows of older records are often short due to trimming of data during archival in order to save disk space;
- Many of the noise windows are disturbed;
- Some records have foreshocks in the noise window.
- Therefore, we decided to combine both methods in BELSHAKE, applying the Goulet method for the signal windows (P, S and coda), and the Perron method for the noise window.

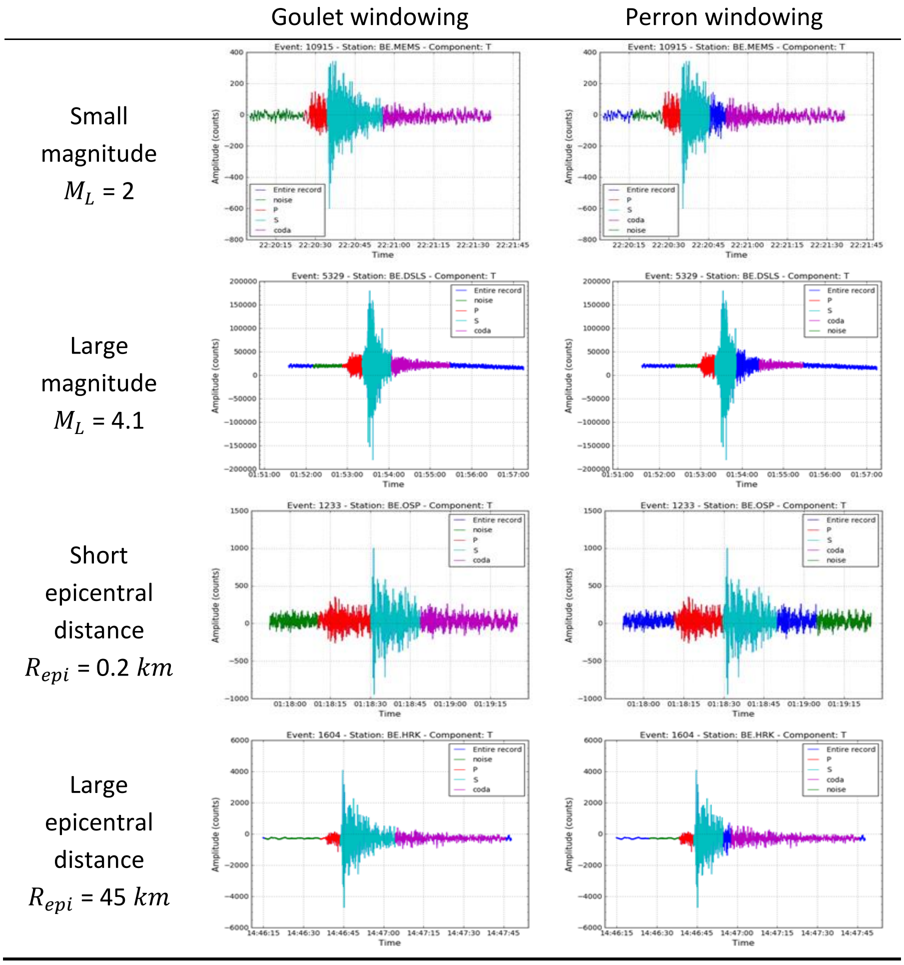

Figure 25. Comparison of Goulet and Perron methods

3.4 Comparison between distribution of noise-window type in BELSHAKE and KiK-net datasets

We also compared the noise flag distribution between the Kik-net dataset used by Perron et al., (2018) and the BELSHAKE database. According to the pie charts in Figure 26, noise-window type 1, which corresponds to pre-event noise window, is selected for most of the events. There are only few events in both of the databases in which the short post-event noise window is selected. The second largest category in both databases is noise-window type 3, which corresponds to long post-event noise window. The percentages are slightly different: compared to the KiK-net dataset, BELSHAKE has less records with noise flags 1 and 2 , and more records with noise flags 0 and 3.

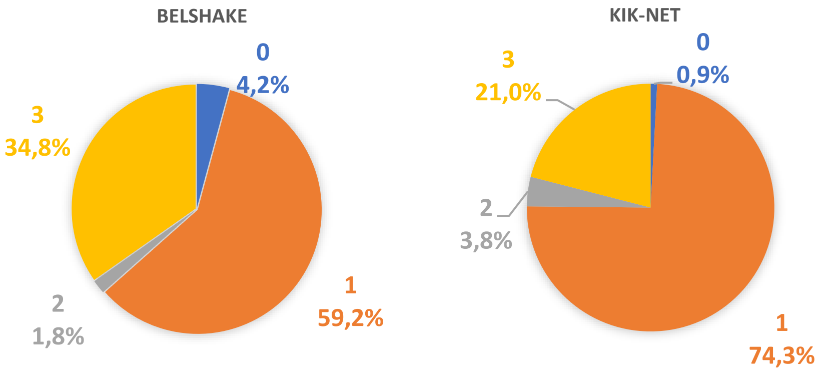

Figure 26. noise flag distribution in BELSHAKE and KiK-net database (Perron et al., 2018)

3.5 Conclusion

Two established approaches Goulet et al., (2014) and Perron et al., (2018) were evaluated for application to the BELSHAKE records. To leverage their respective strengths, a combined method was developed: the Goulet procedure is used to isolate the P-, S-, and coda-wave windows, while the Perron method, refined to minimize record rejection, is applied to the noise window. This hybrid approach ensures consistent, high-quality window definitions that align with practices in other major databases such as NGA-East, RESIF, ITACA, and ESM, forming a robust basis for the subsequent data processing and intensity-measure computations.

4 Validation of the BELSHAKE database

Ground-motion databases play a crucial role in the development of ground-motion prediction equations (GMMs), seismic hazard and risk assessment, and structural design. These databases must meet high standards in processing, quality control, and consistency checking to ensure they contain reliable intensity measures. As outlined in chapter 2, all waveforms underwent a full quality-control step, resulting in three main groups: good, intermediate, and bad quality records. Only the good- and intermediate-quality records were retained for further analysis. For these, intensity measures (IMs) were computed and subsequently subjected to consistency checks, applied in different ways to detect and address any remaining anomalous or inconsistent entries.

Earthquake magnitude alone is often a poor predictor of structural damage, which depends on many factors, including the source (magnitude, stress drop, directivity), path (source-to-site distance, crustal structure) and site (soil properties) parameters, as well as the frequency content of the radiated waves and the natural period of the affected construction. For instance, Baker & Cornell (2006) demonstrated that the spectral shape is a stronger predictor of structural response than magnitude or distance. Similarly, studies analyzing significant ground motion durations have shown how prolonged shaking correlates with an increased collapse risk (Chandramohan et al., 2016). Therefore, the strength of an earthquake is commonly represented by various Intensity Measures (IMs). IMs provide a simplified estimate of the potential damage of an earthquake. Engineers may use IMs to characterize structural response. For that reason, seismic hazard assessments provide results in terms of one or more IMs.

By computing IMs only for good and intermediate-quality records and applying consistency checks thereafter, the resulting dataset ensures both reliability and robustness for subsequent hazard and risk analyses.

4.1 Intensity measures in BELSHAKE

The technical implementation of IM computation in BELSHAKE was primarily carried out within the broader project framework and this chapter of thesis only focuses on the consistency checks applied to the BELSHAKE database using these intensity measures. In BELSHAKE, intensity measures are first systematically computed from the processed reliable waveforms, as listed in Table 4 The most widely used are peak ground motions and response spectra. The other IMs can be categorized as integrals over time series, integrals over part of the response spectrum, averages over part of the response spectrum, and durations.

Furthermore, response spectra and derived IMs (HI, ASI, EPA, EPV and EPD) were not computed for:

- records for which the full instrument correction was not available (only the total sensitivity);
- records which have been manually corrected;
- components/windows with intermediate quality.

Category	Code	Intensity measure	Formula	Unit
Peak ground motion	PGA	Peak Ground Acceleration	$max(\|a(t)\|)$	cm/s^2
	PGV	Peak Ground Velocity	$max(\|v(t)\|)$	cm/s
	PGD	Peak Ground Displacement	$max(\|d(t)\|)$	cm
Response spectra	PSA	Acceleration response spectrum	0.01 – 4 s / 0.25 – 100 Hz, 5% damping	cm/s^2
	PSV	Pseudo-spectral velocity	$PSA * (2\pi f)^{-1}$	cm/s
	SD	Spectral displacement	$PSA * (2\pi f)^{-2}$	cm
Integrals over time series	RMSa	Root-Mean-Square Acceleration	$\sqrt{\frac{1}{T_d}\int a(t)^2\,dt}$	cm/s^2
	AI	Arias Intensity	$(\pi/2g)\int^{T_d} a(t)^2 dt$	m/s
	CAV	Cumulative Absolute Velocity	$\int \|a(t)\| dt$	$g.s$
	sCAV	Standardized CAV	CAV of 1-s windows where PGA ≥ 0.025 g	$g.s$
	bCAV	Bracketed CAV	CAV of portion of $a(t)$ ≥ 0.05 g	$g.s$
Integrals over part of response spectrum	HI	Housner Intensity	$\int_{T=0.1}^{2.5} PSV(T)dT$	cm
	ASI	Acceleration Spectral Intensity	$\int_{T=0.1}^{0.5} PSA(T)dT$	cm/s
Average over part of response spectrum	EPA	Effective Peak Acceleration	$\overline{PSA[0.1 \le T \le 0.5]}/2.5$	cm/s^2
	EPV	Effective Peak Velocity	$\overline{PSV[0.7 \le T \le 2]}/2.5$	cm/s
	EPD	Effective Peak Displacement	$\overline{SD[2.5 \le T \le 4.0]}/2.5$	cm
Duration	D5_75	Significant (Arias) duration	T corresponding to buildup from 5% to 75% of cumulative AI	s
	D5_95	Significant (Arias) duration	T corresponding to buildup from 5% to 95% of cumulative AI	s
	Db5PcG	Bracketed duration	T of portion between first and last occurrence of $a(t)$ ≥ 0.05 g	s

Table 4. Definition of intensity measures used in BELSHAKE

These IMs were calculated following established methods, in particular the frequency-domain approach for response spectra (Jin et al., 2004; Okawa et al., 2007). Computations were validated against independent strong-motion databases (e.g., ESM, RESIF) to ensure consistency with international standards.

Figure 27 presents a representative example: the distribution of PGA values as a function of epicentral distance and magnitude. In a first approximation, these results appear quite consistent and comparable to the RESIF database (Traversa et al., 2020).

PGA - R_{epi}	PGA - M_L

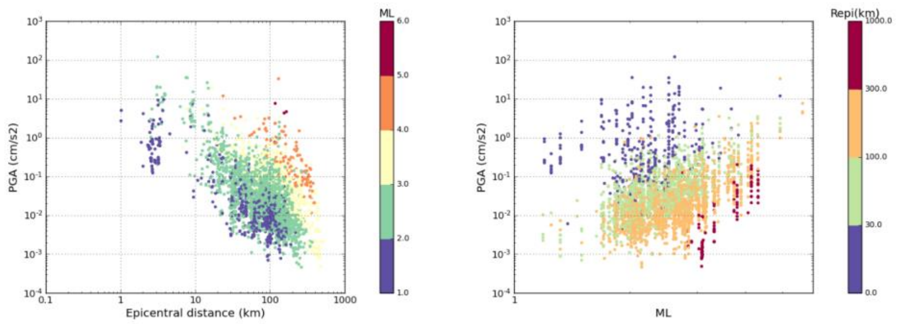

Figure 27. Distribution of PGA values computed for the geometric mean of the horizontal components and for the full window (P+S+coda) as a function of epicentral distance (left), and magnitude M_L (right) in the BELSHAKE database. Left: colors represent the M_L classes ; Right: colors represent the epicentral distance classes

4.2 Consistency checks

After all records were processed and intensity measures were calculated from them, we applied consistency checks using several methods to identify problematic records in our dataset. Outliers were examined, and problematic records were either corrected and reprocessed or removed from the database.

4.2.1 Comparison of different horizontal components

First, we conducted a comparison involving the PGV obtained from the processed records using various horizontal components. We calculated the following ratios: $PGV_{GM}/PGV_{RotD100}$, PGV_{GM}/PGV_{RotD50}, PGV_{GM}/PGV_{SH}, and $PGV_{SH}/PGV_{RotD100}$ across the P, S, signal, and full windows. Figure 28 visually presents the PGV ratios between GM and RotD100 for different windows, encompassing the entire BELSHAKE database.

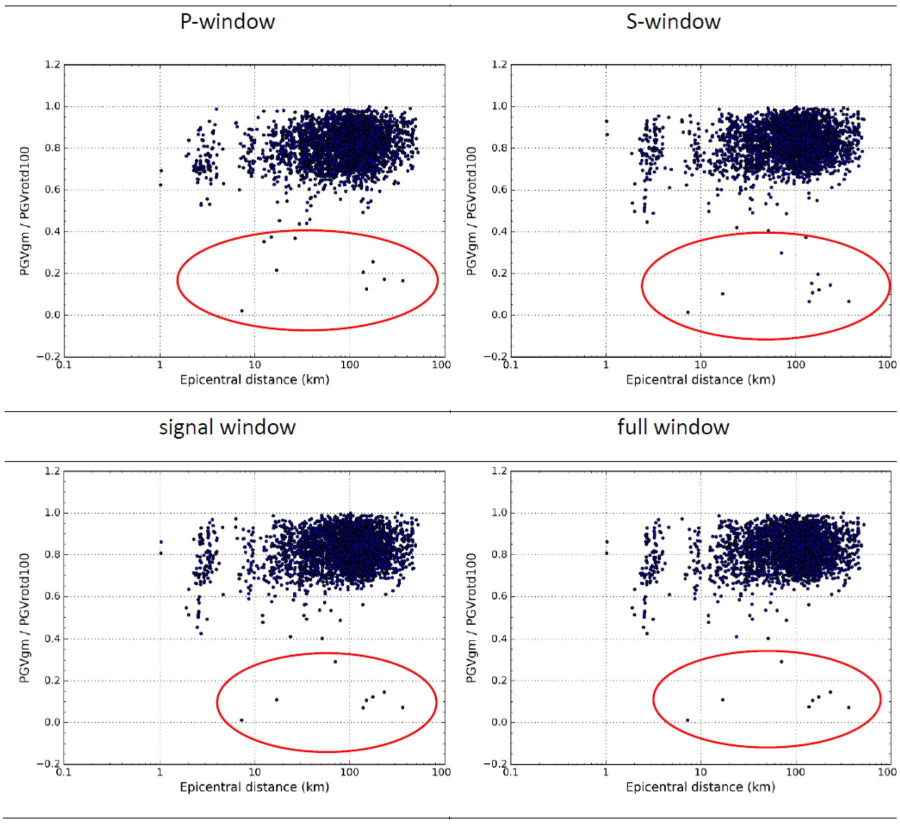

Figure 28. PGVGM/PGVRotD100 for entire BELSHAKE dataset, computed individually for P, S, signal (P+S), and full windows. Outliers are indicated by red ovals.

After reviewing the data within the P, S, signal, and full windows, we identified that the outliers were attributed to a specific problem. When we refer to "outliers" here, we are specifically pointing to the data records where the PGV_{GM} to $PGV_{RotD100}$ ratio falls below 0.4, as these records yield meaningful insights. In certain instances, like the one in Figure 29, one of the horizontal components exhibited significantly lower amplitude compared to the other horizontal component. We had not initially detected this discrepancy during our visual inspection of the waveforms. The derived intensity measures have been removed from the database, and these components with anomalous amplitude have been flagged, so that they will be skipped when intensity measures are recomputed.

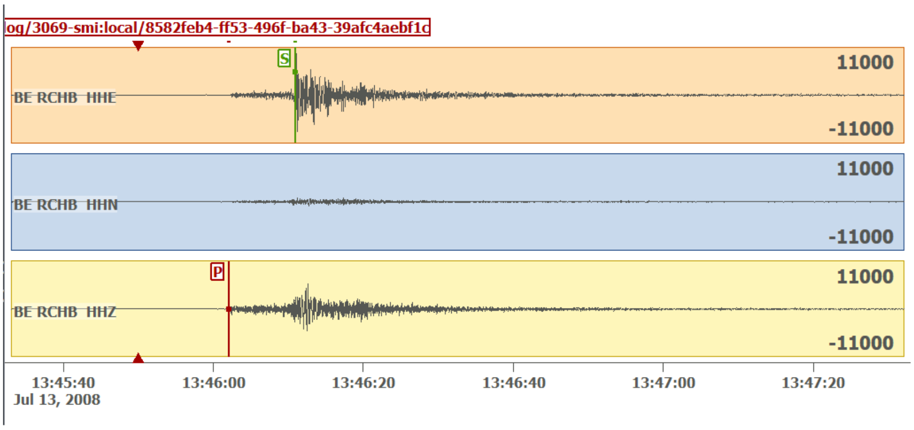

Figure 29 - Event #3069 recorded by station BE.RCHB, the N-component has much lower amplitude than E-component, which leads to very low ratio of PGVGM /PGVRotD100.

Interestingly, we didn't find any problems when looking at the waveforms corresponding to the outliers in the P-window. The amplitude of both horizontal components was quite similar in those cases, so that wasn't the cause. Eventually, we realized that for certain records, the vertical component (Z) had been swapped with one of the horizontal components. Figure 30 shows the three components of a record with this problem. This issue was identified in several events recorded by station BE.HRK. We swapped the vertical and horizontal components for these problematic records and ran the processing again. This allowed us to recalculate the correct intensity measures for these cases.

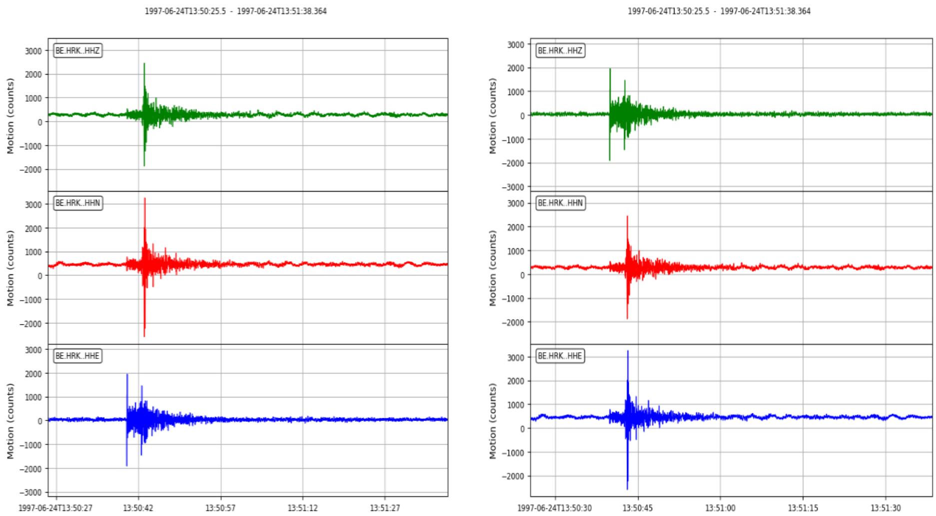

Figure 30. The waveform recorded by station BE.HRK for event #1223 in BELSHAKE which led to $PGV_{GM}/PGV_{RotD100}<0.4$ in P-window. Left: original, uncorrected waveform where the E-component has been mistakenly swapped with the Z-component. Right: corrected waveform

4.2.2 Comparison of vertical and horizontal components

Secondly, we calculated the ratio between the PGV obtained from the processed record using horizontal components and the PGV from the vertical component (Z). This involved evaluating the ratios $PGV_{RotD100}/PGV_Z$, PGV_{RotD50}/PGV_Z, and PGV_{GM}/PGV_Z across the P, S, signal, and full windows. Figure 31 shows the ratio of PGV_{GM}/PGV_Z for different windows and the outliers with high ratio and low ratio in red and blue color, respectively.

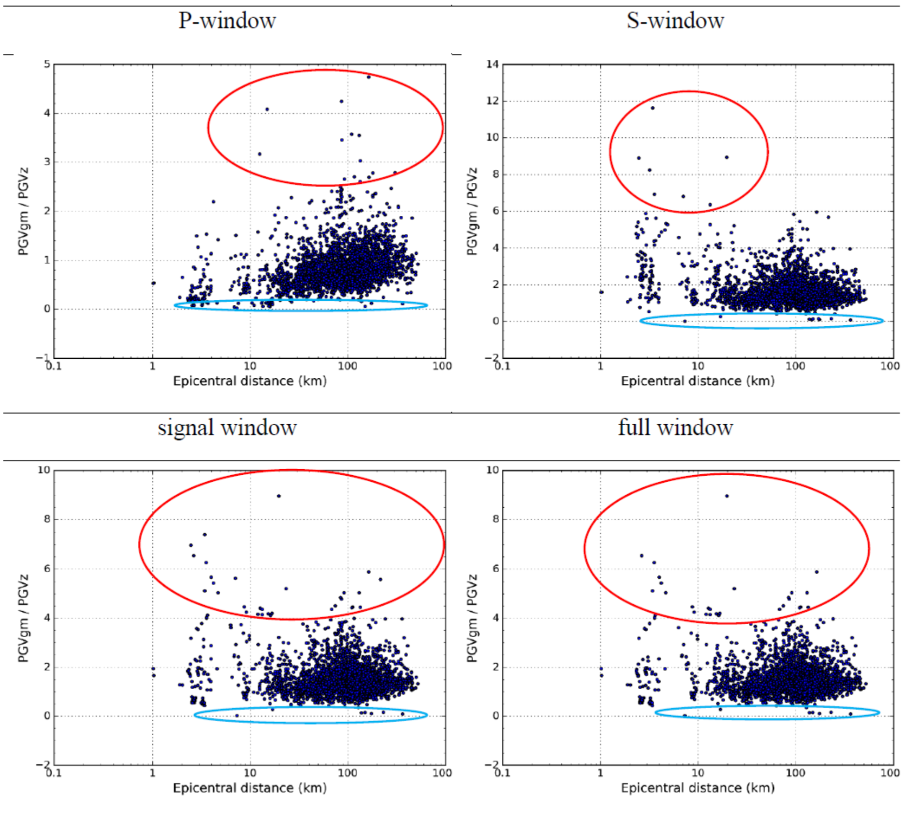

Figure 31 - PGV_{GM}/PGV_Z for entire BELSHAKE database, computed individually for P, S, signal (P+S), and full windows. Outliers with high ratio are indicated by red ovals; the lower threshold of outliers may differ across windows. Outliers with low ratio are indicated by blue ovals; the higher threshold of outliers may differ across windows

Within the majority of the records featuring a large ratio, the underlying issue was that the vertical component (Z) exhibited a lower amplitude compared to the horizontal components. The specific threshold for what constitutes a "large ratio" and leads to relevant findings varies across different windows. For the PGV_{GM}/PGV_Z, in the P-window, we consider a ratio exceeding 2.5 indicative of potentially problematic records, while in the S window, a ratio exceeding 6 is the criterion. In the signal and full windows, a ratio surpassing 4 serves as an indicator. We inspected all potentially anomalous records. The majority of them appear to be short-distance records (R_{epi} < 20 km). As high H/V ratios may be a characteristic feature of short-distance records, we did not remove them. These are exceptional records, but not problematic. Cases where the H/V ratio is high in the S-window, but not in the P-window, are not considered as problematic either. If both the S- and the P-window show high H/V ratios, we check the amplitudes of the noise window. If that is also consistently higher on the horizontal components, the record is suspicious. This appears to be the case for several events recorded by BE.MEU, BE.HOK and BE.CTH and partly BE.UCCS. Figure 32 shows an example recorded by station BE.CTH. At this point, we don't know if the anomalous H/V ratios are due to a site effect or due to a problem with the instrument.

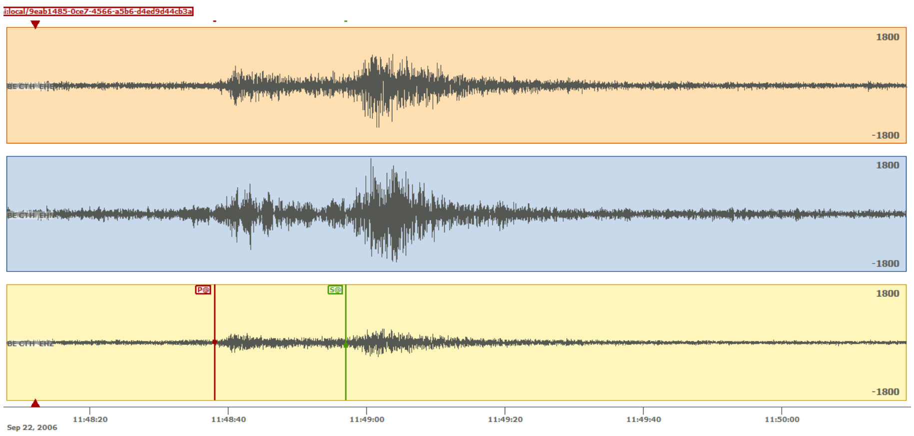

Figure 32 - Waveform of earthquake in PYRMONT (DE) with M_L = 2.5, recorded by station BE.CTH, in which the Z-component (bottom) has lower amplitude than the 2 horizontal components leading to $PGV_{GM}/PGV_Z>6$ in the signal window

On the other hand, when one of the horizontal components exhibited a lower amplitude compared to the other horizontal component, this led to a low ratio. Again, it's important to note that our definition of a "low ratio" varies across different ratios and different windows. For PGV_{GM}/PGV_Z, in the P-window, a ratio of less than 0.1 is indicative of relevant result, while in the S-window, a ratio less than 0.5 and in the signal and full windows, a ratio lower than 0.2 are the criteria for identifying relevant results.

There are fewer records showing anomalously small H/V ratios than anomalously high H/V ratios. Most of them correspond to records where one of the horizontal components has an anomalous amplitude, and these were already identified in the previous step (visual check of waveforms). A suspicious case is station BE.MOLA where a number of records have very small H/V ratios in the P-window. An example is shown in Figure 33. We think that this may be an effect of resonance (probably due to bad emplacement), as suggested by the peak between 20 and 30 Hz in the FAS of the vertical component (Figure 34). This issue will be further investigated by applying bandpass filtering with a lower high-cut frequency to assess whether it resolves the observed anomaly.

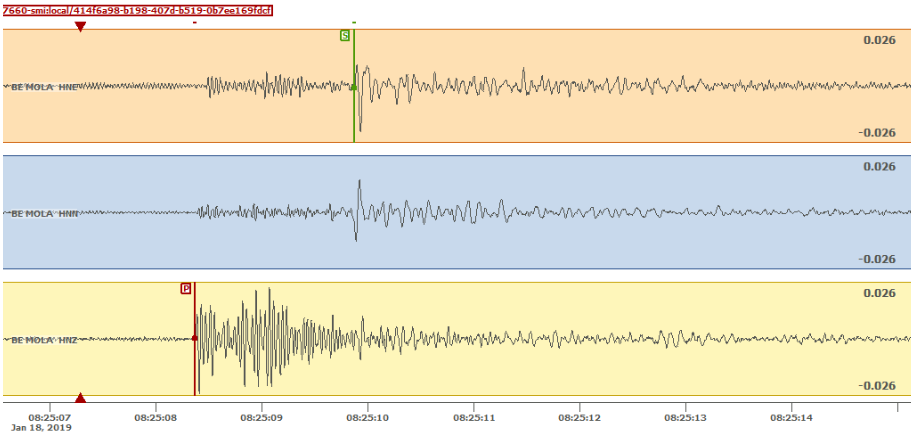

Figure 33 - Example of waveforms recorded by BE.MOLA station during Dessel earthquake in LEBACH (DE) with ML = 1.5

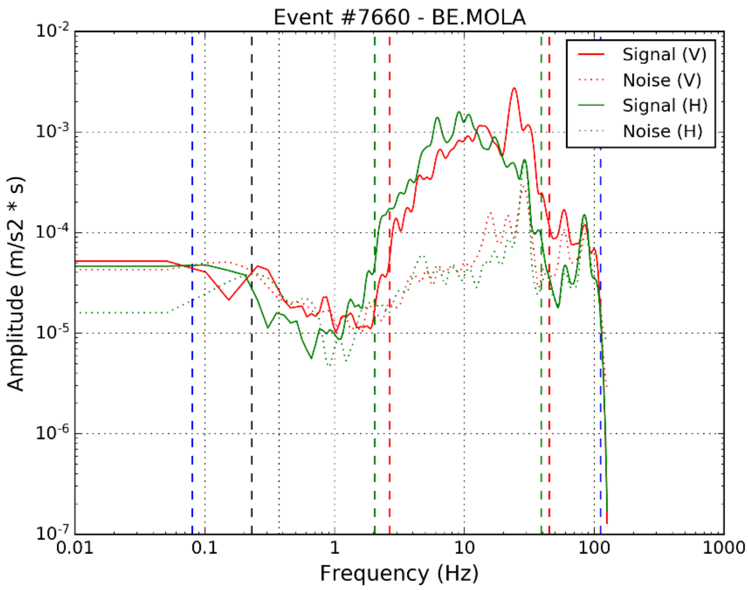

Figure 34 – FAS of Dessel earthquake with ML = 1.5 recorded by BE.MOLA station. An anomalous peak is observed on the vertical component between 20 and 30 Hz.

To address all these except for the waveform recorded by BE.MOLA, we systematically identified and flagged all such records within the database.

4.2.3 Analysis of residuals of ad hoc GMM

The third check involves a comparison between the PGA and PGV obtained from the processed records with the predictions from a generic ground motion prediction equation (GMM) fitted to the observations. The model selected to perform the residual check is the GMM by Traversa et al., (2020).

$$log_{10}Y = F_D(R,M) + F_M(M) + e_1$$

Where:

$$F_D(R,M) = \left(c_1 + c_2\left(M - M_{ref}\right)\right) log_{10}\left(\frac{\sqrt{R^2+h^2}}{R_{ref}}\right) - c_3\left(\sqrt{R^2+h^2} - R_{ref}\right)$$

Is the distance scaling component;

$$F_M(M) = b_1\left(M - M_{ref}\right)$$

is the magnitude scaling component;

And e_1 is the global offset or total residual.

In the regression, the M_L magnitude has been used and the coefficients c_1, c_2, c_3 and b_1 are determined from the regression.

The reference distance and magnitude values are set to R_{ref} = $1km$ and M_{ref} = 3.7, the same values as used by Traversa et al., (2020) for the RESIF dataset.

This serves as a basic check for identifying outliers. Total residuals have been derived for the full window using various components, including GM, RotD100, and RotD50.

Figure 35 shows the standardized residuals (i.e., the residuals divided by the overall standard deviation) as a function of M_L and epicentral distance for both PGA and PGV, utilizing the GM component.

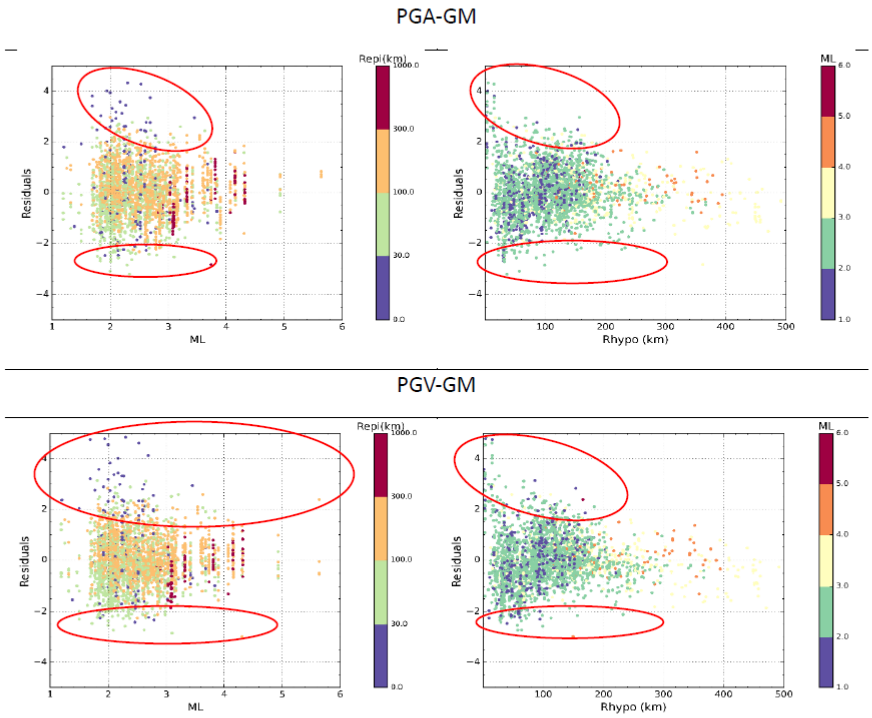

Figure 35 - Standardized residuals as function of M_L (left) and R_{epi} (right). Colors are function of R_{epi} (left) and M_L (right), shown for PGA and PGV using GM component

The majority of standardized residuals fall within the range of ±2 standard deviations, with nearly all of them falling between ±3. The presence of outliers (residuals > 3) is minimal and likely corresponds to the issues we've previously identified.

4.2.3.1 temporal evolution of residuals for each station

Further insight can be gained by analyzing the temporal evolution of residuals for each station individually. This involved computing residuals across various intensity measures and components. During this analysis, we identified anomalies in the residuals for three specific stations, namely BE.UCCS, BE.HRK, and BE.HUM, which exhibited notable shifts within a specific time period. Figure 36, Figure 37, and Figure 38 illustrate the evolution of total residuals for PGA recorded at these stations, where each point represents a single event and the residuals are presented in chronological order.

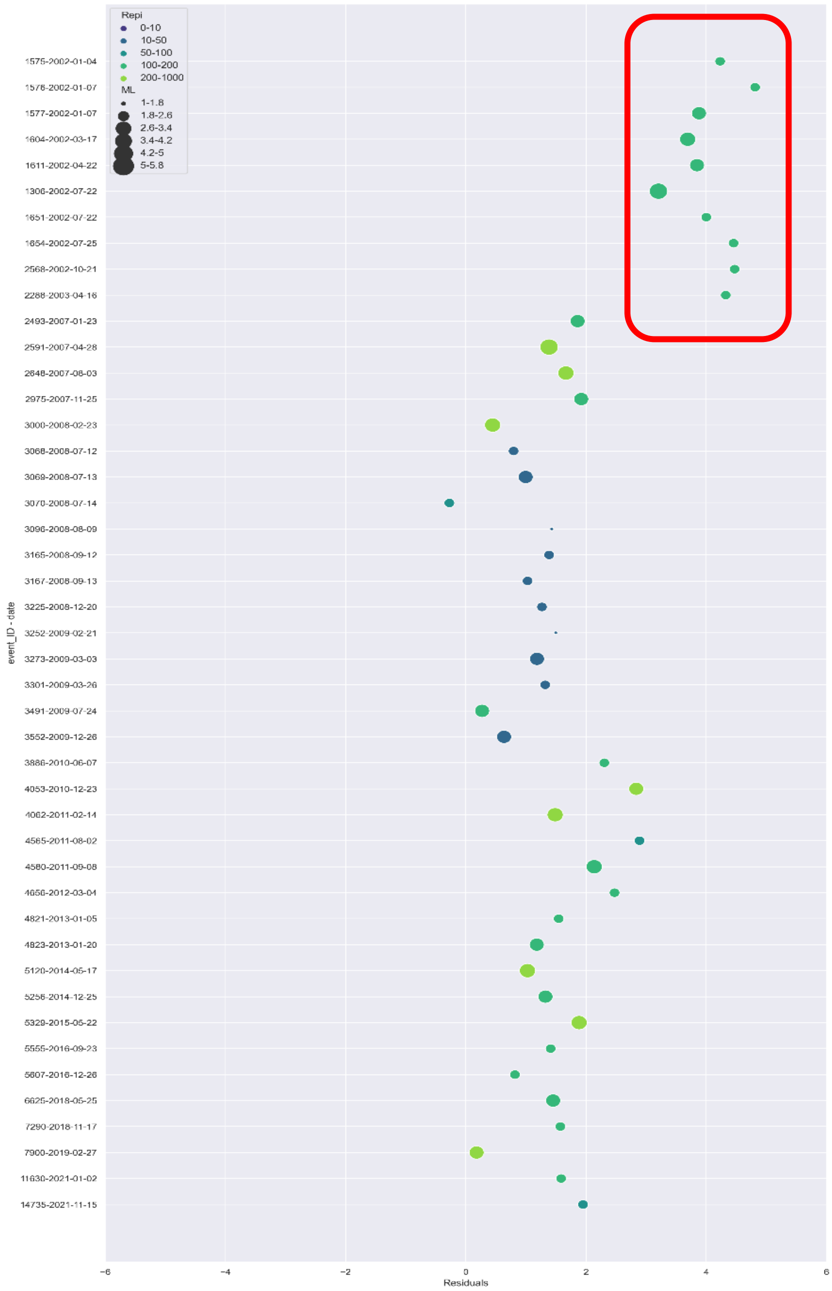

Figure 36 - Evolution of total residual for PGA recorded at BE.UCCS station. Colors are function of the record epicentral distance and circle sizes are function of event M_L magnitude

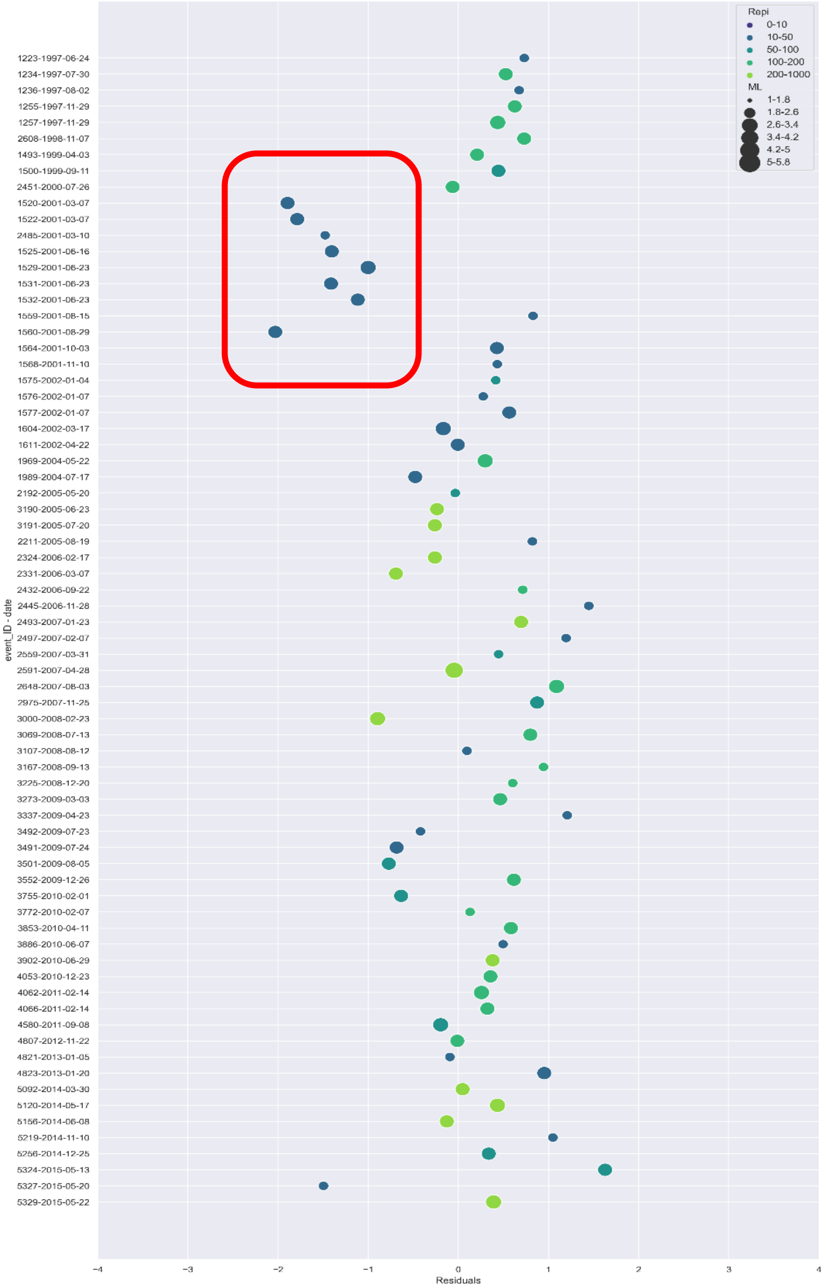

Figure 37 - Evolution of total residual for PGA recorded at BE.HRK station. Colors are function of the record epicentral distance and circle sizes are function of event M_L magnitude

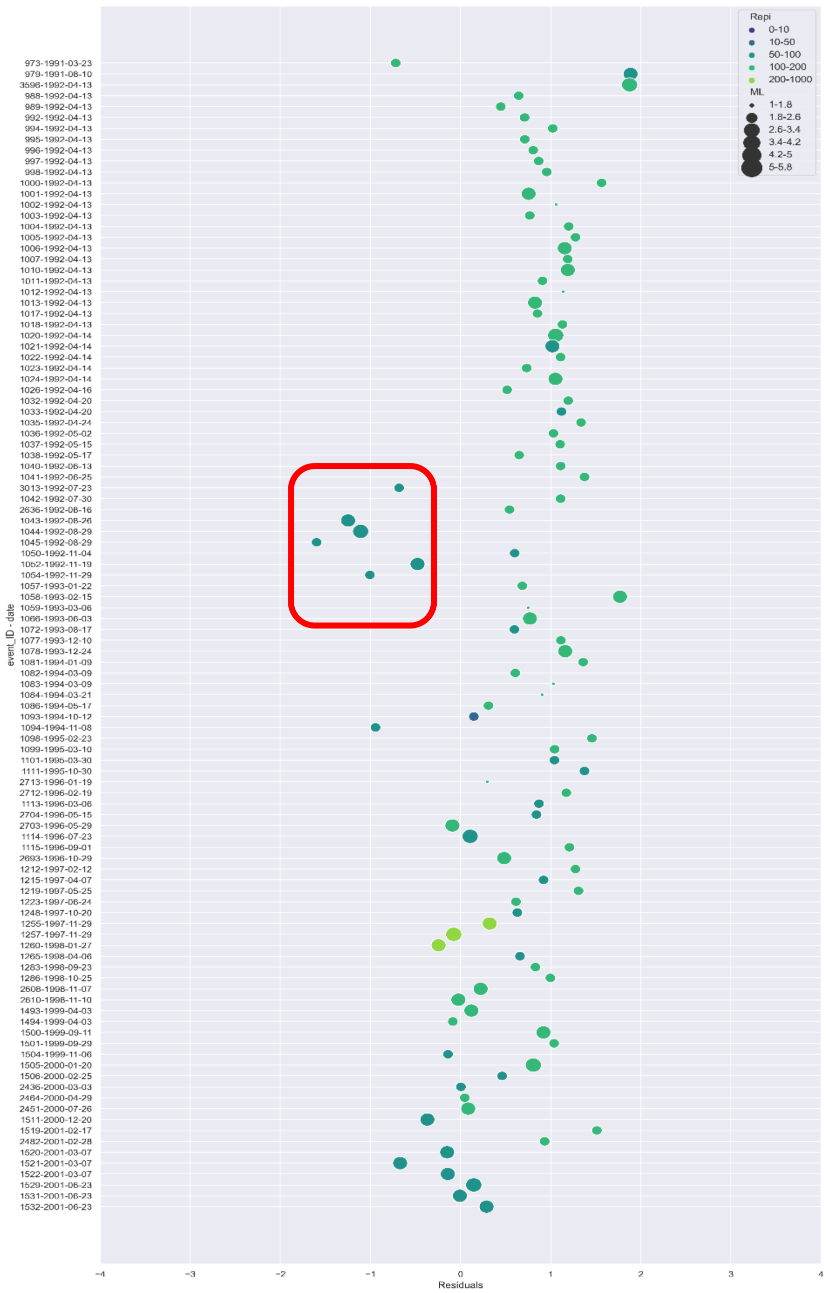

Figure 38 - Evolution of total residual for PGA recorded at BE.HUM station. Colors are function of the record epicentral distance and circle sizes are function of event M_L magnitude

The inquiries conducted to determine the causes of the shifts in residuals for these three stations revealed that:

- BE.UCCS: This issue is a result of instrument response problems, as the affected period corresponds to a particular station deployment. It appears that two instruments were operating simultaneously during part of this period, but we verified that the problems are not the result of inadvertently attaching the response of the wrong instrument.
- BE.HRK: There was no apparent change in the station deployment (and hence the instrument response) during the affected period, and the outliers are not a consequence of swapped vertical and horizontal components (a problem which we detected before for this station)It should also be noted that at least 1 event in this period shows normal residuals, and that there are also some outliers at later times. It is suspected that this group of outliers is associated with a particular earthquake source, as many of them originate from the same area (a seismic swarm in the region of Voerendaal, The Netherlands).
- BE.HUM: Similarly, no conspicuous changes in the instrument response can be seen here. Similar to BE.HRK, there are several events with normal residuals during the same period, as well as 1 outlier at a later time. The cause of these outliers may be similar to that of BE.HRK, as most are related to a small seismic sequence near Barbençon-Beaumont.

The BE.UCCS records have been corrected and reprocessed, but the divergent BE.HRK and BE.HUM records have not been corrected or removed for the time being.

4.2.3.2 Comparison of residuals of collocated sensors

Comparison of collocated sensors is very useful in tracking errors and inconsistencies in the dataset (Traversa et al., 2020). Comparison of the IM values for common events allows checking their relative consistency. In several cases, this concerns a seismometer and an accelerometer (e.g., BE.UCCS/BE.UCCA, BE.MOL5/BE.MOLB, BE.MOLS/BE.MOLA). The agreement between BE.MOLS and BE.MOLA is not good, which is probably because the two instruments are not close enough. For the two other cases, the agreement is quite good for PGV, but not for PGA (Figure 39) Inspection of the waveform data shows that in both cases the records are affected by high-frequency disturbances, probably resonance due to unfavourable emplacement. In both cases, the issue appears to be solved for the most recent recorded events.

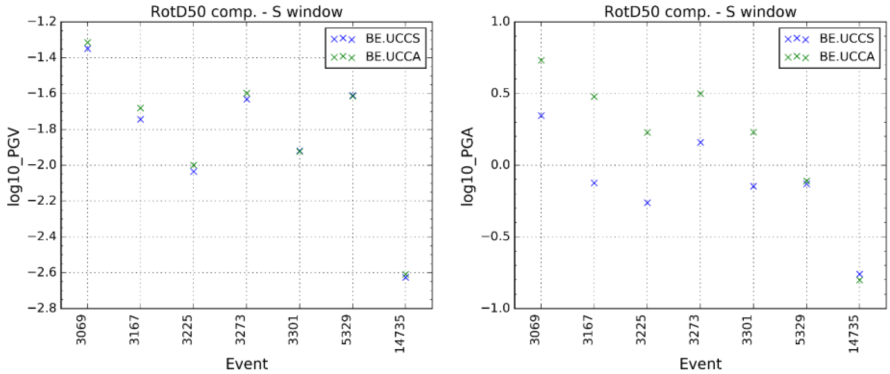

Figure 39. Comparison of IMs (RotD50 component, S window) computed for common events recorded by stations BE.UCCS and BE.UCCA. Left: PGV; Right: PGA

In the Membach underground gallery, a short-period seismometer (BE.MEMS) has been operating next to two broadband seismometers: BE.MEMB (1994-2005) and BE.MEMH (2006-present). The agreement between BE.MEMS and BE.MEMH is quite good (Figure 40). This is an important result, demonstrating that short-period and broadband seismometers provide equivalent results over a relatively broad frequency range. The agreement between BE.MEMS and BE.MEMB is mostly good, except for some events (for all IMs). There is likely a problem with the instrument response of BE.MEMB for these events, so we flagged them as unreliable and removed the corresponding IMs from the database.

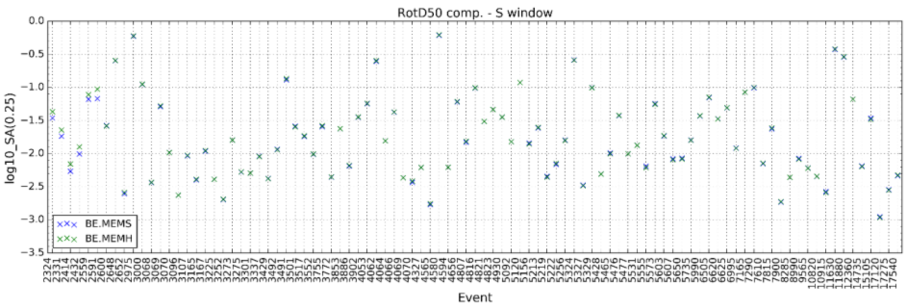

Figure 40. Comparison of 0.25 s spectral acceleration (RotD50 component, S window) computed for common events recorded by stations BE.MEMS and BE.MEMH

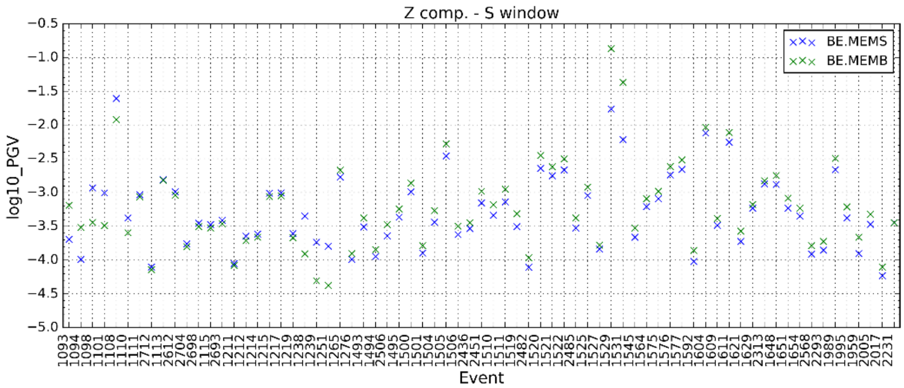

Figure 41.Comparison of PGV (Z component, S window) computed for common events recorded by stations BE.MEMS and BE.MEMB

4.2.3.3 Comparison of residual from the generic GMM model and the station residual from M_L estimation

In the next step for each station, we conducted a comparison between the mean residual from fitting the generic GMM model and the mean station residual from M_L estimation. It is expected that there should be some correlation between both, as positive/negative residuals are indicative of amplitudes that are too high/low in both cases.

To provide an overall perspective, we computed the average of the mean generic GMM residual for the GM component of PGA, PGV and PGD, and compare it with the mean M_L residual for each station. In this comparison, we only include the stations which have recorded a minimum of 10 records. 60 stations have been studied. The result is shown in Figure 42. The X-axis of the plot depicts the network station codes. The left Y-axis represents the standardized residuals for PGA (orange curve), PGV (green curve) and PGD (blue curve), while the right Y-axis corresponds to the mean M_L residuals (black curve), scaled by a factor of four to cover a comparable range in the plot. The plot highlights a clear similarity in the trends between the mean M_L and PGA/PGV residuals across all stations, but only moderate similarity with PGD, although M_L is measured from displacement amplitudes (on the Z-component). Compared to PGD, the M_L residuals consistently exhibit more pronounced changes or higher values within the same trend. Overall, these comparisons suggest a general correlation. The station exhibiting the largest difference for PGD is BE.UCCS, which was previously identified as partly problematic during the comparison of station-specific residuals with the generic GMM. Therefore, the significant difference observed for BE.UCCS could be attributed to the previously identified issue.

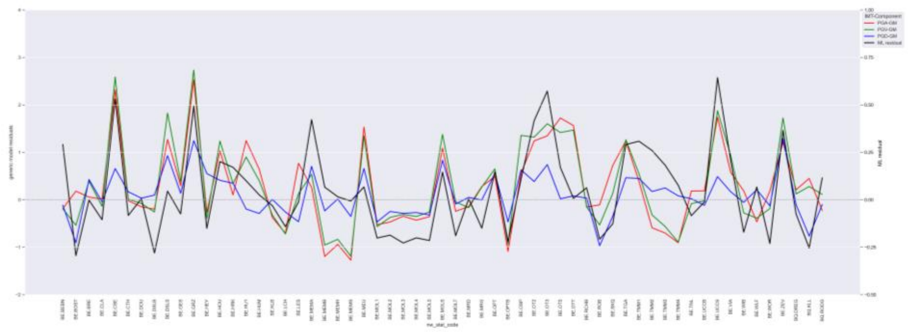

Figure 42. Comparison of M_L residuals (black) and mean standardized generic GMM residuals for PGD (blue), PGV (green) and PGA (orange), for different stations using GM component

4.3 Conclusions

This chapter presented the consistency evaluation of the BELSHAKE database, based on a series of checks applied to the computed intensity measures. These analyses enabled the detection and correction of residual issues that had not been identified in earlier processing stages, and further improved the quality of the database.

During the consistency analysis, several issues within the BELSHAKE database were identified and addressed. Records exhibiting anomalous amplitudes on one component were flagged, and the corresponding derived intensity measures (IMs) were removed, affecting approximately 15 records. At station BE.HRK, where the vertical (Z) component had been mistakenly swapped with a horizontal component, 27 records were corrected, and their IMs were recomputed. Instrument response corrections were also applied for one or more deployments at several stations, including BE.UCCS. Resonance problems were detected on certain accelerometers, and although IMs were recomputed using an adapted frequency range, this adjustment did not completely resolve the issue. Despite the limited number of events recorded by both seismometers and accelerometers, the results indicate that IMs from both sensor types are comparable when the instruments are installed under similar conditions. Comparisons between short-period and broadband seismometers also show good agreement. Several stations exhibited anomalous horizontal-to-vertical (H/V) ratios, which require further investigation.

The systematic flagging and correction of identified anomalies enhance transparency and traceability. The validated dataset now provides a reliable and well-documented foundation for subsequent analyses.

5 Analysis of the anelastic attenuation parameter kappa in Belgium

This chapter presents a comprehensive analysis of the methods and results used to compute anelastic seismic attenuation kappa (κ), with a focus on estimating site kappa (κ_0) and kappa gradient (κ_r) across different sites and crustal domains in Belgium. Kappa is a key parameter describing anelastic high frequency attenuation and plays an important role in ground motion modeling, site specific seismic hazard assessments, and host to target adjustments in ground motion models. The first part of this chapter presents computation and evaluation of kappa of each seismic record in the BELSHAKE database. It details the methodologies used for kappa calculation, data filtering, and the relationship between kappa, distance, and other seismic attenuation parameters such as $t^*$and Q. Emphasis is placed on refining the kappa-distance relationship through a systematic filtering process and examining the resulting κ_0 and goodness of fit of the κ–distance regressions. κ_0 and κ_r are then estimated using three distinct methods: the Free kappa gradient method (FKG), the Joint kappa gradient method (JKG), and the Mixed effects regression (MER). κ_0 and κ_r values are important for understanding respectively the regional and local variability of crustal properties, and accurate estimation of these values is critical for improving seismic models and geophysical interpretations. Each of these approaches is explored in detail, highlighting their advantages and challenges. By integrating these methodologies and results, this chapter aims to provide a clear framework for the robust estimation of kappa and its components, offering insights into its practical applications for seismic hazard analysis and infrastructure resilience.

5.1 Anelastic attenuation

Anelastic attenuation refers to the irreversible loss of seismic wave energy as waves propagate through the Earth due to intrinsic material damping and scattering by crustal heterogeneities. Unlike geometrical spreading, which redistributes energy over a larger area without loss, anelastic attenuation results in a true reduction of seismic energy, particularly affecting the amplitude of seismic waves.

At high frequencies, attenuation effects are commonly parameterized using the kappa (κ) parameter introduced by Anderson and Hough (1984). The κ parameter provides a practical description of the exponential decay of the high-frequency portion of the acceleration Fourier amplitude spectrum and is widely used in engineering seismology.

According to Anderson and Hough (1984) the acceleration Fourier amplitude spectrum of an S wave is characterized by three domains with distinct behaviors:

- Low frequency range, where the spectrum increases with ω^2,
- Mid frequency range, where the spectrum is relatively flat, and
- High frequency range, where the spectrum decays with increasing frequency.

This high frequency decay can be described in the form of the equation:

$$A = A_0 \, e^{-\pi f \kappa}$$

where $A(f)$ is the Fourier amplitude at frequency f, A_0 is a constant, and κ (in seconds) represents the slope of the exponential decay. The κ parameter thus captures the combined effects of near-surface attenuation and propagation path effects, and is often interpreted as a proxy for the frequency-independent component of attenuation.

Despite its widespread use, κ's physical meaning and estimation methods vary significantly, leading to inconsistencies in its application. Accurate estimation of κ is essential in addressing site effects, regional tectonic variability, and near surface geological structures. Several studies emphasize the importance of kappa in refining seismic hazard assessments and improving earthquake ground motion models.

5.1.1 Theory

The simplest description of seismic wave attenuation can be modeled using the oscillation of a mass attached to a spring.

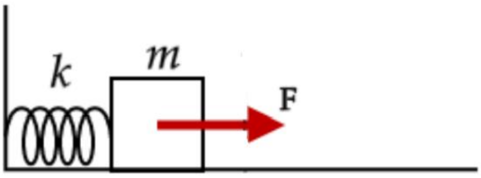

Figure 43. Model used to explain seismic attenuation processes

Consider a mass m attached to a spring with a constant k, sliding on a smooth surface. If no friction is present, the equation of motion for the system is determined by the spring force and the inertial force acting on the moving mass:

$$m\ddot{x} + kx = 0$$

This equation can be rewritten as:

$$\ddot{x} + {}^{k}/_{m}\, x = 0$$

the angular frequency of oscillation ω can be written as:

$$\omega^2 = {}^{k}/_{m}$$

We obtain:

$$\ddot{x} + \omega^2 x = 0$$

by assuming a solution of exponential form:

$$x(t) = e^{\lambda t}$$

And substituting this into the differential equation:

$$\lambda^2 e^{\lambda t} + \omega^2 e^{\lambda t} = 0$$

Which simplifies to:

$$\lambda^2 + \omega^2 = 0$$

Then we obtain:

$$\lambda = \pm i\omega$$

Then the general solution to the equation is characterized by harmonic motion:

$$x(t) = Ae^{i\omega t} + Be^{-i\omega t}$$

Where A and B are constants determined by initial conditions.

Once the motion begins, it persists indefinitely, oscillating at the system's natural frequency, ω. To account for damping, a force proportional to the velocity of the mass is introduced, representing friction between the moving mass and the surface. This results in the modified equation:

$$m\ddot{x} + \gamma\dot{x} + kx = 0$$

Or equivalently:

$$\ddot{x} + \epsilon\omega\dot{x} + \omega^2 x = 0$$

Where:

$$\epsilon = {}^{\gamma}/_{m\omega}$$

Here, γ and ϵ are the coefficients of friction.

The solution to this modified equation is:

$$x(t) = A_0 e^{-\epsilon\omega t} \sin\,(\omega t\sqrt{(1-\epsilon^2)}$$

Where $x(t)$ is the displacement of spring at time t and A_0 is the initial amplitude at t=0.

The term $\epsilon\omega$ is the rate of exponential decay and it controls how fast the motion decays:

Higher ϵ = stronger damping = faster decay.

The time dependent amplitude corresponds to:

$$A(t) = A_0 e^{-\epsilon\omega t}$$

This represents a harmonic oscillation that decays exponentially over time.

If $\epsilon = 0$, the system returns to the non-attenuated case, there's no damping and the amplitude remains constant.

Otherwise, the attenuation coefficient ϵ can be defined using the quality factor Q as:

$$\epsilon = {}^{1}/_{2Q}$$

Where Q is defined as the ratio between the initial energy and the energy lost per cycle of oscillation:

$$Q = {}^{2\pi E}/_{\Delta E}$$

Q is thus dimensionless, and a higher Q value indicates less energy loss and lower attenuation, meaning seismic waves can travel further with less dissipation of energy. In contrast, a lower Q value signifies higher energy loss and higher attenuation.

The amplitude as a function of time becomes:

$$A(t) = A_0 e^{-\omega t/_{2Q}}$$

This shows how the amplitude decreases exponentially over time, with the rate of decay depending on ω (angular frequency) and Q (quality factor).

Alternatively, we can express the amplitude as a function of distance traveled:

$$A(x) = A_0 e^{-\left({}^{f\pi}/_{Q\mathrm{v}}\right)x}$$

Where v is the velocity of the wave and $f = {}^{\omega}/_{2\pi}$. x denotes the distance along the propagation path, and can be approximated using the focal depth h and epicentral distance R_{epi} as:

$$x = \sqrt{(h^2 + R_{epi}^2)}$$

It is obvious from this equation that for a constant value of Q, a high frequency wave will be attenuated more quickly than a low frequency wave. Indeed, for a given distance, a high frequency wave will oscillate more than a low frequency wave.

5.1.2 Intrinsic and scattering attenuation

Seismic waves undergo energy loss as they propagate through the earth due to several attenuation mechanisms. Understanding these mechanisms is important for accurate seismic hazard analysis, ground motion modeling, and interpretation of subsurface structures. Attenuation refers to the decrease in seismic wave amplitude due to energy dissipation and redistribution as waves travel through Earth's materials. It is commonly quantified using the quality factor Q, where a higher Q implies lower attenuation and vice versa. The primary types of attenuation are:

- Intrinsic Attenuation (Q_I)
- Path Attenuation (or Scattering Attenuation, Q_S)

The total quality factor Q_T is typically expressed as the sum of the intrinsic and path attenuation components. Richards and Menke (1983) suggested that:

$$1/Q_T = 1/Q_I + 1/Q_S$$

This relationship assumes that energy losses due to these mechanisms are independent.

5.1.2.1 Intrinsic (aneslatic) attenuation

In an idealized, purely elastic Earth, seismic waves would attenuate only due to geometric spreading, which is the expansion of wave energy over distance. However, because the earth is not perfectly elastic, seismic waves also experience anelastic attenuation, a process where wave energy is dissipated over time. Intrinsic attenuation refers to the conversion of seismic wave energy into heat due to the anelastic (non-recoverable) behavior of Earth materials. This extra energy loss is frequency-dependent and arises from various energy loss mechanisms or physical processes like:

- Grain boundary friction (internal friction)
- Dislocation movement
- Fluid flow in pores
- Thermoelastic relaxation

Intrinsic attenuation is determined by the microscopic properties of the medium. The overall effects of internal friction are quantified by the dimensionless quality factor Q_I.

Given that intrinsic attenuation is primarily attributed to shear mechanisms, P-waves generally experience less attenuation than S-waves. The respective quality factors are denoted as $Q\alpha$ for P-waves and as $Q\beta$ for S-waves. For materials where attenuation is solely due to shear processes, the relationship $Q\alpha = 9/4Q\beta$ holds.

Intrinsic attenuation is highly sensitive to factors such as temperature, pressure, mineral composition, and fluid saturation. It is typically stronger in sedimentary basins, fault zones, and unconsolidated materials, where anelastic processes are more prominent. Consequently, the seismic quality factor (Q) varies throughout the Earth's crust, reflecting temperature heterogeneities. Tectonically active regions, which generally exhibit higher heat flux, tend to be more attenuating than tectonically stable, colder regions.

Within the typical seismic frequency range of approximately 0.001 to 1.0 Hz, attenuation is often considered frequency independent. However, at higher frequencies, Q becomes frequency dependent and generally increases with frequency, reflecting the influence of additional attenuation mechanisms that become significant at smaller wavelengths.

5.1.2.2 Path (scattering) attenuation

Various reflections and refractions contribute to the scattering of wave energy. Path or scattering attenuation occurs when seismic energy is redistributed due to heterogeneities in the Earth's crust and mantle such as fractures, faults, or layers with contrasting seismic velocities. Unlike intrinsic attenuation, scattering doesn't necessarily result in energy loss, but rather spreads energy away from the main wavefront, reducing the coherent amplitude of seismic waves. This type of attenuation is prominent in crustal domains with high heterogeneity and is particularly relevant at high frequencies. Takemura et al., (2015) showed that small-scale velocity inhomogeneities in subsurface structure tend to predominantly affect the high-frequency components of the wave field, causing further energy loss where waves are more sensitive to small-scale inhomogeneities.

Despite advancements, isolating the effects of intrinsic and scattering attenuation remains challenging due to Earth's complex heterogeneity.

5.1.3 Frequency dependence of Q

Richards and Menke (1983) found that at high frequencies, the observed Q resulting from wave propagation through a stratified medium is frequency independent. Similarly, Frankel and Clayton (1986) observed the same result for attenuation in a similar medium. However, the observed attenuation in a medium may also exhibit frequency dependence, depending on the characteristics of the medium's heterogeneities. As a result, there are cases where Q is frequency dependent and others where it remains frequency independent.

Anderson and Hough (1984) demonstrated that attenuation processes contribute to a frequency independent Q, Q_i, and on the other hand, one or more attenuation mechanisms contribute to a frequency dependent component, Q_d. If these two components are added in the same way as above, we obtain:

$$^{1}/_{Q_T} = {}^{1}/_{Q_i} + {}^{1}/_{Q_d}$$

where the frequency dependent term in numerous study is presented in power law form of quality factor Q (Abercrombie, 1999):

$$Q(f) = Q_0({}^{f}/_{f_0})^{\eta}$$

f_0 is reference frequency and is commonly taken to be 1 Hz (Aki and Chouet, 1975). And Q_0 is the value of Q at this frequency. Q typically increases with frequency ($\eta > 0$), and large values of $\eta \sim$ 0.5-1 are observed in studies involving surface wave, Lg Q, Lg coda Q and deep boreholes (Nuttli, 1973).

5.1.4 Relation with kappa and t^*

In the case of body waves, we account for the effects of attenuation with the t^* parameter defined as travel time t divided by Q:

$$t^* = {}^{t}/_{Q}$$

Generally, the quality factor Q increases with depth, indicating that seismic waves experience less energy loss as they propagate through deeper levels. Since Q varies, t^* is generally expressed as the integral which accounts for the cumulative attenuation experienced by the seismic wave along its travel path:

$$t^* = \int {}^{dt}/_{Q} = \sum_i {}^{t_i}/_{Q_i}$$

with the subscript i indicating the i layer of the earth in a stratified Earth.

Substituting $t^* = {}^{t}/_{Q}$ into equation (1), we obtain:

$$A = A_0\, e^{-\pi f t^*}$$

This equation describes the spectral amplitude decay of a seismic wave over its propagation's path.t^* is larger for S waves, so they will attenuate more rapidly with distance than P waves (Goraj, 2000). This expression is structurally similar to the first equation which is:

$$A = A_0\, e^{-\pi f \kappa}$$

Anderson and Hough (1984) showed that κ and t^* can be considered equivalent only under specific assumptions: that the source spectrum follows the standard ω^{-2} model, that the frequency-independent contribution to Q can be separated from any frequency dependence, that the spectral decay is dominated by the direct wave rather than scattered energy, and that site resonance effects are negligible. The latter condition is particularly important, since shallow resonances or near-surface amplification can bias κ estimates: Anderson and Hough (1984) first noted this issue, Parolai and Bindi (2004) quantified such bias theoretically for layered soils, and Ktenidou and Abrahamson (2016) demonstrated that even rock κ_0 values can be influenced by broadband near-surface amplification. Nevertheless, when these simplifying assumptions are reasonably satisfied, κ and t^* converge to the same physical meaning, making κ a practical proxy for Q_β in cases where direct estimates remain unavailable (Campbell 2009; Parolai et al., 2022).

Under the assumption of frequency-independent Q, the similarity between these equations implies that:

$$\kappa = t^*$$

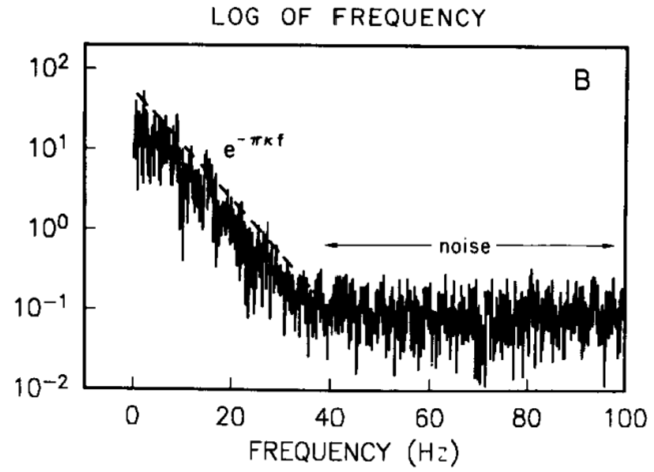

Figure 44. Fourier amplitude spectrum in Linear-log axes of the N85°E component of strong ground acceleration recorded at Cucapah during the Mexicali Valley earthquake of 9 June 1980 (M_L = 6.2). Accelerograph was a digital recorder which samples at a rate of 200/sec (Anderson and Hough, 1984).

5.2 Calculation of whole-path kappa values

5.2.1 Methods to determine kappa

There are various methods to compute kappa, each tailored to different datasets, assumptions, and purposes. These approaches can involve directly analysing seismic wave spectra, using transfer functions or response spectra, or leveraging advanced inversion techniques. The choice of the method often depends on the availability of data, the frequency range of interest, and the specific goals of the study, such as isolating site effects or separating source, path, and site contributions. Below, we outline the primary methods used for kappa estimation (Ktenidou et al., 2014).

- Acceleration Spectrum Method:

Following the classical approach of Anderson and Hough, it involves determining the slope of the high-frequency decay of the Fourier spectrum of S-waves. Since these measurements include a component of horizontal wave propagation influenced by Q, extrapolating them to zero distance, assuming frequency independent Q, yields the site specific attenuation parameter (κ_0). It requires selecting a frequency range above f_c (source corner frequency) to avoid trade-offs with source parameters. Therefore, the method works best for larger magnitudes.

- Transfer Function Method:

The transfer function method is a method that only calculates the site specific kappa from the high frequency portion of the site transfer function, derived through source-path-site inversions on a set of records from various events and stations (Drouet et al., 2010a). The measurement avoids amplification peaks and uses one station as a reference, neglecting its site effects.

- Source Spectrum Method:

Oth et al., (2011) proposed an alternative method to estimate κ_0 by analyzing the high-frequency decay directly from source spectra (κ_r^{SS}). They first correct observed spectra for whole path attenuation by referencing all recordings to a distance of 5 km, where attenuation is minimal. They then remove site amplification effects, excluding any high frequency decay so that the remaining spectral decay reflects a near-zero distance estimate of κ_0 that avoids extrapolation. Since this yields one value per event, site-specific κ_0 obtained by averaging over multiple events. A similar approach was used by Margaris and Boore (1998).

- Response Spectrum Method:

The Response Spectrum method calculates kappa by relating it to the spectral shape of the normalized response spectrum, rather than the high-frequency decay of the Fourier spectrum (Silva and Darragh, 1995). It uses stochastically generated acceleration response spectra and site amplification derived from the site profile. These simulated spectra are normalized and compared to observed data to compute the best-fit kappa. Unlike previous methods, this approach utilizes the entire frequency band and reduces trade-offs with stress drop by normalizing the response spectra by peak ground acceleration.

- Broadband Inversions:

These methods analyze the full frequency band to separate source, path, and site effects. They assume a specific spectral shape for the earthquake source and aim to extract kappa when the earthquake's corner frequency overlaps with the frequency range used for the measurement. One of the advantages compared to classic approach is that this allows kappa estimation for smaller magnitude events by resolving trade-offs between parameters like stress drop and corner frequency (Anderson and Humphrey Jr, 1947).

- Displacement Spectrum Method:

The Displacement Spectrum method, proposed by Biasi and Smith (2001), extends the classic approach by measuring kappa using earthquakes with very small magnitudes (M <1), where data is abundant. This method uses the Fourier displacement spectrum below the corner frequency (f_c), in contrast to the standard approach using the acceleration spectrum above f_c. One advantage is that the displacement spectrum provides a stronger theoretical basis for measuring kappa (the theoretical basis for treating the displacement spectrum at the source as flat below f_c is actually stronger than the basis for treating the acceleration spectrum as flat above it, because the latter depends on the validity of the ω^{-2} assumption), and it avoids the assumptions used in the acceleration spectrum (Ktenidou et al., 2014).

5.2.2 Calculation in BELSHAKE

For the BELSHAKE records, the κ parameter was calculated using the classical definition, which involves measuring the slope of the S-wave Fourier amplitude spectrum in log-linear scale at high frequencies. For all the records in BELSHAKE database, the minimum and maximum frequencies (f_1 and f_2) for the linear portion of the Fourier amplitude spectrum were visually selected for all three components of each record. These frequencies were chosen within the reliable frequency range (fmin-fmax) previously established based on a minimum signal-to-noise ratio of 3 and were carefully chosen to avoid including resonance peaks caused by site effects and to stay above the corner frequency. The κ value was calculated by dividing the slope of the linear portion of the spectrum by π. The slope was determined by fitting a line to the smoothed spectrum using the ordinary least squares method. Figure 45 illustrates the Fourier amplitude spectrum of the S-wave window for the Z, E, and N components of the BE.BEBN station record of an earthquake. The smoothed Fourier spectrum is shown in red, while the fitted line within the selected frequency range is displayed in green. For the horizontal component, kappa is computed as the arithmetic average of kappa values in east and north components.

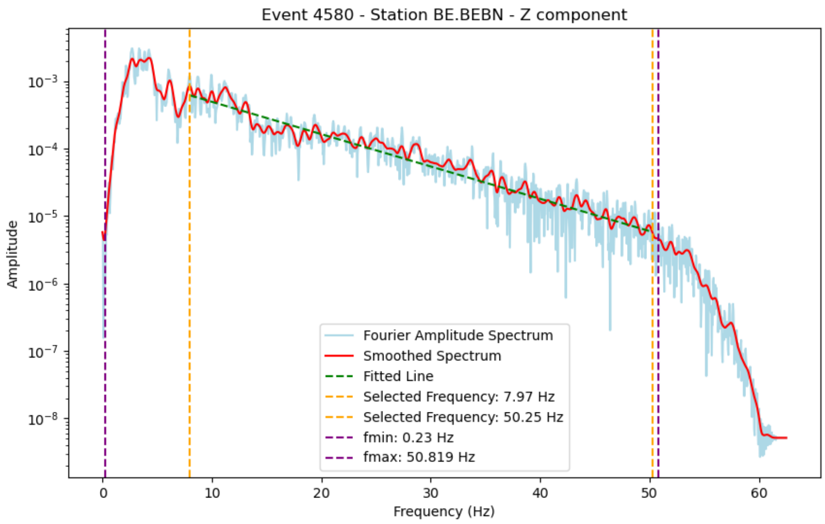
Event 4580 - Station BE.BEBN - Z component
Amplitude
Frequency (Hz)
Fourier Amplitude Spectrum
Smoothed Spectrum
Fitted Line
Selected Frequency: 7.97 Hz
Selected Frequency: 50.25 Hz
fmin: 0.23 Hz
fmax: 50.819 Hz

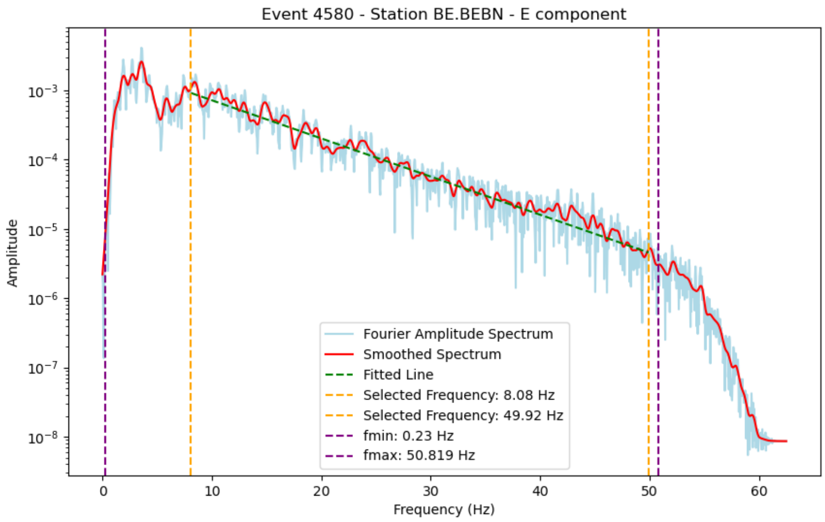
Event 4580 - Station BE.BEBN - E component
Amplitude
Frequency (Hz)
Fourier Amplitude Spectrum
Smoothed Spectrum
Fitted Line
Selected Frequency: 8.08 Hz
Selected Frequency: 49.92 Hz
fmin: 0.23 Hz
fmax: 50.819 Hz

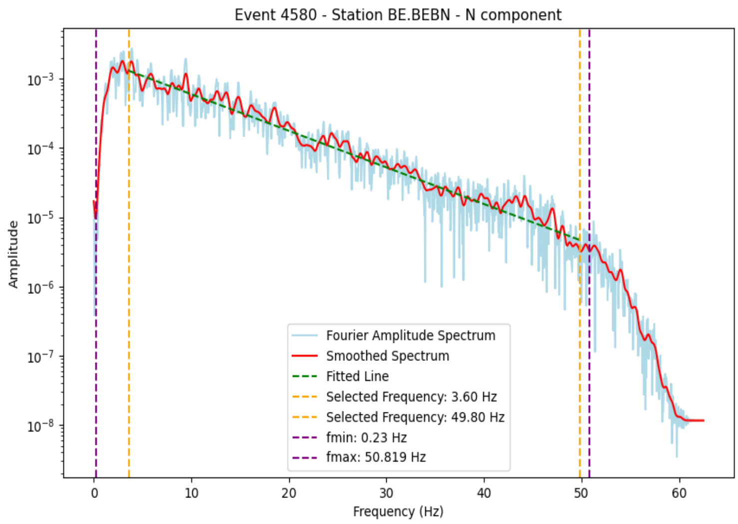

Figure 45. Illustration of determination of kappa from acceleration Fourier amplitude spectra for a three-components record of an earthquake in Goch (DE) with M_L = 4.3 by station BE.BEBN. Blue curve: Fourier amplitude spectrum of the S-. Red curve :smoothed Fourier amplitude spectrum. Green line: fitted line to the smoothed Fourier amplitude spectrum by OLS method. Dashed purple lines show fmin and fmax corresponding to the minimum and maximum frequency established based on minimum signal to noise ratio equal to 3. Dashed yellow lines show selected frequencies for the linear portion to compute κ.

5.2.3 Data filtering

After calculating kappa values for each station, we assessed their relationship with epicentral distance (R_{epi}), observing a general trend of increasing κ with increasing R_{epi} (Figure 46). However, while most stations followed this trend, certain anomalies were observed as vertically aligned clusters in the κ versus R_{epi} plots. Upon reviewing these records, it was determined that these anomalies were attributable to induced earthquakes, short-distance records, and shallow depths. Consequently, a filtering process was applied to evaluate the impact of excluding these records on the κ values at different stages.

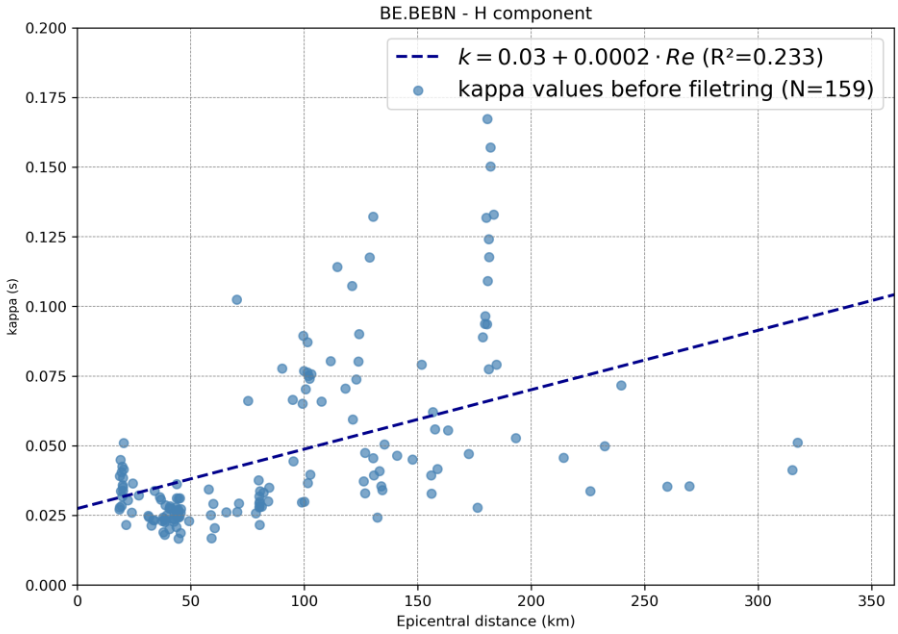

Figure 46. Relationship between kappa and epicentral distance for BE.BEBN station in the horizontal direction

To refine the kappa values and exclude anomalies from the dataset, ensuring a more accurate estimation of kappa values versus distance, we applied a systematic filtering process. Upon identifying anomalies, we filtered the data and then evaluated the κ_0 values and the $R2$ values of the kappa-distance relationship. This evaluation was conducted to determine whether the filtering improved the results or potentially degraded them.

- Filter 1: excluding all induced earthquakes.
- Filter 2: excluding all induced earthquakes, and records with both a R_{epi} less than 50 km and a depth less than 7 km simultaneously, as well as any visual outlier.
- Filter 3: excluding all induced earthquakes, and all records with depth less than 8 km, as well as any visual outlier.

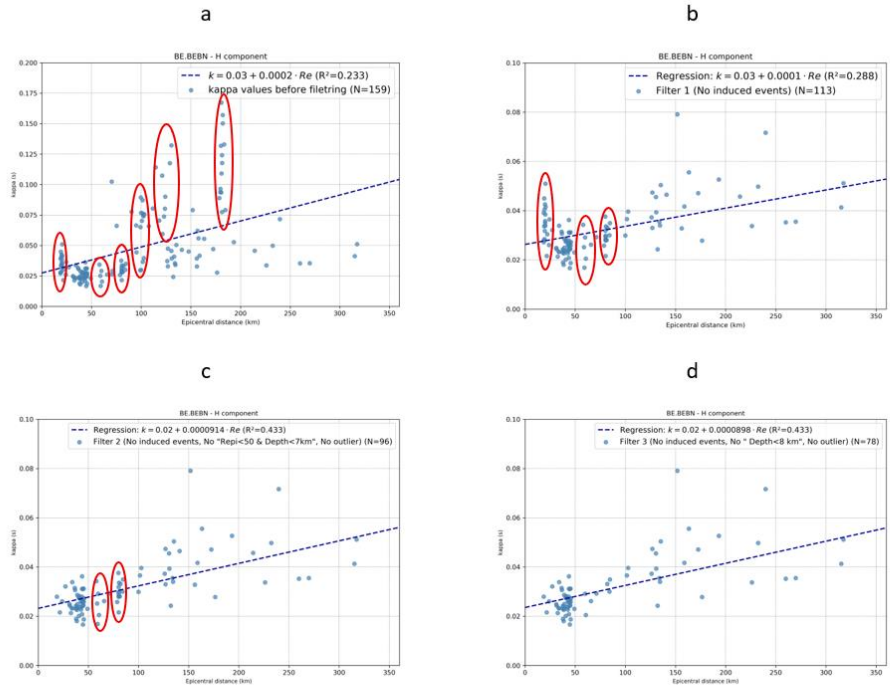

Figure 47. Comparison of kappa-distance plots for the H component of station BE.BEBN, with three filtering approaches. (a) kappa values before any filtering on k-distance data, (b) after applying filter 1, (c) after applying filter 2, (d) after applying filter 3. Some vertical lines and the outliers have been marked.

The filtering process was applied in three stages to improve the fit of the kappa-distance relationship. The impact of each filtering method on the regression quality was analyzed to assess the effectiveness of each step.

Filter 1, which considers only natural earthquake records, with R^2 value of 0.296 indicates a poor regression fit. The first panel in Figure *47* displays the κ values versus epicentral distance for BE.BEBN station after applying Filter 1. It highlights the issues of poor regression fit and the persistence of vertical lines in the datapoints, suggesting that further filtering is necessary.

In Filter 2, we excluded records with both shallow depths and short epicentral distances (R_{epi} < 50 km and depth < 7 km) to remove vertical clusters of data points that negatively impact the regression fit. This filtering enhanced the overall fit of the regression, as shown in the second panel of Figure *47*.

The third panel in Figure *47* shows the results after applying Filter 3, which further refines the data by excluding all shallow-depth records with depths less than 8 km, regardless of the distance, to resolve residual issues from Filter 2. This filter eliminates remaining vertical alignments in the kappa-R_{epi} plots, improving overall fit and reducing variability.

For some stations, such as BE.GES and BE.CLA, the R^2 values decrease due to a reduced number of data points after applying stricter filtering criteria. For instance, where over 50 data points were initially available, filtering reduced the sample size to fewer than 20 in some cases. This decrease in data points can lead to increased variability and a less accurate representation of the kappa-distance relationship. Additionally, the non-linearity of the data may not be adequately captured by linear regression with such limited data, further contributing to the lower R^2 values. However, to ensure consistency across all stations and to avoid including unreliable data, we chose to proceed with the reduced dataset.

Overall, filter 1 includes vertical lines in the kappa plots due to shallow-depth records. Filter 2 improves the estimation by excluding shallow-depth records with short epicentral distances and visual outliers, resulting in more robust regression. Despite this, some vertical lines still persist for larger epicentral distances. Filter 3, by removing all records with depths less than 8 km and outliers, offers the most accurate kappa estimation, resolving the remaining issues. Although Filter 3 results in a slight decrease in R^2 values for a few stations, specifically for the H component at BE.CLA (0.19 to 0.17) and BE.MEMS (0.13 to 0.11), and for the Z component at seven stations; the differences are minimal. In contrast, stations that show improved R^2 under Filter 3 generally exhibit more substantial gains. Given the limited impact of the decreases and the clear advantages in estimation accuracy, applying a uniform filtering process across all stations is preferable to customizing it on a station-by-station basis. Therefore, we applied Filter 3 to all stations, as it remains the most reliable approach, offering better fitting and more consistent results.

5.2.4 Comparison with t^*

To evaluate the consistency of our κ estimates, we compared the κ values obtained for the horizontal component with equivalent t^* (t-star) values, which were determined independently in the BELSHAKE database (Vanneste et al., 2025) as a byproduct of moment magnitude estimation from displacement spectra. The latter was done using the python package SourceSpec (https://github.com/SeismicSource/sourcespec) (Satriano, 2025; Satriano et al., 2016), in which anelastic attenuation is modeled as $exp(-\pi f t^*)$, with the attenuation parameter t^*defined as:

$$t^* = \int \frac{dr}{Q_\beta(r)\beta(r)} = \frac{t}{\overline{Q_\beta}}$$

Where $Q_\beta(r)$ is the spatially varying shear-wave quality factor and $\beta(r)$ is the shear-wave velocity along the ray path (Cormier, 1982). As the S-wave arrival time is generally known, this can be simplified to travel time t divided by the average quality factor over the path $\overline{Q_\beta}$.

In principle, Q_β also varies with frequency. However, if Q_β is assumed to be frequency-independent, as is the case in SourceSpec, t^* becomes equivalent to the site attenuation parameter κ, and both are expressed in seconds.

It should be noted that these t^* values are the result of an automated spectral fitting procedure, focused on the low-frequency part of the displacement spectrum, whereas our κ values are derived from dedicated, interactive fitting of the high-frequency part of the acceleration spectrum of (Satriano et al., 2016; Satriano, 2025). Despite these methodological differences, comparison κ and t^* values for each event recorded by a given station show a good agreement, and for most stations, the Pearson correlation coefficient indicates a strong linear relationship. Figure 48 demonstrates this for station BE.BEBN, where a correlation coefficient of *r* = 0.75 demonstrates the reliability of the computed κ values in the database.

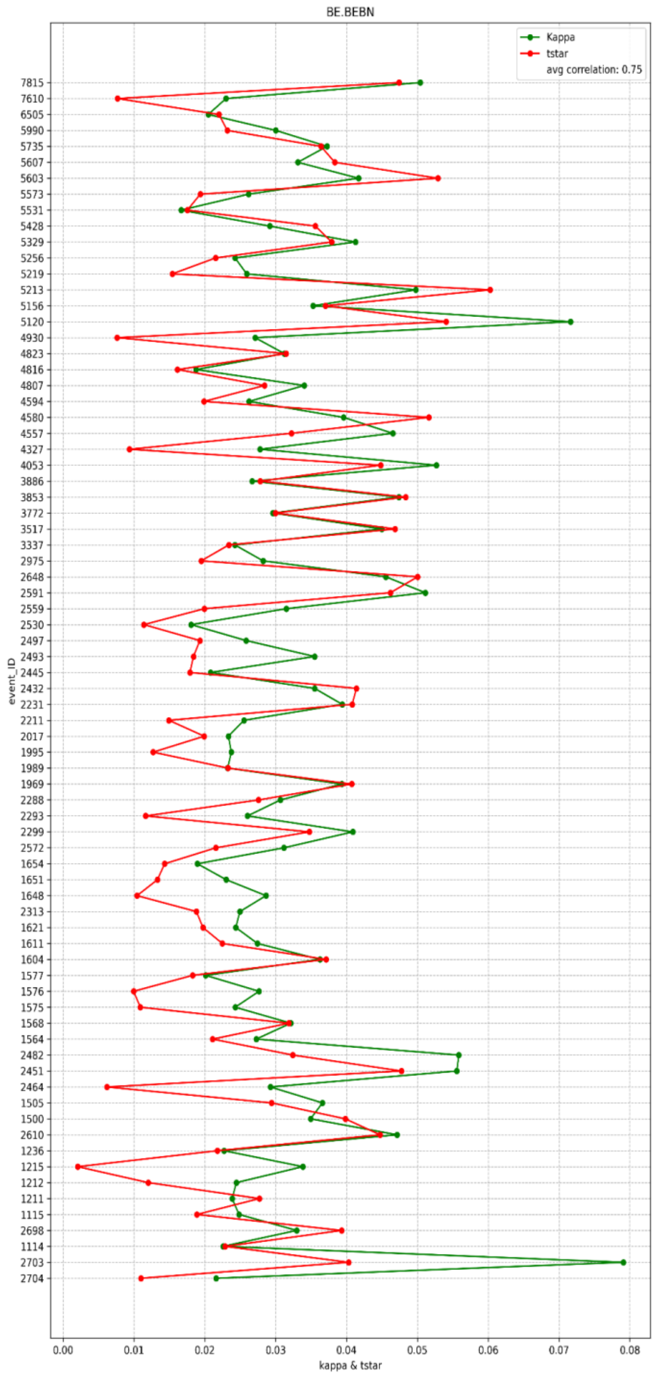

Figure 48. Correlation between κ and t^*value for BE.BEBN Station

5.3 Decomposition of kappa into site kappa and kappa gradient components

Anderson and Hough (1984) demonstrated that κ values determined for different records at a given station increase more or less linearly with distance, which can be written as:

$$\kappa = \kappa_0 + \kappa_r . r = \kappa_0 + \kappa_{path}$$

The intercept κ_0, i.e. κ extrapolated to zero-distance, represents a site-specific component, while the slope or gradient κ_r describes how fast κ increases with distance, which reflects regional attenuation. The product of κ_r and distance (r) thus corresponds to the path-dependent component (κ_{path}). The left panel of Figure 49 demonstrates the site and path components of κ for a single station. To obtain more robust estimates of the regional kappa gradient, data from multiple stations within the same crustal domain are often combined: by subtracting the κ_0 value of each station, we obtain κ_{path} to which a line can be fitted, the slope of which represents κ_r of the given crustal domain. This is illustrated in the right panel of Figure 49.

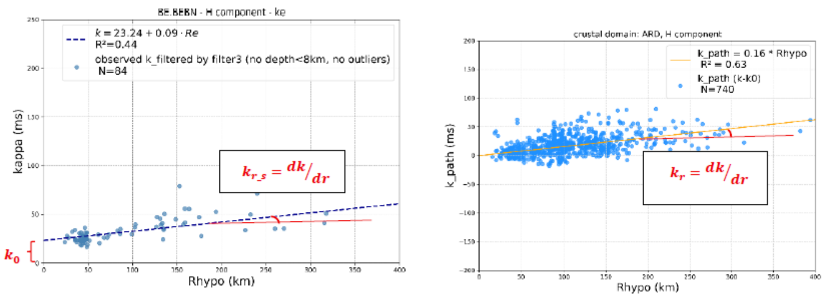

Figure 49. Left: κ_0 value computed by extrapolating the kappa-distance regression line for a particular station (BE.BEBN) to zero distance.
Right: κ_r value as the slope of the kappa-distance regression of the ARD crustal domain.

Figure 50 illustrates the distribution of seismic events and recording stations used in this study to estimate κ_0 and κ_r values. The event station network is densest in the central and eastern parts of Belgium, particularly within the ARD and the RVG, where both the number of events and the density of nearby stations are highest. These domains therefore can provide the most robust constraints on κ_0 and κ_r due to the abundance of data. The ABM is also relatively well covered, especially in its southeastern part, whereas the western and central-northern parts show much sparser coverage. The HAIN domain shows the sparsest coverage, with comparatively fewer seismic events and less dense station distribution; moreover, most source-site paths extend beyond the limits of this domain, which may affect the reliability of κ_r estimates in this region.

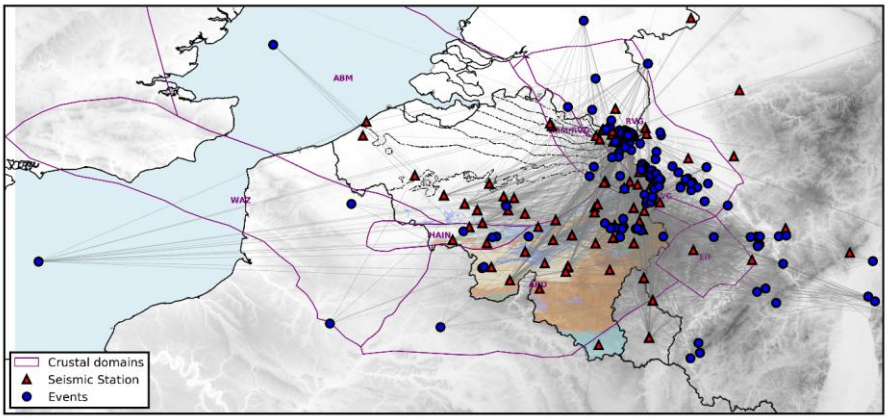

Figure 50. Map showing all pairs of seismic events (blue circles) and recording stations (red triangles) used for κ_0 and κ_r estimation. Gray lines connect events to stations, illustrating the coverage density across Belgium. The figure highlights clear differences in event–station coverage between the main crustal domains.

5.3.1 Estimation methods

Three methods employed for estimating κ_0 and κ_r values, which we named the FKG, JKG and MER. Each method has its own advantages and challenges.

- FKG is a relatively straightforward approach that estimates κ_0 and κ_r values for individual stations. Then, κ values from different stations in a crustal domain are combined, after subtracting the respective κ_0 values, in order to estimate the κ_r for the crustal domain. While computationally efficient, it is sensitive to data quality and availability, often resulting in unreliable estimates when stations have insufficient or missing data.

- JKG offers a more integrated approach by combining information from multiple stations in the same crustal domain. This method employs optimization techniques to simultaneously estimate a common κ_r and individual κ_0 values for each station, but it requires predefined ranges for model parameters, which can limit its flexibility and accuracy in certain scenarios. Despite these limitations, it offers a more sophisticated and robust framework for estimating κ_r in more data-rich environments.

- MER, in contrast, adopts a statistical framework that accounts for both fixed and random effects in the data. This method is particularly advantageous for complex datasets where there is varying data availability across stations. It offers a statistically robust method for jointly estimating both common and individual κ_r and κ_0 values, making it well-suited for cases where data variability needs to be accounted for.

In the following sections, we provide a detailed examination of these three methodologies, outlining the underlying steps and presenting the results of their application. The performance of these methods in estimating κ_0 and κ_r values across different crustal domains is compared for both horizontal and vertical components. We also discuss the advantages and limitations of each approach. To assess the degree of agreement between the methods, we use the Intraclass Correlation Coefficient (ICC), which serves as the primary metric for evaluating the consistency and reliability of the results.

5.3.2 Crustal domains in the Belgian tectonic context

For the purpose of this study, we subdivided Belgium into four main crustal domains, which were simplified from the more detailed seismotectonic model by Verbeeck et al., (2009). ABM (Anglo-Brabant Massif), ARD (Ardenne), RVG (Roer Valley Graben) and HAIN (Hainaut), as illustrated in Figure 5. ABM is a tectonic block connecting the Brabant Massif in Belgium with the Anglia Basin in England. In Belgium, it mainly consists of Early Paleozoic shales and metasandstones, which were strongly folded during the Brabantian phase of the Caledonian orogeny. These rocks are capped by Cretaceous limestones and marls, and a cover of Neogene sands and clays that becomes thicker towards the NNE, reaching > 1000 m at the Dutch border. ARD is a tectonic block that was deformed during the Upper Paleozoic Variscan orogeny and consists of an E-W oriented tectonic structure where Devonian and Carboniferous sandstones, shales and limestones are exposed in synclines and anticlines. Several Lower Paleozoic metamorphic inliers are present. To the south, ARD is overlain by Triassic and Jurassic sediments. Quaternary deposits are only present in incised river valleys and are usually thin. HAIN is a narrow (only 15 km wide) basin at the northern edge of the Ardenne, which is probably formed as a pull-apart basin connecting the Weald-Artois shear zone (WAZ) to the west. In this basin, Cretaceous chalk and limestones are at the surface in the west, and Carboniferous coal, mud- and sandstones in the east. HAIN is limited in depth up to max. 6 km (Camelbeeck et al., 2025) and was overthrusted on top of the ABM during the Variscan orogeny. RVG is a tectonic zone characterized by active normal faulting since the Late Oligocene. This graben is filled with thick layers of loose Tertiary marine sands and clays, covered by Quaternary alluvial gravels and sands. The bedrock, composed of Late Cretaceous to Early Neogene limestone, is situated at a depth of more than 1000 m in the center of the graben, compared to only a few hundred meters on its flanks. ABM/RVG marks a transition zone between both crustal domains. Here, the top of the basement quickly plunges to the NE and it is overlain by Upper Devonian and Carboniferous sand- and limestones deposited during early development of the RVG. Similarly, ARD/RVG indicates the zone where faulting in the RVG affected the ARD. Both ARD/RVG and ABM/RVG are characterized by predominantly NW-SE- to NNW-SSE-trending normal faulting due to RVG extension.

5.3.3 Results

5.3.3.1 Free kappa gradient method

In this section, we compute and analyse the κ_0 and κ_r values by the FKG. The method involves the following steps:

The kappa values were fitted using the ordinary least squares (OLS) method.

The following values were extracted for each station:

- κ_0: site-specific kappa value for each station;
- kappa gradient of each station (κ_{r_s}): slope representing the change in kappa with distance for each station (notated with subscript to distinguish it from κ_r which is used to denote the kappa gradient of a crustal domain, see below);

- R^2: Goodness of fit;

Stations exhibiting high κ_0 values along with negative κ_{r_s} (e.g., BE.CTH) are marked as unreliable in Table S1 and Table S2 were excluded from further analysis with this method due to their indication of anomalous behavior, which could distort the overall results. This behavior was mainly due to the insufficient data available for these stations.

In the next step, we aim to isolate the path effect from the kappa values. To achieve this, we subtract the computed κ_0 values from the kappa values, leaving only path-related attenuation. The formula for calculating path attenuation for each record is:

$$\kappa_{path} = \kappa - \kappa_0$$

By isolating κ_{path}, we focus solely on the path attenuation, which describes how seismic waves are attenuated as they travel through the Earth's crust. This is supposed to have some regional uniformity, in contrast to κ_0.

Next, we create separate datasets of κ_{path} values for all the stations in one crustal domain for both H and Z components. For each crustal domain and component, we find the slope of the relationship between κ_{path} and hypocentral distance (R_{hypo}) which corresponds to the kappa gradient of that crustal domain and component (κ_r). The values were fitted using the OLS method under the constraint that:

$$\kappa_{path} = 0 \text{ at } R_{hypo} = 0$$

We begin by analyzing all stations in the BELSHAKE dataset and then continue with only those that meet the minimum data requirements for reliable estimation.

In the first phase of analysis, we considered all the stations of BELSHAKE dataset into analysis. The plots below present kappa values as a function of R_{hypo} for individual stations, with two stations provided as examples. Each plot includes the fitted linear regression line used to estimate the site specific kappa parameters: κ_0 (intercept), κ_{r_s} (slope), along with coefficient of determination (R^2) and the number of data points (N).

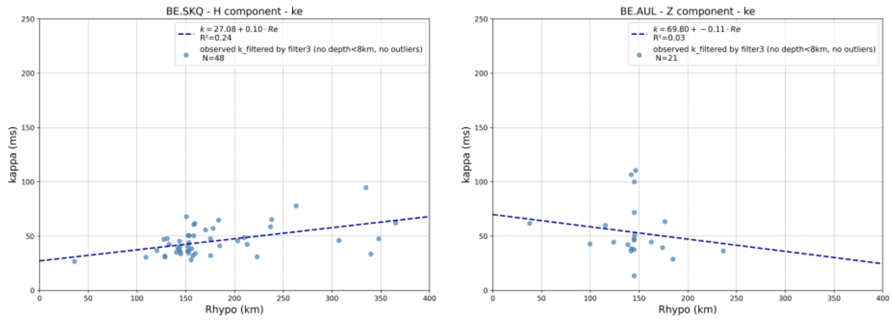

Figure 51. Kappa values as a function of R_{hypo} for two individual stations from the BELSHAKE dataset, with the legend displaying the κ_0, κ_{r_s}, R^2 and the number of data points for each station.

Table S1 and S2 in supplement file summarize the κ_0, κ_{r_s}, R^2 values, and the number of records for each station and component that was analysed with the FKG. In general, the horizontal component (H) tends to have higher κ_0 values compared to the vertical component (Z). Stations such as BE.MASA, NL.ROLD, and NL.GUR1 are marked as unreliable and excluded after this phase due to their unusually high κ_0 and negative κ_{r_s} values. There are some other stations marked as unreliable because of negative κ_0 value or low R^2 value. All these issues typically arise for stations with insufficient data (mostly 2 or 3 records), which can lead to unreliable estimates using this method. Some stations such as BE.HUM, BE.MEU, and BE.SNF have slightly negative κ_{r_s} values, but are not marked as unreliable. This decision is based on the fact that, although the κ_{r_s} values are negative, they are very close to zero and the number of data points is sufficient to allow a reliable estimation. These stations are marked green in Table S2.

In the next step, we isolated the path effect from the kappa values by removing the site-specific effect associated with each station. Each plot below shows the κ_{path} ($\kappa - \kappa_0$) versus R_{hypo} values for Z component of all crustal domains. For each crustal domain and component, we determined the κ_r by fitting the κ_{path} values to R_{hypo}. Figure 52 shows the κ_{path} and κ_r, fitted number of records and R^2 value for each case. In general, κ_r are much more robust than those estimated for individual stations. The HAIN crustal domain lacks data for the H component and is therefore excluded from the analysis.

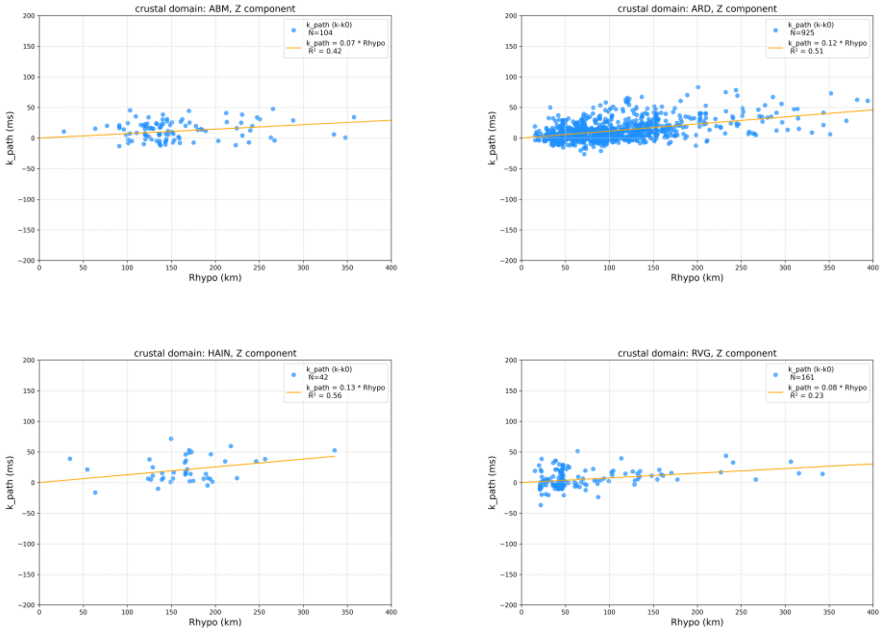

Figure 52. Fitting the κ_{path} values to R_{hypo} using the FKG considering *__all stations__. The legend displays the number of records , κ_r ($\kappa_{path} = \kappa_r * R_{hypo}$) , and R^2 values for the Z component of each crustal domain. The fitting is done with the assumption that κ_{path} = 0 at R_{hypo} = 0.*

Crustal Domain	Component	κ_r (ms/km)	κ_0 range (ms)	R^2	N
ABM	H	0.14	10 – 40	0.59	85
ARD	H	0.16	5 – 60	0.64	747
RVG	H	0.11	9 – 76	0.37	145
ABM	Z	0.07	3 – 37	0.42	104
ARD	Z	0.12	2 – 39	0.51	925
HAIN	Z	0.13	27 – 38	0.56	42
RVG	Z	0.08	17 -78	0.23	161

Table 5. κ_r and κ_0 range estimates for different crustal domains and components by FKG. The table also present the R^2 values, and the number of records (N) for each crustal domain and component considering *__all stations__*

Table 5 summarizes the estimated κ_r values along with the range of site-specific κ_0 values. A comparison of κ_r and κ_0 range across crustal domains reveals:

- The κ_r ranges from 0.11 to 0.16 (ms/km) for the H component. ARD has the highest and RVG has the lowest κ_r in H component.
- The κ_r ranges from 0.07 to 0.13 (ms/km) for the Z component. HAIN has the highest and ABM has the lowest κ_r in Z component.
- The horizontal components show consistently higher kappa gradients than the vertical components.
- RVG has the highest κ_0 range among all the crustal domains. ABM has the lowest κ_0 range.

In the second phase of the analysis, we focused on a smaller subset of stations within each crustal domain. Using Table S1 and Table S2 as references, we selected stations that had an adequate amount of data and reliable estimates for both κ_{r_s} and κ_0. This subset was chosen such that all crustal domains were represented in the analysis. The stations included in this analysis were:

- ABM: BE.RQR, BE.SKQ, BE.UCCS
- ARD: BE.BEBN, BE.CLA, BE.CTH, BE.DOU, BE.GES, BE.KLB, BE.LCH, BE.MEMS, BE.MRD, BE.ROB, BE.STI, BE.VIA
- RGV: BE.HRK, BE.BEBN

Crustal domain	component	κ_r (ms/km)	R^2	N
ABM	H	0.11	0.79	17
ARD	H	0.14	0.70	488
RVG	H	0.08	0.48	99
ABM	Z	0.06	0.41	95
ARD	Z	0.12	0.55	893
RVG	Z	0.07	0.29	153

Table 6. κ_r estimates for different crustal domains and components by FKG considering only <u>selected stations</u>.

The results from the selected stations in Table 6 align closely with those from all of the stations in Table 5:

- The κ_r ranges from 0.08 to 0.14 in H component. ARD has the highest (consistent with the result of all stations) and RVG has the lowest κ_r in H component.
- The κ_r ranges from 0.06 to 0.15 in Z component. HAIN has the highest and ABM has the lowest κ_r in the Z component (consistent with the result of all stations).
- Generally, the horizontal components show consistently higher κ_r than the vertical components (consistent with the result of all stations).
- Overall, the R^2 values generally improved for most domains and components when using the selected stations, indicating that, although there is less data overall, the selected stations provide a more reliable fit for the κ_r, particularly in crustal domains with multiple reliable stations.
- The κ_r increases when using the selected stations, but the change is small.

5.3.3.2 Joint kappa gradient method

In this method, we applied a joint fit of the kappa gradient to the observed kappa values across all stations within a given crustal domain. All stations in the database contributed to the analysis. This method follows an approach that tries to minimize the root-mean square error (RMSE) between observed and predicted κ values, where we impose a common κ_r for all stations in the same domain but allow each station an individual κ_0.

Input Parameters: The function takes several inputs:

- Observed kappa values for all stations in a crustal domain.
- Hypocentral distances (R_{hypo}).
- Station codes for each record

- A predefined lower and upper bounds of κ_r and κ_0 values.

Joint gradient fitting:

- The function iterates over a range of possible common κ_r and κ_0 values to minimize the error between the observed and fitted values.
- The goal is to determine a common κ_r, for all stations within the domain, along with an individual κ_0 value for each station.
- Sensitivity Analysis: We apply sensitivity analysis to identify the optimal ranges for κ_0 values, ensuring that our fitted parameters accurately reflect the data.

Sensitivity analysis

JKG fit function requires the specification of ranges (or bounds) for κ_r and κ_0 values. The initial κ_0 and κ_r ranges tested were (0, 100) ms and (0, 0.3) ms/km respectively, chosen based on the κ_0 and κ_r values obtained with the FKG. Using this range, the H components produced results comparable to the FKG, showing similar κ_r but with slightly lower R^2 values. However, the Z components all displayed identical κ_r equal to 0.04, and very different from the results of the FKG as shown in bold in Table S3. This occurred because this first selected κ_0 range caused the optimization function to get stuck in a local minimum, preventing it from finding the optimal kappa gradient. Furthermore, this issue arose due to the inclusion of all stations in the analysis, rather than restricting it to only reliable ones.

To address this, we explored five additional κ_0 ranges with a minimum of zero and maximum values of 90, 80, 70, 60, and 50, instead of 100 ms. Comparison of R^2 values for these different ranges showed some fluctuations with respect to those obtained with FKG. However, the range of (0, 50) provided the best overall results in terms of R^2, and the best agreement with the κ_r obtained with FKG. Therefore, this range has been used for subsequent sections. Table S4 and Table S5 show the computed κ_0 for all stations together with the standard deviation value, and κ_r for each crustal domain and component obtained with JKG. These values have been computed with κ_r range = (0, 0.3) and κ_0 range = (0, 50). Figure 53 presents plots of κ_{path} versus R_{hypo} for the Z component of different crustal domains.

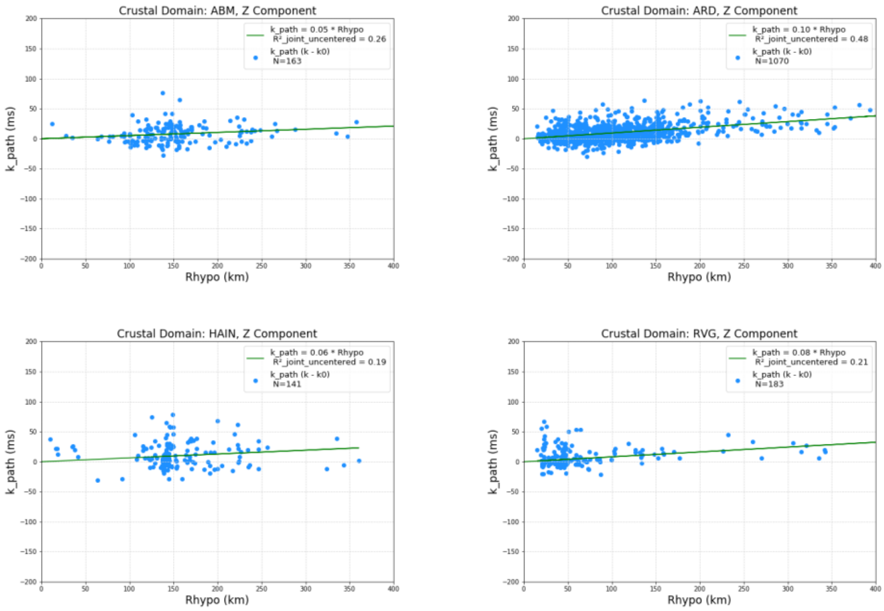

Figure 53. κ_{path} versus R_{hypo} for all crustal domains and components derived with JKG

Table 7 present the κ_r and κ_0 range computed for each crustal domain and component.

Crustal domain	Component	$\kappa_r (ms/km)$	κ_0 range (ms)	κ_r Stddev
ABM	H	0.16	2 - 50	0.64
ARD	H	0.15	5 - 50	0.07
RVG	H	0.15	18 - 50	1.22
ABM	Z	0.05	3 - 50	1.24
ARD	Z	0.10	2 - 50	0.01
HAIN	Z	0.06	12 - 50	0.37
RVG	Z	0.08	14 - 50	0.02

Table 7. Estimated κ_r and κ_0 range and standard deviation of κ_r for all the crustal domains and components by JKG

The comparison shows that:

- The κ_r ranges from 0.15 to 0.16 for the H component. There is not much difference between the κ_r of different crustal domains.
- The κ_r ranges from 0.05 to 0.10 for the Z component. ARD has the highest and ABM has the lowest κ_r in Z component (consistent with the result of FKG).
- Generally, the horizontal components show consistently higher kappa gradients than the vertical components (consistent with the result of the FKG).
- H component in RVG crustal domain has the highest κ_0 range (consistent with the results from the FKG), while ABM has the lowest κ_0 range (also consistent with the results from the FKG). It's important to note that all crustal domains have a maximum κ_0 equal to 50 ms since this method sets a predefined range for κ_0, with a maximum κ_0 value of 50 ms across all crustal domains. This upper limit is essential for ensuring that the optimization method can accurately predict the κ_r, as mentioned in the sensitivity analysis section. When the maximum κ_0 exceeds 50 ms, the optimization method struggles to accurately fit the common κ_r.
- Some stations in the HAIN and RVG domains have a low number of observations (N = 4 or less), which may impact the reliability of JKG estimates. Many of the stations with the highest κ_0 value (50 ms) fall into this category. In contrast, stations in the ARD and ABM domains have a significantly higher number of records, providing more reliable κ_0 and RMSE estimates. Overall, it can be concluded that although this method assigns a κ_0 to all stations, including those with very few data points, the reliability of the results for these stations may be questionable.

Figure 54 compares kappa values versus R_{hypo} for two individual stations with the JKG fit represented by the respective κ_0 and the κ_r.

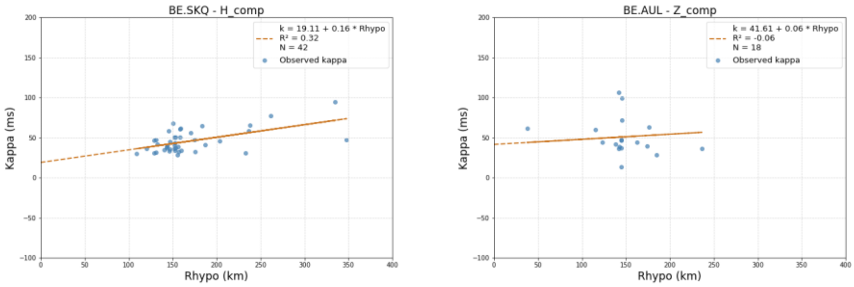

Figure 54. Plots of kappa values versus R_{hypo} for two individual stations. The brown line represents the station-specific κ_0 as the intercept and κ_r as the slope derived by JKG

JKG for analyzing kappa values across multiple stations within crustal domains proves to be a reliable approach for determining both joint κ_r and station-specific κ_0 values. This method reduces errors across stations within the same crustal domain, leading to consistent κ_r values. By assigning a common gradient to each domain while allowing individual κ_0 values for stations, it provides a robust solution for fitting kappa data.

Based on the results of this method, ARD has the highest and ABM the lowest κ_r on the Z component. On the H component, κ_r is similar for both ARD and RVG, with ABM displaying the highest κ_r, although the differences are minimal. RVG has the highest average of κ_0 and ABM has the lowest average of κ_0 among other crustal domains.

5.3.3.3 Mixed effect regression

MER is a powerful tool for analyzing data with both fixed and random effects, making it ideal for handling grouped datasets. In this context, the fixed effects or global values refer to the overall slope and intercept of the linear relationship between kappa and R_{hypo} for each crustal domain. Random effects, on the other hand, capture the deviation in the slope and intercept of the linear regression between kappa and R_{hypo} for individual stations within each crustal domain. The random intercept specific to each station plus the global intercept reflects the site-specific kappa value. Similarly, the random slope for each station, when added to the global slope, reflects the station-specific linear slope. For subsequent analyses, the key parameters of interest are the site kappa values for each station and the kappa gradient across crustal domains.

The motivation to employ MER in kappa analysis arises from:

- Handling Grouped Data: MER is well-suited for datasets where observations are grouped (e.g., data from multiple stations), allowing the model to account for both overall trends in a crustal domain, and station-specific variations. The model captures the variation in kappa values across individual stations by incorporating random intercepts and slopes. This enables the model to reflect local geological conditions, ensuring more accurate predictions at each station.

- Improved Estimation of Parameters: The model considers all data across stations, leading to more stable and reliable parameter estimates by reducing variability that could arise if stations were analyzed separately (FKG).

- Addressing Uncertainty in Slope: MER accounts for variability in slope estimates, which enhances the accuracy of the model's predictions and helps avoid errors that could result from using only fixed effects (more accurate variance comparing to JKG).

- Managing Uneven Data Distribution: These models can handle situations where data is uneven across stations. Some stations may have more data points than others, but the model can still account for these differences.

The general form of the MER used in this study is:

$\text{kappa}_{j,k}$ = (Global Intercept_i + Random Intercept_j) + (Global Slope_i + Random Slope_j) × $R_{hypo\,j,k}$ + ϵ_j

where:

- $\text{Kappa}_{j,k}$: The kappa value predicted for station j in the crustal domain i and event k.

- global intercept i (fixed effect): representing the average baseline κ_0 across all stations in the crustal domain i.

- random intercept for station j: reflecting the station-specific deviation from the global intercept i. This captures the unique κ_0 value for each station.
- global slope i (fixed effect): representing the overall gradient of kappa with respect to hypocentral distance (κ_r) across the crustal domain i.
- random slope for station j: representing the deviation in slope from the global slope specific to station j. This term allows the κ_r to vary for each station.
- $R_{hypo_{j,k}}$: The hypocentral distance associated with station j and event k.
- ϵ_j: The residual error term for station j, capturing any remaining unexplained variation in kappa at that station.

In MER, parameter estimation is achieved by minimizing the combined variance that includes both the random effects variance (station-specific deviations) and the residual error variance (unexplained variation within stations). This approach optimizes the model to account for differences among stations while also capturing the overall trend across each crustal domain.

Model implementation

While estimating the MER with the python module statsmodels (Seabold and Perktold, 2010), we initially encountered convergence issues that prevented the models from fitting properly. These convergence problems often stem from model complexity or numerical instability in the optimization process. To validate and diagnose the source of these issues, we conducted a preliminary analysis in R (Dorie, 2015), where the model convergence was more effectively diagnosed. This validation helped us pinpoint that the problem was related to numerical instability rather than the model structure itself.

To address the convergence issues, we encountered in Python while fitting MER, we took several steps informed by a preliminary analysis in R, where model convergence diagnostics were more accessible. Here is what we did to enhance model convergence:

- Rescaling kappa:

We rescaled the kappa variable by converting it to milliseconds to improve its compatibility with the optimizer. This scaling adjustment reduces large discrepancies between variable magnitudes, which can lead to issues in optimization and make the model more numerically unstable.

- Flexible optimization options:

In Python, we configured the fitting function to try multiple optimization methods, providing flexibility to avoid the default method's limitations and find an approach better suited to each group of data. Table S6 and Table S7 present the results of the MER applied to all stations across all crustal domains for H and Z components, respectively. The table includes the global intercept, random intercept, and station-specific intercept, along with the global slope, random slope, and station-specific slope. Stations with a negative station-specific slope are flagged as unreliable. Additionally, stations with a negative station-specific intercept should also be considered unreliable. However, with this method, all stations have a positive station-specific intercept. This indicates that, using this method, the majority of the stations yield a reliable estimate of κ_0.

Fixed effects

Table 8 shows the global intercept and global slope (fixed effects), marginal and conditional R^2 values. These results are presented for each crustal domain and component. The marginal R^2 quantifies the proportion of variance explained solely by the fixed effects (i.e., the global intercept and slope), whereas the conditional R^2 represents the proportion of variance explained by the full model, including both fixed effects and random effects associated with station-to-station variability. The difference between conditional and marginal R^2 therefore reflects the contribution of random effects to the overall model performance. R^2 is the classical R_squared value computed from the residuals of the MER, using the fitted values that include both fixed and random effects. It represents the proportion of total variance in κ explained by the full model. The standard deviation of κ_r provides an estimate of the uncertainty associated with the fixed effects slope.

Crustal domain	component	Global Intercept (ms)	Global slope κ_r (ms/km)	Marginal R^2	Conditional R^2	R^2	κ_r std.dev
ABM	H	24	0.17	0.18	0.60	0.41	0.03
ARD	H	23	0.16	0.29	0.55	0.46	0.01
RVG	H	47	0.10	0.09	0.70	0.66	0.02
ABM	Z	18	0.09	0.15	0.24	0.26	0.02
ARD	Z	23	0.10	0.15	0.45	0.43	0.01
HAIN	Z	45	0.03	0	0.04	0.07	0.06
RVG	Z	51	0.10	0.09	0.64	0.59	0.02

Table 8. Result of fixed effect for all crustal domains and components by MER

To analyze the attenuation of seismic waves across the crustal domains of Belgium, we can focus on the global κ_r for each crustal domain for the Z and H components. In this method, similar to JKG approach, we use the global slope (fixed effect) of the kappa values, since they exhibit similar values. Based on Table 8:

- The κ_r ranges from 0.10 to 0.17 for the H component. ABM has the highest and RVG has the lowest κ_r.
- The κ_r ranges from 0.03 to 0.10 for the Z component. ARD and RVG have the highest and HAIN has the lowest κ_r.
- Generally, the horizontal components show consistently higher κ_r than the vertical components (consistent with the result of FKG and JKG).

Figure 55 illustrates the results of MER for each crutsal domain and component. Each color corresponds to a different station. The points represent the predicted values of kappa based on the MER for each record, and the lines connecting these points represent the station-specific slope and intercept for each station. The varying slopes highlight the complexity of the data and the importance of considering station-specific effects in the analysis.

In some crustal domains and components, a limited number of stations exhibit slopes that deviate from the general pattern observed at other stations. For example, in the ABM–H domain, station BE.BOST shows a negative slope. These anomalous stations are clearly visible in Figure 55. Such stations, and those from neighbouring countries due to limited amount of data, are considered problematic and were therefore excluded from the analysis. The resulting κ–distance plots after exclusion are shown in Figure

56, and all subsequent analyses are based on the reduced dataset without these stations.

The MER offers a more nuanced representation of kappa variability by accounting for both regional trends and site-specific deviations. Compared to the FKG, it yields more reliable estimates for stations with limited data by drawing strength from global domain level trends. In contrast to JKG, it allows for more precise modelling by assigning each station its own κ_0 and κ_{r_s}, thereby capturing local variations more effectively. However, the model's performance declines in the HAIN-Z domain, primarily due to limited data availability. In this region, two of the five stations exhibit negative slopes, and the global κ_r (≈0.01) was very low before excluding problematic stations from this domain. Even after removing these stations, the results remain unsatisfactory; the global κ_r (≈0.03) is still low and one of the remaining stations which initially showed a positive slope subsequently exhibits a negative slope (BE.AUL in HAIN-Z in Figure 55). Beyond the issue of sparse data, the HAIN domain is relatively small and has been shown in previous studies to exhibit stronger attenuation than other crustal domains in Belgium (Camelbeeck et al., 2022). Most events recorded by its stations originate outside the domain, with seismic waves passing through one or two other domains before arrival. This inconsistency likely reflects the combined effects of strong attenuation (high κ_0) at short distances within HAIN and much lower attenuation at greater distances. As these signals propagate into HAIN, abrupt changes in attenuation properties may cause significant signal loss, which can result in near-zero or even negative κ_r for this crustal domain.

Random effects

The random intercepts and slopes of different stations in each crustal domain reflect station-specific deviations from the global intercept and slope values of that crustal domain. Stations with positive random slope have higher slope compared to the global values. Stations with negative random slope have lower slope compared to the global values. These random values were then added to the global values to derive the station specific values. Figure 57 shows the random intercept of each station in each crustal domain and component. The dashed red line at zero indicates the baseline.

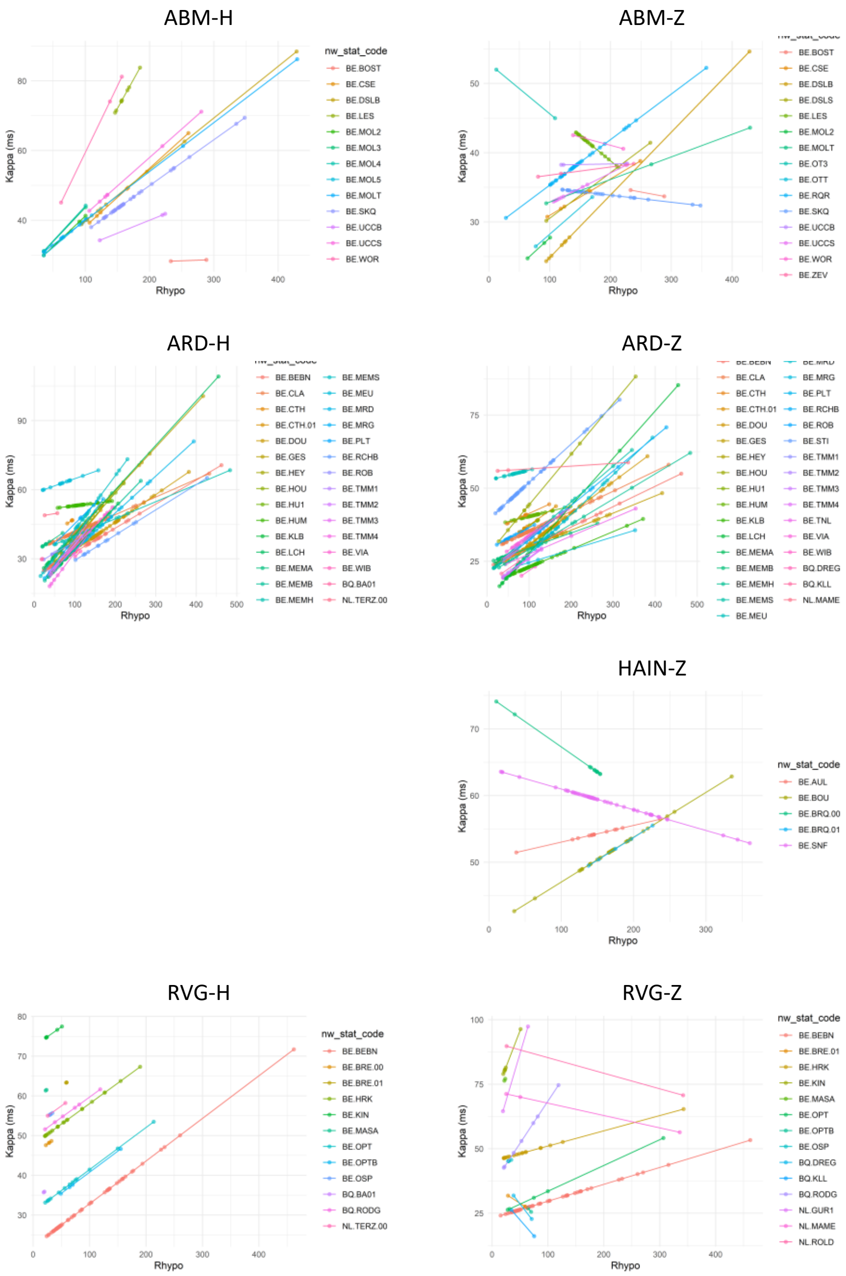

Figure 55. Station-specific slope and intercept (random+fixed) for each station within each crustal domain and component derived with MER before excluding problematic stations which includes stations from neighboring countries and those with negative station-specific slopes

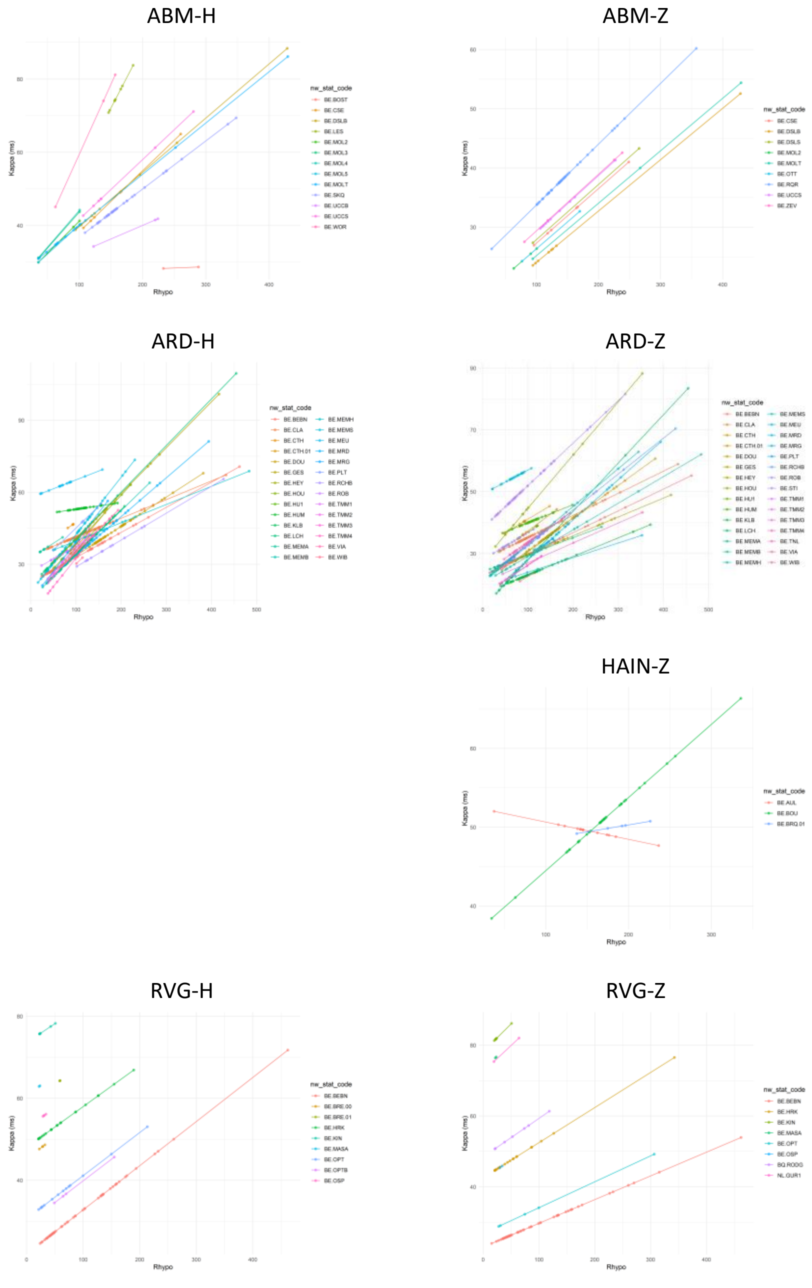

Figure 56. station-specific slopes (κ_{r_s}) and intercepts (κ_0) derived with MER for the H and Z component of stations of all of the crustal domains, after removing problematic stations which includes stations from neighboring countries and those with negative station-specific slopes.

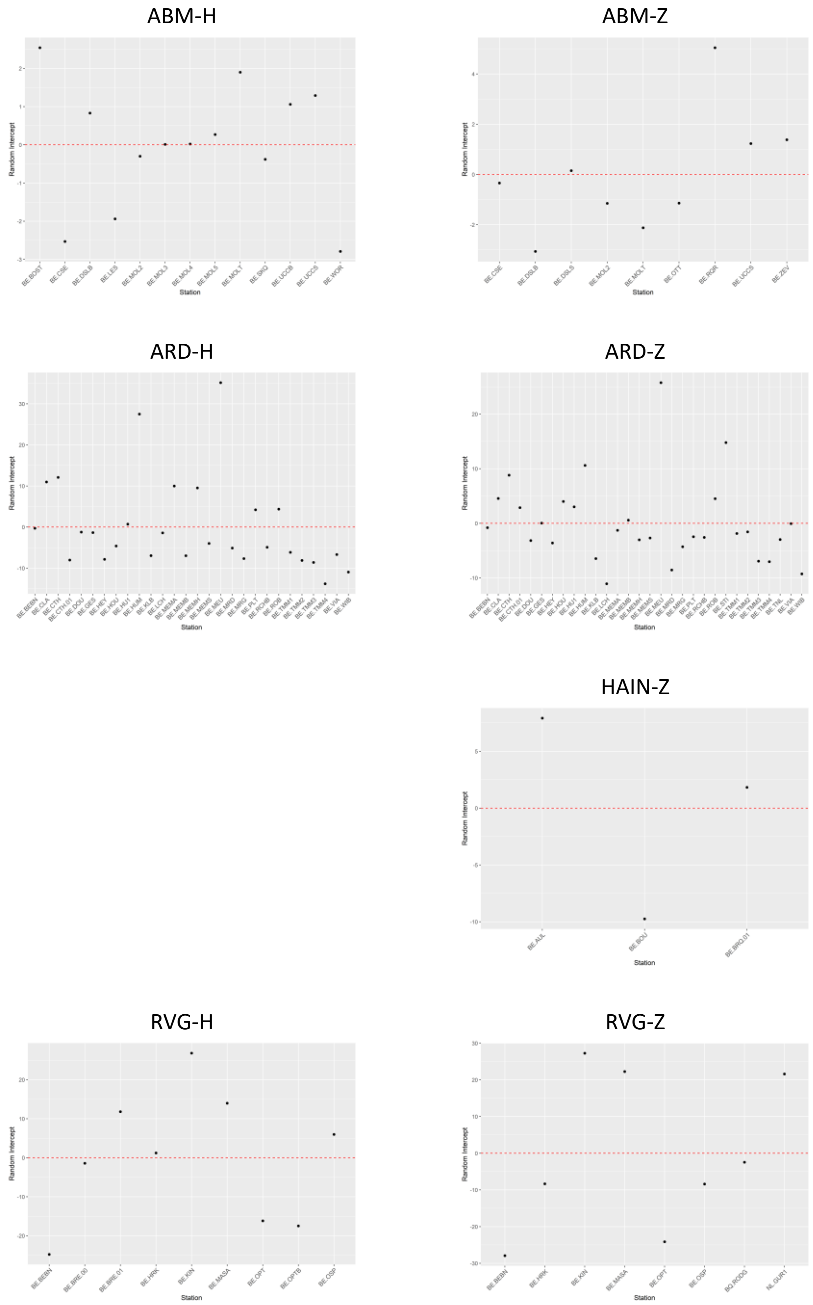

Figure 57. Random intercept for each station within each crustal domain and component derived with MER after excluding problematic stations

Evaluation of fit quality

Observed vs predicted values

The plots below display the relationship between the predicted values generated by the model and the observed values of kappa for each tectonic domain (and component). The blue line represents a linear regression fit, The Pearson correlation factor which quantifies how closely the predicted values align with the observed values of kappa, is shown on the plot. This value reveals a generally strong relationship between the predicted and observed kappa values, suggesting good model performance in most cases. For instance, the RVG_H and RVG_Z domains show very strong correlations (r = 0.81 and r = 0.78 respectively), indicating that the model's predictions closely align with the observed values. Similarly, the ABM_H, ARD_H, and ARD_Z domains also exhibit moderate positive correlations (r = 0.65, r = 0.68 and r = 0.66), suggesting that the model performs reasonably well in these domains. However, the ABM_Z domain has a relatively lower correlation (r = 0.52), suggesting a weaker alignment between predicted and observed values. The HAIN_Z domain, with an even lower correlation (r = 0.28), indicates that the model's predictions do not align well with the observed kappa values probably due to lack of data in this crustal domain.

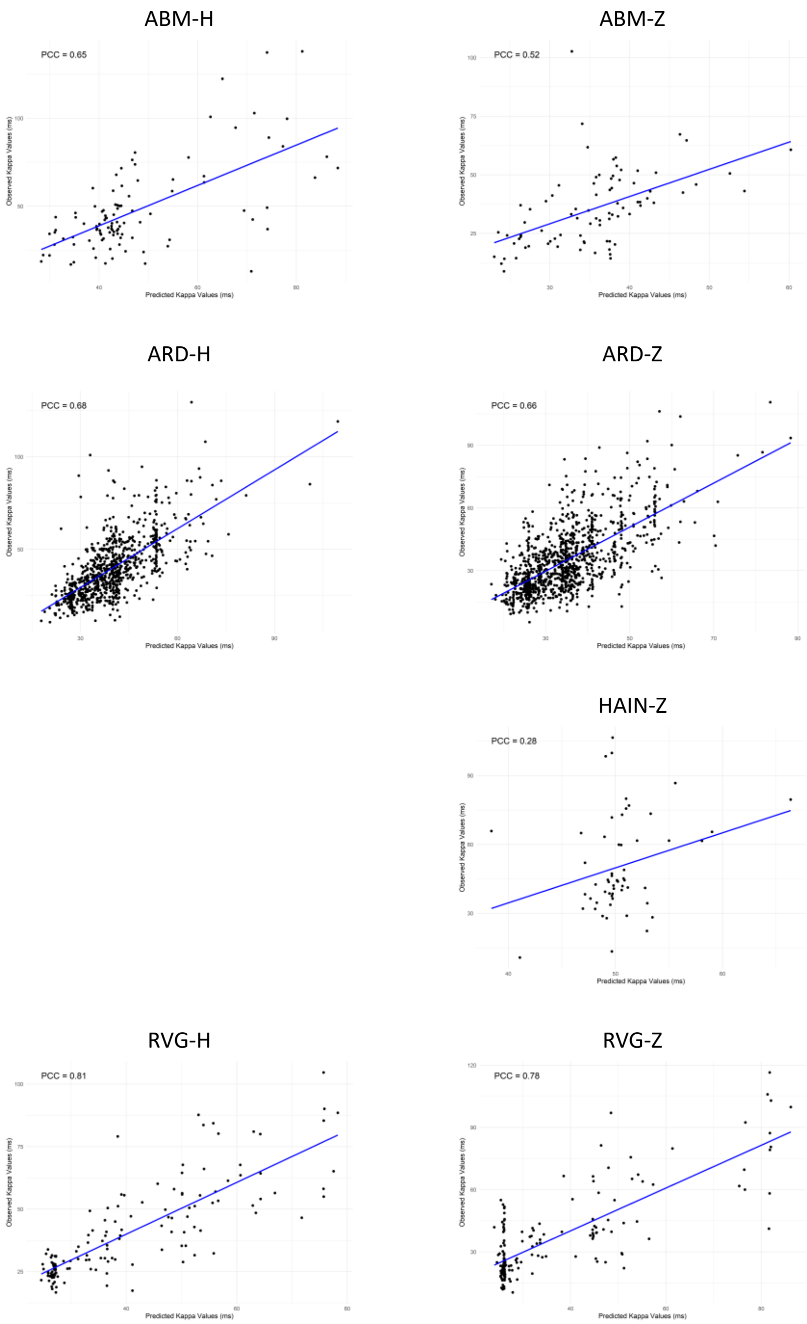

Figure 58. Observed versus predicted kappa values along with Pearson correlation factor (PCC) using MER after excluding problematic stations

Residual versus fitted values

These plots show the residuals (the differences between observed and predicted values) plotted against the fitted values from the MER. This is an additional way to evaluate how well the model predicts kappa. The dashed red horizontal line at zero serves as a reference point, representing the ideal case where the predicted and observed values are equal. Overall, the residuals in all crustal domains are distributed between approximately -50 and 50 ms, with only a few points falling outside this range that can be attributed to previously identified stations with lack of data. The residuals show an almost balanced distribution around the zero residual line, with no systematic shift either upwards or downwards. This suggests that there is no apparent trend indicating that the model consistently overestimates or underestimates the observed kappa values, demonstrating a lack of bias in the model's predictions.

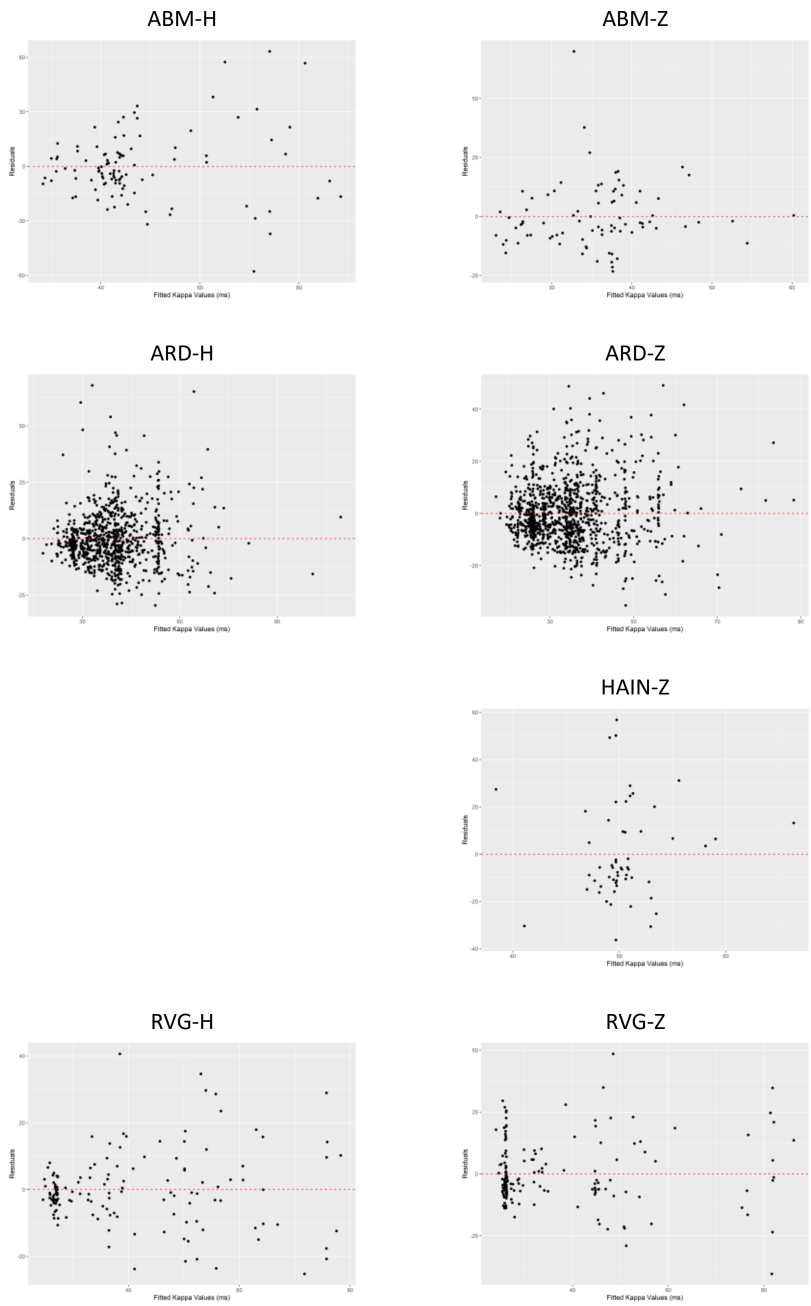

Figure 59. Residual versus fitted values obtained with the Mer for each crustal domain and component after excluding problematic stations

Mixed effects model on pooled data

Given the limited amount of data available for certain crustal domains, such as HAIN, we pooled all recordings across Belgium and applied the MER to the combined dataset. This unified approach allows us to assess the overall attenuation characteristics of the Belgian crust while still accounting for site-specific variability through random station effects. We thus obtained a kappa gradient of 0.16 ms/km for the H component and 0.09 ms/km for the Z component.

component	κ_r (ms/km)	marginal R^2	conditional R^2	R^2	κ_r stddev
H	0.16	0.24	0.58	0.47	0.02
Z	0.09	0.09	0.59	0.45	0.01

Table 9. Estimated κ_r, R^2, and standard deviation values obtained with MER for both H and Z components with pooled data of all crustal domains in Belgium

Table 9 shows that pooling enhances model performance compared to individual domains with limited data, such as HAIN and ABM, at the cost of a small reduction of fit quality compared to well-sampled domains like RVG and ARD. This indicates that results for domains with abundant data are best interpreted from their individual analyses, whereas pooled results offer a more robust representation for domains with sparse observations.

5.3.3.4 Final Results

Table 10 lists κ_r values obtained by the three methods, along with the final adopted κ_r value, R^2 values and standard deviation for different methods and crustal domains.

Crustal domian	Component	FKG method κ_r	FKG method R^2	JKG method κ_r	JKG method R^2	JKG method Std.dev	MER method κ_r	MER method Marginal R^2	MER method Conditional R^2	MER method R^2	MER method κ_r std.de	Final adopted κ_r
ABM	H	0.14	0.59	0.16	0.54	0.40	0.17	0.18	0.60	0.41	0.03	**0.17**
ARD	H	0.16	0.64	0.15	0.62	0.15	0.16	0.29	0.55	0.46	0.01	**0.16**
RVG	H	0.11	0.37	0.15	0.24	0.46	0.10	0.09	0.70	0.66	0.02	**0.13**
ABM	Z	0.07	0.42	0.05	0.24	0.24	0.09	0.15	0.24	0.26	0.02	**0.08**
ARD	Z	0.12	0.51	0.10	0.49	0.09	0.10	0.15	0.45	0.43	0.01	**0.10**
HAIN	Z	0.13	0.56	0.06	0.19	0.4	0.03	0	0.04	0.07	0.06	**0.05**
RVG	Z	0.08	0.23	0.08	0.21	0.2	0.10	0.09	0.64	0.59	0.02	**0.09**

Table 10. Estimated κ_r values, obtained with the three different fitting methods for both H and Z components in all crustal domains of Belgium.

For final κ_r, since the values obtained from the JKR and MER showed minimal variation across different crustal domains, we assigned an average of these values as a final κ_r value to each domain and component. The final adopted κ_r value ranges from 0.13 to 0.17 ms/km for H and from 0.05 to 0.10 ms/km for Z components. The standard deviations of κ_r obtained with the MER are generally small across all crustal domains, indicating stable and reliable estimates. The lowest standard deviations are observed for the ARD and RVG zones (0.006–0.016), while slightly higher values appear for HAIN and ABM (up to 0.056). These results are consistent with the events-stations coverage of the different zones (Figure 50): regions with denser data coverage, such as ARD and RVG, yield smaller standard deviations, reflecting more constrained and consistent estimates of κ_r. In contrast, zones with sparser coverage exhibit slightly larger uncertainties. The reported R^2 values indicate that the H component generally yields higher R^2 than the Z component. The R^2 values from FKG and JKG are very similar to each for both H and Z components, with only small differences (e.g., ABM-H: 0.59 vs. 0.53; ARD-H: 0.64 vs. 0.61; Z components mostly between 0.2–0.5 for both), except for HAIN-Z where the divergence is more noticeable. This indicates that the two approaches explain the variability in the data to a comparable degree. The MER reveals the added value of incorporating station-specific random effects: while marginal R^2 values remain low (≤0.3), indicating that domain-level fixed effects alone explain only a small portion of the variance, the conditional R^2 values increase substantially (0.24–0.77). This clear improvement shows that most of the variance in κ is captured when local, station-specific effects are included.

To better characterize and quantify the station-specific variance and associated standard deviation, we explicitly calculated the random-effects variance following the extended approach proposed by Johnson (2014) which generalizes the widely used framework of Nakagawa and Schielzeth (2013) to models with both random intercepts and random slopes. Rather than approximating random-effects variance from a simplified intercept-only model, we computed it directly by incorporating the full covariance structure of the random effects and averaging over the random-effects design matrix. This approach captures not only the variance of the random intercepts and slopes but also their covariance,

ensuring a more complete representation of between-station variability. Applying this approach to our dataset yielded station standard deviations ranging from 3.89 to 23.21 ms, indicating substantial site-to-site variability in κ across the Belgian crustal domains. The relatively large values reflect the strong influence of local site conditions, and possibly instrumentation differences, all of which cause certain stations to deviate markedly from the global trends. This finding also explains why conditional R^2 values substantially exceed marginal R^2. For instance, in the H component the increase from marginal to conditional R^2 is evident: ABM (0.18 → 0.60), ARD (0.29 → 0.55), and RVG (0.09 → 0.70). For the Z components, the marginal R^2 values are lower than for H components, showing that vertical estimates are considerably more difficult to capture with only global trends. Although accounting for random effects leads to substantial relative improvements in some vertical cases, such as RVG-Z (0.07 → 0.77) and ARD-Z (0.15 → 0.45), the final R^2 values remain low in poorly constrained domains like ABM-Z (0.15 → 0.24) and HAIN-Z (0 → 0.04). This confirms that much of the variance remains unaccounted even after including random effects in these Z components. It can be concluded that the MER can provide meaningful improvements, but it is still not always sufficiently powerful to fully overcome the limitations imposed by very scarce data in some of the crustal domains or components.

Table S8 and Table S9 summarize the estimated site kappa values for the H and Z components, respectively, by the three methods. The final selected site kappa value for each station is listed in the rightmost column of each table, and it was primarily selected based on the MER, which integrates both within- and between-station variability, offering improved statistical robustness when multiple observations were available (i.e., two or more data points per station). In cases where only a single observation was present, estimates derived from JKG were used instead.

5.3.3.5 Comparison of co-located stations

The comparison of κ_0 values for co-located stations in Belgium provides an assessment of how κ_0 estimates vary for different instruments and installation depths at the same site. Among the studied sites, only BE.UCCS/BE.UCCB, BE.OPT/BE.OPTB, and BE.DSLS/BE.DSLB form surface borehole pairs, whereas the other station groups (e.g., BE.MOL4/BE.MOLT, BE.MEMB/BE.MEMH/BE.MEMS) are installed at similar depths but employ different instruments. At MOL, κ_0 values show very good agreement with differences of about 2 ms In contrast, the MEM site exhibits a marked discrepancy, where κ_0 differs by up to 16 ms between MEMB/MEMS and MEMH. This variability is unlikely to result from site structure, since all sensors are co-located, and instead can point to instrumental effects, or it could be due to the relatively large uncertainties; this requires further investigation. BE.MEMB shows the lowest residual standard deviation, suggesting it provides the most internally consistent κ_0 estimate and may therefore be considered the most reliable instrument at this site.

For co-located surface and borehole sensors, borehole sensors should exhibit lower κ_0, because incident waves have to travel through less sediments, which are characterized by stronger attenuation. The extent of this effect depends on borehole depth. At Uccle (site UCC), κ_0 estimates are identical for the surface and borehole instruments. However, the residual standard deviations differ markedly, suggesting that while both instruments yield the same average κ_0 value, the borehole station provides a more stable and reliable fit with less scatter in the residuals, likely due to reduced influence from surface noise and heterogeneity. At the OPT site, the surface station (BE.OPT) shows higher κ_0 values than the borehole station (BE.OPTB). The residual standard deviation is also lower for BE.OPTB compared to BE.OPT, indicating that the borehole installation yields a more stable and less variable

κ_0 estimate, same as Uccle site. A similar pattern is observed at BE.DSLS and BE.DSLB. In our results, κ_0 values are 25 ms at BE.DSLB (a 602 m-deep borehole in Cretaceous bedrock) and 42 ms at BE.DSLS (surface), yielding a difference of 17 ms. This is smaller than the $\kappa_{sediment} = 48\, ms$ estimated by Vanneste et al., (2011) in a PSHA study for a low-category nuclear waste disposal site, where $\kappa_{sediment}$ was determined from the high-frequency slope of the spectral transfer function (for horizontal shear waves) between BE.DSLS and BE.DSLB. While both studies capture the expected increase of κ_0 from bedrock to the surface, our results indicate a smaller cumulative attenuation contribution from the sediment column (17 vs. 48 ms).

station	$\boldsymbol{\kappa_0}$ $(\boldsymbol{ms})$ H component	Residual std dev
BE.MOL4	24	0.5
BE.MOLT	26	9.19
BE.MEMB	16	8.64
BE.MEMH	32	13.32
BE.MEMS	19	13.62
BE.UCCS	25	27.1
BE.UCCB	25	9.82
BE.OPT	31	14.53
BE.OPTB	29	11.01
BE.DSLS	42	-
BE.DSLB	25	22.2

Table 11. κ_0 values of H component of the co-located stations. These values are based on the final selected κ_0 estimates as presented in Table S2 and Table S3 of the electronic supplement

5.3.4 Equivalent apparent (frequency-independent) Q values

κ_r is linked to another attenuation parameter, the effective quality factor of the S-wave (Futterman, 1962; Knopoff, 1964). The relationship between Q and κ has been thoroughly discussed by (Campbell, 2009).

In practice, κ is generally assumed to represent the intrinsic, frequency-independent component of Q. Under this assumption, κ_r can be linked to Q_i through a simple relation (Hough et al., 1988; Ktenidou et al., 2015)

$$Q_i = \frac{1}{V_s\,\kappa_r}$$

where κ_r is the kappa gradient of a crustal domain, and V_s is the average shear-wave velocity of the crust. This formulation enables regional κ_r to be converted into estimates of frequency-independent Q. However, the assumption of frequency-independent κ is debatable, because depending on the heterogeneities, the frequency-dependent scattering cannot be ruled out (Edwards et al., 2015; Ktenidou et al., 2015). Additionally, some studies such as (Mayor et al., 2017) do not treat Q_i as a purely frequency-independent parameter. At higher frequencies (above about 1 Hz), attenuation is known to vary with frequency (Sato et al., 2012), with Q generally increasing as frequency increases. Anderson and Hough (1984) also noted that Q_i may be approximately frequency-independent in the shallow crust (< 5 km), while any frequency-dependent contribution at greater depths would likely have only a minor influence on the overall assumption of frequency independence for the distances considered in their study. In this study, we use the frequency independent assumption to derive Q_i values for Belgian crustal domains and compare them with estimates from neighboring regions, including the southeastern Alps (Gentili and Franceschina, 2011) Provence, France (Perron et al., 2017) and coda-Q tomography in metropolitan France (Mayor et al., 2017).

Higher Q_i corresponds to lower attenuation, while lower Q_i indicates stronger attenuation. For the Belgian crust, we adopt a representative shear-wave velocity of V_s = 3600 m/s which is an average value based on the velocity model of Camelbeeck (1993). This assumption affects the absolute Q values , but does not influence the estimated κ, κ_0, or κ_r values themselves. Applying this relation, κ_r values estimated for each domain were converted into Q_i, and the results are summarized in Table 12. The obtained values range from about 1600 to 2100 (H component) and from 2700 to 5500 (Z component). However, as mentioned earlier, the κ_r estimations for the

HAIN–Z domain are not reliable; therefore, the corresponding Q_i value is excluded from interpretation. Considering this, the Q_i values for the Z component range more realistically from about 2700 to 3900. The Q_i values based on the pooled data lie between the corresponding Q_i ranges for the H and Z components, reflecting the stabilizing effect of pooling across different crustal domains.

Crustal domain	Component code	$\boldsymbol{Q_i}$
ABM	H	1634
ARD	H	1736
RVG	H	2137
ABM	Z	3968
ARD	Z	2778
RVG	Z	3086
Pooled data	H	1736
Pooled data	Z	3086

Table 12. Q value across all crustal domains and components in Belgium

5.4 INTERPRETATION OF RESULTS

5.4.1 Relationship between κ_0 and V_{S30}

The κ_0 estimates for the H component from the three methods were compared with globally expected κ_0 values based on V_{S30} (Van Houtte et al., 2011; Stanko et al., 2017), considering only stations with measured V_{S30} values, sufficient data for reliable estimation, and those located on EC8 soil classes A or B. As illustrated in Figure 60, the expected ranges are represented as two sets of box plots: one set based on the compilation of $\kappa_0 - V_{S30}$ values published for different regions in the world by Stanko et al., (2017) for which we considered for each station, a V_{S30} range of ±100 m/s around the measured value and extracted the corresponding κ_0 values, providing an expected κ_0 range for each station; the other set corresponds to the $\kappa_0 - V_{S30}$ model developed by Van Houtte et al., (2011) using KiK-Net and NGA data.

Figure 60 shows that all three fitting methods generally produce κ_0 estimates within these expected global ranges for stations with low V_{S30} values (associated with soft soil sites). This indicates that all these methods are effective under such conditions; however, it should be noted that the expected global ranges are wider for low V_{S30} sites, making it more likely for estimates to fall within them. The FKG also performs reasonably well but generates an outlier at BE.OPTB and BE.ROB. In contrast, JKG and MER, as well as the final adopted values, are more consistent: they typically fall inside the interquartile boxes or, at worst, along the whiskers, showing that they align well with the spread of global values.

For bedrock sites (V_{S30} > 800 m/s), the results show that κ_0 values remain relatively similar across low (800–1200 m/s), intermediate (1200–1800 m/s), and high (>1800 m/s) V_{S30} values. The obtained values are in line with global values up to about 1500 m/s (except for the two outliers), but not for higher V_{S30} values. Instead, they appear to remain constant, consistent with the observation by Ktenidou et al., (2015) that κ_0 tends to stabilize at high V_{S30}, suggesting the existence of regional hard-rock asymptotic κ_0 values. This would imply that bedrock with high V_{S30} in Belgium does not show the low κ_0 values typical of hard rock in other regions of the world (e.g., $\kappa_0 \approx$ 0.005–0.006 s at CENA sites with $V_{S30} \approx 2000$ m/s, based on Ktenidou et al., (2016). Instead, the attenuation at short travel paths in Belgium may be influenced more by shallow crustal heterogeneity and regional geological context than by the near-surface shear-wave velocity alone.

The MER achieves full station coverage (100%), meaning it estimates the site kappa for all stations with available records, even those with very few recordings. Of these, 80.0% fall within the expected range, with a mean deviation of 8.17 ms. JKG has slightly lower coverage at 90.0%, with 77.8% of values falling within the expected range and a mean deviation of 6.25 ms. In contrast, the FKG also has 90.0% coverage, but only 44.4% of estimates fall within the expected range, with the highest mean deviation of 13.00 ms. In summary, the MER demonstrated the most consistent performance across the full range of V_{S30} values, particularly for sites with V_{S30} between 800 and

1500 m/s. JKG produced the most accurate estimates in terms of average deviation, while the FKG showed significant limitations.

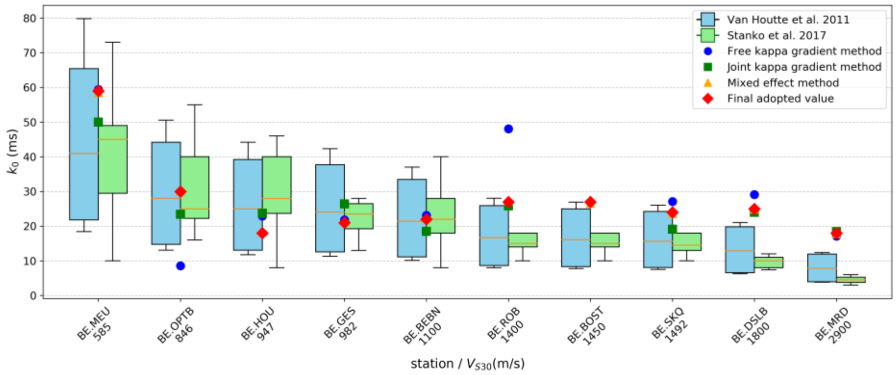

Figure 60. Comparison of κ_0 estimates for stations with measured V_{S30} and sufficient data for reliable estimation. The blue and green boxplots show the ranges reported by Van Houtte et al., (2011) and Stanko et al., (2017), respectively, for each station. The boxes represent the interquartile range (IQR, 25^{th}–75^{th} percentile), and the whiskers indicate the full range of reported values. The orange line shows the median value. The markers indicate method-specific estimates: blue circles for the FKG, green squares for JKG, and orange triangles for the MER. The red diamonds represent the final adopted κ_0 value for each station. Stations are ordered by increasing V_{S30} value.

5.4.2 Comparison with previous studies in Belgium

Previous attenuation studies in different crustal domains in Belgium have highlighted notable regional variations. These studies were mainly based on macroseismic data and are therefore not directly comparable to the present results in terms of resolution and quantity. In the ABM crustal domain, asymmetric attenuation has been reported, with faster N–S decay and slower E–W decay (Neefs et al., 2024; Van Noten et al., 2017). However, travel paths in our study are mostly E-W and do not allow us to corroborate this anisotropy. For the HAIN domain, fast attenuation for shallow events has been observed, which is attributed to low-velocity coal layers and a highly fractured crust (Camelbeeck et al., 2022, 2025). Our findings confirm that κ_0 values at HAIN stations are systematically higher than in other domains. However, these results must be interpreted with caution, as HAIN is poorly covered by the travel paths we used, and few records were available for the vertical component only. The regional kappa gradient could not be determined. Previous studies reported rapid attenuation for low-magnitude events in the RVG, attributed to site effects (Van Noten et al., 2017). In our study, the vertical component in the RVG exhibits the highest κ_r, whereas the horizontal components show the lowest values.

We compared our κ_0 and κ_r values with those from Goraj (2000), who analyzed seismic attenuation in Belgium using permanent and temporary stations from 1985–1992. This earlier work for 65 earthquakes (1056 usable data points), reported κ trends with distance and depth, revealing that κ generally decreased over the first 50 km of distance and increased between 50 and 200 km (Figure 61), as well as regional differences, with higher κ in Hainaut than in the Ardennes, and station-specific anomalies at Membach (MEM). The latter two findings are consistent with our results. The result of regression fit (similar to the FKG in this study) between κ and distance is shown in Table 13. Some of the stations, such as ODL, THN, and BAR, are no longer operational. For the other stations, for H component we compared the parameters a and b, which correspond to κ_r and κ_0 respectively in our results.

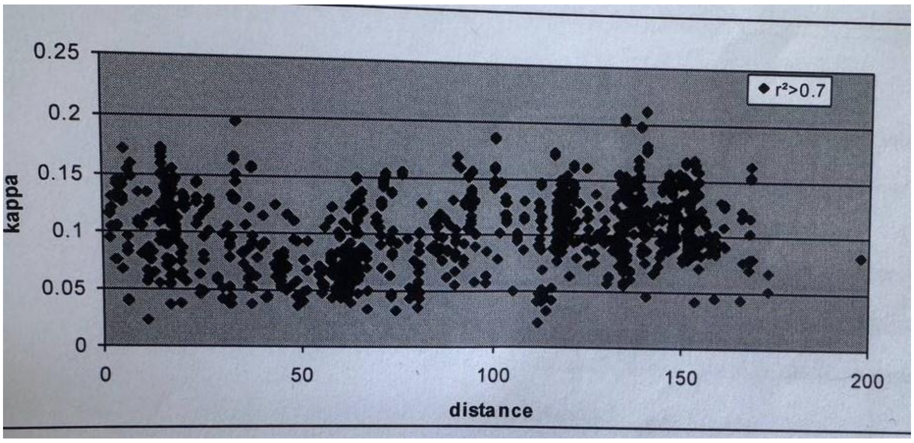

Figure 61. kappa versus distance for all records in the previous study (Goraj 2000), which appears to show a dual behavior of the data

In a more direct comparison, we matched results from individual stations in the earlier study to our estimates from the three fitting methods. κ_0 comparisons (Figure 62, top) show that JKG and MER yield more stable and consistent station estimates than the earlier study, which exhibits greater variability, particularly at BE.LES, BE.KIN, and BE.MEU, similar to the FKG in our study. κ_r comparisons (Figure 62, bottom) show a similar pattern: our JKG and MER approaches produce stable values, while the earlier study includes pronounced outliers (e.g., BE.HUM, BE.VIA) and the FKG shows frequent negative or near zero values, indicating instability (e.g. BE.LES, BE.ROB). These results confirm that robust statistical frameworks (JKG or MER) provide more reliable κ parameter estimation across stations and regions.

Station	a($\boldsymbol{\kappa_r}$) ($\boldsymbol{s/km}$)	b($\boldsymbol{\kappa_0}$) ($\boldsymbol{s}$)	$\boldsymbol{R^2}$
KIN	0.0089	0.0015	0.2316
HUM	0.0009	0.0169	0.215
MEM	0.0002	0.0528	0.1993
LES	0.00008	0.0815	0.0176
SNF	0.00004	0.1385	0.0022
RQR	0.0001	0.1126	0.0275
MEU	-0.0002	0.1209	0.1422
STI	-0.0004	0.1435	0.1459
ODL	0.0412	0.0308	0.2771
THN	0.0038	0.0333	0.2794
ROB	0.0002	0.054	0.0721
WIB	0.0002	0.0213	0.1535
VIA	0.0005	0.0181	0.3569
STP	-0.0213	0.4926	0.7846
WLF	0.0002	0.0762	0.0744
AUL	-0.00006	0.1242	0.0091
BAR	-0.0006	0.1231	0.223
BOU	0.0002	0.0782	0.1636
DOU	-0.00006	0.01215	0.0095

Table 13. Attenuation parameters (a = κ_r, b = κ_0) from an earlier study for 19 seismic stations in Belgium. Note that the MEM station in the previous study corresponds to the current MEMS station in BELSHAKE.

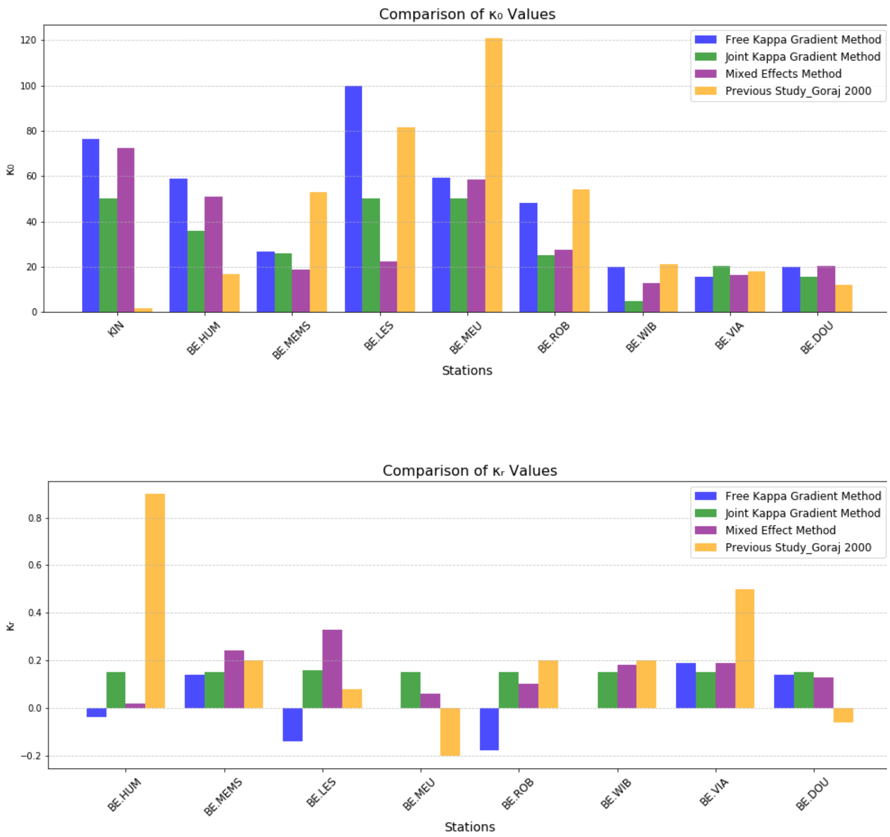

Figure 62. Comparison of κ_0 (top) and κ_r (bottom) values across similar stations between previous study (Goraj 2000) and BELSHAKE

Another study (El Bouch et al., 2002) provided a quantitative assessment of seismic attenuation in Belgium based on vertical-component coda-wave analysis of 86 local earthquakes recorded between 1985 and 1992. They derived frequency-dependent relationships of the form $Q_c = Q_0 f^{\alpha}$ for six crustal regions, with Q_0 ranging from 17 to 31 and α between 1.07 and 1.54 across the 1–32 Hz frequency band. Their result for all stations in eastern Belgium, gives $Q_c(26\,Hz) \approx 1704$, which agrees well with our pooled Q_H value (1736). However, as the study of (El Bouch et al., 2002) is based on vertical component, this value should more appropriately be compared to our vertical Q_V estimate, which is higher, and therefore the agreement with Q_H should be interpreted with caution.

In a probabilistic seismic hazard assessment (PSHA) of the Belgian nuclear power plant sites, Vanneste et al., (2015) conducted a limited study of the κ_0 value for the Cretaceous rocks outcropping at station BE.BEBN for the purpose of host-to-target adjustment of GMMs (Al Atik et al., 2014). They determined κ on the horizontal components for 68 events in a distance range between 4.2 and 227 km using a similar method as used in this study. Based on simple OLS regression between κ and epicentral distance (equivalent to the FKG), they obtained $\kappa_0 = 27 \pm 30\, ms$. The kappa gradient was not reported, however. In our study, the final κ_0 value for the horizontal component of BE.BEBN is 22 ms, in very good agreement with this earlier estimate.

The regional kappa gradient can be compared with the anelastic attenuation considered in the local magnitude scale. The Belgian M_L scale (Camelbeeck, 1985) is based on the attenuation of the vertical displacement amplitude A of the 1 Hz Lg wave, which is modeled (Nuttli, 1973) as a function of epicentral distance R_{epi} (km):

$$A\left(R_{epi}\right) = K R_{epi}{}^{-5/6} exp\left(-\gamma R_{epi}\right)$$

In this equation, K is a constant, while γ represents the anelastic attenuation and is related to the regional kappa gradient:

$$\gamma = \pi f \kappa_r$$

with $f = 1Hz$.

Camelbeeck (1985) determined γ from two datasets of single-station paper records of several earthquakes in central and southern Europe up to ~800 km distance, and obtained a value of $\gamma{\sim}0.0026\, km^{-1}$, which is thus equivalent to $\kappa_r{\sim}0.83\ ms/km$. More recently, Vanneste et al., (2025.b.subm.) recalibrated the Belgian M_L scale based on the BELSHAKE database and using an improved geometrical spreading model. They found significantly lower values: ~0.18 ms/km for the geometric mean of the horizontal components and ~0.10 ms/km for the vertical component. Our results from pooled data for the horizontal component, $\kappa_r = 0.16\, ms/km$ aligns closely with the recent horizontal estimate, confirming moderate regional attenuation. For the vertical components, our value $\kappa_r = 0.09\ ms/km$ is also very close to the recent vertical estimate. Overall, this comparison shows that our results support the updated, lower anelastic attenuation and stronger geometrical spreading attenuation inferred by Vanneste *et al.,* (2025.b.subm).

5.4.3 Comparison with studies in neighbouring regions

In this section, we compare our findings in terms of $\kappa_0$and frequency independent regional quality factor Q_i estimations with those from neighboring regions. While several studies are available for France, comparable analyses are much more limited for other neighboring countries.

Site kappa (κ_0) estimations:
In mainland France**,** Douglas et al., (2010) estimated κ_0 from 263 accelerograms recorded by the French RAP network and found that values in France are intermediate between western North America (≈40 ms on rock) and eastern North America (≈6 ms on rock). Rock sites in the Alps yield κ_0 ≈ 25 ms, while overall values for the French regions range from 20 to 30 ms, somewhat higher than Switzerland (12–15 ms) and lower than central Europe, mainly Germany (≈50 ms). These rock site values compare well with our Belgian station BE.GES (V_{S30}≈982m/s), BE.BEBN (V_{S30}≈1100m/s), BE. ROB (V_{S30}≈1400m/s) and BE.SKQ (V_{S30}≈1492m/s) where we obtained κ_0 = 21, 22, 27, 24 s respectively (based on Figure 60 and Table S2 in the electronic supplement), indicating similar high-frequency attenuation at hard-rock sites. In southeastern France (Provence), Perron et al., (2017) carried out a site-specific study of κ in an area of low-to-moderate seismicity. They showed that site amplification significantly biases κ_0 estimates, even at hard-rock sites, and leads to large discrepancies at stiff-soil sites, where κ_0 values from κ_{AS} method (Anderson and Hough, 1984) and κ_{DS} method based on displacement spectra (Biasi and Smith, 2001) differed by a factor of two. Despite this, both approaches gave consistent results at the two hard-rock sites (V_{S30} ≈ 2000 m/s), with κ_0 ≈ 30 ms (uncorrected for site amplification). This value is at the higher end of $\kappa_0 - V_{S30}$ correlations and is consistent with the relatively strong attenuation previously reported in Provence and the Alps. These results are also consistent with κ_0 values for our hard rock sites where we obtained κ_0 = 25 ms for BE.DSLB (V_{S30}≈ 1800m/s) and κ_0 = 34 ms for BE.CLA (V_{S30}≈ 2900m/s).

Drouet et al., (2010) applied the κ_{TF} method based on Fourier transfer functions and obtained generally smaller values than those from Douglas et al., (2010) and more scattered values, in some cases even negative, depending on site conditions. Another study by Ktenidou et al., (2021) used the same κ_{TF} method for eight stations in France and reported different values. These recent κ_{TF} re-evaluations reduce this variability and yield higher, more stable values. Figure 63 shows the κ_0 –V_{S30} relationship in log scale for several Belgian stations (the same as in Figure 60) and for different French stations with κ_0 values obtained with various methods. Belgian sites cluster in the 20–30 ms range across V_{S30} ≈ 800-2000 m/s, while French datasets diverge more strongly. The Ktenidou et al., (2021) values show good consistency with Belgium in the V_{S30} ≈ 1000–2000 m/s range. The Douglas (2010) values are also close to the Belgian estimates, particularly for V_{S30} between ≈ 800–2000 m/s, although two French κ_0 estimates in this range can be considered outliers. In contrast, the results of Drouet et al., (2010) exhibit a systematic downward shift, with many values below 15 ms, even at V_{S30} ≈ 1000–2000 m/s, where the Douglas and Ktenidou et al., (2021) datasets remain consistent with Belgium. Overall, French κ_0 span ≈ 6-30 ms, with higher values in the Alps and Provence, lower values in the Pyrenees, and systematic offsets between κ_{AS} and κ_{TF} methods.

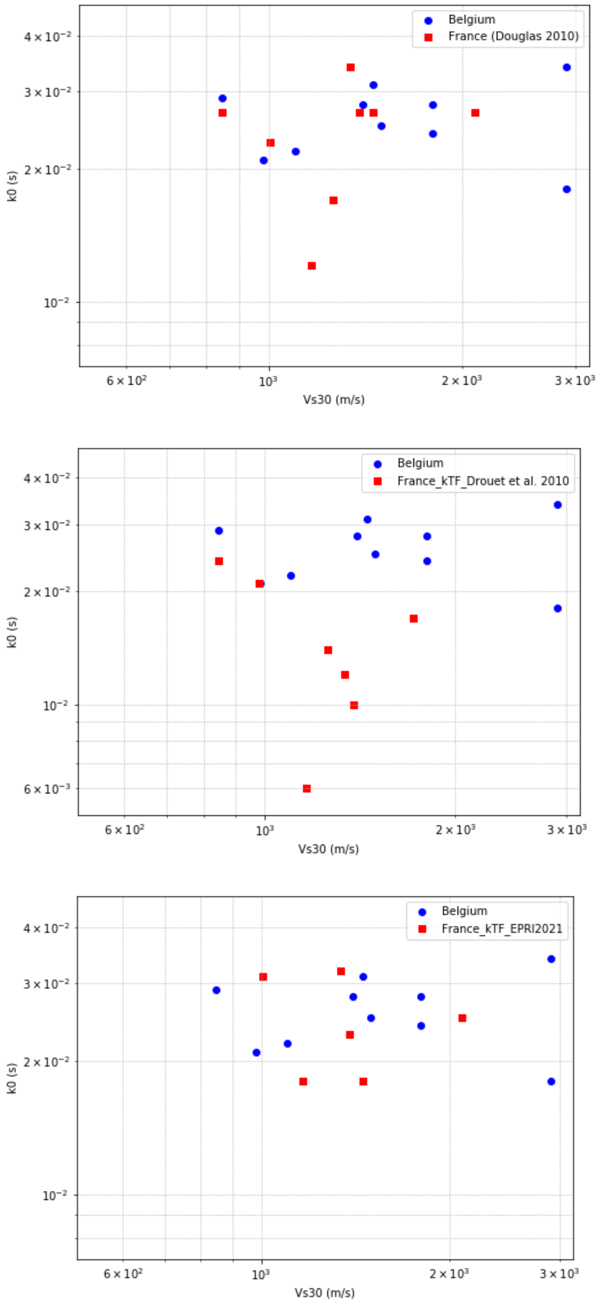

Figure 63.Comparison of V_{S30}–κ_0 relationships between Belgium and different studies in France (from top to bottom: Douglas, 2010; Drouet et al., 2010; Ktenidou et al.(EPRI), 2021).

In northern Italy, Gentili and Franceschina (2011) reported κ_0 values ranging from 17 to 53 ms and a kappa gradient κ_r≈ 0.14 ms/km in the southeastern Alps and northern Dinarides, assuming an average S wave velocity β = 3.34 km/s, corresponding to a frequency-independent quality factor Q_i≈2140. In comparison, our results for Belgium show κ_0 values of H component from 14 to 59 ms. The κ_r in Belgium ranges from 0.13 to 0.17 ms/km, with corresponding frequency-independent quality factors (Q_i) ranging from ~1600 to 2100. These results suggest that the anelastic attenuation characteristics in Belgium are broadly comparable to those in the southeastern Alps and northern Dinarides.

Quality factors (Q):
In the study by Drouet et al., (2010) the attenuation properties of the different French regions were quantified using the frequency-dependent quality factor $Q(f_\mathrm{k}) = Q_0 \cdot f_k^{\alpha}$, where Q_0 represents the quality factor at 1 Hz, and α describes the frequency dependence of attenuation. Based on their inversion results, Q_0 was found to vary across different French regions: 336 ± 15 in the Alps, 1163 ± 247 in the Upper Rhine Graben, and 790 ± 31 in the Pyrenees. These values indicate that attenuation is decreasing from the Alps, the Pyrenees and the Central Massif towards the Rhine Graben. The study by Ktenidou et al., (2021) found very similar values for Q_0 across different French regions: 347 in the Alps, 1374 in the Rhine Graben, and 928 in the Pyrenees.

Table 14 summarizes the Q relationships reported for different regions of France by different studies. Since most of the studies in France have reported frequency-dependent Q models we compared our Q_i estimates for Belgium with the frequency-dependent Q models developed for different regions of France, over the same frequency range used in our analysis. The median minimum and maximum frequencies we considered for computing κ are 9 Hz and 27 Hz, respectively, based on all available records of H component. Using this frequency range, the corresponding Q ranges were calculated for all regional attenuation functions listed in Table 14. The average Q for the pooled H component (1736) lies above the upper limit of the Pyrenees range and lower than the range estimated for the Upper Rhine Graben, indicating that the Belgian crust exhibits lower attenuation on the H component than the Alps and Pyrenees but stronger attenuation than the Upper Rhine Graben, placing Belgium in an intermediate position relative to these French regions.

Study\Region	Alps	Pyrenees	Upper Rhine Graben	Armorican, Central Massif	Aquitaine, Brabant, Southeast
Ktenidou et al., (2021)	$347f^{0.31}$	$928f^{0.15}$	$1374f^{0.17}$		
	686-964	1290-1521	1996-2406		
Calvet and Margerin (2013)	-	$400\ f^{0.4}$	-	-	-
		963-1495			
Drouet et al., (2010)	$336f^{0.32}$	$790f^{0.15}$	$1163f^{0.19}$	-	-
	679-965	1098-1295	1766-2175		
Campillo and Plantet (1991)			$320\ f^{0.5*}$		
			960-1663		

*Table 14. Summary of frequency-dependent and intrinsic quality factor relations, reported for various tectonic regions of France. For each Q relation, the minimum and maximum Q values were calculated using $f_{min} = 9\ Hz$ and $f_{max} = 27$ Hz, corresponding to the median frequencies of the range employed to estimate kappa for horizontal components in BELSHAKE.*Includes intrinsic + scattering effects.*

In another study, Mayor et al., (2017) estimated Q_i in and around France (including Belgium) from coda waves on the vertical component in five frequency bands (1–2, 2–4, 4–8, 8–16, and 16–32 Hz), presenting maps of normalized values Q_i/Q_m, where Q_m is the spatial average of Q_i for each band. Q_i exhibits strong lateral variations, of the order of ±50% around Q_m, with low Q_i in sedimentary basins and higher Q_i in crystalline massifs. The average Q_m values increase with frequency, from about 190 at 1– Hz 2, 400 at 2–4 Hz, 720 at 4–8 Hz, 1,220 at 8–16 Hz, up to 2,250 at 16–32 Hz, with the high-frequency range (16–32 Hz) being most comparable to our study. Since Mayor et al., (2017) used the vertical component, the appropriate comparison is with our pooled vertical attenuation. Based on their maps, Belgium exhibits higher vertical-component Q_i than the Alps, Pyrenees, and Upper Rhine Graben, with values comparable to those of central western France, and the very high vertical-component Q_c reported for Belgium (exceeding 2600) aligns well with our pooled vertical attenuation value $Q_Z = 3086$.

In Germany envelope-inversion studies at the KTB deep-drilling site (Fielitz and Wegler, 2015) indicate that intrinsic absorption dominates over scattering in the 6–72 Hz range, with Q_i increasing from roughly 400 to 3000 across the band. At representative frequencies $f = 10\ Hz$ and $f = 32Hz$, the Q_i values are approximately 800 and 1900, respectively. For BELSHAKE Q_i in the 10–32 Hz band ranges from 1600 to 2100, indicating substantially stronger attenuation beneath the KTB site at low frequencies. At 32 Hz, Q_i remains lower at KTB, but the difference and thus the contrast in attenuation is markedly smaller at the higher frequency.

5.5 Conclusions

This chapter presented a comprehensive evaluation of kappa, the high-frequency anelastic attenuation parameter, in Belgium, based on the BELSHAKE database.

Kappa (κ) values were computed from S-wave acceleration Fourier amplitude spectra for both horizontal and vertical components, following the classic Anderson and Hough (1984) definition. The derived κ values were first compared with independently obtained estimates of the equivalent t^* attenuation parameter, showing strong correlations and confirming the consistency of the measurements.

These κ values were then decomposed into site-specific components (κ_0) and regional kappa gradients (κ_r) across four distinct crustal domains, allowing for a detailed characterization of both local and regional attenuation behavior. Three fitting methods were tested; FKG, JKG, and MER. While the FKG is simple and computationally efficient, it is highly sensitive to data availability and cannot always provide accurate estimates. JKG offers a more sophisticated approach but can suffer from optimization range issues that limit its effectiveness. The MER, by contrast, is better equipped to handle the complexities of crustal domain data, making it the most dependable option for estimating κ_r of each crustal domain and κ_0 for each station.

Final values of station-specific κ_0 are derived from the MER and range from ~14 to 59 ms for horizontal components and from ~12 to 53 ms for vertical components. The regional kappa gradient, κ_r was derived by averaging the results of JKG and MER, ranges from 0.13 to 0.17 ms/km for the horizontal component and from 0.05 to 0.1 ms/km for the vertical component in different crustal domains. Considering S-wave velocities of 3.6 km/s for all crustal domains, the frequency-independent quality factor (Q_i) ranges from ~1600 to 2100 for the horizontal and from ~2700 to 3900 for the vertical components. Overall, the results are more robust for the horizontal components than for the vertical components. These parameters have been integrated into the BELSHAKE database and will support improved ground-motion modeling and probabilistic seismic hazard assessment in Belgium, enabling more accurate host-to-target adjustments for GMMs and better accounting for regional and site-specific attenuation effects.

Comparison with earlier Belgian studies revealed consistency in regional trends and station anomalies, while also demonstrating the advantages of modern statistical approaches in reducing outliers and stabilizing estimates. κ_0-V_{S30} comparisons with global trends indicated that κ_0 values are quite similar for all bedrock sites, both with low (800-1200 m/s), intermediate (1200-1800 m/s) and high (> 1800 m/s) V_{S30} values. This would imply that bedrock with high V_{S30} in Belgium does not show the low κ_0 values typical of hard rock in other regions of the world, Instead, the observed κ_0 values reflect the heterogeneity of the Belgian crust, supporting the asymptotic κ_0 conceptual model proposed by Ktenidou et al., (2015).

Using pooled data across Belgian crustal domains, the horizontal component shows κ_r ≈ 0.09 ms/km and Q_H ≈ 1736, while the vertical component shows κ_r ≈ 0.16 ms/km and Q_Z ≈ 3086. These values also align with attenuation parameters fitted from the Belgian local magnitude scale, confirming their physical relevance. Although our Q_i estimates for Belgium are frequency-independent, when compared over the same frequency range that we used to compute κ_r with the frequency-dependent Q models for France, our pooled horizontal Q_H (1736) lies above the Pyrenees range and within the Upper Rhine Graben range, indicating that the Belgian crust occupies an intermediate position between these two French regions. For the vertical component, studies by Mayor et al., (2017) consistently identify Belgium as a high Q region, with Q_i exceeding 2600, in agreement with our pooled vertical estimate of Q_Z (3086).

Overall, while this study provides a robust framework for quantifying κ and its decomposition into κ_0 and κ_r across Belgium, certain limitations must be acknowledged. The relatively modest R^2 values highlight that the κ-distance relationship cannot be fully captured by a linear gradient, suggesting that additional factors such as complex scattering and frequency dependence of kappa may play an important role. Moreover, the estimated κ_r values are likely most reliable for the ARD domain, which is best covered, whereas coverage in other crustal domains, in particular HAIN, remains partial and requires further data to ensure representativeness. Future work should therefore focus on refining site-specific κ_0 estimates using alternative approaches, such as ambient noise analysis, as shown by e.g. Moratto et al., (2025), and on exploring frequency-dependent quality factors through generalized inversion methods e.g. Oth et al., (2008), which would enable a more comprehensive description of anelastic attenuation.

6 Evaluation of candidate ground motion models (GMM) for Belgium

The objective of this chapter is (1) to select a list of candidate ground-motion prediction equations (GMMs) from the large volume of published GMMS that could be suitable for application in Belgium, and (2) to evaluate the goodness of fit these GMMs against the BELSHAKE database, using a series of statistical tests. The statistical evaluation aims to determine which of these models best capture the ground-motion characteristics observed in Belgium, thereby supporting improved seismic hazard assessments. The outcome includes both a list of tested candidate GMMs and the identification of those that best fit the Belgian ground-motion data.

Since the BELSHAKE database primarily contains recordings from small-to-moderate magnitude events, the goodness of fit evaluation is performed over this available magnitude range. This range overlaps only with the lower bound of applicability of many published GMMs, as these models are generally developed and validated using datasets dominated by moderate-to-large earthquakes. As a result, the evaluation focuses on assessing model performance within the magnitude range that can be tested empirically. While GMMs that perform well at lower magnitudes may also be considered suitable candidates for extrapolation to higher magnitudes, it should be noted that model rankings can be sensitive to the magnitude range used for testing. In particular, (Beauval et al., 2012) showed that GMM rankings may change when models are evaluated separately against low- and high-magnitude datasets. This limitation is therefore kept in mind when interpreting the results and drawing conclusions from the BELSHAKE-based evaluation.

In probabilistic seismic hazard analysis (PSHA), GMMs play a central role in estimating the conditional probability that ground motions will exceed a given acceleration threshold, given an earthquake in a specified location. Although many GMMs are developed using data from moderate-to-large earthquakes ($M_w \geq 5$), several more recent models now support lower magnitude ranges down to M_w 3.0 or even lower. This is particularly important because of the limited magnitude range of the Belshake dataset, and also because low-magnitude events ($M_w < 5$) can still contribute significantly to hazard estimates in low-seismicity regions, even for long return periods (Beauval et al., 2006, 2008). This makes reliable ground-motion prediction across the full magnitude range including lower magnitudes essential for robust PSHA in regions like Belgium.

However, GMMs developed in high seismicity regions using large magnitude data may not accurately capture ground motion behavior for small events in low seismicity areas. Several studies have shown that these models can overestimate ground motions for lower magnitudes due to nonlinear magnitude scaling issues (Bommer et al., 2010). Additionally, regional differences in ground motion characteristics, especially for smaller earthquakes have been reported in various parts of the world. For instance, Chiou et al., (2010) and Atkinson and Morrison (2009) found that the ground motions of smaller earthquakes may be more sensitive to the regional differences and crustal stress states. Two key factors help explain this observation:

- Stress drop variability and possible magnitude dependence for small earthquakes: Observed regional differences in short-period ground-motion amplitudes may reflect differences in average stress drop between regions. These differences have been interpreted to decrease with increasing magnitude, suggesting possible magnitude dependence of stress drop in at least some regions, although this remains subject to debate (Chiou et al., 2010).
- Depth-related variability of stress drop: Some studies indicate that earthquake stress drop may increase with depth. However, due to large uncertainties in $\Delta\sigma$ estimates and limited constraints on absolute stress, this relationship is not universally established and remains dependent on regional conditions (Bocchini et al., 2025).

In the United Kingdom, for example, limited strong-motion data and local magnitude scaling uncertainties have required the development of tailored GMMs and the use of multiple models in logic-tree approaches to account for epistemic uncertainty (Musson, 2012). Similar strategies could be valuable in Belgium, where strong-motion recordings from moderate events remain sparse, and epistemic uncertainty is also significant. Moreover, it has been shown that the use of models with similar ground-motion predictions can lead to an underestimation of total uncertainty, emphasizing the importance of model diversity in hazard calculations (Bommer et al., 2015).

In Belgium, such regional variability is particularly important. Previous studies have shown that in certain areas, such as the Hainaut coal basin, intensity data attenuate much more rapidly with distance compared to surrounding regions. Camelbeeck et al., (2022) also noted that uniform GMMs are typically applied across all zones in hazard models may lead to overestimation of contribution of Hainaut seismicity. This highlights the importance of evaluating and selecting GMMs that are locally appropriate in terms of regional attenuation behavior.

6.1 GMM selection

For the BELSHAKE dataset, nearly 20 GMMs are evaluated (see Table 15), including all updated models employed in site-specific PSHA studies in Belgium during the past decade (Vanneste and Camelbeeck, 2022), as well as models applied in recent national hazard studies in France (Drouet et al., 2020), Germany (Grünthal et al., 2018), and the UK (Villani et al., 2019; Mosca et al., 2022). In addition, several other GMMs of particular interest are included.

The selected models can be grouped into several "families" based on their underlying ground-motion datasets: European (n=4), NGA-West (n=6), NGA-East (n=4), Global (n=1), Japanese (n=2), local/regional models (n=4), and induced models(n=5). Special attention is given to the Douglas et al., (2013) GMM developed for geothermally induced seismicity, which includes 36 different ground-motion relation variants based on different combinations of stress drop, attenuation quality factor Q, and high-frequency kappa attenuation.

	Belgium (Vanneste et al., 2014)	**UK (Mosca et al., 2022 ; Villani et al., 2019)**	**Germany (Grünthal et al., 2018)**	**France (Drouet et al., 2020)**	**Other**
Europe	Akkar et al., (2014) Bindi et al., (2014)	Akkar et al., (2014) Bindi et al., (2014)	Akkar et al., (2014) Bindi et al., (2014) Derras et al., (2014)		Kotha et al., (2020)
NGA-West	Boore & Atkinson (2008)	Boore et al., (2014) Chiou & Youngs (2014) Campbell & Bozorgnia (2014)		Abrahamson et al., (2014)	
NGA-East	Atkinson & Boore (2006) Campbell (2003, SHARE)* Toro (2002, SHARE) *	Atkinson & Boore (2006)			Yenier & Atkinson (2015)
Japan (crustal)	Zhao et al., (2006) *				
Global	Cauzzi et al., (2015)	Cauzzi et al., (2015)	Cauzzi et al., (2015)	Cauzzi et al., (2015)	
Local	Rietbrock et al., (2013)	Rietbrock et al., (2013) Rietbrock & Edwards (2019)		Drouet & Cotton (2015)	
Induced seismicity					Atkinson (2015) Douglas et al., (2013)

*Table 15. Overview of selected GMMs, based on recent GMM studies in Belgium (Vanneste et al., 2022) and neighboring countries, and organized in GMM "families" (depending on regional database). Legend: *Not defined for PGV*

For PGA, PGV and SA, various implementations of each GMM were assessed, accounting for differences in distance metrics, stress drop assumptions, faulting styles, and type of horizontal component. The best performing implementation for each GMM was selected for further comparison. Table 16 shows the selected GMMs for PGA, PGV, and SA, identified using the BELSHAKE database and grouped according to their respective model families.

	PGA	**PGV**	**SA**
Europe	AkkarEtAlRjb2014Armenia, BindiEtAl2014Rhyp, DerrasEtAl2014, KothaEtAl2020, KothaEtAl2020ESHM20	AkkarEtAlRjb2014, BindiEtAl2014RjbEC8, DerrasEtAl2014, KothaEtAl2020, KothaEtAl2020ESHM20	AkkarEtAlRjb2014, BindiEtAl2014RhypEC8NoSOF, DerrasEtAl2014, KothaEtAl2020, KothaEtAl2020ESHM20
NGA-West	AbrahamsonEtAl2014RegCHN, ChiouYoungs2014, CampbellBozorgnia2014HighQJapanSite, BooreEtAl2014HighQ, BooreAtkinson2008Prime, BindiEtAl2017Rhypo	AbrahamsonEtAl2014RegCHN, ChiouYoungs2014, CampbellBozorgnia2014HighQJapanSite, BooreEtAl2014HighQ, BooreAtkinson2008Prime	AbrahamsonEtAl2014RegCHN, ChiouYoungs2014PEER, CampbellBozorgnia2014HighQJapanSite, BooreEtAl2014HighQNoSOF, BooreAtkinson2008Prime, BindiEtAl2017Rhypo
NGA-East	YenierAtkinson2015BSSA, AtkinsonBoore2006Modified2011, Campbell2003SHARE, ToroEtAl2002SHARE	YenierAtkinson2015BSSA, AtkinsonBoore2006SGS	YenierAtkinson2015BSSA, AtkinsonBoore2006SGS, Campbell2003SHARE, ToroEtAl2002SHARE
Global & Japan	CauzziEtAl2014Eurocode8NoSOF, ZhaoEtAl2006SInterCascadia	CauzziEtAl2014FixedVs30NoSOF	CauzziEtAl2014RhypoGermany, ZhaoEtAl2006SInterCascadia
Local	RietbrockEdwards2019Mean, RietbrockEtAl2013SelfSimilar, DrouetAlpes2015RjbHR_50bars	RietbrockEdwards2019Low, RietbrockEtAl2013SelfSimilar, DrouetBrazil2015withDepth	RietbrockEtAl2013SelfSimilar, DrouetAlpes2015Rjb_50bars
Induced	Atkinson2015, DouglasEtAl2013StochasticSD100Q1800K040	Atkinson2015, DouglasEtAl2013StochasticSD100Q1800K040	Atkinson2015, DouglasEtAl2013StochasticSD010Q1800K020

Table 16. Selected GMM variants for PGA, PGV and SA based on the BELSHAKE database

6.2 Overview of some of the selected GMMs

This subsection presents a detailed summary of the key characteristics for the subset of selected GMMs identified as the best-performing models for different intensity measures. The summary includes their development datasets, magnitude and distance applicability ranges, tectonic region types, intensity measures supported, and any region-specific modifications. This technical overview aims to improve transparency in GMM selection and highlight their relevance to the seismic context of Belgium and neighboring regions.

6.2.1 AkkarEtAl2014

Akkar et al., (2014) developed a ground-motion prediction equation for active shallow crustal regions, using strong-motion recordings from seismically active areas bordering the Mediterranean Sea and extending into the Middle East. The model is based on a subset of the RESORCE-2012 database, including only records from stations with measured V_{S30}, thereby improving the reliability of site characterization.

Akkar et al., (2014) provide several GMM variants based on different distance metrics, including pan-European formulations using Joyner Boore distance (AkkarEtAlRjb2014), hypocentral distance (AkkarEtAlRhypo2014), and epicentral distance (AkkarEtAlRepi2014), as well as a region-specific Armenia variant of the R_{jb} model (AkkarEtAlRjb2014Armenia). In this study, AkkarEtAlRjb2014Armenia is selected for PGA, and AkkarEtAlRjb2014 is selected for PGV and SA.

The GMM predicts PGA, PGV, and 5% damped SA over the period range 0.01–4 s, using the average horizontal component. Aleatory variability is described through total, inter-event, and intra-event standard deviations.

The applicability range of the model covers magnitudes M_w 4.0–7.6 and Joyner Boore distances (R_{jb}) between 0 and 200 km, for shallow crustal earthquakes with focal depths ≤ 30 km. The model is applicable to sites with V_{S30} values between 150 and 1,200 m/s, and style-of-faulting effects are well constrained for normal, strike-slip, and reverse ruptures. Although it is acknowledged that there is a possibility of over-estimating motions at the lower limit, there is some uncertainty at the upper end, which is poorly constrained by the data (which only extends to M_w 7.6). Akkar et al., (2014) emphasize that the original motivation was not to provide models that can be used with confidence at M_w 4, but rather to remove the bias in the models at the commonly used lower limit of M_w 5 in PSHA, following the recommendation by Bommer et al., (2007) to include data to one magnitude unit lower than the minimum threshold in PSHA integrations. However, it is concluded that the new models can be used for magnitudes as small as M_w 4.0.

6.2.2 BindiEtAl2014

The Bindi et al., (2014) ground-motion prediction equation was developed for active shallow crustal regions, with particular focus on Europe and the Middle East. The model supports PGA, PGV, and 5% damped SA over 23 spectral periods ranging from 0.02 to 3.0 s. Ground motions are defined in terms of the geometric mean of the as-recorded horizontal components, and the model provides estimates of total, inter-event, and intra-event standard deviations.

Several model variants are provided by Bindi et al., (2014), reflecting different choices of distance metric and site characterization. These include a formulation based on R_{jb} (BindiEtAl2014Rjb), a formulation using hypocentral distance (BindiEtAl2014Rhyp), a hypocentral-distance formulation incorporating Eurocode 8 site classification (BindiEtAl2014RhypEC8), and a variant using EC8 site classes without explicit consideration of style-of-faulting effects (BindiEtAl2014RhypEC8NoSOF). For the BELSHAKE dataset, the BindiEtAl2014Rhyp variant is selected for PGA, the BindiEtAl2014RjbEC8 variant for PGV, and the BindiEtAl2014RhypEC8NoSOF variant for SA.

The applicability range of the model covers moment magnitudes M_w between 4.0 and 7.6 and source-to-site distances up to 300 km, expressed either as R_{jb} or R_{hypo}. The equations are intended for shallow crustal earthquakes with hypocentral depths not exceeding 35 km. Site conditions are described using the Eurocode 8 (EC8) soil classification, including four site classes from A to D, and the style of faulting is represented using four categories: normal, reverse, strike-slip, and unspecified.

The GMM is based on the RESORCE-2011 database, which contains strong-motion recordings from Europe, the Middle East, and the Mediterranean region. The full dataset used in the development consists of 2,126 recordings at a spectral period of 0.1 s, associated with 365 earthquakes recorded by 697 stations. In addition, a subset of the data including only stations with measured V_{S30} values and earthquakes with specified focal mechanisms was used to evaluate the accuracy of the median predictions and the variability of the model. This subset comprises 1,224 recordings from 345 stations and 255 earthquakes.

6.2.3 AbrahamsonEtAl2014

Abrahamson et al., (2014) ground-motion prediction equation was developed for active shallow crustal regions. The model supports PGA, PGV, and 5% damped SA over a broad period range from 0 to 10 s. Ground motions are defined using the orientation-independent average horizontal component RotD50. The model provides total, inter-event, and intra-event standard deviations, with variability that is explicitly dependent on magnitude.

Several model variants of Abrahamson et al., (2014) are available, accounting for regional differences in attenuation and site response. These include the standard NGA-West2 formulation (AbrahamsonEtAl2014), as well as regionally adjusted variants for China (AbrahamsonEtAl2014RegCHN), Japan (AbrahamsonEtAl2014RegJPN), Italy (AbrahamsonEtAl2014RegITA), and Taiwan (AbrahamsonEtAl2014RegTWN). For the BELSHAKE dataset, the AbrahamsonEtAl2014RegCHN variant is selected for PGA, PGV, and SA.

The applicability range of the model spans moment magnitudes M_w from 3.0 to 8.5 and rupture distances (R_{rup}) from 0 to 300 km. Site effects are parameterized using V_{S30}, and the model is applicable for sites with V_{S30} values greater than or equal to 180 m/s, although it is noted that the model is not well constrained for very stiff sites with V_{S30} values exceeding 1,000 m/s.

The model was developed using the NGA-West database, which includes earthquakes with moment magnitudes ranging from 3.0 to 7.9. Although the largest magnitude represented in the dataset is M_w 7.9, the authors indicate that the model can be reasonably extrapolated to magnitudes up to M_w 8.5.

6.2.4 ChiouYoungs2014

The Chiou and Youngs (2014) ground-motion prediction equation was developed for active shallow crustal regions. The model supports PGA, PGV, and PSA over the period range 0.3–1 s. Ground motions are defined using the orientation-independent average horizontal component RotD50. The model provides total, inter-event, and intra-event standard deviations.

Several model variants of Chiou and Youngs (2014) are available, reflecting regional adjustments or specific modelling options. These include the standard NGA-West2 formulation (ChiouYoungs2014), regional variants for Japan (ChiouYoungs2014Japan), Italy (ChiouYoungs2014Italy), and the Wenchuan earthquake region (ChiouYoungs2014Wenchuan), as well as a variant including explicit near-fault effects (ChiouYoungs2014NearFaultEffect). In addition, the ChiouYoungs2014PEER variant represents a PEER NGA-West2 implementation with minor implementation-level differences. For the BELSHAKE dataset, the ChiouYoungs2014 formulation is selected for PGA and PGV, while ChiouYoungs2014PEER is selected for SA.

The applicability range of the model depends on faulting style. For strike-slip earthquakes, the model is applicable over the magnitude range 3.5 ≤ M_w ≤ 8.5, while for reverse and normal faulting earthquakes the applicable range is 3.5 ≤ M_w ≤ 8.0. The lower bound of M_w 3.5 reflects the inclusion of a large number of small earthquakes in this update. However, because all earthquakes with M_w < 6 used in the model development originate from California, caution is advised when applying the model to M_w < 6 earthquakes in other active tectonic regions. The model is applicable for R_{rup} between 0 and 300 km and for depths to the top of the ruptured plane of 20 km or less. Site conditions are represented by V_{S30} values ranging from 180 to 1,500 m/s (Chiou and Youngs, 2014).

6.2.5 CampbellBozorgnia2014

The Campbell and Bozorgnia, (2014) ground-motion prediction equation is part of the NGA-West2 project and was developed for active shallow crustal tectonic regions. The model supports PGA, PGV, and 5%-damped linear PSA over a wide period range from 0.01 to 10s, and predicts the RotD50 horizontal component.

Several model variants of Campbell and Bozorgnia, (2014) are available, reflecting different assumptions regarding crustal attenuation, site response, and regional behavior. These include the standard NGA-West2 formulation (CampbellBozorgnia2014), a variant adjusted for high-Q crustal regions (CampbellBozorgnia2014HighQ), a variant incorporating Japan-specific attenuation and shallow site response effects (CampbellBozorgnia2014HighQJapanSite), and variants that exclude explicit style-of-faulting terms (CampbellBozorgnia2014NoSOF). For the BELSHAKE dataset, the CampbellBozorgnia2014HighQJapanSite variant is selected for PGA, PGV, and SA.

Aleatory variability is described through total, inter-event, and intra-event standard deviations, with magnitude-dependent behavior. The model is applicable to magnitudes M_w ≥ 3.3 for California earthquakes and M_w ≥ 5.5 globally, with maximum magnitudes depending on faulting style (up to M_w 8.5 for strike-slip, M_w 8.0 for reverse, and M_w 7.5 for normal faults). Distance applicability extends to R_{rup} of 0–300 km, and site conditions are parameterized using V_{S30} values between 150 and 1500 m/s. Additional parameters include sediment depth (0–10 km), depth to the top of rupture (0–20 km), hypocentral depth (0–20 km), and fault dip angles between 15° and 90°. The model was developed using the expanded PEER NGA-West2 database.

The regional adaptation implemented in the Japan-specific high-Q variant is based on the observation that shallow site response in Japan differs from that in other regions, requiring a modified shallow site term. For other regions with multiple recorded earthquakes, Campbell and Bozorgnia, (2014) found broadly similar shallow site effects, suggesting that the general site term is adequate unless Japan-like conditions are expected. The model incorporates regionally independent geometric spreading, regionally dependent anelastic attenuation, and magnitude-dependent aleatory variability, addressing limitations identified in earlier NGA-West1 formulations.

6.2.6 BooreEtAl2014

The Boore et al., (2014) ground-motion prediction equation was developed within the NGA-West2 project. The model is intended for active shallow crustal tectonic regions and should not be applied to other tectonic regimes, such as subduction zones or stable continental regions, unless its applicability can be independently verified. The GMM supports PGA, PGV, and 5%-damped SA over a broad period range from 0.01 to 10s, and predicts the RotD50 horizontal component.

Several model variants of Boore et al., (2014) are available, reflecting regional differences in crustal attenuation and site response. These include the standard global-average formulation (BooreEtAl2014), as well as variants specifically adapted for high-Q crustal regions (BooreEtAl2014HighQ) and versions that exclude explicit style-of-faulting terms (BooreEtAl2014HighQNoSOF). For the BELSHAKE dataset, the BooreEtAl2014HighQ variant is selected for PGA, PGV, and SA.

The applicability ranges of the model include moment magnitudes from 3.0 to 8.5 for strike-slip and reverse-slip earthquakes, and 3.0 to 7.0 for normal-faulting earthquakes. Distances are defined using the R_{jb} and extend from 0 to 400 km. Site conditions are parameterized using V_{S30} values between 150 and 1500 m/s, and basin effects are accounted for through basin depths ranging from 0 to 3.0 km.

The GMM was developed using data primarily from California, Taiwan, Japan, China, the Mediterranean region (Italy, Greece, Turkey), and Alaska. Analysis of these datasets revealed regional variations in attenuation behavior, introducing additional epistemic uncertainty when applying the model to other active crustal regions. Specifically, California, New Zealand, and Taiwan exhibit distance attenuation trends close to the global average (referred to as Average Q), Japan and Italy show faster attenuation (Low Q), while China and Turkey display slower attenuation (High Q).

To account for high-Q regions, the model incorporates targeted adjustments, including modified anelastic attenuation terms to reflect reduced crustal damping, adjusted site amplification functions consistent with local site conditions, and corrections to the distance-scaling term to better capture regional attenuation characteristics (Boore et al., 2014).

6.2.7 Rietbrock2013

The Rietbrock et al., (2013) ground-motion prediction model was developed for stable continental regions (SCRs) and is specifically intended for intraplate tectonic settings. The model predicts PGA, PGV, and 5%-damped PSA (0.01 – 10s), uses the R_{jb} as the distance metric, and assumes a self-similar stress drop, meaning that the stress drop is independent of earthquake magnitude. This assumption is practically applied for the stable continental regions, where local values of Δσ are generally readily available only for small earthquakes (M_w < 4), whereas the ground motion predictions of interest tend to be for larger earthquakes (M_w 5 – 6).

Several model variants are provided by Rietbrock et al., (2013) to represent epistemic uncertainty in source scaling and stress-drop behavior in stable continental regions. These include a self-similar stress-drop formulation (RietbrockEtAl2013SelfSimilar), as well as variants corresponding to low, mean, and high stress-drop assumptions, implemented as RietbrockEtAl2013Low, RietbrockEtAl2013Mean, and RietbrockEtAl2013High, respectively. For the BELSHAKE dataset, the RietbrockEtAl2013SelfSimilar variant is selected for PGA, PGV, and SA.

The applicability range of the model spans moment magnitudes M_w 3.0 to 8.0 and source-to-site distances from 0 to 300 km. These ranges are consistent with its intended use in regions characterized by low seismicity, where strong-motion observations from moderate-to-large earthquakes are sparse but hazard assessments require extrapolation to higher magnitudes.

The model was developed using a stochastic point-source simulation approach, calibrated with parameters derived from local weak-motion recordings collected over several decades by the seismic network of the British Geological Survey.

6.2.8 DouglasEtALstochastic2013

The ground-motion prediction equations of Douglas et al., (2013) were developed for geothermal and induced seismicity environments, where earthquakes are typically of small magnitude and occur at shallow depths. The model is intended to represent ground motions generated by anthropogenic seismic sources, such as geothermal reservoirs, and is therefore distinct from GMMs developed for tectonic earthquakes. The model predicts 5% damped PSA over a range of short periods (0.1 – 1s) and uses the geometric mean of the two horizontal components. The applicable magnitude range is M_w 1.0–5.0, and the distance metric is R_{hypo}, applicable over distances of 1–50 km.

A key feature of the model is that it explicitly provides coefficients for multiple combinations of source and attenuation parameters, allowing flexible exploration of epistemic uncertainty in induced-seismicity ground motions.

Several model variants are therefore available, reflecting different assumptions regarding stress drop, crustal attenuation, and high-frequency decay. These include stress-drop values of 1, 10, and 100 bar, quality-factor values of Q = 200, 600, and 1800, and kappa values of 5, 20, 40, and 50 ms. For the BELSHAKE dataset, the variant DouglasEtAl2013StochasticSD100Q1800K040 is selected, corresponding to a stress drop of 100 bar, Q = 1800, and κ = 0.04 s.

The model adopts a stochastic simulation approach based on a single-corner Brune source spectral model, incorporating regional seismological parameters such as geometric spreading, anelastic attenuation, and site amplification.

6.2.9 Atkinson 2015

The Atkinson (2015) ground-motion prediction equation was developed specifically for induced seismicity, such as earthquakes associated with oil and gas activities, including wastewater disposal and hydraulic fracturing. The model is intended for application to small-to-moderate magnitude events at short source-to-site distances, conditions that are not well represented in conventional tectonic GMMs. The model supports PGA, PGV, and 5% damped PSA (for short periods), and provides total, inter-event, and intra-event standard deviations. Ground motions are defined for the geometric mean of the two horizontal components.

Several model variants of Atkinson (2015) are provided to represent epistemic uncertainty in the median ground-motion level for induced seismicity. These include the central (median) model (Atkinson2015), as well as lower and upper median branches implemented as Atkinson2015Lower and Atkinson2015Upper, respectively. These variants allow exploration of uncertainty in predicted ground motions for induced earthquakes. For the BELSHAKE dataset, the Atkinson2015 median formulation is selected for PGA, PGV, and SA. Site conditions are represented by a soft-rock reference condition with a near-surface shear-wave velocity of V_{S30} ≈ 760 m/s, to which all recorded motions are adjusted.

The applicability ranges of the model are M_w 3.0–6.0 and R_{hypo} from 0 to 40 km.

The GMM was derived through regression analysis of ground-motion data from the NGA-West2 database, restricted to small-to-moderate magnitude events recorded at short distances. The resulting functional form is intentionally simple and consistent with both the empirical observations and independent stochastic point-source simulations. A key conclusion of Atkinson (2015) is that near-source ground motions from induced earthquakes can be significantly larger than those predicted by many conventional NGA-West2 GMMs. This behavior is attributed primarily to the very shallow focal depths of induced events, which place the rupture only a short distance below the epicenter and can lead to unusually high amplitudes at close distances.

6.2.10 YenierAtkinson2015

The Yenier and Atkinson (2015) GMM is based on an equivalent point-source stochastic simulation framework, in which source, path, and site effects are explicitly parameterized and calibrated to empirical observations. The model was developed using a host-to-target adjustment strategy, with the host region defined by earthquake data from California (NGA-West2 database) and the target region corresponding to Central and Eastern North America (CENA), represented by data from the NGA-East database. This approach allows the decoupled influence of source properties and attenuation characteristics to be transferred from a well-instrumented active region to a stable continental region.

The GMM supports PGA, PGV, and 5% damped PSA over a wide period range (T = 0–10 s). Ground-motion amplitudes are defined for the orientation-independent average horizontal component (RotD50). Site effects are referenced to a rock site condition with V_{S30} = 760 m/s, consistent with the reference condition adopted in both NGA-West2 and NGA-East frameworks.

Several model variants are provided by Yenier and Atkinson (2015) to reflect alternative assumptions regarding attenuation behavior and calibration strategy. These include variants commonly implemented as YenierAtkinson2015, YenierAtkinson2015BSSA, and related formulations that differ slightly in the treatment of distance attenuation and reference conditions. For the BELSHAKE dataset, the YenierAtkinson2015BSSA variant is selected for PGA, PGV, and SA.

The model is applicable over a broad range of moment magnitudes (M_w 3.0–8.0) and source-to-site distances up to 600 km, reflecting its intended use for regional-scale hazard applications in stable continental regions. The functional form is specifically designed to reproduce the slower attenuation and distinct magnitude scaling observed in CENA compared to active tectonic regions.

6.2.11 CauzziEtAL2014

The Cauzzi et al., (2014) ground-motion prediction equation adopts a functional form that incorporates magnitude saturation and oversaturation, distance saturation, the use of rupture R_{rup} as predictor, and a geometric attenuation term dependent on magnitude, allowing it to describe ground-motion behavior over a wide magnitude and distance range.

The database used to develop this GMM was assembled and processed independently of the NGA-West2, SHARE, and RESORCE databases. It comprises approximately 1,880 pairs of orthogonal horizontal component records from 98 global earthquakes, including 49 events from Japan, 35 from the Pan-European region, 7 from the western United States, 5 from New Zealand, and 2 from China and Taiwan. The dataset includes a substantial number of long-period recordings, which are of particular relevance for engineering applications and for capturing epistemic uncertainty in ground-motion prediction.

Site conditions in the dataset are described using Eurocode 8 (CEN, 2004) ground classes, with approximately 7% of records on class A, 43% on class B, 40% on class C, and 10% on class D sites. For the majority of the dataset (1,660 records), the mean V_{S30} value is approximately 365 m/s. Although the authors acknowledge the potential limitations of using V_{S30} as a proxy for site amplification across a wide range of vibration periods, this choice is supported by the observed dominant site-response periods in the dataset and by previous studies demonstrating a strong correlation between V_{S30} and deeper subsurface structure.

Focal mechanisms are classified following Boore and Atkinson (2008), with 20 normal-faulting, 26 reverse-faulting, and 43 strike-slip earthquakes included. The GMM supports PGA, PGV, and 5% damped SA over a broad period range (T = 0–10 s), with ground-motion amplitudes defined for the orientation-independent average horizontal component (RotD50).

The model is applicable to shallow crustal earthquakes with moment magnitudes M_w 4.5–7.9, rupture distances R_{rup} from 0 to 150 km, and focal depths ≤ 20 km (Cauzzi et al., 2014).

Several model variants are provided by Cauzzi et al., (2014) to reflect different assumptions regarding site characterization and style-of-faulting effects. These include CauzziEtAl2014, CauzziEtAl2014FixedVs30, CauzziEtAl2014NoSOF, CauzziEtAl2014Eurocode8NoSOF, and regionally adapted formulations such as CauzziEtAl2014RhypoGermany. For the BELSHAKE dataset, the variants CauzziEtAl2014Eurocode8NoSOF, CauzziEtAl2014FixedVs30NoSOF, and CauzziEtAl2014RhypoGermany are selected for PGA, PGV and SA respectively.

6.3 Statistical measures

Over the past two decades, several measures have been proposed to evaluate the goodness of fit between a GMM and observed ground motion. In this study we employ the following measures:

- Likelihood (LH) Measure:

Introduced by Scherbaum et al., (2004), the LH measure is based on absolute standardized residuals and is designed to assess both the model fit and the validity of its statistical assumptions. When the predicted and observed ground motion data have matching means and variances, the LH distribution is uniform between 0 and 1. While LH can be visualized as a histogram, it is often summarized by its median value, where 0.5 indicates a perfect fit. Deviations from 0.5 suggest either a systematic bias or a mismatch in variance between the model and the observed data (Scherbaum et al, 2004).

- Log-Likelihood (LLH) Measure:

Proposed by Scherbaum et al., (2009), the LLH measure builds on information theory and evaluates how well a GMM probabilistically predicts observed data. The LLH is also typically represented as a histogram, with greater skewness toward lower values indicating better model performance. Differences in average LLH between two models are a good estimate of the relative information loss and can be used to rank GMMs, which is an advantage over the LH measure. However, LLH still cannot distinguish between model bias and variance mismatch (Scherbaum et al., 2009).

- Euclidean-Based Distance Ranking (EDR) (Kale & Akkar, 2013):

To address the limitations of LLH, particularly its tendency to favor GMMs with large standard deviations that better match aleatory variability, Kale and Akkar (2013) introduced the EDR metric. EDR comprises three components:

1. MDE (Modified Euclidean Distance): Represents the total probability difference between observed and predicted data across a range of standard deviations (σ), and typically ranges from 0.5 to 3.2.

2. Kappa (κ): Not to be confused with the high frequency decay parameter, this index quantifies the bias between the median predicted values and the trend of observed ground motion amplitudes. The optimal κ value is 1.0.

3. EDR Score: The overall ranking metric, calculated using both the normalized MDE and the square root of κ ($\sqrt{\kappa}$), providing a balanced evaluation of both dispersion and bias (Kale and Akkar, 2013).

- Residual Trend with Distance (Rtrend):

None of the ranking methods account for the trend of residuals with distance in GMM attenuation. While the κ score reflects trends in observed ground motion, it does not indicate whether the trend is positive or negative. Rtrend explicitly captures this directional trend, providing additional insight into how well a GMM models distance decay. An upward or downward trend indicates that the selected GMM attenuates faster or slower than the observed intensities.

- Mean Bias Error (MBE):

The MBE metric is used to quantify the average deviation between predicted and observed spectral acceleration (SA) values. Unlike LLH or EDR, which incorporate both probabilistic and dispersion-related considerations, MBE directly evaluates systematic bias in the model. It is calculated as the mean of the residuals (logarithmic differences between predicted and observed SA). Lower absolute MBE values indicate better agreement between predictions and observations. In this study, MBE is applied specifically to assess model performance for SA, serving as a simple yet effective indicator of bias.

The statistical measures are computed using analysis scripts developed in an earlier study by Vanneste et al., (2024) and subsequently applied to the BELSHAKE database.

6.4 GMM ranking for BELSHAKE

The performance of GMMs in all families was analyzed using the selected statistical measures. We limited the observed ground-motion values from the BELSHAKE database to those recorded on bedrock (soil class A) and considered only the S-wave window of the records. To compute predicted ground-motion values with the selected GMMs, we consider appropriate site conditions with V_{S30} = 1100 m/s, corresponding to the modal value for Belgian bedrock stations, we automatically select the appropriate distance metric and type of horizontal components supported by each GMM, and we take into account the focal mechanism of the associated events (if supported by the GMM), assuming strike-slip faulting when it could not be determined. In the first step, we selected records with a minimum magnitude (Mmin) of 2.5 and evaluated PGA, PGV and SA. Later on, we will also consider a higher Mmin value that is closer to the valid magnitude range of most GMMs, but still yielding a sufficient number of records, and extend the evaluation to a number of periods for spectral acceleration.

The results for PGA and PGV are shown in spider diagrams, showing the relative scores of different GMMs for the different metrics along the axes. The plots are grouped per GMM family. A number of GMMs have different implementations, accounting for different distance metrics, stress drop assumptions, faulting styles and type of horizontal components. For those cases, only the best performing implementation is shown in the plots. *Figure 64* shows the results for PGA and *Figure 65* those for PGV.

We evaluated GMM performance for SA at various periods from 0.015 to 1.2 s using several statistical measures, including LH, LLH, EDR, and MBE. While these measures generally provide consistent results, some exhibit fluctuations that make it difficult to clearly identify the best-performing GMM. For example, although the LH measure often provides a visually clearer representation of performance, it can still show noticeable variations across periods for different GMMs, complicating model selection. Considering these issues, and the clearer differentiation provided by MBE, we focus on MBE for the evaluation presented here. Therefore, for simplicity, only MBE-based results for different GMM families are shown in the SA line plots in Figure 66.

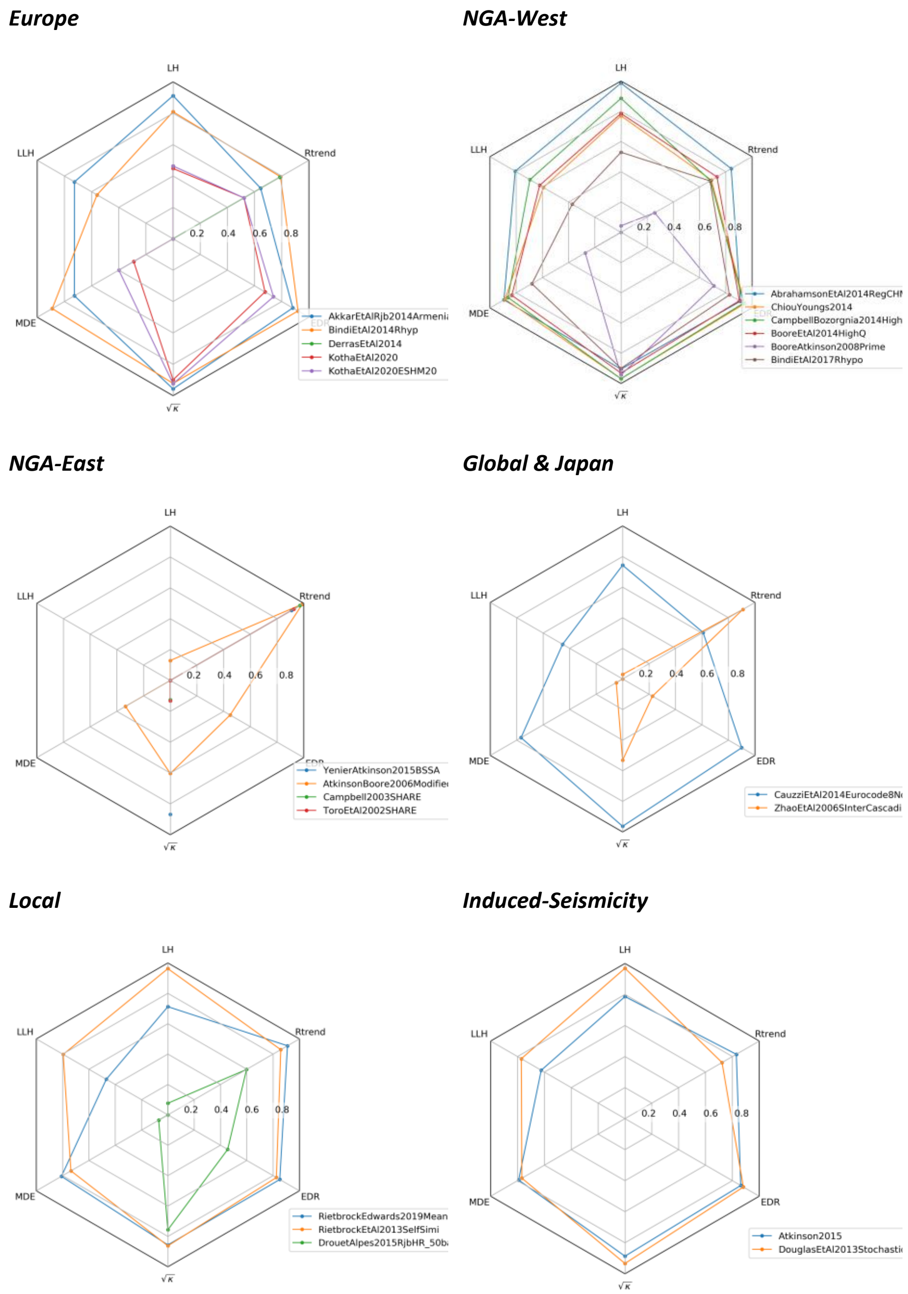

*Figure 64. Spider diagrams showing goodness-of-fit measures for PGA predicted by different GMMs grouped by family, with respect to the events with M≥2.5 in the BELSHAKE database, Goodness-of-fit measures are normalized to different minimum and maximum values (LH: abs(LH -0.5) * 2; LLH: 1.75 – 3.75; MDE: 1 –2; √κ: 1 – 2.5; EDR: 1 – 4)*

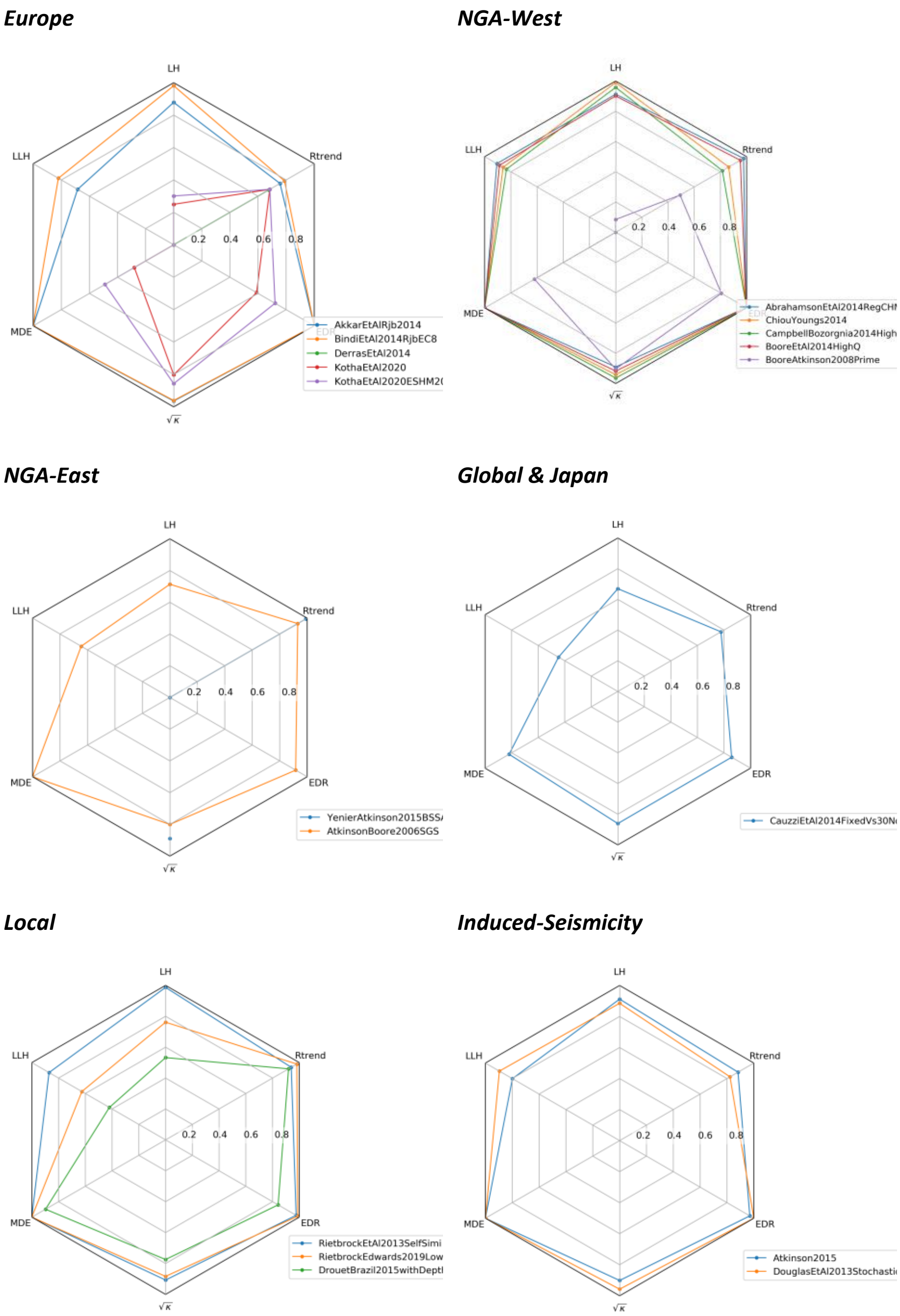

Figure 65. Spider diagrams showing goodness-of-fit measures for PGV predicted by different GMMs grouped by family, with respect to the events with M≥2.5 in the BELSHAKE database

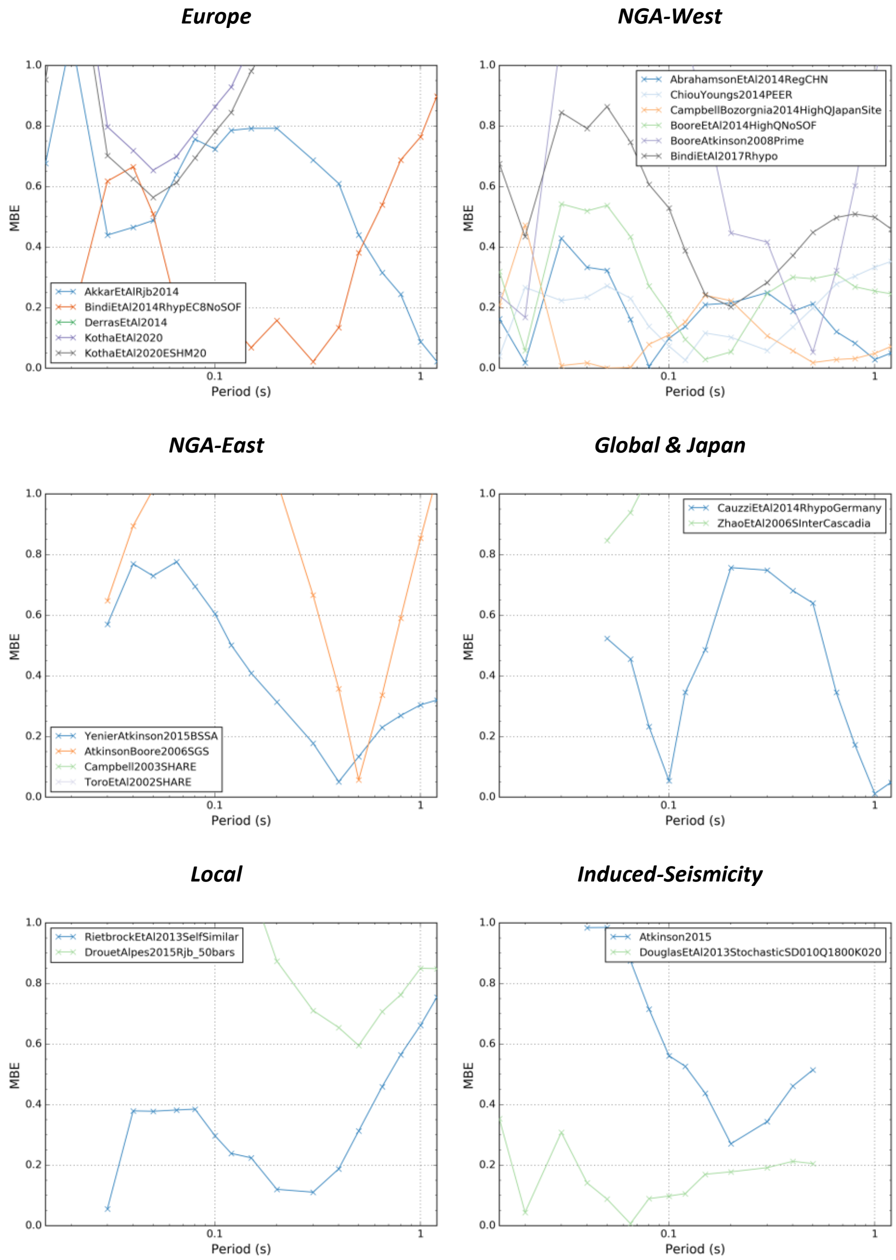

Figure 66. Plots showing MBE as a goodness of fit measure for SA predicted by different GMMs grouped by family, with respect to the events with M≥2.5 in the BELSHAKE database

To rank the GMMs, we prioritized EDR as the most important measure, followed by κ, with the remaining criteria considered thereafter. Among the European GMMs, AkkarEtAl2014 performed the best for PGA, and BindiEtAl2014 performed the best for PGV. The NGA-West GMMs generally exhibited strong and consistent performance, with the exception of BindiEtAl2017Rhypo for PGA and BooreAtkinson2008Prime for both PGA and PGV, which performed poorly and were excluded from further steps. Within the NGA-East GMMs, only Atkinson and Boore (2006) showed good performance for PGV; however, its poor fit for PGA led to its exclusion, and no GMM from this family was selected. Among the Global & Japan GMMs, CauzziEtAl2014 delivered strong results, particularly in EDR and κ, but its relatively poor performance in other measures, especially LLH, led to its exclusion. For the Local GMMs, RietbrockEdwards2013 was selected for both PGA and PGV. RietbrockEdwards2019 exhibited low LH and especially LLH scores for both PGA and PGV and was excluded. Within the Induced GMMs, Atkinson2015 performed well for PGV and was selected. However, its LH score for PGA was unsatisfactory, leading to its exclusion. DouglasEtAl2013StochasticSD100Q1800K040 demonstrated consistently strong performance across all measures for both PGA and PGV and was selected from this family.

For SA, GMMs were evaluated using Mean bias error (MBE) across a range of periods. Among the European GMMs, overall performance was limited, but BindiEtAl2014RhypCECNosoF exhibited relatively low MBE values at moderate periods. The NGA-West models showed the most stable and consistently low MBE values, particularly CampbellBozorgnia2014HighQJapanSite and AbrahamsonEtAl2014RegCHN. In the NGA-East family, YenierAtkinson2015SSA demonstrated better performance relative to the rest of the group, although it showed high MBE at short periods ($T < 0.1$s). In the Local GMM family, RietbrockEtAl2013SelfSimilar showed strong SA performance across most periods. Within the Global & Japan group, CauzziEtAl2014HypoGermany showed moderate performance, while ZhaoEtAl2006InterCascadia had high MBE at short periods. For Induced-Seismicity, DouglasEtAl2013Stochastic again stood out with consistently low MBE, confirming its reliability across all ground-motion types.

Following this, we compared the selected GMMs for PGA and PGV and SA, as shown in Figure 67, and ranked them based on their overall performance. The final ranking provides insight into the most suitable GMMs for our data. The selected list remains nearly identical for all three intensity measures. GMMs for different intensity measures remain the same, although their specific versions may vary. Some GMM families have multiple models represented in the selected list, while others are not included.

PGA

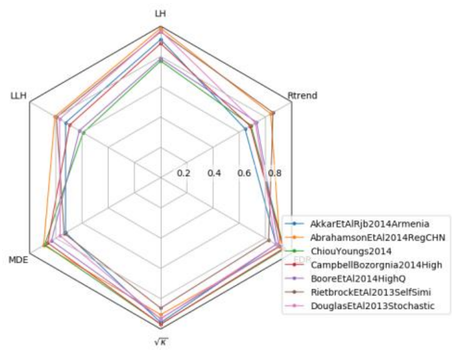

PGV

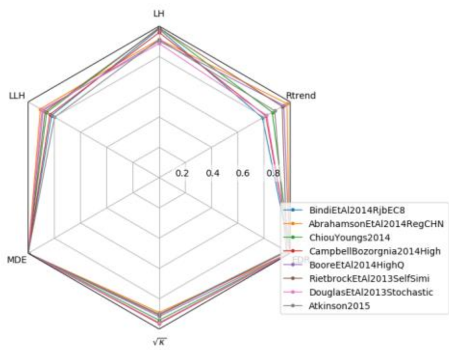

SA

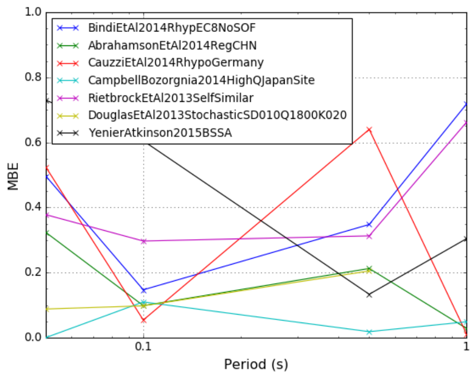

Figure 67. Spider diagrams showing the goodness-of-fit measures for the best-performing GMMs for PGA and PGV, and line plots presenting MBE as the sole goodness-of-fit measure for SA, with respect to the events with Mmin = 2.5 in BELSHAKE database

For PGA, all the selected GMMs perform well, with minimal differences in their overall scores. ChiouYoungs2014, CampbellBozorgnia2014, and AbrahamsonEtAl2014 rank the highest in terms of EDR, though the remaining GMMs follow closely behind. RietbrockEdward2013 ranks the lowest for EDR and κ, but it has high scores in LH, LLH, and Rtrend. Conversely, ChiouYoungs2014 has the lowest LLH score among the models. Overall, the most consistent GMMs for PGA are AbrahamsonEtAl2014, CampbellBozorgnia2014, and DouglasEtAl2013Stochastic, as they maintain strong performance across multiple key measures.

For PGV, the scores are even closer compared to PGA, indicating a more uniform performance among the selected models. Similar to PGA, the EDR scores for PGV are consistently high across all models. DouglasEtAl2013Stochastic, BooreEtAl2014, and AbrahamsonEtAl2014 achieve the highest EDR scores, along with top rankings in the LLH measure, reinforcing their reliability across different ground motion parameters.

For SA, CampbellBozorgnia2014HighQJapanSite, DouglasEtAl2013Stochastic, and AbrahamsonEtAl2014RegCHN demonstrate the most consistently low MBE across all periods, indicating higher predictive accuracy. In contrast, models such as CauzziEtAl2014RhypoGermany, RietbrockEtAl2013SelfSimilar, BindiEtAl2014RhypoEC8NoSOF, and YenierAtkinson2015BSSA exhibit more variable results, with higher MBE values at certain periods. This reflects greater deviations from observed ground motion and suggests reduced reliability across different periods for these GMMs.

The plots illustrating different goodness-of-fit measures for AbrahamsonEtAl2014RegCHN and DouglasEtAl2013StochasticSD100Q1800K040 as examples are shown in *Figure 68* for PGA and *Figure 69* for PGV. Both GMMs exhibit very good κ scores (close to 1) for both PGA and PGV. In both GMMs, the median LH values are close to 0.5, indicating good LH scores for both PGA and PGV. Their LLH values are lower than the other GMMs leading to high scores. Additionally, a comparison of the histogram of normalized residuals against a standard normal distribution shows no significant bias. The mean (μ) remains close to zero, while the standard deviation (σ) is close to 1 in most cases, further confirming the robustness of these GMMs in predicting ground motion.

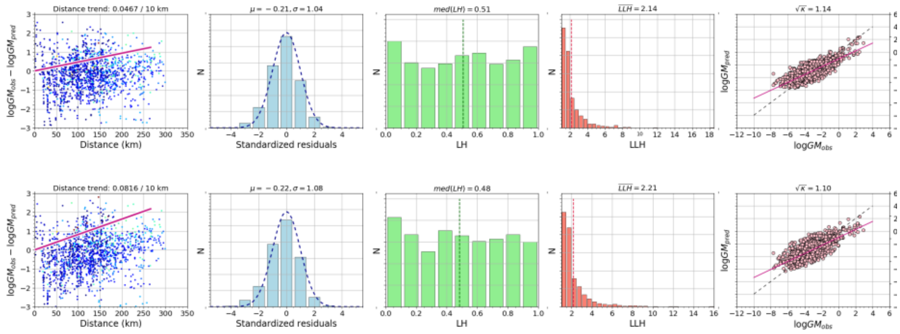

Figure 68. Goodness-of-fit measures for PGA predictions by the top-performing GMMs; Top: AbrahamsonEtAl2014RegCHN, Bottom: DouglasEtAl2013StochasticSD100Q1800K040

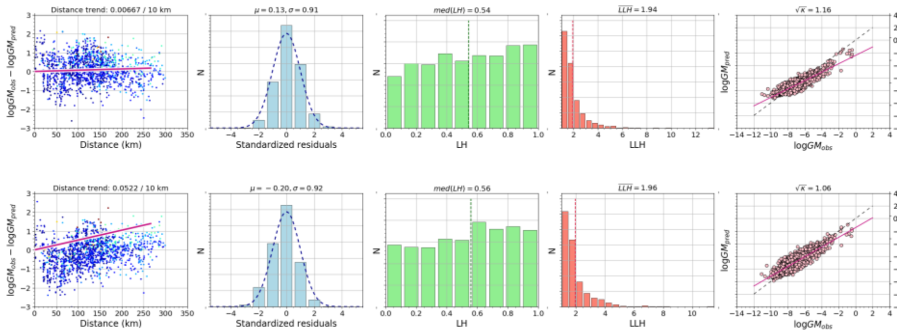

Figure 69. Goodness-of-fit measures for PGV predictions by the top-performing GMMs; Top: AbrahamsonEtAl2014RegCHN, Bottom: DouglasEtAl2013StochasticSD100Q1800K040

6.5 Effect of magnitude threshold on GMM evaluation

To evaluate the sensitivity of GMM performance to the choice of magnitude threshold, we conducted a comparative analysis on the best selected GMMs using a higher minimum magnitude, Mmin=3.0. This adjustment reduced the number of records from 1,468 (with Mmin = 2.5) to 390. Figure 70 presents the results for PGA and PGV, highlighting that the performance of some GMMs has shifted with the higher magnitude threshold.

PGA

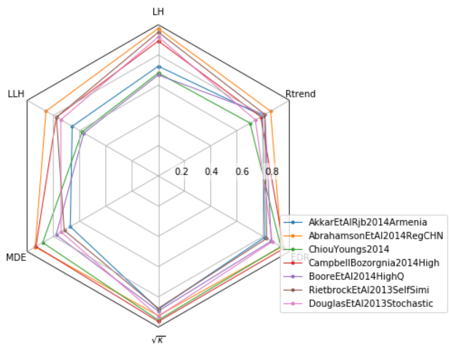

PGV

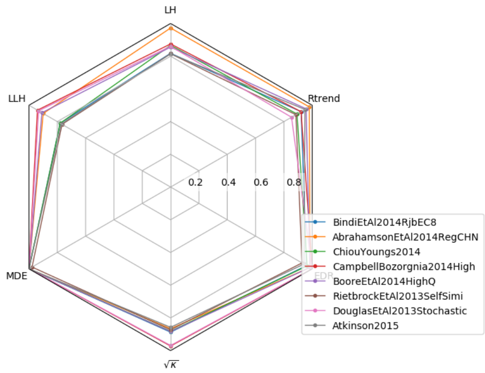

SA

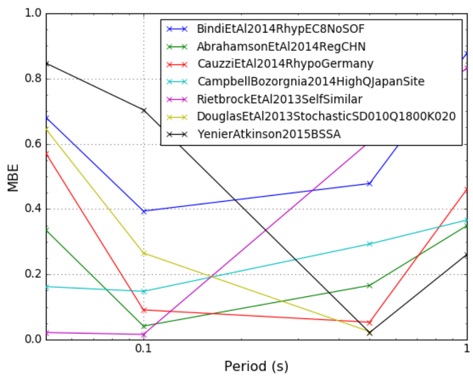

Figure 70. Plots showing the goodness-of-fit measures for the best-performing GMMs for PGA, PGV, and SA, with respect to the events with Mmin = 3 in BELSHAKE database

For both PGA and PGV, using Mmin = 2.5 results in more consistent and closely clustered GMM performance, while increasing the threshold to Mmin = 3.0 leads to greater score deviation and a noticeable inward shift in LLH and LH scores, indicating reduced fit for some models. For example, ChiouYoungs2014 and AkkarEtAl2014Armenia show declines in LLH scores for PGA.

For SA, CampbellBozorgnia2014HighQJapanSite and AbrahamsonEtAl2014RegCHN continue to exhibit consistently low MBE values across periods, indicating a strong and stable fit to the observed data. In contrast, DouglasEtAl2013StochasticSD010Q1800K020 shows slightly elevated MBE values, particularly for lower magnitudes, suggesting that its fit is more sensitive to the amount of available data compared to the more robust performance of CampbellBozorgnia and Abrahamson models. Among the less stable models, RietbrockEtAl2013SelfSimilar and YenierAtkinson2015BSSA show the highest variability in MBE across periods, and BindiEtAl2014 consistently produces high MBE values, reflecting a poorer fit to the data.

Overall, removing the magnitude bin of 2.5–3.0 negatively impacts the LLH scores of some GMMs in PGA and PGV evaluations. However, other measures such as Rtrend, k, MDE, and EDR remain largely unchanged, and the results for these measures are very similar across both thresholds. For SA, while some GMMs continue to perform well, others show reduced stability or fit with fewer data points. This higher variability of goodness-of-fit results is likely caused by the significantly lower number of test data. In general, the results, and in particular the ranking order, remain in relatively good agreement with those based on Mmin = 2.5. Thus, we will maintain the selection based on Mmin = 2.5, as it is more robust.

6.6 The selected variants of Douglas et al., (2013) GMM

We selected the DouglasEtAl2013StochasticSD100Q1800K040 model as the best fitting among the 36 tested combinations for PGA and PGV, and the DouglasEtAl2013StochasticSD010Q1800K020 model for SA. These model versions use a quality factor Q = 1800 and site kappa values of 40 ms and 20 ms, and stress drops of 100 and 10 bars, respectively. To assess the plausibility of this selection, we compared these parameters with those derived specifically for Belgium.

First, the quality factor Q quantifies anelastic attenuation, representing the energy loss due to internal friction as seismic waves propagate through the

Earth's materials. Based on the chapter 5 of the kappa analysis for BELSHAKE, Q is estimated using the relation:

$$Q = {}^{1}/_{V_s\ \kappa_r}$$

where V_s is the average shear-wave velocity along the path, assumed to be 3.6 km/s based on the Belgian regional velocity model. The average κ_r values, derived from our kappa analysis, were 0.16 ms/km for the horizontal component, corresponding to a Q value of approximately 1736. This closely aligns with the Q = 1800 used in the selected Douglas models.

Second, the site-specific kappa values (κ_0) for stations located on soil class A in Belgium averaged 23 ms for the horizontal component. These values fall well within the 20–40 ms range used in the selected Douglas model versions for PGA, PGV and SA. This alignment supports the suitability of the chosen models. Only stations on soil class A were included in this analysis, consistent with the data used for model fitting.

Finally, based on the moment magnitude analysis in the BELSHAKE project, estimated stress drops range mostly between 1 and 100 bars, with a median value around 10 bars. This is in agreement with the selected GMMs, which assume 100 bars for PGA and PGV, and 10 bars for SA.

This comparison confirms that the selected Douglas model parameters are consistent with regional attenuation and stress drop characteristics in Belgium.

6.7 GMM ranking for a combined dataset of BELSHAKE and RESIF

To enhance the dataset with records from higher-magnitude events, we integrated ground motion data from the RESIF database in France with our existing BELSHAKE dataset. The selected GMMs for PGA, PGV, and SA were subsequently applied to this combined dataset to assess GMMs performance under broader seismic data.

From the RESIF we have applied a filter to include only events occurred within the geographical region defined by the coordinates:

- Longitude: 0° to 10°,

- Latitude: 47.5° to 52°.

This region (NE of France) was selected due to its similar attenuation characteristics to Belgium providing a more regionally consistent comparison (see chapter 5). In this filtered subset, all records within the geographic boundary and with source-to-site distances equal to or less than 300 km were retained; those exceeding this distance were excluded. The addition of this part of RESIF data contributed 238 new records to the PGA and PGV datasets of BELSHAKE. These new records were primarily in the magnitude range of 3.0–4.0, and 5.0 to 5.5 thereby improving the representation of moderate-to-higher and high magnitude events in the analysis. A breakdown is shown in Table 17.

Magnitude Bin	BELSHAKE	RESIF	filtered RESIF	Combined (BELSHAKE+filtered RESIF)
2.5–3.0	5825	1280	46	5871
3.0–3.5	2620	2894	90	2710
3.5–4.0	926	2518	84	1010
4.0–4.5	501	800	6	507
4.5–5.0	73	272	2	75
5.0–5.5	0	202	10	10
5.5–5.8	52	0	0	52
Total	9997	7966	238	10235

Table 17. Number of ground motion records per magnitude bin in the BELSHAKE, RESIF (filtered), and combined datasets for PGA and PGV. The addition of RESIF data primarily enhances the representation of moderate to high magnitude events (M_L > 3), particularly in the 3.0–4.0 range.

This augmentation gives a slightly extended magnitude coverage, particularly in the higher bins. Figure 71 and Figure 72 present the spider diagrams showing the performance of various GMMs grouped by family on the combined dataset for PGA and PGV, respectively. The same GMM families and candidate models used in the analysis with the BELSHAKE database were maintained. The evaluation results for the combined dataset were nearly identical, both in terms of numerical scores and the relative rankings of GMMs within each family. This consistency is not unexpected, given that the number of filtered RESIF records represents only about 1% of the records used in BELSHAKE, making strong differences in model evaluation unlikely. A summary of the consistent findings for PGA and PGV is provided below. The results for SA are not discussed again here, as they were found to be identical to those obtained in the original BELSHAKE analysis.

European GMMs:

- Akkaretal2014 remained the best-performing model for PGA.
- Bindietal2014 again performed best for PGV.

NGA-West GMMs:
These models continued to show strong and stable performance, with the exception of:

- BindiEtAl2017Rhypo (excluded due to poor PGA performance)
- BooreAtkinson2008Prime (excluded for poor results in both PGA and PGV).

NGA-East GMMs:

- AtkinsonBoore2006 showed moderate performance for PGV, but its low LLH score led to exclusion.
- No models from this family were ultimately selected, mirroring the BELSHAKE case.

Global & Japan GMMs:

- Cauzzietal2014 performed well in EDR and κ, but was excluded due to low LLH performance.

Local GMMs:

- RietbrockEdwards2013 was selected for both PGA and PGV.

- RietbrockEdwards2019 had low LH and LLH scores and was excluded.

Induced GMMs:

- Atkinson2015 performed well for PGV and was selected, but it was not selected for PGA due to its unsatisfactory LH score.
- DouglasEtAl2013Stochastic consistently delivered excellent performance for both PGA and PGV and was selected.

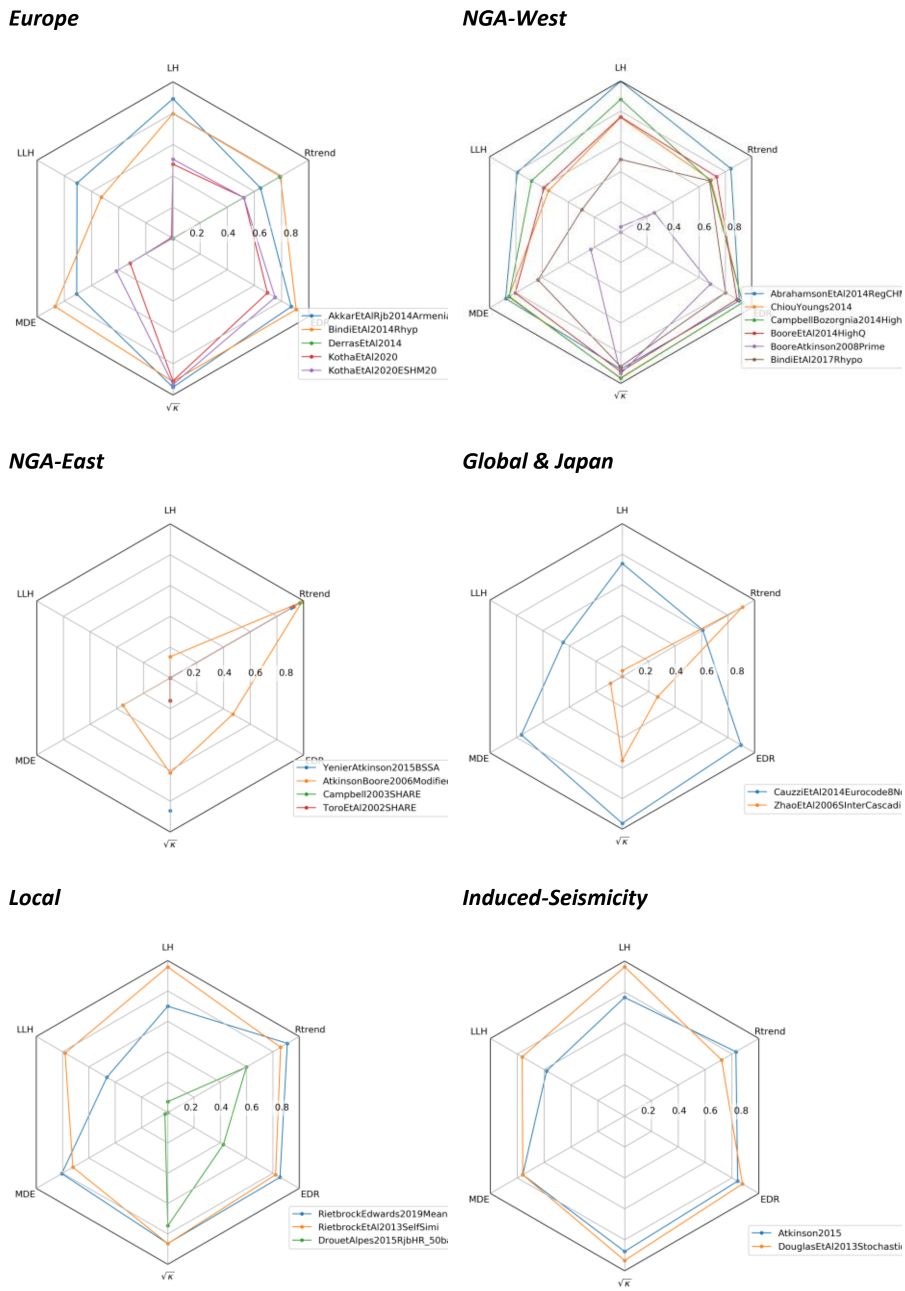

Figure 71. Spider diagrams showing goodness-of-fit measures for PGA predicted by different GMMs grouped by family, based on the combined BELSHAKE and RESIF datasets, with respect to the events with Mmin≥2.5 in BELSHAKE database

Europe

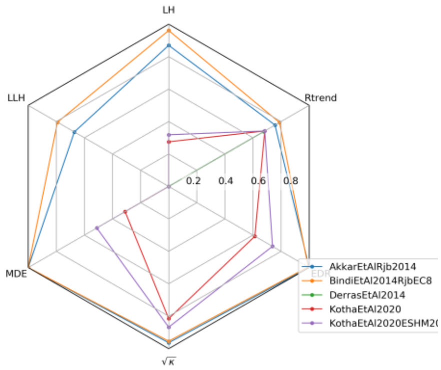

NGA-West

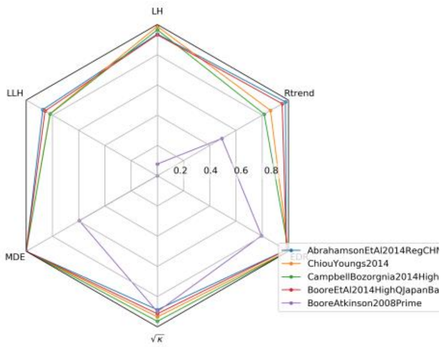

NGA-East

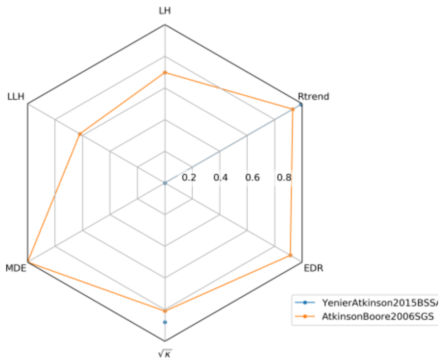

Global & Japan

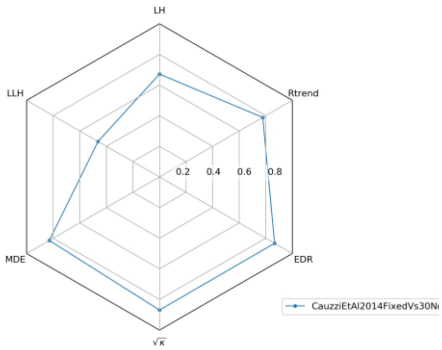

Local

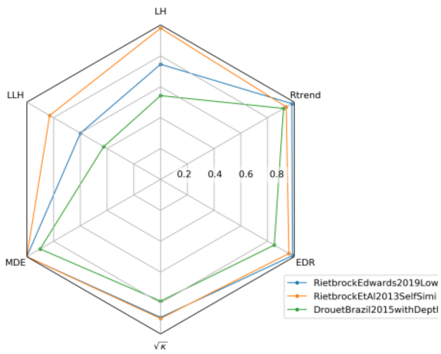

Induced-Seismicity

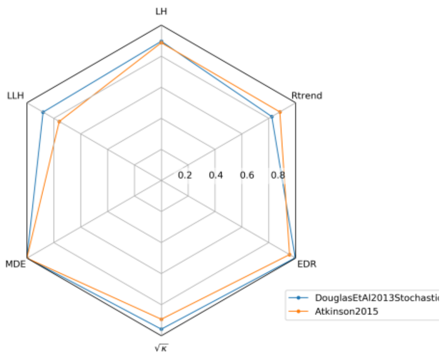

Figure 72. Spider diagrams showing goodness-of-fit measures for PGV predicted by different GMMs grouped by family, based on the combined BELSHAKE and RESIF datasets, with respect to the events with Mmin≥2.5 in BELSHAKE database

Figure 73 presents a comparison of the best-performing GMMs for each intensity measure. The selected GMMs are nearly identical to those identified in the BELSHAKE analysis, with only two additions:

- Atkinson2015 was also selected for PGA.
- BindiEtAl2014RjbEC8 was included for PGV.

The comparative performance among selected models again showed very similar trends to the original BELSHAKE results:

PGA:

- All selected GMMs performed well with minimal differences in their total scores.
- ChiouYoungs2014, CampbellBozorgnia2014, and AbrahamsonEtAl2014 achieved the highest EDR scores.
- RietbrockEdward2013 had lower EDR and κ scores, but strong LLH, LH, and Rtrend.
- ChiouYoungs2014 had the lowest LLH.
- Overall, AbrahamsonEtAl2014, CampbellBozorgnia2014, and DouglasEtAl2013Stochastic emerged as the best GMMs for PGA.

PGV:

- The PGV scores were even more uniform than PGA, again highlighting robust performance across models.
- Top EDR scores were achieved by DouglasEtAl2013Stochastic, BooreEtAl2014, and AbrahamsonEtAl2014.
- These models also ranked highly in LLH, confirming their reliability.

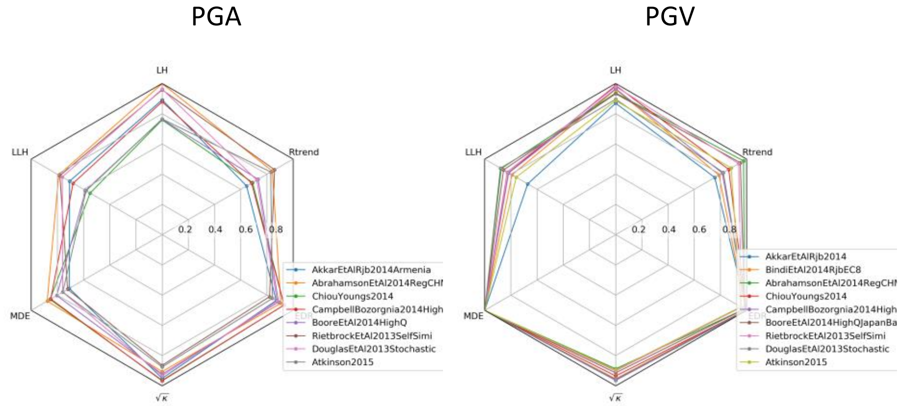

Figure 73. Spider diagrams showing goodness-of-fit measures for the best performing GMMs for PGA, PGV based on the combined BELSHAKE and RESIF datasets

6.8 Conclusions

This chapter presented an evaluation of a broad set of ground-motion prediction equations (GMMs) against the BELSHAKE ground-motion database, with the objective of identifying the models most appropriate for seismic hazard assessment in Belgium. The selection encompassed GMMs from diverse families, including European, NGA-West, NGA-East, Japanese, global, and induced-seismicity models, reflecting the wide range of source characteristics, site conditions, magnitude scales, and intensity measure types.

Multiple statistical measures were used to quantify the agreement between observed and predicted ground motions. These results enabled a comparative assessment of GMM performance and informed the ranking of models based on their predictive capabilities. Although no single model consistently outperformed all others across all measures and scenarios, a subset of GMMs demonstrated strong and robust performance.

Notably, variants of the models of Abrahamson et al., (2014), Campbell & Bozorgnia (2014), Douglas et al., (2013), and Boore et al., (2014) performed well for Belgian bedrock conditions and are recommended for future seismic hazard studies in Belgium, particularly as part of logic-tree frameworks to account for epistemic uncertainty. These four selected GMMs share important attributes that contribute to their robust performance. All models cover a broad range of earthquake magnitudes, with Abrahamson et al., Campbell & Bozorgnia, and Boore et al. supporting moderate to large magnitudes typically starting from M_w 3.0, extending up to M_w 8.5 depending on fault type and tectonic setting. The stochastic model of Douglas et al. is specifically designed to handle lower magnitudes, ranging from M_w 1.0 to 5.0, making it well-suited for small to moderate events. These magnitude ranges align well with the low to moderate magnitudes of the BELSHAKE dataset and likely contribute significantly to the strong agreement observed.

To evaluate the sensitivity of GMM performance to the magnitude threshold, we conducted a comparative analysis using a higher minimum magnitude, Mmin = 3.0. The results indicated that some GMM families experienced minor performance shifts. Removing the 2.5–3.0 magnitude bin impacted LH and LLH scores for certain models, typically in a negative direction, However, other scores (Rtrend, k, MDE, EDR) remained consistent across both thresholds. As it is likely that the significantly lower number of records is the cause of this higher variability, we retained the selection based on the original threshold of Mmin = 2.5.

To extend the dataset with moderate-to-higher magnitude events, a subset with 238 records in northeastern France from RESIF database were added to BELSHAKE, selected for regional similarity and with distances ≤ 300 km. These records, mainly in the M_w 3.0–4.0 and 5.0–5.5 ranges, modestly expanded the magnitude coverage. However, since the added data represented only ~1% of the total dataset, GMM evaluation results for PGA, PGV, and SA remained nearly unchanged.

In summary, the analyses identified a set of GMMs that show strong potential for application in future seismic hazard assessments in Belgium. Their consistent performance across our analysis supports their consideration in logic-tree frameworks where epistemic uncertainty is explicitly accounted for.

7 Conclusions

This thesis set out to build a robust foundation for ground-motion modelling in Belgium, a region where low-to-moderate seismicity and the scarcity of strong-motion recordings have historically limited the ability to test, adapt, or develop ground-motion models. By contributing to the BELSHAKE database and to the establishment of a complete workflow from waveform selection to attenuation analysis and GMM evaluation, the work addresses this gap in a systematic and transparent manner.

7.1 Development of a regionally consistent ground-motion database

A primary outcome of this thesis is the BELSHAKE ground-motion database, representing the first systematically assembled and quality-controlled dataset of earthquake ground motions for Belgium. The database integrates waveform data from the Royal Observatory of Belgium with selected records from neighboring regions, ensuring adequate representation of key events such as the 1992 Roermond earthquake.

Explicit event-selection criteria, based on magnitude, spatial coverage, event type, and recording period, were defined to ensure consistency with the objectives of ground-motion modelling and engineering applications. The resulting dataset, comprising several thousand records, reflects the intrinsic characteristics of Belgian seismicity, including the dominance of small-magnitude events and the limited availability of near-source recordings.

A critical component of this work was the implementation of a comprehensive waveform quality-control procedure. Comprehensive visual quality control, combined with targeted corrections and explicit documentation of persistent issues, ensured that only reliable waveforms informed the later analyses.

7.2 Hybrid waveform windowing

A second key contribution is the development of a hybrid waveform windowing strategy that combines the strengths of the Goulet and Perron approaches. This method provides consistent definitions of P-wave, S-wave, coda, and noise windows, while maximizing the number of usable records by accommodating incomplete or partially disturbed pre-event noise. A reliable noise window is an essential prerequisite for reproducible signal to noise ratio estimation and frequency-range selection This is particularly important for weak-motion datasets, where noise conditions often limit the usability of recordings.

7.3 Validation of intensity measures

A third contribution is the systematic validation of a wide suite of intensity measures (IMs). These IMs constitute the primary interface between seismological observations and engineering application. A systematic validation procedure was implemented using multiple complementary approaches, including component-ratio analysis, horizontal-to-vertical comparisons, and residual analysis against a reference ground-motion model. This process identified a small set of remaining anomalous cases and also demonstrated the overall consistency of the data and the reliability of the derived IM values. The result is a carefully curated dataset that supports both engineering applications and ground-motion modelling.

7.4 Characterization of attenuation through kappa analysis

A major contribution of this thesis is the characterization of high-frequency anelastic attenuation in Belgium through the estimation of the κ parameter. Using multiple estimation approaches, κ_0 (site specific kappa value) and κ_r (kappa gradient of crustal domain) values were derived for different stations and crustal domains across Belgium, together with frequency-independent quality factor (Q) estimates. These results highlight systematic differences between stations and crustal domains and provide physically interpretable inputs for adjusting ground-motion models between reference and target regions, as well as for the development of future ground-motion models specifically for Belgium.

7.5 Evaluation of ground-motion models

The final part of the thesis evaluated a broad set of published GMMs against the BELSHAKE database. By applying a suite of complementary statistical measures; capturing bias, variance, likelihood and attenuation trends, the analysis produced a balanced assessment of each model's ability to reproduce the recorded data. The results provide essential empirical constraints and highlight which GMMs most closely reflect observed ground motion in Belgium. A small subset of models, primarily from the NGA-West and stochastic families, emerged as consistently strong performers across

PGA, PGV and spectral ordinates. Their selection offers a rational, data-driven starting point for future seismic hazard analyses.

8 Perspectives and Recommendations

8.1 Transferability and best practices for low-seismicity regions

Beyond its regional focus, this thesis provides a set of best practices that are directly applicable to other low-to-moderate seismicity regions. These include:

- The implementation of comprehensive waveform quality control with full traceability
- The adoption of hybrid windowing strategies tailored to weak-motion datasets
- The application of multi-metric validation frameworks for IMs
- The use of mixed-effects regression to estimate site kappa and kappa gradients, improving the reliability of estimates for stations or regions with limited data.

These elements collectively provide a robust framework for constructing ground-motion databases in regions where data are sparse and heterogeneous.

8.2 Usability for engineering and seismic hazard applications

The practical impact of the thesis is that it provides the data and physical constraints needed to reduce epistemic uncertainty in future seismic hazard models for Belgium. First, the BELSHAKE database supplies a transparent and quality-controlled set of processed waveforms and intensity measures that can be used to test and compare candidate ground-motion models. Second, the κ-analysis provides regionally constrained attenuation parameters, including κ_0, κ_r and equivalent Q values, which are directly relevant for adapting imported models to Belgian crustal conditions. Third, the GMPE evaluation identifies a subset of models that best reproduce the observed Belgian data, offering a defensible starting point for future logic-tree construction.

For hazard maps, this means that future PSHA studies can move away from relying only on generic foreign models and instead use models selected and adjusted on the basis of Belgian observations. For local seismic action assessment, especially at important sites, the thesis provides processed waveforms, validated intensity measures, and site-related parameters that can support more consistent characterization of expected shaking and help refine engineering input motions.

The datasets and results produced in this thesis are directly usable by engineers and seismic hazard modellers. The availability of uniformly processed waveforms, validated intensity measures, and detailed metadata enables:

- Calibration and testing of ground-motion models for regional applications
- Development of regionally consistent hazard models
- Assessment of structural demand using physically consistent input data
- The inclusion of κ_0, κ_r, Q and V_{S30} parameters further enables host-to-target adjustments, allowing imported models to be adapted to Belgian conditions.

In this context, the findings can also support the selection of ground-motion time histories for engineering design. The BELSHAKE database can be queried using standard selection criteria such as magnitude, source-to-site distance, site conditions (e.g. V_{S30}), and intensity measures, allowing the identification of records consistent with specific design scenarios. The availability of quality controlled waveforms, validated metadata, and well defined usable frequency ranges further ensures that selected records are physically reliable. While the database is dominated by weak motions and therefore does not provide a sufficient basis on its own for selecting records representative of larger design earthquakes, it offers important constraints on regional attenuation and site effects. These constraints can be used to adapt stronger records from other regions through host-to-target adjustments, and to verify the physical consistency of selected or simulated input ground motions with Belgian conditions. In this way, the thesis contributes to establishing a regionally consistent framework for ground-motion selection in engineering applications.

8.3 Implications for logic-tree construction in PSHA

The results of this thesis provide several elements that can inform the construction and weighting of logic-tree branches in probabilistic seismic hazard analysis:

- The GMM evaluation results provide a basis for selecting candidate models as logic-tree branches

- The multi-metric performance analysis can support relative weighting of models based on their ability to reproduce observed data
- The κ and Q estimates provide physically based constraints for defining alternative branches representing regional attenuation properties

While the thesis does not prescribe definitive logic-tree weights, it provides the quantitative basis required to develop them in a defensible and data-driven manner.

8.4 Limitations and extrapolation to larger magnitudes

A key limitation of the BELSHAKE dataset is its dominance of small-magnitude events (M_L 2–4). As a result, the conclusions regarding ground-motion scaling and model performance are primarily constrained within this magnitude range.

The results should therefore not be interpreted as a direct calibration of Belgian ground motions at damaging magnitudes, but rather as regional constraints on key physical parameters that remain relevant at larger magnitudes. In particular, the thesis improves the characterization of site conditions, attenuation, and model compatibility—essential components of hazard assessment. Extrapolation to larger magnitudes, which are most relevant for seismic hazard, should therefore be undertaken with caution. In particular:

- Stress drop and attenuation characteristics may not scale linearly
- Model performance rankings may change when applied outside the calibration range

Upscaling to higher magnitudes should therefore be done by combining these regional constraints with models that are already valid over a broader magnitude range. In practice, this means selecting candidate GMMs that perform well against BELSHAKE at low magnitudes, and then adapting them to Belgian conditions through host-to-target adjustments, especially using the κ_0, κ_r and V_{S30} results derived in this thesis. This provides a physically justified pathway for extrapolation, while still acknowledging that the magnitude-scaling part of the models remains less constrained by local data.

A further step would be to supplement BELSHAKE with additional moderate-magnitude data from comparable neighbouring regions, or to use simulation-based approaches constrained by the attenuation and stress-drop results obtained here. The thesis already points in that direction by showing that some stochastic or high Q models are more compatible with Belgian observations than others.

8.5 Recommendations for future PSHA in Belgium

Based on the results of this thesis, a practical strategy for the next generation of seismic hazard assessment in Belgium would involve:

- Selecting a subset of well-performing GMMs identified in this study
- Applying host-to-target adjustments using BELSHAKE-derived κ, Q, and V_{S30} values
- Incorporating multiple models within a logic-tree framework to represent epistemic uncertainty
- Validating model predictions against the BELSHAKE dataset where applicable

In practice, this implies starting from a host GMPE framework and progressively introducing Belgian-specific adjustments, while maintaining multiple models within a logic-tree to capture residual epistemic uncertainty. However, additional developments are required before fully region-specific models can be established, including improved constraints on large-magnitude behaviour and further refinement of attenuation models.

8.6 Future developments and research directions

Several avenues for future work emerge naturally from this thesis:

- Expansion of the database through integration of new recordings and regional datasets
- Extension of attenuation analysis to frequency-dependent Q models
- Development of non-ergodic ground-motion models that explicitly account for regional and site-specific effects
- Integration of BELSHAKE results into fully probabilistic hazard frameworks
- Improved characterization of site conditions and V_{S30} distributions across Belgium

In addition, closer integration with engineering applications, including record selection methodologies and structural-response analyses, would further enhance the practical impact of the dataset.

8.7 Final perspective

Taken together, the components of this thesis, database construction, waveform quality control, hybrid windowing, IM consistency checking, anelastic attenuation kappa characterisation, and multi-metric GMM evaluation form a coherent methodological framework for ground-motion analysis in Belgium. The BELSHAKE database and its associated products represent a comprehensive and internally consistent set of ground-motion resources for the region.

Beyond their immediate application to GMM testing, these results provide the basis required for refining seismic-hazard models, improving host-to-target adjustments, and ultimately reducing epistemic uncertainty in Belgian hazard assessments. The methodologies and datasets developed here are not only relevant for Belgium but also offer a transferable framework for other regions facing similar challenges of limited data and low seismicity.

Future work can build directly on these foundations. Key directions include incorporating additional recordings from regional networks as they become available, extending κ analyses toward frequency-dependent Q models, exploring non-ergodic ground-motion modelling approaches, and integrating BELSHAKE-derived results into logic-tree hazard frameworks. As seismic monitoring capabilities in Belgium continue to advance, the methods and datasets presented here will play a crucial role in supporting more accurate, regionally tailored seismic hazard assessments.

9 PhD thesis publications and outreach

PEER-REVIEWED PUBLICATIONS:

- **Onvani Mahsa**, Vanneste Kris. Analysis of the site-specific and regional components of kappa across crustal domains in Belgium. Seismica Journal. 2026, Submitted.
  preprint available on Research Square:
  https://doi.org/10.21203/rs.3.rs-8484319/v1.
- Vanneste Kris, **Onvani Mahsa**, Rapagnani Giovanni, Van Noten Koen. The BELSHAKE database of earthquake ground motion in Belgium. Seismological Research Letters, 2025.
  https://doi.org/10.1785/0220250321

NON PEER-REVIEWED:

- Vanneste Kris, **Onvani Mahsa**, WAVEFORM processing in BELSHAKE, THE BELGIAN ground-motion databse, In Proceedings of the 18th world conference on earthquake engineering, pp. 1-5. 2024.

DATASETS:

- **Onvani Mahsa** ; Vanneste Kris. BELSHAKE kappa dataset. [Dataset]. Royal Observatory of Belgium.
  https://doi.org/10.5281/zenodo.17857380
- Vanneste Kris; **Onvani Mahsa**. Belgian ground-motion database (BELSHAKE) flatfile. [Dataset]. Royal Observatory of Belgium. https://doi.org/10.5281/zenodo.15241694

CONTRIBUTIONS TO (INTER)NATIONAL CONFERENCES

- **Onvani Mahsa**, Vanneste, Kris. “The BELSHAKE Project”, *RMS Meeting*, Netherlands, June 2022.
- **Onvani Mahsa;** Vanneste Kris; Almeida João. “BELSHAKE project”, BELQUA 2023 Annual Scientific Workshop, Brussels, 7 March 2023.

- **Onvani Mahsa;** Vanneste Kris; Almeida João. “BELSHAKE project”, *IUGG General Assembly 2023*, Berlin, Germany, 11–20 July 2023.
- **Onvani Mahsa;** Vanneste Kris; Almeida João. “BELSHAKE project”, ‘Workshop on ground motion modelling in France and surrounding regions, Cadarache Castle, France, October 2023.
- **Onvani Mahsa,** Vanneste Kris. “Analysis of the site-specific and regional components of kappa across crustal domains in Belgium based on the BELSHAKE database”, 102nd Journées Luxembourgeoises de Géodynamique, Luxembourg, November 2024.
- **Onvani Mahsa,** Vanneste Kris. “Analysis of the site-specific and regional components of kappa across crustal domains in Belgium based on the BELSHAKE database”, EGU25, Vienna, April 2025.

10 Bibliography

Abercrombie, R.E. (1999) “A summary of attenuation measurements from borehole recordings of earthquakes: the 10 Hz transition problem,” *Q of the Earth: Global, Regional, and Laboratory Studies*, pp. 475–487.

Abrahamson, N.A., Silva, W.J. and Kamai, R. (2014) “Summary of the ASK14 ground motion relation for active crustal regions,” *Earthquake Spectra*, 30(3), pp. 1025–1055.

Aki, K. (1980) “Scattering and attenuation of shear waves in the lithosphere,” *Journal of Geophysical Research: Solid Earth*, 85(B11), pp. 6496–6504.

Aki, K. and Chouet, B. (1975) “Origin of coda waves: source, attenuation, and scattering effects,” *Journal of geophysical research*, 80(23), pp. 3322–3342.

Akkar, S., Sandıkkaya, M. A., & Bommer, J. J. (2014). "Empirical ground-motion models for point-and extended-source crustal earthquake scenarios in Europe and the Middle East". *Bulletin of earthquake engineering*, 12(1), 359-387.

Anderson, J.G. and Hough, S.E. (1984) “A model for the shape of the Fourier amplitude spectrum of acceleration at high frequencies,” *Bulletin of the Seismological Society of America*, 74(5), pp. 1969–1993.

Anderson, J.G. and Humphrey Jr, J.R. (1947) “A least squares method for objective determination of earthquake source parameters,” *Seismological Research Letters*, 62(3–4), pp. 201–209.

Al Atik, L., Kottke, A., Abrahamson, N., & Hollenback, J. (2014). "Kappa (κ) scaling of ground-motion prediction equations using an inverse random vibration theory approach". *Bulletin of the Seismological Society of America*, *104*(1), 336-346.

Atkinson, G.M. (2015) “Ground-motion prediction equation for small-to-moderate events at short hypocentral distances, with application to induced-seismicity hazards,” *Bulletin of the Seismological Society of America*, 105(2A), pp. 981–992.

Atkinson, G.M. and Morrison, M. (2009) “Observations on regional variability in ground-motion amplitudes for small-to-moderate earthquakes in North America,” *Bulletin of the Seismological Society of America*, 99(4), pp. 2393–2409.

Baker, J.W. and Allin Cornell, C. (2005) “A vector-valued ground motion intensity measure consisting of spectral acceleration and epsilon,” *Earthquake Engineering & Structural Dynamics*, 34(10), pp. 1193–1217.

Baker, Jack W. "Conditional mean spectrum: Tool for ground-motion selection." *Journal of structural engineering* 137, no. 3 (2011): 322-331.

Beauval, C., Tasan, H., Laurendeau, A., Delavaud, E., Cotton, F., Guéguen, P., & Kuehn, N. (2012). "On the testing of ground-motion prediction equations against small-magnitude data". *Bulletin of the Seismological Society of America*, *102*(5), 1994-2007.

Biasi, G.P. and Smith, K.D. (2001) “Site effects for seismic monitoring stations in the vicinity of Yucca Mountain,” *Nevada, MOL20011204*, 45.

Bindi, D., Massa, M., Luzi, L., Ameri, G., Pacor, F., Puglia, R., & Augliera, P. (2014). "Pan-European ground-motion prediction equations for the average horizontal component of PGA, PGV, and 5%-damped PSA at spectral periods up to 3.0 s using the RESORCE dataset". *Bulletin of earthquake engineering*, *12*(1), 391-430.

Bocchini, Gian Maria, Armin Dielforder, Kilian B. Kemna, Rebecca M. Harrington, and Elizabeth S. Cochran. "Earthquake stress-drop values delineate spatial variations in maximum shear stress in the Japanese forearc lithosphere." *Communications Earth & Environment* 6, no. 1 (2025): 858.

Bolt, B.A., Abrahamson, N.A. and Lee, W.H.K. (2003) “Estimation of strong seismic ground motions,” *International Geophysics Series*, 81(B), pp. 983–1002.

Bommer, J. J., Douglas, J., Scherbaum, F., Cotton, F., Bungum, H., & Fah, D. (2010). "On the selection of ground-motion prediction equations for seismic hazard analysis". *Seismological Research Letters*, *81*(5), 783-793.

Bommer, J.J., Coppersmith, K.J., Coppersmith, R.T., Hanson, K.L., Mangongolo, A., Neveling, J., Rathje, E.M., Rodriguez-Marek, A., Scherbaum, F., Shelembe, R. and Stafford, P.J. (2015). "A SSHAC level 3 probabilistic seismic hazard analysis for a new-build nuclear site in South Africa”, *Earthquake Spectra*, *31*(2), pp.661-698.

Bommer, J.J. and Acevedo, A.B. (2004) “The use of real earthquake accelerograms as input to dynamic analysis,” *Journal of Earthquake Engineering*, 8(spec01), pp. 43–91.

Bommer, J. J., & Crowley, H. (2017). “The purpose and definition of the minimum magnitude limit in PSHA calculations”. Seismological Research Letters, 88(4), 1097–1106. https://doi.org/10.1785/0220170015

Bommer, J.J. and Scott, S.G. (2000) “The feasibility of using real accelerograms for seismic design,” *Implications of recent earthquakes on seismic risk*, 2, pp. 115–126.

Boore, D. M., Stewart, J. P., Seyhan, E., & Atkinson, G. M. (2014). “NGA-West2 equations for predicting PGA, PGV, and 5% damped PSA for shallow crustal earthquakes”. *Earthquake Spectra*, *30*(3), 1057-1085.

Boore, D.M. and Bommer, J.J. (2005) “Processing of strong-motion accelerograms: needs, options and consequences,” *Soil Dynamics and Earthquake Engineering*, 25(2), pp. 93–115.

Buscetti, M., Traversa, P., Perron, V., Rischette, P., Hollender, F., & Shible, H. (2025). “Epos-France Database of Earthquake Ground Motion for Mainland France”: 1996–2021 Updated Version. *Seismological Research Letters*, *96*(2A), 1214-1226.

Calvet, M. and Margerin, L. (2013) “Lapse-time dependence of coda Q: Anisotropic multiple-scattering models and application to the Pyrenees,” *Bulletin of the Seismological Society of America*, 103(3), pp. 1993–2010.

Camelbeeck, T. (1985) “Recent seismicity in Hainaut—scaling laws from the seismological stations in Belgium and Luxemburg,” in *Seismic Activity in Western Europe: with Particular Consideration to the Liège Earthquake of November 8, 1983*. Springer, pp. 109–126.

Camelbeeck, T., Van Noten, K., Lecocq, T., & Hendrickx, M. (2022). “The damaging character of shallow 20th century earthquakes in the Hainaut coal area (Belgium)”. *Solid Earth*, *13*(3), 469-495.

Camelbeeck, T., Van Noten, K., and Lecocq, T. (2025) “The 1965–1970 seismic episode in the Hainaut coal basin (Belgium): a key period to analyse the triggered nature of a century-long seismic activity,” *Geologica Belgica* [Preprint].

Camelbeeck, Thierry. (1993) *"Mécanisme au foyer des tremblements de terre et contraintes tectoniques: le cas de la zone intraplaque belge." PhD diss.,* . UCL-Université Catholique de Louvain, 1993.

Campbell, K.W. (2009) “Estimates of shear-wave Q and κ 0 for unconsolidated and semiconsolidated sediments in Eastern North America,” *Bulletin of the Seismological Society of America*, 99(4), pp. 2365–2392.

Campbell, K.W. and Bozorgnia, Y. (2014) “NGA-West2 ground motion model for the average horizontal components of PGA, PGV, and 5% damped linear acceleration response spectra,” *Earthquake Spectra*, 30(3), pp. 1087–1115.

Campillo, M. and Plantet, J.L. (1991) “Frequency dependence and spatial distribution of seismic attenuation in France: experimental results and possible interpretations,” *Physics of the earth and planetary interiors*, 67(1–2), pp. 48–64.

Cauzzi, C., Edwards, B., Fäh, D., Clinton, J., Wiemer, S., Kästli, P., Cua, G. and Giardini, D., (2014) “New predictive equations and site amplification estimates for the next-generation Swiss ShakeMaps”. *Geophysical Journal International*, *200*(1), pp.421-438.

Chandramohan, Reagan, Jack W. Baker, and Gregory G. Deierlein. "Quantifying the influence of ground motion duration on structural collapse capacity using spectrally equivalent records." *Earthquake Spectra* 32, no. 2 (2016): 927-950.

Chiou, B., Youngs, R., Abrahamson, N., & Addo, K. (2010). “Ground-motion attenuation model for small-to-moderate shallow crustal earthquakes in California and its implications on regionalization of ground-motion prediction models”. *Earthquake spectra*, *26*(4), 907-926.

Chiou, B.S.-J. and Youngs, R.R. (2014) “Update of the Chiou and Youngs NGA model for the average horizontal component of peak ground motion and response spectra,” *Earthquake Spectra*, 30(3), pp. 1117–1153.

Cormier, V.F. (1982) “The effect of attenuation on seismic body waves,” *Bulletin of the Seismological Society of America*, 72(6B), pp. S169–S200.

Dainty, A.M. (1981) “A scattering model to explain seismic Q observations in the lithosphere between 1 and 30 Hz,” *Geophysical Research Letters*, 8(11), pp. 1126–1128.

Dorie, V. and Dorie, M.V. (2015) “Package ‘blme,’” *Bayesian Linear Mixed-Effects Models. URL https://CRAN. R-project. org/package= blme* [Preprint].

Douglas, J., Gehl, P., Bonilla, L. F., & Gélis, C. (2010). “A κ model for mainland France. *Pure and applied geophysics’*, *167*(11), 1303-1315.

Drouet, S., Ameri, G., Le Dortz, K., Secanell, R., & Senfaute, G. (2020). “A probabilistic seismic hazard map for the metropolitan France”. *Bulletin of Earthquake Engineering*, *18*(5), 1865-1898.

Drouet, S., Cotton, F. and Guéguen, P. (2010) “v S 30, κ, regional attenuation and M w from accelerograms: application to magnitude 3–5 French earthquakes,” *Geophysical Journal International*, 182(2), pp. 880–898.

Edwards, B., Ktenidou, O. J., Cotton, F., Fäh, D., Van Houtte, C., & Abrahamson, N. A. (2015). “Near-surface attenuation (Kappa0) determination at hard rock sites in Switzerland”. *Geophysical Journal International*, *202*(3), 1627-1645.

Edwards, B. and Douglas, J. (2013) “Selecting ground-motion models developed for induced seismicity in geothermal areas,” *Geophysical Journal International*, 195(2), pp. 1314–1322.

ElBouch Abdelhali, Thierry Camelbeeck, Henri Martin. 2002. “Atténuation des ondes sismiques en belgique et dans les régions limitrophes à partir de la coda des tremblements de terre locaux.“ Geologica Belgica (2002) 5/1-2: 17-29.

Fielitz, D. and Wegler, U. (2015) “Intrinsic and scattering attenuation as derived from fluid induced microseismicity at the German Continental Deep Drilling site,” *Geophysical Journal International*, 201(3), pp. 1346–1361.

Frankel, A. and Clayton, R.W. (1986) “*Finite Difference Simulations of Seismic Scattering Implications for the Propagation of Short-Period Seismic Waves in the Crust and Models of Crustal Heterogeneity*, *JOURNAL OF GEOPHYSICAL RESEARCH*.

Futterman, W.I. (1962) “Dispersive body waves,” *Journal of Geophysical research*, 67(13), pp. 5279–5291.

Gentili, S. and Franceschina, G. (2011) “High frequency attenuation of shear waves in the southeastern Alps and northern Dinarides,” *Geophysical Journal International*, 185(3), pp. 1393–1416.

Goulet, C.A. and Cramer, C.H. (2014) “PEER NGA-East Database”, Pacific Earthquake Engineering Center, PEER Report 2014/17.

Grünthal, G., Stromeyer, D., Bosse, C., Cotton, F., & Bindi, D. (2018) “Correction to: The probabilistic seismic hazard assessment of Germany—version 2016, considering the range of epistemic uncertainties and aleatory variability”. *Bulletin of Earthquake Engineering*, *16*(10), 4397-4398.

Hancock, J. and Bommer, J.J. (2007) “Using spectral matched records to explore the influence of strong-motion duration on inelastic structural response,” *Soil Dynamics and Earthquake Engineering*, 27(4), pp. 291–299.

Hough, S. E., J. G. Anderson, J. Brune, F. Vernon III, Jon Berger, J. Fletcher, L. Haar, L. Hanks, and L. Baker. (1988) "Attenuation near Anza, California." *Bulletin of the Seismological Society of America* 78, no. 2 (1988): 672-691.

Van Houtte, C., Drouet, S. and Cotton, F. (2011) “Analysis of the origins of κ (kappa) to compute hard rock to rock adjustment factors for GMPEs,” *Bulletin of the Seismological Society of America*, 101(6), pp. 2926–2941.

Iervolino, I., Manfredi, G. and Cosenza, E. (2006) “Ground motion duration effects on nonlinear seismic response,” *Earthquake engineering & structural dynamics*, 35(1), pp. 21–38.

Johnson, P.C.D. (2014) “Extension of Nakagawa & Schielzeth’s R2GLMM to random slopes models,” *Methods in ecology and evolution*, 5(9), pp. 944–946.

Goraj Veronique (2000) “*Etude de l’attenuation des ondes S dans la croute en Belgique*“. Master’s thesis, Universite Catholique de Louvain.

Kagawa, T., Irikura, K. and Somerville, P.G. (2004) “Differences in ground motion and fault rupture process between the surface and buried rupture earthquakes,” *Earth, Planets and Space*, 56(1), pp. 3–14.

Kale, Ö. and Akkar, S. (2013) “A new procedure for selecting and ranking ground-motion prediction equations (GMPEs): The Euclidean distance-based ranking (EDR) method,” *Bulletin of the Seismological Society of America*, 103(2A), pp. 1069–1084.

Katsanos, E.I., Sextos, A.G. and Manolis, G.D. (2010) “Selection of earthquake ground motion records: A state-of-the-art review from a structural engineering perspective,” *Soil dynamics and earthquake engineering*, 30(4), pp. 157–169.

Knopoff, L. (1964) “Crustal stresses and seismodynamic characteristics in the upper crust,” *Rev. Geophys*, 2, pp. 625–660.

Krischer, Lion, James Smith, Wenjie Lei, Matthieu Lefebvre, Youyi Ruan, Elliott Sales De Andrade, Norbert Podhorszki, Ebru Bozdağ, and Jeroen Tromp (2016). "An adaptable seismic data format." *Geophysical Supplements to the Monthly Notices of the Royal Astronomical Society* 207, no. 2 : 1003-1011.

Ktenidou, O. J., Cotton, F., Abrahamson, N. A., & Anderson, J. G. (2014). Taxonomy of κ: A review of definitions and estimation approaches targeted to applications. *Seismological Research Letters*, *85*(1), 135-146.

Ktenidou, O. and Abrahamson, N.A. (2016) “Empirical estimation of high-frequency ground motion on hard rock,” *Seismological Research Letters*, 87(6), pp. 1465–1478.

Ktenidou, O. J., Abrahamson, N. A., Drouet, S., & Cotton, F. (2015). Understanding the physics of kappa (κ): Insights from a downhole array. *Geophysical Journal International*, *203*(1), 678-691.

Ktenidou, O. J., Abrahamson, N. A., Darragh, R. B., & Silva, W. J. (2016) “A methodology for the estimation of kappa (κ) for large datasets. Example application to rock sites in the NGA-East database”.

Ktenidou, O.-J.; D.R.B.; S.W.J.; T.P.; B.Y. and Corporate author: Electric Power Research Institute (EPRI) (2021) *Seismic Hazard Research Kappa and High-Frequency Ground Motion Effects at Hard-Rock Sites*. Palo Alto, CA.

Kurama, Y.C. and Farrow, K.T. (2003) “Ground motion scaling methods for different site conditions and structure characteristics,” *Earthquake engineering & structural dynamics*, 32(15), pp. 2425–2450.

Kwon, O.-S. and Elnashai, A. (2006) “The effect of material and ground motion uncertainty on the seismic vulnerability curves of RC structure,” *Engineering structures*, 28(2), pp. 289–303.

Lee, L.H., Lee, H.H. and Han, S.W. (2000) “Method of selecting design earthquake ground motions for tall buildings,” *The structural design of tall buildings*, 9(3), pp. 201–213.

Lin, P.-S. and Lee, C.-T. (2008) “Ground-motion attenuation relationships for subduction-zone earthquakes in northeastern Taiwan,” *Bulletin of the Seismological Society of America*, 98(1), pp. 220–240.

Luzi, L., Puglia, R., Russo, E., D'Amico, M., Felicetta, C., Pacor, F., ... & Zare, M. (2016). The engineering strong-motion database: A platform to access Pan-European accelerometric data. *Seismological Research Letters*, *87*(4), 987-997.

Malhotra, P.K. (2003) “Strong-motion records for site-specific analysis,” *Earthquake Spectra*, 19(3), pp. 557–578.

Mayor, J., Traversa, P., Calvet, M., & Margerin, L. (2018). Tomography of crustal seismic attenuation in Metropolitan France: implications for seismicity analysis. *Bulletin of Earthquake Engineering*, *16*(6), 2195-2210.

Moratto, L., Panebianco, S., Satriano, C., Stabile, T. A., & Priolo, E. (2025) “Using ambient noise k 0 estimation to improve microearthquake source parameters assessment in the High Agri Valley”. *Geophysical Journal International*, *242*(2), ggaf191.

Mosca, I., Sargeant, S., Baptie, B., Musson, R. M. W., & Pharaoh, T. C. (2022). The 2020 national seismic hazard model for the United Kingdom. *Bulletin of Earthquake Engineering*, *20*(2), 633-675.

Musson, R. (2012) “On the nature of logic trees in probabilistic seismic hazard assessment,” *Earthquake Spectra*, 28(3), pp. 1291–1296.

Nakagawa, S. and Schielzeth, H. (2013) “A general and simple method for obtaining R2 from generalized linear mixed-effects models,” *Methods in ecology and evolution*, 4(2), pp. 133–142.

Neefs, B., Van Noten, K., Vanneste, K., & Camelbeeck, T. (2024). The Belgian traditional macroseismic (BTM) database of the twentieth century. *Journal of Seismology*, 1-32.

Van Noten, K., Lecocq, T., Sira, C., Hinzen, K. G., & Camelbeeck, T. (2017). “Path and site effects deduced from merged transfrontier internet macroseismic data of two recent M4 earthquakes in northwest Europe using a grid cell approach”. *Solid Earth*, *8*(2), 453-477.

Nuttli, O.W. (1973) “Seismic wave attenuation and magnitude relations for eastern North America,” *Journal of Geophysical Research*, 78(5), pp. 876–885.

Onvani Mahsa ; Vanneste Kris. “*BELSHAKE kappa dataset”.* [Dataset]. Royal Observatory of Belgium. https://doi.org/10.5281/zenodo.17857380

Oth, A., Bindi, D., Parolai, S., & Wenzel, F. (2008). S-wave attenuation characteristics beneath the Vrancea region in Romania: new insights from the inversion of ground-motion spectra. *Bulletin of the Seismological Society of America*, *98*(5), 2482-2497..

Pacor, Francesca, Roberto Paolucci, Lucia Luzi, Fabio Sabetta, Andrea Spinelli, Antonella Gorini, Mario Nicoletti, Sandro Marcucci, Luisa Filippi, and Mauro Dolce. (2011) "Overview of the Italian strong motion database ITACA 1.0." *Bulletin of Earthquake Engineering* 9, no. 6 (2011): 1723-1739.

Papageorgiou, A.S. and Aki, K. (1983) “A specific barrier model for the quantitative description of inhomogeneous faulting and the prediction of strong ground motion. Part II. Applications of the model,” *Bulletin of the Seismological Society of America*, 73(4), pp. 953–978.

Parolai, S., Lai, C. G., Dreossi, I., Ktenidou, O. J., & Yong, A. (2022). « A review of near-surface QS estimation methods using active and passive sources”. *Journal of Seismology*, *26*(4), 823-862.

Parolai, S. and Bindi, D. (2004) “Influence of soil-layer properties on k evaluation,” *Bulletin of the Seismological Society of America*, 94(1), pp. 349–356.

Perron, V., Hollender, F., Bard, P. Y., Gélis, C., Guyonnet-Benaize, C., Hernandez, B., & Ktenidou, O. J. (2017). “Robustness of kappa (κ) measurement in low-to-moderate seismicity areas: Insight from a site-specific study in Provence, France”. *Bulletin of the Seismological Society of America*, *107*(5), 2272-2292.

Perron, V., Laurendeau, A., Hollender, F., Bard, P. Y., Gélis, C., Traversa, P., & Drouet, S. (2018) “Selecting time windows of seismic phases and noise for engineering seismology applications: A versatile methodology and algorithm”. *Bulletin of Earthquake Engineering*, *16*(6), 2211-2225..

Richards, P.G. and Menke, W. (1983) “*THE APPARENT ATTENUATION OF A SCATTERING MEDIUM”*, *Bulletin of the Seismological Society of America*. *73*(4), 1005-1021.

Rietbrock, A., Strasser, F. and Edwards, B. (2013) “A stochastic earthquake ground-motion prediction model for the United Kingdom,” *Bulletin of the Seismological Society of America*, 103(1), pp. 57–77.

Sato, H., Fehler, M.C. and Maeda, T. (2012) "*Seismic wave propagation and scattering in the heterogeneous earth"*. Springer.

Satriano, C. (2025) "SourceSpec Documentation."

Satriano, C., Mejia Uquiche, A.R. and Saurel, J.-M. (2016) "Spectral estimation of seismic moment, corner frequency and radiated energy for earthquakes in the Lesser Antilles," in *AGU fall meeting abstracts*, pp. S13A-2518.

Sawada, T. (1992) " Relation between maximum amplitude ratios (a/v, ad/v^ 2) and spectral parameters of earthquake ground motion". In *Proc. of 10th World Conf. on Earthquake Eng.* (Vol. 2, pp. 617-622).

Scherbaum, F., Cotton, F. and Smit, P. (2004) "On the use of response spectral-reference data for the selection and ranking of ground-motion models for seismic-hazard analysis in regions of moderate seismicity: The case of rock motion," *Bulletin of the seismological society of America*, 94(6), pp. 2164–2185.

Scherbaum, F., Delavaud, E. and Riggelsen, C. (2009) "Model selection in seismic hazard analysis: An information-theoretic perspective," *Bulletin of the Seismological Society of America*, 99(6), pp. 3234–3247.

Seabold, S. and Perktold, J. (2010) "Statsmodels: econometric and statistical modeling with python.," *SciPy*, 7(1), pp. 92–96.

Shome, N., Cornell, C. A., Bazzurro, P., & Carballo, J. E. (1998). "Earthquakes, records, and nonlinear responses". *Earthquake spectra*, *14*(3), 469-500.

Silva, W., & Darragh, R. B. (1995). "*Engineering characterization of strong ground motion recorded at rock sites. Final report* (No. EPRI-TR-102262)". Electric Power Research Inst.(EPRI), Palo Alto, CA (United States); Pacific Engineering and Analysis, Inc., El Cerrito, CA (United States).

Stanko, D., Markušić, S., Ivančić, I., Mario, G., & Gülerce, Z. (2017) "Preliminary estimation of Kappa parameter in Croatia". In *IOP Conference Series: Earth and Environmental Science* (Vol. 95, No. 3, p. 032014). IOP Publishing.

Stewart, J. P., Chiou, S. J., Bray, J. D., Graves, R. W., Somerville, P. G., & Abrahamson, N. A. (2002) "Ground motion evaluation procedures for performance-based design". *Soil dynamics and earthquake engineering*, *22*(9-12), 765-772.

Takemura, S., Furumura, T. and Maeda, T. (2015) “Scattering of high-frequency seismic waves caused by irregular surface topography and small-scale velocity inhomogeneity,” *Geophysical Journal International*, 201(1), pp. 459–474.

Traversa, Paola, Emeline Maufroy, Fabrice Hollender, Vincent Perron, Vincent Bremaud, Hussein Shible, Stéphane Drouet et al. "RESIF RAP and RLBP dataset of earthquake ground motion in mainland France." *Seismological Research Letters* 91, no. 4 (2020): 2409-2424.

Tso, W.K., Zhu, T.J. and Heidebrecht, A.C. (1992) “Engineering implication of ground motion A/V ratio,” *Soil Dynamics and Earthquake Engineering*, 11(3), pp. 133–144.

Vanneste,K., Vleminckx, B., Verbeeck, K., and Camelbeeck T. (2014) "Development of seismic hazard maps for Belgium." In *Workshop: Results of the European Project*.

Vanneste, K., Vleminckx, B., Verbeeck, K., Camelbeeck, T., (2015) “*Seismic Hazard Re-Evaluation of the Nuclear Power Plant sites Doel and Tihange Seismological Analyses and PSHA”*. Royal Observatory of Belgium.

Vanneste, K. and Camelbeeck, T. (2022) “Testing the applicability of GMPEs for the Hainaut region (Belgium) using macroseismic intensity data,” in *EGU General Assembly Conference Abstracts*, pp. EGU22-4093.

Vanneste, K., Camelbeeck, T. and Lecocq, T. (2025) “Recalibration of the local magnitude scale of the Belgian seismic network: Improved models of geometrical spreading and path duration”, Seismica (submitted). Preprint available on Research Square: https://doi.org/10.21203/rs.3.rs-7850272/v1.

Vanneste, K. and Onvani, M. (2025) “Belgian ground-motion database (BELSHAKE) flatfile,” *Royal Observatory of Belgium* [Preprint]. Available at: https://doi.org/https://doi.org/10.5281/zenodo.15241694.

Verbeeck, K., Vanneste, K. and Camelbeeck, T. (2009) “Seismotectonic zones for probabilistic seismic-hazard assessment in Belgium,” *ONDRAF/NIRAS, Brussels* [Preprint].

Villani, Manuela, Barbara Polidoro, Rory McCully, Thomas Ader, Ben Edwards, Andreas Rietbrock, Ziggy Lubkowski, Tim J. Courtney, and Martin Walsh (2019) "A selection of GMPEs for the United Kingdom based on instrumental and macroseismic datasets." *Bulletin of the Seismological Society of America* 109, no. 4: 1378-1400.

Yenier, E. and Atkinson, G.M. (2015) “Regionally adjustable generic ground-motion prediction equation based on equivalent point-source simulations: Application to central and eastern North America,” *Bulletin of the Seismological Society of America*, 105(4), pp. 1989–2009.

Youngs, R., Power, M. and Chin, C. (2006) “Design ground motion library,” in *Proceedings, 8th National Conference on Earthquake Engineering*, p. 10.

11 Supplementary information

Table S1. Summary of κ_0, κ_{r_s}, R^2 values, and the number of records for the H component of all stations; analyzed by Free kappa gradient method.

station	Component	$\boldsymbol{\kappa_0}$ $(\boldsymbol{ms})$	$\boldsymbol{\kappa_{r\_s}}$ $(\boldsymbol{ms/km})$	$\boldsymbol{R^2}$	$\boldsymbol{N}$	reliability
BE.BEBN	H	23.09	0.10	0.45	85	
BE.BOST	H	-0.66	0.10	0.15	3	unreliable
BE.BRE.00	H	35.68	0.41	0.97	5	
BE.BRE.01	H	151.93	-1.45	0.12	4	unreliable
BE.CLA	H	35.45	0.06	0.10	96	
BE.CSE	H	-33.46	0.42	0.46	7	unreliable
BE.CTH	H	31.82	0.21	0.32	5	
BE.CTH.01	H	-9.15	0.48	0.57	11	unreliable
BE.DOU	H	19.90	0.14	0.23	78	
BE.DSLB	H	29.08	0.13	0.31	8	
BE.DSLS	H	39.52	0.20	1.00	2	
BE.GES	H	21.82	0.19	0.54	75	
BE.HEY	H	-2.74	0.40	0.93	9	unreliable
BE.HOF	H	19.15	0.92	1.00	2	
BE.HOU	H	22.90	0.17	0.47	17	
BE.HRK	H	53.32	0.04	0.07	28	
BE.HU1	H	-17.56	0.53	0.73	6	unreliable
BE.HUM	H	58.85	-0.04	0.01	58	
BE.KAN	H	55.38	0.60	1.00	2	
BE.KIN	H	76.28	0.06	0.00	7	
BE.KLB	H	6.00	0.30	0.28	90	
BE.LCH	H	20.86	0.20	0.64	38	
BE.LES	H	99.94	-0.14	0.05	10	
BE.MASA	H	88.91	-1.13	0.46	3	unreliable
BE.MEMA	H	31.37	0.21	0.28	8	
BE.MEMB	H	12.41	0.28	0.27	36	
BE.MEMH	H	34.02	0.08	0.17	25	
BE.MEMS	H	26.83	0.14	0.31	68	
BE.MEU	H	59.44	0.13	0.06	25	
BE.MOL2	H	10.26	0.32	0.97	3	
BE.MOL3	H	27.76	0.21	1.00	2	
BE.MOL4	H	28.95	0.21	1.00	2	
BE.MOL5	H	34.06	0.01	1.00	2	
BE.MOLT	H	28.75	0.14	0.72	20	

station	Component	$\kappa_0\ (ms)$	$\kappa_{r\_s}\ (ms/km)$	R^2	N	reliability
BE.MRD	H	17.10	0.16	0.61	36	
BE.MRG	H	27.62	0.09	0.21	11	
BE.OPT	H	26.16	0.16	0.47	15	
BE.OPTB	H	8.54	0.33	0.99	4	
BE.OSP	H	38.25	0.57	0.86	5	
BE.PLT	H	21.29	0.25	0.53	6	
BE.RCHB	H	16.13	0.11	0.57	17	
BE.ROB	H	48.07	-0.18	0.05	18	
BE.SKQ	H	27.08	0.10	0.24	48	
BE.TMM1	H	9.81	0.29	0.77	8	
BE.TMM2	H	-5.24	0.51	0.87	8	unreliable
BE.TMM3	H	4.69	0.35	0.88	8	
BE.TMM4	H	-2.07	0.38	0.93	8	unreliable
BE.TNL	H	99.15	-0.16	0.87	4	unreliable
BE.UCCB	H	-0.44	0.15	0.44	5	unreliable
BE.UCCS	H	103.51	-0.18	0.04	11	
BE.VIA	H	15.65	0.19	0.21	74	
BE.WIB	H	20.00	0.00	0.00	3	
BE.WLF	H	28.79	0.11	0.26	68	
BE.WOR	H	0.10	0.62	0.38	3	
BE.ZEV	H	34.05	0.10	0.68	4	
BQ.BA01	H	-9.44	2.13	1.00	2	unreliable
BQ.HILG	H	159.15	-2.19	0.02	3	unreliable
BQ.RODG	H	31.88	0.39	0.25	6	
GE.WLF	H	27.02	0.04	0.02	5	
NL.GUR1	H	38.68	0.16	1.00	2	
NL.TRZ.00	H	157.35	-2.43	1	2	unreliable

Table S2. Summary of of κ_0, κ_{r_s}, R^2 values, and the number of records for the Z component of all stations; analyzed by free kappa gradient method

station	Component	κ_0 (ms)	κ_{r_s} (ms/km)	R^2	N	reliability
BE.AUL	Z	69.80	-0.11	0.03	21	
BE.BEBN	Z	22.71	0.09	0.22	125	
BE.BON	Z	2.39	0.20	1.00	2	
BE.BOST	Z	-6.29	0.14	0.08	3	unreliable
BE.BOU	Z	26.88	0.15	0.21	44	
BE.BRE.01	Z	22.53	0.12	0.05	5	
BE.BRQ.00	Z	82.89	-0.05	0.00	14	
BE.BRQ.01	Z	37.88	0.03	0.02	8	
BE.CLA	Z	29.62	0.06	0.10	104	
BE.COI	Z	69.32	-0.44	1.00	2	unreliable
BE.CSE	Z	4.62	0.19	0.50	9	
BE.CTH	Z	33.64	0.07	0.05	15	
BE.CTH.01	Z	10.23	0.27	0.17	10	
BE.DOU	Z	15.91	0.14	0.22	117	
BE.DSLB	Z	6.65	0.14	0.60	11	
BE.DSLS	Z	3.13	0.18	1.00	2	
BE.GES	Z	24.42	0.06	0.16	63	
BE.HEY	Z	-0.64	0.33	0.54	10	
BE.HOU	Z	20.43	0.25	0.66	12	
BE.HRK	Z	45.71	0.04	0.03	28	
BE.HU1	Z	-18.88	0.51	0.53	7	unreliable
BE.HUM	Z	43.04	-0.02	0.00	67	
BE.KAN	Z	29.53	0.00	1.00	2	unreliable
BE.KIN	Z	77.87	0.12	0.00	9	
BE.KLB	Z	18.54	0.05	0.10	69	
BE.LCH	Z	11.16	0.17	0.74	42	
BE.LES	Z	52.86	-0.07	0.03	37	
BE.MASA	Z	104.82	-1.18	0.61	3	unreliable
BE.MEMA	Z	21.43	0.10	0.09	9	
BE.MEMB	Z	26.13	0.10	0.04	51	
BE.MEMH	Z	22.08	0.08	0.38	29	
BE.MEMS	Z	21.70	0.11	0.44	141	
BE.MEU	Z	61.26	-0.07	0.02	45	
BE.MOL2	Z	-0.34	0.24	0.98	3	unreliable

station	Component	$\kappa_0\ (ms)$	$\kappa_{r\_s}\ (ms/km)$	R^2	N	reliability
BE.MOLT	Z	37.06	0.12	0.05	4	
BE.MRD	Z	7.09	0.20	0.43	45	
BE.MRG	Z	18.82	0.02	0.20	5	
BE.OPT	Z	20.64	0.14	0.75	7	
BE.OPTB	Z	16.87	0.12	0.92	3	
BE.OSP	Z	37.09	0.10	0.35	6	
BE.OTT	Z	-11.33	0.26	1.00	2	unreliable
BE.PLT	Z	53.13	-0.15	0.21	7	
BE.RCHB	Z	16.83	0.13	0.34	25	
BE.ROB	Z	32.41	0.02	0.00	32	
BE.RQR	Z	26.35	0.09	0.15	57	
BE.SKQ	Z	26.82	0.03	0.03	38	
BE.SNF	Z	71.21	-0.05	0.03	84	
BE.STI	Z	38.87	0.15	0.20	95	
BE.TMM1	Z	30.18	-0.09	0.17	6	
BE.TMM2	Z	5.00	0.31	0.61	6	
BE.TMM3	Z	12.44	0.13	0.31	9	
BE.TMM4	Z	10.18	0.14	0.88	6	
BE.TNL	Z	26.72	0.03	0.07	7	
BE.UCCB	Z	49.79	-0.05	0.03	7	
BE.UCCS	Z	19.04	0.13	0.13	16	
BE.VIA	Z	17.39	0.15	0.12	77	
BE.WIB	Z	23.57	-0.12	1.00	2	unreliable
BE.WLF	Z	27.10	0.10	0.14	74	
BE.WOR	Z	150.44	-0.41	0.63	3	unreliable
BE.ZEV	Z	39.22	-0.01	0.01	6	
BQ.DREG	Z	39.93	-0.27	1.00	2	unreliable
BQ.HILG	Z	199.21	-3.13	0.01	3	unreliable
BQ.KLL	Z	20.59	-0.05	1.00	2	unreliable
BQ.RODG	Z	40.09	0.20	0.16	8	
GE.WLF	Z	27.47	-0.03	0.12	5	
NL.GUR1	Z	86.38	-0.15	0.50	3	unreliable

Table S3. Sensitivity analysis, result of κ_r, and R^2 values across different κ_0 ranges. Note improved R^2 values for results obtained with (0, 50) ms κ_0 range

crustal domain	component	$\boldsymbol{\kappa_r}$ ($\boldsymbol{ms/km}$)	$\boldsymbol{R^2}$	$\boldsymbol{N}$
		κ_r range = (0, 0.3), κ_0 range = (0, 100)		
ABM	H	0.04	0.10	115
ABM	Z	**0.04**	0.17	163
ARD	H	0.15	0.64	857
ARD	Z	**0.04**	0.18	1070
HAIN	H	0.07	1.00	1
HAIN	Z	**0.04**	0.06	141
RVG	H	0.12	0.26	163
RVG	Z	**0.04**	0.10	183
		κ_r range = (0, 0.3), κ_0 range = (0, 90)		
ABM	H	0.04	0.10	115
ABM	Z	0.04	0.17	163
ARD	H	0.15	0.63	857
ARD	Z	0.04	0.18	1070
HAIN	H	0.12	1.00	1
HAIN	Z	0.07	0.18	141
RVG	H	0.12	0.25	163
RVG	Z	0.04	0.10	183
		κ_r range = (0, 0.3), κ_0 range = (0, 80)		
ABM	H	0.07	0.24	115
ABM	Z	0.04	0.17	163
ARD	H	0.15	0.63	857
ARD	Z	0.04	0.18	1070
HAIN	H	0.15	1.00	1
HAIN	Z	0.12	0.36	141
RVG	H	0.13	0.24	163
RVG	Z	0.04	0.10	183
		κ_r range = (0, 0.3), κ_0 range = (0, 70)		
ABM	H	0.12	0.40	115
ABM	Z	0.04	0.17	163
ARD	H	0.07	0.32	857
ARD	Z	0.04	0.18	1070
HAIN	H	0.19	1.00	1
HAIN	Z	0.12	0.36	141
RVG	H	0.13	0.25	163
RVG	Z	0.04	0.11	183

crustal domain	component	$\boldsymbol{\kappa_r}$ $(\boldsymbol{ms/km})$	$\boldsymbol{R}^2$	$\boldsymbol{N}$
		κ_r range = (0, 0.3), κ_0 range = (0, 60)		
ABM	H	0.12	0.41	115
ABM	Z	0.04	0.17	163
ARD	H	0.12	0.50	857
ARD	Z	0.07	0.36	1070
HAIN	H	0.23	1.00	1
HAIN	Z	0.03	0.04	141
RVG	H	0.12	0.20	163
RVG	Z	0.07	0.19	183
		κ_r range = (0, 0.3), κ_0 range **= (0, 50)**		
ABM	H	0,16	0,53	115
ABM	Z	0,05	0,26	163
ARD	H	0,15	0,61	857
ARD	Z	0,1	0,48	1070
HAIN	H	0,25	1	1
HAIN	Z	0,06	0,19	141
RVG	H	0,15	0,24	163
RVG	Z	0,08	0,21	183

Table S4. Derived κ_0 values of H component for all stations and κ_r for each crustal domain, calculated using the joint kappa gradient fit function. Note that standard deviations for this method are based on an approximation of the inverse Hessian matrix in the optimizer, which does not appear to be stable and often results in unrealistically high values.

crustal domain	component	station	$\boldsymbol{\kappa_0}$ $(\boldsymbol{ms})$	$\boldsymbol{\kappa_0}$ Std dev	$\boldsymbol{\kappa_r}$ $(\boldsymbol{ms}/\boldsymbol{km})$	reliability
ABM	H	BE.BOST	0	68,97	0,16	
ABM	H	BE.CSE	13	139,23	0,16	
ABM	H	BE.DSLB	24	130,12	0,16	
ABM	H	BE.DSLS	43	306,08	0,16	
ABM	H	BE.GRZ	37	306,66	0,16	
ABM	H	BE.LES	50	125,68	0,16	unreliable
ABM	H	BE.MOL1	25	304,1	0,16	
ABM	H	BE.MOL2	23	178,07	0,16	
ABM	H	BE.MOL3	31	216,44	0,16	
ABM	H	BE.MOL4	33	216,53	0,16	
ABM	H	BE.MOL5	24	216,52	0,16	
ABM	H	BE.MOLS	50	308,44	0,16	unreliable
ABM	H	BE.MOLT	26	85,15	0,16	
ABM	H	BE.OT2	8	305,67	0,16	
ABM	H	BE.OT3	16	304,83	0,16	
ABM	H	BE.OTT	0		0,16	
ABM	H	BE.SKQ	19	83,01	0,16	
ABM	H	BE.UCCB	3	190,58	0,16	
ABM	H	BE.UCCS	50	119,35	0,16	unreliable
ABM	H	BE.WOR	50	182,19	0,16	unreliable
ABM	H	BE.ZEV	22	319,05	0,16	
ARD	H	BE.ANSA	22	225,95	0,15	
ARD	H	BE.BEBN	18	28,42	0,15	
ARD	H	BE.CLA	26	29,2	0,15	
ARD	H	BE.CTH	37	113,76	0,15	
ARD	H	BE.CTH.01	22	69,6	0,15	
ARD	H	BE.DOU	16	37,93	0,15	
ARD	H	BE.GES	26	32,81	0,15	
ARD	H	BE.HEY	19	76,39	0,15	
ARD	H	BE.HOU	24	60,6	0,15	
ARD	H	BE.HU1	26	102,49	0,15	
ARD	H	BE.HUM	36	34,99	0,15	

crustal domain	component	station	κ_0 (ms)	κ_0 Std dev	κ_r (ms/km)	reliability
ARD	H	BE.KAN	50	226,66	0,15	unreliable
ARD	H	BE.KLB	19	28,77	0,15	
ARD	H	BE.LCH	25	39,67	0,15	
ARD	H	BE.MEMA	33	80,01	0,15	
ARD	H	BE.MEMB	18	41,21	0,15	
ARD	H	BE.MEMH	21	56,3	0,15	
ARD	H	BE.MEMS	26	31,49	0,15	
ARD	H	BE.MEU	50	55,97	0,15	unreliable
ARD	H	BE.MRD	18	47,47	0,15	
ARD	H	BE.MRG	23	72,69	0,15	
ARD	H	BE.PLT	33	94,06	0,15	
ARD	H	BE.RCHB	7	68,72	0,15	
ARD	H	BE.ROB	26	57,41	0,15	
ARD	H	BE.STWA	31	226,01	0,15	
ARD	H	BE.THEA	23	225,93	0,15	
ARD	H	BE.TMM1	20	80,7	0,15	
ARD	H	BE.TMM2	21	80,71	0,15	
ARD	H	BE.TMM3	19	80,66	0,15	
ARD	H	BE.TMM4	14	80,66	0,15	
ARD	H	BE.TNL	30	227,96	0,15	
ARD	H	BE.VEV	17	226,22	0,15	
ARD	H	BE.VIA	20	32,36	0,15	
ARD	H	BE.WIB	5	131,84	0,15	
ARD	H	BQ.BA01	28	159,74	0,15	
ARD	H	BQ.DREG	19	225,87	0,15	
ARD	H	NL.HGN	50	264,61	0,15	unreliable
ARD	H	NL.MAME	50	229,6	0,15	unreliable
ARD	H	NL.TERZ.00	48	159,89	0,15	unreliable
HAIN	H	BE.CLHA	26		0,25	
RVG	H	BE.BEBN	18	52,86	0,15	
RVG	H	BE.BRE.00	44	159,22	0,15	
RVG	H	BE.BRE.01	50	161,94	0,15	unreliable
RVG	H	BE.BREA	37	317,57	0,15	
RVG	H	BE.HRK	47	71,04	0,15	
RVG	H	BE.KAN	50	324,05	0,15	unreliable
RVG	H	BE.KIN	50	130,83	0,15	unreliable
RVG	H	BE.KINA	50	332,47	0,15	unreliable

crustal domain	component	station	κ_0 (ms)	κ_0 Std dev	κ_r (ms/km)	reliability
RVG	H	BE.MASA	50	184,04	0,15	unreliable
RVG	H	BE.OPT	27	90,89	0,15	
RVG	H	BE.OPTB	24	163,48	0,15	
RVG	H	BE.OSP	50	159,45	0,15	unreliable
RVG	H	BQ.BA01	29	224,6	0,15	
RVG	H	BQ.BA02	39	317,52	0,15	
RVG	H	BQ.DREG	13	319,34	0,15	
RVG	H	BQ.RODG	47	132,97	0,15	
RVG	H	BQ.TGA	50	318,74	0,15	unreliable
RVG	H	NL.GUR1	37	318,87	0,15	
RVG	H	NL.HGN	50	554,55	0,15	unreliable
RVG	H	NL.MAME	50	345,56	0,15	unreliable
RVG	H	NL.ROLD	50	353,23	0,15	unreliable
RVG	H	NL.TERZ.00	50	225,4	0,15	unreliable

Table S5. Derived κ_0 values of Z component for all stations and κ_r for each crustal domain, calculated using the joint kappa gradient fit function. Note that standard deviations for this method are based on an approximation of the inverse Hessian matrix in the optimizer, which does not appear to be stable and often results in unrealistically high values.

crustal domain	component	station	$\boldsymbol{\kappa_0}$ $(\boldsymbol{ms})$	$\boldsymbol{\kappa_0}$ Std dev	$\boldsymbol{\kappa_r}$ $(\boldsymbol{ms/km})$	reliability
ABM	Z	BE.BOST	7	128,24	0,05	
ABM	Z	BE.CSE	24	74,4	0,05	
ABM	Z	BE.DSLB	16	66,99	0,05	
ABM	Z	BE.DSLS	26	120,32	0,05	
ABM	Z	BE.GRZ	17	159,95	0,05	
ABM	Z	BE.LES	34	48,44	0,05	
ABM	Z	BE.MOL1	27	160,57	0,05	
ABM	Z	BE.MOL2	16	94,02	0,05	
ABM	Z	BE.MOL3	19	160,84	0,05	
ABM	Z	BE.MOL4	13	159,34	0,05	
ABM	Z	BE.MOL5	13	159,24	0,05	
ABM	Z	BE.MOLT	21	111,08	0,05	
ABM	Z	BE.OT2	24	160,12	0,05	
ABM	Z	BE.OT3	50	113,46	0,05	
ABM	Z	BE.OTT	14	116,18	0,05	
ABM	Z	BE.RQR	32	42,04	0,05	
ABM	Z	BE.SKQ	24	50,61	0,05	
ABM	Z	BE.UCCA	33	167,98	0,05	
ABM	Z	BE.UCCB	34	89,55	0,05	
ABM	Z	BE.UCCS	27	59,82	0,05	
ABM	Z	BE.WOR	50	100,52	0,05	unreliable
ABM	Z	BE.ZEV	32	88,73	0,05	
ARD	Z	BE.BEBN	21	17,69	0,1	
ARD	Z	BE.BON	17	170,52	0,1	
ARD	Z	BE.CLA	26	20,73	0,1	
ARD	Z	BE.COI	38	170,7	0,1	
ARD	Z	BE.CTH	34	57,47	0,1	
ARD	Z	BE.CTH.01	30	61,02	0,1	
ARD	Z	BE.DOU	22	22,99	0,1	
ARD	Z	BE.GES	19	26,93	0,1	
ARD	Z	BE.HEY	21	57,47	0,1	
ARD	Z	BE.HOU	38	55,32	0,1	

crustal domain	component	station	κ_0 (ms)	κ_0 Std dev	κ_r (ms/km)	reliability
ARD	Z	BE.HU1	31	77,09	0,1	
ARD	Z	BE.HUM	30	24,08	0,1	
ARD	Z	BE.KAN	25	170,64	0,1	
ARD	Z	BE.KLB	13	24,57	0,1	
ARD	Z	BE.LCH	17	30,81	0,1	
ARD	Z	BE.MEMA	22	64,58	0,1	
ARD	Z	BE.MEMB	21	26,77	0,1	
ARD	Z	BE.MEMH	20	39,58	0,1	
ARD	Z	BE.MEMP	36	170,66	0,1	
ARD	Z	BE.MEMS	22	16,73	0,1	
ARD	Z	BE.MEU	49	27,81	0,1	
ARD	Z	BE.MRD	20	31,92	0,1	
ARD	Z	BE.MRG	6	86,3	0,1	
ARD	Z	BE.PLT	19	70,8	0,1	
ARD	Z	BE.RCHB	24	42,03	0,1	
ARD	Z	BE.ROB	27	32,31	0,1	
ARD	Z	BE.STI	42	20,52	0,1	
ARD	Z	BE.THEA	21	170,67	0,1	
ARD	Z	BE.TMM1	20	76,49	0,1	
ARD	Z	BE.TMM2	23	76,68	0,1	
ARD	Z	BE.TMM3	15	60,67	0,1	
ARD	Z	BE.TMM4	12	76,63	0,1	
ARD	Z	BE.TNL	11	86,88	0,1	
ARD	Z	BE.VEN	17	170,73	0,1	
ARD	Z	BE.VIA	24	23,44	0,1	
ARD	Z	BE.WIB	5	120,55	0,1	
ARD	Z	BQ.BA01	24	170,54	0,1	
ARD	Z	BQ.DREG	21	120,79	0,1	
ARD	Z	BQ.KLL	13	120,66	0,1	
ARD	Z	NL.MAME	50	99,39	0,1	unreliable
ARD	Z	NL.TERZ.00	14	170,54	0,1	
ARD	Z	NL.VKB	20	173,22	0,1	
HAIN	Z	BE.AUL	42	84,72	0,06	
HAIN	Z	BE.AUL.00	50	273,08	0,06	unreliable
HAIN	Z	BE.BOU	41	81,5	0,06	
HAIN	Z	BE.BRQ.00	50	92,15	0,06	unreliable
HAIN	Z	BE.BRQ.01	29	127,5	0,06	

crustal domain	component	station	κ_0 (ms)	κ_0 Std dev	κ_r (ms/km)	reliability
HAIN	Z	BE.SNF	50	70,24	0,06	
RVG	Z	BE.BEBN	22	21,92	0,08	
RVG	Z	BE.BRE.01	23	86,29	0,08	
RVG	Z	BE.BREA	37	171,35	0,08	
RVG	Z	BE.HRK	44	37,61	0,08	
RVG	Z	BE.KAN	26	171,61	0,08	
RVG	Z	BE.KIN	50	68,44	0,08	unreliable
RVG	Z	BE.KINA	50	172,91	0,08	unreliable
RVG	Z	BE.MASA	50	124,66	0,08	unreliable
RVG	Z	BE.OPT	24	79,55	0,08	
RVG	Z	BE.OPTB	20	121,85	0,08	
RVG	Z	BE.OSP	42	85,86	0,08	
RVG	Z	BQ.BA01	22	171,33	0,08	
RVG	Z	BQ.DREG	21	121,61	0,08	
RVG	Z	BQ.KLL	14	121,65	0,08	
RVG	Z	BQ.RODG	50	65,77	0,08	
RVG	Z	BQ.TGA	45	171,7	0,08	
RVG	Z	NL.GUR1	50	124,93	0,08	unreliable
RVG	Z	NL.MAME	50	103,18	0,08	unreliable
RVG	Z	NL.ROLD	50	129,62	0,08	unreliable
RVG	Z	NL.TERZ.00	8	171,71	0,08	
RVG	Z	NL.VKB	21	182,79	0,08	

Table S6. Result of mixed effect method for H component of all crustal domains and stations

Crustal domain	Component	station	Random intercept	Random slope	Global intercept	Global slope κ_r	Station specific κ_0	Station specific slope κ_{r_s}
ABM	H	BE.BOST	2,54	-0,17	24,08	0,17	26,63	0,01
ABM	H	BE.CSE	-2,53	-0,01	24,08	0,17	21,56	0,17
ABM	H	BE.DSLB	0,83	-0,03	24,08	0,17	24,91	0,15
ABM	H	BE.LES	-1,94	0,16	24,08	0,17	22,15	0,33
ABM	H	BE.MOL2	-0,3	0	24,08	0,17	23,78	0,17
ABM	H	BE.MOL3	0,01	0,02	24,08	0,17	24,09	0,2
ABM	H	BE.MOL4	0,02	0,03	24,08	0,17	24,11	0,2
ABM	H	BE.MOL5	0,27	-0,02	24,08	0,17	24,36	0,16
ABM	H	BE.MOLT	1,9	-0,03	24,08	0,17	25,98	0,14
ABM	H	BE.SKQ	-0,38	-0,04	24,08	0,17	23,7	0,13
ABM	H	BE.UCCB	1,06	-0,1	24,08	0,17	25,14	0,07
ABM	H	BE.UCCS	1,29	-0,01	24,08	0,17	25,37	0,16
ABM	H	BE.WOR	-2,79	0,21	24,08	0,17	21,29	0,38
ARD	H	BE.BEBN	-0,28	-0,06	22,68	0,16	22,4	0,1
ARD	H	BE.CLA	10,98	-0,09	22,68	0,16	33,66	0,08
ARD	H	BE.CTH	12,1	-0,04	22,68	0,16	34,77	0,13
ARD	H	BE.CTH.01	-8,02	0,06	22,68	0,16	14,66	0,22
ARD	H	BE.DOU	-1,22	-0,04	22,68	0,16	21,46	0,12
ARD	H	BE.GES	-1,34	0,03	22,68	0,16	21,34	0,19
ARD	H	BE.HEY	-7,85	0,04	22,68	0,16	14,83	0,21
ARD	H	BE.HOU	-4,6	0,04	22,68	0,16	18,07	0,2
ARD	H	BE.HU1	0,72	0	22,68	0,16	23,4	0,17
ARD	H	BE.HUM	27,51	-0,14	22,68	0,16	50,19	0,03
ARD	H	BE.KLB	-6,95	0,02	22,68	0,16	15,73	0,19
ARD	H	BE.LCH	-1,41	0,03	22,68	0,16	21,27	0,19
ARD	H	BE.MEMA	10	-0,04	22,68	0,16	32,68	0,12
ARD	H	BE.MEMB	-6,97	0,02	22,68	0,16	15,71	0,18
ARD	H	BE.MEMH	9,53	-0,09	22,68	0,16	32,21	0,08
ARD	H	BE.MEMS	-3,98	0,07	22,68	0,16	18,7	0,24
ARD	H	BE.MEU	35,16	-0,09	22,68	0,16	57,84	0,07
ARD	H	BE.MRD	-5,11	0	22,68	0,16	17,57	0,16
ARD	H	BE.MRG	-7,67	0,08	22,68	0,16	15,01	0,24
ARD	H	BE.PLT	4,22	0,02	22,68	0,16	26,9	0,18
ARD	H	BE.RCHB	-4,91	-0,05	22,68	0,16	17,77	0,11
ARD	H	BE.ROB	4,38	-0,06	22,68	0,16	27,06	0,1
ARD	H	BE.TMM1	-6,14	0,04	22,68	0,16	16,54	0,2
ARD	H	BE.TMM2	-8,12	0,07	22,68	0,16	14,56	0,23
ARD	H	BE.TMM3	-8,6	0,05	22,68	0,16	14,08	0,22
ARD	H	BE.TMM4	-13,8	0,07	22,68	0,16	8,88	0,24
ARD	H	BE.VIA	-6,68	0,03	22,68	0,16	16	0,19
ARD	H	BE.WIB	-10,95	0,02	22,68	0,16	11,73	0,18
RVG	H	BE.BEBN	-24,77	0,01	46,8	0,1	22,03	0,11
RVG	H	BE.BRE.00	-1,41	0	46,8	0,1	45,39	0,1
RVG	H	BE.BRE.01	11,81	0	46,8	0,1	58,61	0,1
RVG	H	BE.HRK	1,22	0	46,8	0,1	48,02	0,1
RVG	H	BE.KIN	26,82	-0,01	46,8	0,1	73,61	0,09
RVG	H	BE.MASA	13,99	0	46,8	0,1	60,79	0,1
RVG	H	BE.OPT	-16,17	0,01	46,8	0,1	30,63	0,11
RVG	H	BE.OPTB	-17,48	0,01	46,8	0,1	29,32	0,11
RVG	H	BE.OSP	5,98	0	46,8	0,1	52,77	0,1

Table S7. Result of mixed effect method for Z component of all crustal domains and stations

Crustal domain	Component	station	Random intercept	Random slope	Global intercept	Global slope κ_r	Station specific κ_0	Station specific slope κ_{r_s}
ABM	Z	BE.CSE	-0,34	0	18,42	0,09	18,08	0,09
ABM	Z	BE.DSLB	-3,06	-0,01	18,42	0,09	15,36	0,09
ABM	Z	BE.DSLS	0,15	0	18,42	0,09	18,57	0,09
ABM	Z	BE.MOL2	-1,15	0	18,42	0,09	17,27	0,09
ABM	Z	BE.MOLT	-2,12	0	18,42	0,09	16,3	0,09
ABM	Z	BE.OTT	-1,14	0	18,42	0,09	17,28	0,09
ABM	Z	BE.RQR	5,04	0,01	18,42	0,09	23,46	0,1
ABM	Z	BE.UCCS	1,23	0	18,42	0,09	19,65	0,1
ABM	Z	BE.ZEV	1,38	0	18,42	0,09	19,8	0,1
ABM	Z	BE.CSE	-0,34	0	18,42	0,09	18,08	0,09
ABM	Z	BE.DSLB	-3,06	-0,01	18,42	0,09	15,36	0,09
ABM	Z	BE.DSLS	0,15	0	18,42	0,09	18,57	0,09
ABM	Z	BE.MOL2	-1,15	0	18,42	0,09	17,27	0,09
ABM	Z	BE.MOLT	-2,12	0	18,42	0,09	16,3	0,09
ARD	Z	BE.BEBN	-0,8	-0,02	23,49	0,1	22,68	0,07
ARD	Z	BE.CLA	4,56	-0,02	23,49	0,1	28,05	0,07
ARD	Z	BE.CTH	8,81	-0,01	23,49	0,1	32,29	0,09
ARD	Z	BE.CTH.01	2,87	0,01	23,49	0,1	26,35	0,11
ARD	Z	BE.DOU	-3,15	0,01	23,49	0,1	20,34	0,11
ARD	Z	BE.GES	0,04	-0,03	23,49	0,1	23,52	0,06
ARD	Z	BE.HEY	-3,6	0,01	23,49	0,1	19,89	0,11
ARD	Z	BE.HOU	4,01	0,08	23,49	0,1	27,49	0,17
ARD	Z	BE.HU1	3,02	0,01	23,49	0,1	26,51	0,1
ARD	Z	BE.HUM	10,61	-0,04	23,49	0,1	34,09	0,06
ARD	Z	BE.KLB	-6,46	-0,04	23,49	0,1	17,02	0,06
ARD	Z	BE.LCH	-11,07	0,06	23,49	0,1	12,41	0,16
ARD	Z	BE.MEMA	-1,28	0	23,49	0,1	22,2	0,1
ARD	Z	BE.MEMB	0,58	-0,04	23,49	0,1	24,07	0,06
ARD	Z	BE.MEMH	-3,02	-0,01	23,49	0,1	20,47	0,09
ARD	Z	BE.MEMS	-2,68	0,03	23,49	0,1	20,81	0,12
ARD	Z	BE.MEU	25,76	-0,02	23,49	0,1	49,25	0,08
ARD	Z	BE.MRD	-8,54	0,03	23,49	0,1	14,95	0,13
ARD	Z	BE.MRG	-4,29	-0,05	23,49	0,1	19,19	0,05
ARD	Z	BE.PLT	-2,45	-0,01	23,49	0,1	21,03	0,09
ARD	Z	BE.RCHB	-2,57	0,02	23,49	0,1	20,92	0,12
ARD	Z	BE.ROB	4,51	-0,01	23,49	0,1	28	0,09
ARD	Z	BE.STI	14,79	0,04	23,49	0,1	38,28	0,14
ARD	Z	BE.TMM1	-1,86	0	23,49	0,1	21,63	0,1
ARD	Z	BE.TMM2	-1,56	0,02	23,49	0,1	21,92	0,11
ARD	Z	BE.TMM3	-6,93	0	23,49	0,1	16,56	0,1
ARD	Z	BE.TMM4	-7,02	0	23,49	0,1	16,46	0,1
ARD	Z	BE.TNL	-2,97	-0,03	23,49	0,1	20,52	0,06
ARD	Z	BE.VIA	-0,05	0,01	23,49	0,1	23,44	0,1
ARD	Z	BE.WIB	-9,26	-0,01	23,49	0,1	14,22	0,08
HAIN	Z	BE.AUL	7,92	-0,05	44,93	0,03	52,85	-0,02
HAIN	Z	BE.BOU	-9,75	0,06	44,93	0,03	35,18	0,09
HAIN	Z	BE.BRQ.01	1,83	-0,01	44,93	0,03	46,76	0,02
RVG	Z	BE.BEBN	-27,9	-0,05	50,88	0,11	22,98	0,07
RVG	Z	BE.HRK	-8,32	-0,01	50,88	0,11	42,57	0,1
RVG	Z	BE.KIN	27,27	0,04	50,88	0,11	78,15	0,16

Crustal domain	Componen t	station	Random intercept	Random slope	Global intercept	Global slope κ_r	Station specific κ_0	Station specific slope κ_{r_s}
RVG	Z	BE.MASA	22,26	0,04	50,88	0,11	73,14	0,15
RVG	Z	BE.OPT	-24,11	-0,04	50,88	0,11	26,77	0,07
RVG	Z	BE.OSP	-8,38	-0,01	50,88	0,11	42,5	0,1

Table S8. Comparison of κ_0 values of H component for all stations in BELSHAKE computed by three methods of free kappa gradient, joint kappa gradient and mixed effect methods, along with the final selected κ_0 value

Crustal domain	Component	station	N	κ_0 (ms)			
				Free kappa gradient method	Joint kappa gradient method	Mixed effects method	Final selected
ABM	H	BE.BOST	3	-0.66	0	26,63	
ABM	H	BE.CSE	7	-33.46	13,37	21,56	**22**
ABM	H	BE.DSLB	8	29.08	24,01	24,91	**25**
ABM	H	BE.DSLS	2	39.52	42,09		**42**
ABM	H	BE.GRZ			35,04		
ABM	H	BE.LES	10	99.94	50	22,15	**22**
ABM	H	BE.MOL1			24,88		
ABM	H	BE.MOL2	3	10.26	21,79	23,78	**24**
ABM	H	BE.MOL3	2	27.76	32,54	24,09	**24**
ABM	H	BE.MOL4	2	28.95	34,25	24,11	**24**
ABM	H	BE.MOL5	2	34.06	23,38	24,36	**24**
ABM	H	BE.MOLS			50		
ABM	H	BE.MOLT	20	28.75	25,99	25,98	**26**
ABM	H	BE.OT2			8,33		
ABM	H	BE.OT3			17,04		
ABM	H	BE.OTT			0		
ABM	H	BE.SKQ	48	27.08	19,11	23,7	**24**
ABM	H	BE.UCCB	5	-0.44	2,8	25,14	**25**
ABM	H	BE.UCCS	11	103.51	50	25,37	**25**
ABM	H	BE.WOR	3	0.10	50	21,29	**21**
ABM	H	BE.ZEV	4	34.05	21,95		
ARD	H	BE.ANSA			22,64		
ARD	H	BE.BEBN	85	23.09	18,5	22,4	**22**
ARD	H	BE.CLA	96	35.45	25,56	33,66	**34**
ARD	H	BE.CTH	5	31.82	38,1	34,77	**35**
ARD	H	BE.CTH.01	11	-9.15	22,16	14,66	**15**

Crustal domain	Component	station	N	κ_0 (ms)			
				Free kappa gradient method	Joint kappa gradient method	Mixed effects method	Final selected
ARD	H	BE.DOU	78	19.90	16,16	21,46	**21**
ARD	H	BE.GES	75	21.82	26,42	21,34	**21**
ARD	H	BE.HEY	9	-2.74	18,54	14,83	**15**
ARD	H	BE.HOU	17	22.90	23,72	18,07	**18**
ARD	H	BE.HU1	6	-17.56	25,33	23,4	**23**
ARD	H	BE.HUM	58	58.85	36,43	50,19	**50**
ARD	H	BE.KLB	90	6	19,27	15,73	**16**
ARD	H	BE.LCH	38	20.86	25,28	21,27	**21**
ARD	H	BE.MEMA	8	31.37	33,02	32,68	**33**
ARD	H	BE.MEMB	36	12.41	17,54	15,71	**16**
ARD	H	BE.MEMH	25	34.02	21,29	32,21	**32**
ARD	H	BE.MEMS	68	26.83	26,09	18,7	**19**
ARD	H	BE.MEU	25	59.44	50	57,84	**58**
ARD	H	BE.MRD	36	17.10	18,45	17,57	**18**
ARD	H	BE.MRG	11	27.62	23,53	15,01	**15**
ARD	H	BE.PLT	6	21.29	33,86	26,9	**27**
ARD	H	BE.RCHB	17	16.13	7,6	17,77	**18**
ARD	H	BE.ROB	18	48.07	25,83	27,06	**27**
ARD	H	BE.STWA			30,12		
ARD	H	BE.THEA			23,51		
ARD	H	BE.TMM1	8	9.81	19,46	16,54	**17**
ARD	H	BE.TMM2	8	-5.24	20,97	14,56	**15**
ARD	H	BE.TMM3	8	4.69	18,13	14,08	**14**
ARD	H	BE.TMM4	8	-2.07	13,53	8,88	**9**
ARD	H	BE.TNL	4	99.15	29,32		
ARD	H	BE.VEV			17,19		
ARD	H	BE.VIA	74	15.65	20,36	16	**16**
ARD	H	BE.WIB	3	20.00	4,29	11,73	**12**
HAIN	H	BE.CLHA			25,69		

Crustal domain	Component	station	N	$\kappa_0\ (ms)$			
				Free kappa gradient method	Joint kappa gradient method	Mixed effects method	Final selected
RVG	H	BE.BRE.00	5	35.68	43,67	45,39	**45**
RVG	H	BE.BRE.01	4	151.93	50	58,61	**59**
RVG	H	BE.BREA			37,9		
RVG	H	BE.HRK	28	53.32	46,61	48,02	**48**
RVG	H	BE.KAN	2	55.38	50		
RVG	H	BE.KIN	7	76.28	50	73,61	**74**
RVG	H	BE.KINA			50		
RVG	H	BE.MASA	3	88.91	50	60,79	**61**
RVG	H	BE.OPT	15	26.16	26,87	30,63	**31**
RVG	H	BE.OPTB	4	8.54	23,44	29,32	**29**
RVG	H	BE.OSP	5	38.25	50	52,77	**53**

Table S9. Comparison of κ_0 values of Z component for all stations in BELSHAKE computed by three methods of free kappa gradient, joint kappa gradient and mixed effect methods, along with the final selected κ_0 value

Crustal domain	Component	station	N	$\kappa_0\ (ms)$			
				Free kappa gradient method	Joint kappa gradient method	Mixed effects method	Final selected
ABM	Z	BE.CSE	9	4.62	23,52	18,08	**18**
ABM	Z	BE.DSLB	11	6.65	16,05	15,36	**15**
ABM	Z	BE.DSLS	2	3.13	25,49	18,57	**19**
ABM	Z	BE.GRZ			16,41		
ABM	Z	BE.LES	37	52.86	33,62	-	**34**
ABM	Z	BE.MOL1			26,67		
ABM	Z	BE.MOL2	3	-0.34	15,57	17,27	**17**
ABM	Z	BE.MOL3			17,96		**18**
ABM	Z	BE.MOL4			12,03		**12**
ABM	Z	BE.MOL5			12,43		**12**
ABM	Z	BE.MOLT	4	37.06	19,73	16,3	**16**
ABM	Z	BE.OT2			23,68		
ABM	Z	BE.OT3			50	-	
ABM	Z	BE.OTT	2	-11.33	13,59	17,28	**17**
ABM	Z	BE.RQR	57	26.35	32,1	23,46	**23**
ABM	Z	BE.SKQ	38	26.82	23,38	-	**23**
ABM	Z	BE.UCCA			31,34		
ABM	Z	BE.UCCB	7	49.79	33,46	-	**33**
ABM	Z	BE.UCCS	16	19.04	26,58	19,65	**20**
ABM	Z	BE.WOR	3	150.44	50	-	
ABM	Z	BE.ZEV	6	39.22	31,55	19,8	**20**

Crustal domain	Component	station	N	$\kappa_0\ (ms)$			
				Free kappa gradient method	Joint kappa gradient method	Mixed effects method	Final selected
ARD	Z	BE.BEBN	125	22.71	20,71	22,68	**23**
ARD	Z	BE.BON	2	2.39	20,68		
ARD	Z	BE.CLA	104	29.62	25,69	28.05	**28**
ARD	Z	BE.COI	2	69.32	31,36		
ARD	Z	BE.CTH	15	33.64	36,04	32,29	**32**
ARD	Z	BE.CTH.01	10	10.23	29,4	26,35	**26**
ARD	Z	BE.DOU	117	15.91	22,23	20,34	**20**
ARD	Z	BE.GES	63	24.42	18,72	23,52	**24**
ARD	Z	BE.HEY	10	-0.64	18,68	19,89	**20**
ARD	Z	BE.HOU	12	20.43	41,4	27,49	**27**
ARD	Z	BE.HU1	7	-18.88	28,52	26,51	**27**
ARD	Z	BE.HUM	67	43.04	29,92	34,09	**34**
ARD	Z	BE.KLB	69	18.54	12,96	17,02	**17**
ARD	Z	BE.LCH	42	11.16	17,63	12,41	**12**
ARD	Z	BE.MEMA	9	21.43	21,08	22,2	**22**
ARD	Z	BE.MEMB	51	26.13	21,33	24,07	**24**
ARD	Z	BE.MEMH	29	22.08	18,95	20,47	**20**
ARD	Z	BE.MEMP			30,09		
ARD	Z	BE.MEMS	141	21.70	22,71	20,81	**21**
ARD	Z	BE.MEU	45	61.26	48,06	49,25	**49**
ARD	Z	BE.MRD	45	7.09	19,61	14,95	**15**
ARD	Z	BE.MRG	5	18.82	7,48	19,19	**19**
ARD	Z	BE.PLT	7	53.13	17,73	21,03	**21**

Crustal domain	Component	station	N	$\kappa_0\ (ms)$ Free kappa gradient method	Joint kappa gradient method	Mixed effects method	Final selected
ARD	Z	BE.RCHB	25	16.83	24,78	20,92	**21**
ARD	Z	BE.ROB	32	32.41	27,8	28	**28**
ARD	Z	BE.STI	95	38.87	42,1	38,28	**38**
ARD	Z	BE.THEA			22,63		
ARD	Z	BE.TMM1	6	30.18	20,48	21,63	**22**
ARD	Z	BE.TMM2	6	5.00	22,55	21,92	**22**
ARD	Z	BE.TMM3	9	12.44	12,35	16,56	**17**
ARD	Z	BE.TMM4	6	10.18	12,79	16,46	**16**
ARD	Z	BE.TNL	7	26.72	7,27	20,52	**21**
ARD	Z	BE.VEN			20,69		
ARD	Z	BE.VIA	77	17.39	24,42	23,44	**23**
ARD	Z	BE.WIB	2	23.57	6,65	14,22	**14**
HAIN	Z	BE.AUL	21	69.80	41,61	52,85	**53**
HAIN	Z	BE.AUL.00			50		
HAIN	Z	BE.BOU	44	26.88	41,12	35,18	**35**
HAIN	Z	BE.BRQ.00	14	82.89	50	<u>74,86</u>	**75**
HAIN	Z	BE.BRQ.01	8	37.88	28,57	46,76	**47**
HAIN	Z	BE.SNF	84	71.21	50	<u>64,09</u>	**64**
RVG	Z	BE.BRE.01	5	22.53	22,63	-	
RVG	Z	BE.BREA			37,19		
RVG	Z	BE.HRK	28	45.71	43,84	42,57	**43**
RVG	Z	BE.KAN	2	29.53	25,31		
RVG	Z	BE.KIN	9	77.87	50	78,15	**77**

Crustal domain	Component	station	$\boldsymbol{N}$	$\boldsymbol{\kappa_0}$ $(\boldsymbol{ms})$			
				Free kappa gradient method	Joint kappa gradient method	Mixed effects method	Final selected
RVG	Z	BE.KINA			50		
RVG	Z	BE.MASA	3	104.82	50	73,14	**73**
RVG	Z	BE.OPT	7	20.64	23,54	26,77	**26**
RVG	Z	BE.OPTB	3	16.87	19,73		**20**
RVG	Z	BE.OSP	6	37.09	42,25	42,5	**42**